technische universität
dortmund

TU Dortmund University

Doctoral Dissertation

Modeling boundary effects in finite-sized mechanical metamaterials via the reduced relaxed micromorphic model and the method of interface forces

M.Sc. *Plastiras Demetriou*

supervised by
Prof. Dr. Angela Madeo

Second reviewer: Prof. Dr. Jean-François Ganghoffer
Third reviewer: Prof. Dr. Giulio Sciarra

July 4, 2025

To my Parents and my Sister

Doctoral dissertation submitted to the Faculty of Architecture and Civil Engineering, TU Dortmund University. Defended on 7 May 2025 in Dortmund.

Abstract

In the last decades, metamaterials have gathered significant attention due to their exotic properties and potential applications. These exotic properties are a result of their engineered microstructure. We are particularly interested in mechanical metamaterials that exhibit band-gaps. Band-gaps are frequency regions for which wave propagation is prohibited and thus metamaterials can be used for vibration isolation.

Band-gaps appear in the dispersion curves calculated via Bloch-Floquet analysis on the unit cell, which is the fundamental building block of periodic metamaterials. The main assumption of Bloch-Floquet analysis is that the material is infinitely extended, possessing no boundaries. However, in real applications, metamaterials are of finite size, and therefore, they must have boundaries, whose geometry depends on the choice of unit cell "cut". For a given periodic metamaterial, there is an infinite number of possible unit cell "cuts" we can choose, that can all reconstruct the same infinitely extended metamaterial just by translation. When dealing with finite-size samples, the choice of "cut" matters, since by choosing a different"cut" we end up with a different geometry on the boundary of the metamaterial. This can cause boundary effects during wave propagation that are not accounted by Bloch-Floquet analysis.

The usual way to model metamaterials is through a finite element analysis while modeling the base microstructure's material with Cauchy elasticity. However, when one wants to model a large size metamaterial, or a structure made out of many metamaterials and traditional materials connected with each other (a metastructure), the computational cost can quickly become unsustainable. Another, more computationally efficient way, is to model them using enriched continuum theories, where we suppose that the microstructured material is now homogeneous, but has extra independent kinematical fields to account for the movements of the microstructure.

In this thesis, the enriched continuum model used to model metamaterials is the reduced version of the relaxed micromorphic model. This model has proven to be effective in the description of band-gap metamaterials and in reducing the computational cost. Its energy density is a function of the displacement $u \in \mathbb{R}^3$ and of an extra independent kinematical field, the non-symmetric micro distortion tensor $P \in \mathbb{R}^{3x3}$, which allows for the description of dispersion and band-gaps. However, even if the reduced relaxed micromorphic model captures the dispersion of a given metamaterial, it does not have a "way" of discriminating between different finite size-metamaterials, if those have been constructed using different unit cell "cuts". We note that this is true for all enriched continuum models since homogenisation is employed, and information on boundary effects is not directly included in the procedure, leading to incomplete description of finite-size metamaterials.

To overcome this difficulty, the method of interface forces is introduced, that allows us to capture boundary effects in finite sized specimens. We apply this method on different finite-sized metamaterials constructed from different "cuts", showing its versatility and effectiveness, concluding that it is an absolutely necessary step one must take, if one wants to use a homogenised description to model metamaterials of finite-size. The two, so-far used, different methods of calculating the appropriate interface forces for a given test are discussed. Furthermore, we propose an ansatz for the expression these interface forces must have on a Cauchy/RRM interface in our tests, and apply this ansatz succesfully to capture boundary effects. We separate boundary effects in general boundary effects related to finite-size, edge effects, and boundary effects that propagate in the bulk, investigate the dependence of edge effects on the number of unit cells in the y-direction and explain the meaning of our findings for the method of interface forces. Moreover, we define edge tests and discuss their potential for edge effect identification.

Lastly, we present examples of how boundary effects can affect the microstructured metamaterials' response, and what conclusions one can draw regarding potential applications.

Declaration

I declare that this dissertation was written independently and that all sources and assistance used were noted in the dissertation.

I declare that this dissertation has not been submitted in its current or another version or in parts at the TU Dortmund University or at another university in connection with a state or academic examination.

Acknowledgements

First and foremost, I would like to thank my supervisor Prof. Angela Madeo, for her continuous help and support, and most importantly for her patience and kindness.

Besides my supervisor, I would like to thank the whole continuum mechanics team, namely: Svenja, Leo, Felix, Gianluca and Jendrik, for all their help these past three years, both on work-related matters and on "completely unrelated" everyday life matters.
In particular I would like to thank:
Jendrik, Gianluca and Svenja for their suggestions and corrections on this manuscript.
Gianluca, for his repeated explanations on all kinds of things and software, the lengthy conversations on understanding things, and the exchange of Mediterranean humour.
Jendrik, for the uncountable corrections of the Latex code of this manuscript, for his explanations on the fitting in *Mathematica*® and for his explanations on many other mathematical topics.
Svenja, for her help on Bloch-Floquet analysis and her overall help, including *Comsol Multiphysics*® and my still under-construction German speaking skills.
Felix, for his help on *Comsol Multiphysics*® and his French hospitality.
Leo, for his help on *Comsol Multiphysics*®, Latex and the cluster.

Furthermore, I would like to thank all the people that made life in Dortmund a little less cloudy, those in Dortmund, namely Svenja, Leo, Felix, Gianluca, Jendrik, Adam, Jan, Markus, Dimi, Nikos, Luis and Tuncer and those abroad. Thanks a lot guys for your help and your friendship!

I would also like to thank my parents and my sister, for their support and unconditional love, for which I will be forever grateful.

This thesis would have not been written without each and every one of you!

Contents

List of Figures

List of Tables

General Introduction

In recent years metamaterials have gathered significant attention due to their remarkable properties and potential applications. Metamaterials are materials with a microstructure that is engineered for the purpose of granting them a particular effective property. Although elastic metamaterials can be engineered to have peculiar properties in statics and dynamics, this thesis is concerned with the modeling of metamaterials that are engineered for applications in the dynamic regime. Specifically we are concerned with band-gap metamaterials, that is, metamaterials that exhibit band-gaps in their dispersion diagrams. Band-gaps are frequency regions for which wave propagation is prohibited and thus metamaterials can be used for shielding applications in the band-gap range.

As often seen in literature, when a metamaterial is used for a shielding application, a Bloch-Floquet analysis is performed on the unit cell in order to calculate its dispersion curves. Then, according to the latter, a finite-size specimen is built using a precise number of unit cells, where this number is appropriate for the specific shielding application. Bloch-Floquet analysis employs Bloch-periodic boundary conditions, which means that the calculated dispersion curves actually properly characterise an infinitely extended metamaterial and therefore, that possesses no boundaries. However, in real applications, metamaterials are of finite size, and therefore, they have boundaries whose geometry depends on the choice of unit cell "cut". The unit cell is the fundamental building block of periodic metamaterials. For a given periodic metamaterial, there is an infinite number of possible unit cell "cuts" we can choose, that can all reconstruct the same infinitely extended metamaterial just by translation. When dealing with finite-size samples, the choice of unit cell "cut" matters, in the sense that by choosing a different"cut" we end up with a different geometry on the boundary of the metamaterial. This can cause boundary effects during wave propagation, that make our metamaterial behave differently than one would expect if the only information considered are the one provided by the dispersion curves. In other words, Bloch-Floquet analysis conveys no information concerning boundary effects in finite size samples, since the dispersion curves that come from this analysis characterise an infinitely extended metamaterial. In this thesis we will therefore see, how this fact affects the modeling of finite-size metamaterials and their potential applications.

The usual way to model metamaterials is through a finite element analysis while modeling the base microstructure's material with Cauchy elasticity. However, when one wants to model a large size metamaterial, or a structure made out of many metamaterials and traditional materials connected with each other (a metastructure), the computational cost can quickly become unsustainable. We can, however take advantage of the fact that metamaterials are periodic and model them using enriched continuum theories. In this way, the computational cost is greatly reduced, and we are also able to take advantage of a reliable and well established continuum theory involving the material's effective properties. Therefore, based on this idea, a significant amount of research has been published regarding the so-called homogenisation of metamaterials.

In the particular case of band-gap metamaterials, different homogenisation strategies exist, but they all work towards the same goal, which is replicating the Bloch-Floquet band structure (i.e. the procedure must lead to a model that produces dispersion curves that are as close as possible to those coming from Bloch-Floquet analysis for the metamaterial under study). The ability of several higher order and enriched continua to describe metamaterial dispersion is discussed extensively based on their dispersion polynomial, providing a guide of how one should think when attempting to model a band-gap metamaterial using an enriched continuum.

In this thesis, the enriched continuum model used to model metamaterials is the reduced version of the relaxed micromorphic model (RRMM). This model has proven to be effective in the description of band-gap metamaterials and in reducing the computational cost. Its energy density is a function of the displacement $u \in \mathbb{R}^3$ and of an extra kinematical field, the non-symmetric micro distortion tensor $P \in \mathbb{R}^{3x3}$, which allows for the description of dispersion and band-gaps. However, even if the reduced

relaxed micromorphic model captures the dispersion of a given metamaterial, it does not have a "way" of discriminating between different finite size-metamaterials, if those have been constructed using different unit cell "cuts". We note that this is true for all enriched continuum models since homogenisation is employed, and information on boundary effects is not directly included in the procedure, leading to incomplete description of the behavior of finite-size metamaterials.

To overcome this difficulty, the method of interface forces is introduced, that can be applied in general to all enriched continua, and allows us to capture boundary effects and model the behavior of finite-sized specimens. The method states that in the case of modeling a finite-sized metamaterial using an enriched continuum, any boundary effect taking place in the microstructured metamaterial must lead to the activation of a suitable surface force on an interface/free boundary, of the enriched continuum. A choice of a different unit cell "cut" leads to a different boundary effect in the microstructured metamaterial, and thus to a different surface force on the interfaces/ free boundaries, of the enriched continuum. We apply this method on different finite-sized metamaterials constructed from different unit cell "cuts", showing its versatility and effectiveness, concluding that it is an absolutely necessary step one must take, if one wants to use a homogenised description to model metamaterials of finite-size. The two, so-far used, different methods of calculating the appropriate interface forces for a given test are discussed. Furthermore, we propose an ansatz for the expression these interface forces must have on a Cauchy/RRM interface in our tests, and apply this ansatz succesfully to capture boundary effects. We pay particular attention to edge effects, where we show that they are not affected by the number of unit cells in the y-direction, and explain what this means for interface forces.

We also briefly present some examples of how boundary effects coming from the choice of unit cell "cut" can affect the microstructured metamaterials' response, and what conclusions one can draw regarding potential applications.

The following manuscript is organized as follows:

- In **Chapter** 1 the concept of metamaterials is introduced and a historical perspective is given. Next, an explanation of Bloch-Floquet analyis is given, the tool that is used for the design of band-gap metamaterials. Finally, the need for a homogenised description of metamaterials is emphasized.
- In **Chapter** 2 Cauchy, higher gradient and enriched continuum theories are introduced. A historical perspective is given and some applications of each theory. For each theory in its isotropic case, the potential for infinite band-gap metamaterial description is demonstrated based on the properties of the dispersion polynomial of each theory.
- In **Chapter** 3 the model used in this thesis, i.e. the reduced relaxed micromoprhic model is introduced. All properties of the model are explained and the potential of the model for the description of infinite-size band-gap metamaterials is discussed extensively.
- In **Chapter** 4 a locally resonant metamaterial is introduced and two finite-sized metamaterials are constructed from two different unit cell "cuts" that correspond to the infinite locally resonant metamaterial. We simulate these finite-sized metamaterials in the frequency domain, first using the full microstructure and Cauchy elasticity, and afterwards using the reduced relaxed micromoprhic model. Comparing the results, the need for a method to capture boundary effects related to the finite-size and therefore the unit cell "cut", is stressed out.
- In **Chapter** 5 the method of interface forces in introduced, in order to capture boundary effects in finite-size specimens made from different unit cell "cuts". The method is applied to capture neglected boundary effects in the case of the locally resonant metamaterial of previous chapter. Cases of edge effects, boundary effects that propagate in the bulk, and more general boundary effects related to finite-size are treated, demonstrating the potential of the method. Regarding edge effects, it is shown that they are not affected by the number of unit cells in the y-direction, as long as this number is bigger than one. The relation of this fact to interface forces is discussed. Furthermore, edge tests are defined and their potential for edge effect prediction is discussed.
- In **Chapter** 6 a labyrinthine acoustic metamaterial is introduced, for which experimental tests have shown, that depending on the choice of unit-cell "cut", it can show higher or lower values of Transmissibility. Four finite-size metamaterials are modeled using the RRMM coupled with the method of interface forces and the method's effectiveness in capturing boundary effects for all four specimens and several frequencies is demonstrated. An ansatz for the interface forces regarding Cauchy/RRMM interfaces is introduced and applied to most cases with success. Lastly, we explain the limits of Bloch-Floquet analysis based on our findings.

- In **Chapter** 7 we show the so-far discovered implications of the choice of unit cell "cut" on the response of finite-sized specimens with examples and discuss possible future applications.

Notational agreement

We denote by $\mathbb{R}^{3\times3}$ the set of real 3×3 second order tensors and by $\mathbb{R}^{3\times3\times3}$ the set of real $3\times3\times3$ third order tensors. The standard Euclidean scalar product on $\mathbb{R}^{3\times3}$ is given by $\langle X,Y\rangle_{\mathbb{R}^{3\times3}}=\operatorname{tr}(X^TY)$ and, thus, the Frobenius tensor norm is $\|X\|^2=\langle X,X\rangle_{\mathbb{R}^{3\times3}}$. Moreover, the identity tensor on $\mathbb{R}^{3\times3}$ will be denoted by $\mathbb{1}$, so that $\operatorname{tr}X=\langle X,\mathbb{1}\rangle$.

We adopt the usual abbreviations of Lie-algebra theory, i.e.

- $\operatorname{Sym}(3):=\{X\in\mathbb{R}^{3\times3}\mid X^T=X\}$ denotes the vector space of all symmetric 3×3 matrices.
- $\mathfrak{so}(3):=\{X\in\mathbb{R}^{3\times3}\mid X^T=-X\}$ is the Lie-algebra of skew symmetric tensors.
- $\mathfrak{sl}(3):=\{X\in\mathbb{R}^{3\times3}\mid \operatorname{tr}(X)=0\}$ is the Lie-algebra of traceless tensors.
- $\mathbb{R}^{3\times3}\cong\mathfrak{gl}(3)=(\mathfrak{sl}(3)\cap\operatorname{Sym}(3))\oplus\mathfrak{so}(3)\oplus\mathbb{R}\mathbb{1}$ is the orthogonal Cartan-decomposition of the Lie-algebra.

For all $X\in\mathbb{R}^{3\times3}$, we consider the decomposition

$$X=\operatorname{dev}\operatorname{sym}X+\operatorname{skew}X+\frac{1}{3}\operatorname{tr}(X)\mathbb{1}\,,$$

where

- $\operatorname{sym}X=\frac{1}{2}(X^T+X)\in\operatorname{Sym}(3)$ is the symmetric part,
- $\operatorname{skew}X=\frac{1}{2}(X-X^T)\in\mathfrak{so}(3)$ is the skew-symmetric part,
- $\operatorname{dev}X=X-\frac{1}{3}\operatorname{tr}(X)\mathbb{1}\in\mathfrak{sl}(3)$ is the deviatoric part.

Throughout this thesis, we denote fourth order tensors $\mathbb{C}\colon\mathbb{R}^{3\times3}\to\mathbb{R}^{3\times3}$ by double struck letters, while Latin subscripts take the values 1,2,3, and we adopt the Einstein convention of sum over repeated indices if not differently specified.

We denote by $\mathbb{C}X$ the the double contraction of a fourth order tensor with a second order tensor. In the Einstein summation convention we write

$$(\mathbb{C}X)_{ij}=\mathbb{C}_{ijkl}X_{kl}\,.$$

The operation of single contraction between tensors of suitable order is denoted as

$$(\sigma n)_i=\sigma_{ij}n_j\,.$$

The gradient of a vector field u and a second order tensor field P are defined respectively as

$$\begin{aligned}(\nabla u)_{ij}&=u_{i,j}\,,\\(\nabla P)_{ijk}&=P_{ij,k}\,.\end{aligned}$$

The divergence of a vector field u and a second order tensor field P are defined respectively as

$$\begin{aligned}\operatorname{Div}u&=u_{i,i}\,,\\(\operatorname{Div}P)_i&=P_{ij,j}\,.\end{aligned}$$

The curl of a vector field u is defined as

$$(\operatorname{curl}u)_i=\varepsilon_{ijk}u_{k,j}$$

where ε_{ijk} is the Levi-Civita third order permutation tensor. Let P be a second order tensor and P_1,P_2,P_3 three vector fields such that

$$P=\begin{bmatrix}P_1^T\\P_2^T\\P_3^T\end{bmatrix}.$$

The Curl of P is defined as

$$\operatorname{Curl} P = \begin{bmatrix} (\operatorname{curl} P_1)^T \\ (\operatorname{curl} P_2)^T \\ (\operatorname{curl} P_3)^T \end{bmatrix}$$

which in index notation is

$$(\operatorname{Curl} P)_{ij} = \varepsilon_{jkl} X_{il,k} \, .$$

Chapter 1

Metamaterials

1.1 Introduction

In the last decades, the research field of metamaterials has attracted increasing attention given the interesting properties that these materials can possess and their potential applications. Metamaterials, from the Greek word "meta" meaning "beyond" or "after", are materials with a microstructure engineered to grant them properties that surpass those usually found in natural materials. In a simpler definition, metamaterials are structures that allow us to engineer the interaction of fields with matter. Though there are many structures that qualify as metamaterials, the most common is that of an arrangement of elements whose size and spacing is much smaller relative to the scale of spatial variation of the exciting field. In this limit, the responses of the individual elements, as well as their interactions, can often be incorporated (or homogenised) into continuous, effective material parameters. The collection of discrete elements is thus replaced conceptually by a hypothetical continuous material. The properties of this hypothetical continuous material are derived both from the inherent properties of its base material, as well as from the geometrical properties of its microstructure, which is precisely what is taken advantage of, when their properties need to be engineered. A 2D natural homogeneous material and a same size periodic structure that qualifies as a metamaterial can be seen in (Fig. 1.1).

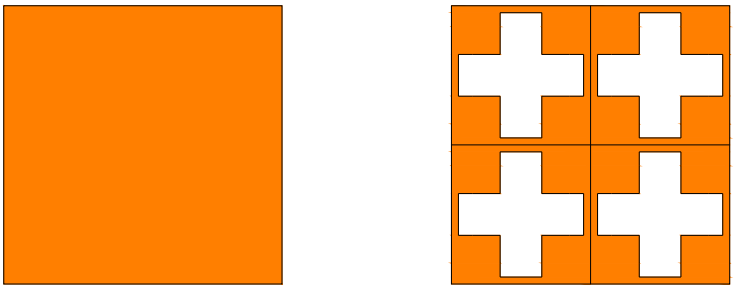

Figure 1.1: Simple distinction between a 2D material (left) and a same size 2D structure that qualifies as a metamaterial (right).

1.2 History

Historically, the first allegation of a metamaterial came from Victor Veselago in 1968 [97], where he proposed that materials with both negative permeability and positive permittivity are possible theoretically. It wasn't until the 2000s though, that this was proven experimentally [91]. The same group showed in the following years, that electromagnetic/photonic metamaterials can show a negative effective index of refraction [87], and that they can be used for exotic lensing and cloaking [69]. This meant that now, in these structures called metamaterials, wave propagation could be controlled in ways that were not possible using natural materials. This sparked a huge interest among researchers, growing the metamaterial field exponentially with time. After such interesting phenomena have been demonstrated in photonic

metamaterials, the ideas were extended to mechanical/phononic metamaterials, where researchers were able to show that elastic metamaterials can possess a negative Poisson's ratio [46], a negative effective mass density [36], simultaneously negative effective shear modulus and mass density, leading to negative refraction [101] and other exotic properties. Other interesting phenomena arising in metamaterials worth mentioning include focusing [10, 31], channeling [5, 43, 58] and chiral effects [23, 24, 61, 77, 78]. Perhaps one of the most unique and interesting properties of metamaterials are band-gaps [40, 52, 55]. Again, an idea initially found in photonic metamaterials, the photonic band-gap, extended in mechanics, gave us the phononic band-gap. What band-gaps are, and what ways have been found so far to create them in elastic/acoustic metamaterials will be explained in the next section.

1.3 Periodic metamaterials and Bloch-Floquet analysis

The most usual class of metamaterials are periodic metamaterials. These are obtained by a periodic repetition of a specific unit cell in space (see Fig. 1.2).

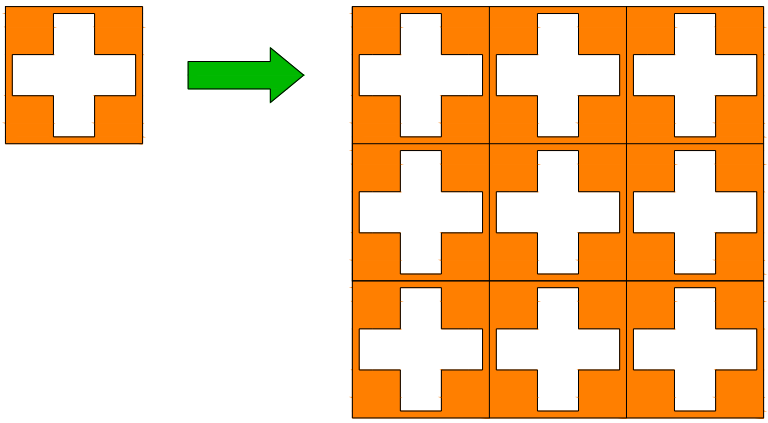

Figure 1.2: A 3×3 periodic metamaterial built by the periodic repetition of a unit cell in space.

Researchers are particularly interested in periodic metamaterials, usually because with the correct design of their structural unit (the unit cell), they can exhibit band-gaps in their dispersion diagrams. Band-gaps are frequency ranges, in which wave propagation is prohibited. In a band-gap, instead of a propagating wave, we have an evanescent wave. Physically this means that the wave is exponentially decayed in space since it is heavily attenuated in the microstructure. Therefore metamaterials with band-gaps can be used to attenuate waves in a frequency region of interest, acting as shields. The next logical question would then be, how does one calculate dispersion diagrams for a given metamaterial?

As mentioned before, metamaterials are periodic media, and wave propagation in periodic media is governed by the Bloch-Floquet theorem. The procedure of applying the theorem and calculating the dispersion curves for the infinitely periodic medium is called Bloch-Floquet analysis. As the name of the analysis states, the method owes it to Felix Bloch [4], who applied Floquet's theory [22] to periodic crystal lattices, providing us with a theory for band structure computation of periodic media. Bloch's theorem was initially used in electronic crystals to calculate the electronic band structure and later extended in photonic and phononic crystals to calculate the corresponding photonic and phononic band structure respectively.

We will briefly explain here how Bloch-Floquet analysis works, for the calculation of dispersion curves for metamaterials. The whole procedure of Bloch-Floquet analysis is explained in detail in [11], from the Bloch-Floquet theorem up to the finite element implementation in *Matlab*®. Here we will only show what is necessary for understanding this thesis.

We assume to have a 2D rectangular periodic structure (see Fig. 1.3 left). The structure is composed of the periodic repetition of the unit cell seen in Fig. 1.3 (right) in two orthogonal directions denoted by d_x , $d_y \in \mathbb{R}^2$ which has dimensions L_x and L_y.

The periodicity of the structure allows us to express the position of each point P in the structure (given by vector $r_P \in \mathbb{R}^2$ in Fig. 1.3) as a function of the position $r_U \in \mathbb{R}^2$ of the corresponding point U in the reference unit cell by adding to the vector r_U, a vector which expresses the translation of the reference

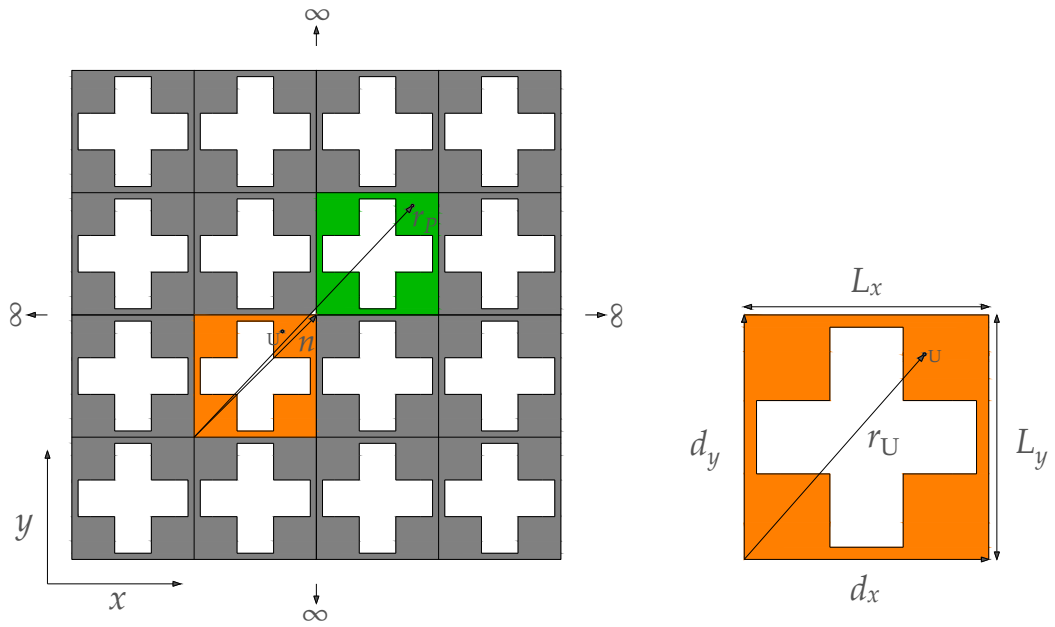

Figure 1.3: Infinitely extended 2D rectangular periodic structure (left) and the unit cell (right).

unit cell across the lattice in order to be in the position of the unit cell that includes point P, namely vector $n = n_x d_x + n_y d_y$ in Fig. 1.3. The vector n represents the number of unit cell shift in $x-$direction (n_x) and in $y-$direction (n_y). This implies that r_P can be expressed as

$$r_P = r_U + n_x d_x + n_y d_y = r_U + n\,. \tag{1.1}$$

We can imagine that if the two unit cells (those that include points U and P respectively) had their own local coordinate system, points U and P would have the same exact coordinates, and this is what is meant by "corresponding points". The Bloch-Floquet theorem states that the solution of a wave propagation problem in a periodic medium can be expressed as a plane wave modulated by a periodic function $\overline{q}$, i.e.

$$q(r,k,\omega) = \overline{q}(r,k)e^{i\langle k,r\rangle}\,e^{i\omega t} \tag{1.2}$$

where $e^{i\omega t}$ is the plane wave with the angular frequency $\omega > 0$, $\overline{q}(r,k)$ is the periodic function, that has a spatial periodicity (i.e. it is periodic in r) due to the periodicity of the structure, and $k \in \mathbb{R}^2$ is the wavevector. A direct consequence of this statement is that wave propagation in an infinite periodic medium can be expressed in terms of the response of a reference unit cell and an exponential term, defining the relative amplitude and phase change as the wave propagates from one unit cell to the next. This, in turn, means that through Equations (1.2) and (1.1), the wave response at a point P in the periodic structure, which we will denote as $q(r_P,k,\omega)$, can be expressed as a function of the response at the corresponding point U in the reference unit cell, denoted as $q(r_U,k,\omega)$ by

$$q(r_P,k,\omega) = q(r_U,k,\omega)e^{i\langle k,n_x d_x + n_y d_y\rangle}\,. \tag{1.3}$$

This can be equivalently written as

$$q(r_P,k,\omega) = q(r_U,k,\omega)e^{i\langle k,r_P - r_U\rangle}\,. \tag{1.4}$$

Thanks to the Bloch-Floquet theorem, in order to implement Bloch-Floquet analysis in any finite element software, we only need to import the geometry of our unit cell and not of the infinite periodic structure. Then we need to enforce equation (1.4) on opposite boundaries of the unit cell (see Fig. 1.4 left), on the unknown of our problem, which is the displacement field $u \in \mathbb{R}^2$.

Then equation (1.4) becomes

$$u(r_P,k,\omega) = u(r_U,k,\omega)e^{i\langle k,r_P - r_U\rangle} \tag{1.5}$$

where $u \in \mathbb{R}^2$ is the displacement field. Equation (1.5) is what is called a Floquet-Bloch periodic boundary condition. This is exactly what we apply on the boundaries of our unit cell and it must be applied on all pairs of opposite boundaries of the unit cell (orange and green boundaries in Fig. 1.4). The reason for

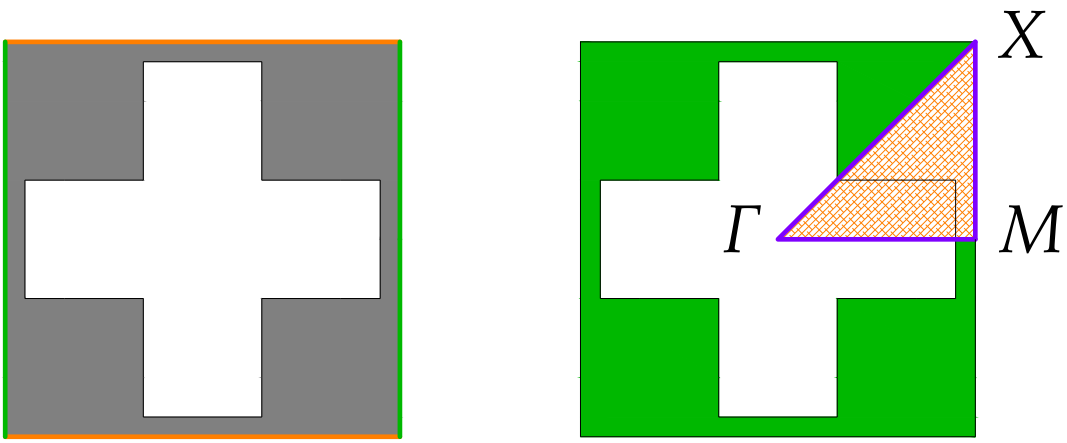

Figure 1.4: Boundaries for application of Floquet-periodicity during Bloch-Floquet analysis (left) and the Irreducible Brillouin Zone (right).

this is that these two sets of boundaries (green or orange) are what connect the unit cell to adjacent unit cells, and they therefore carry corresponding points for which the Bloch-Floquet theorem holds. Since we applied Floquet periodicity on the displacement, which is our unknown, this periodicity automatically holds for the stress and the traction on the boundaries, since they are functions of the unknown. After the application of the Floquet-Bloch periodicity on the boundaries, theoretically we could discretize our geometry with finite elements and solve a generalised eigenvalue problem in which the wavenumber is given by us, the eigenvalues are the frequencies ω, and the eigenvectors are the different mode shapes of the unit cell.

This procedure would lead to the calculation of dispersion surfaces if this was done for all possible wavenumbers in k-space. However, the 2π periodicity of the dispersion surfaces has been proven in [6]. Taking advantage of this, and exploiting symmetries of the wave propagation problem and symmetries of the geometry of the unit cell, the values of the wavenumber that one must use, to get all the necessary information in order to describe wave propagation in the infinite periodic structure, are restricted to a zone called the Irreducible Brillouin Zone (in short: IBZ) [11].

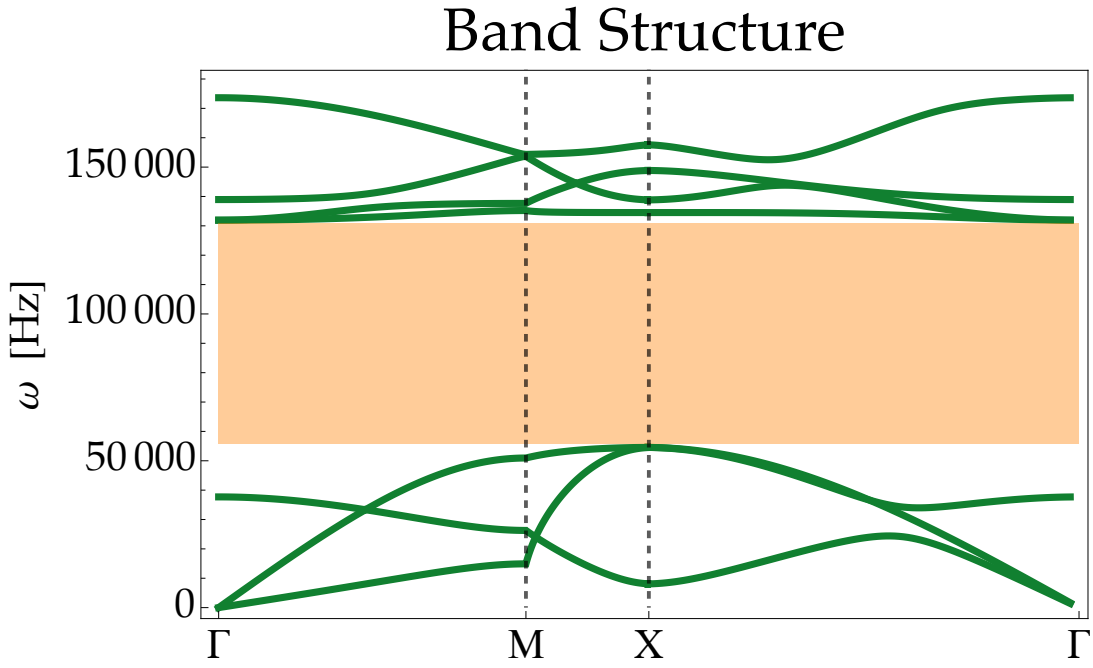

Figure 1.5: Band structure (or dispersion diagram) for the cross unit cell shown in Fig. 1.4 for a side length of the unit cell equal to 2 cm and the base material being structural steel. A band-gap can be seen colored in orange. The greek letters on the x-axis correspond to specific wavenumbers shown with the same Greek letters in Fig. 1.4, thus implying the "scanning" of the IBC by the k-vectors.

For the unit cell showed in this section, the Irreducible Brillouin Zone is the orange-hatched triangle in Fig. 1.4. The wavenumber can take values that span the whole area of the IBZ, but we are usually interested in the minima and maxima of the dispersion surfaces. Consequently, we evaluate the dispersion surfaces on the boundary of the IBZ, namely the Irreducible Brillouin Contour (IBC) (see Fig. 1.4 for the IBC of the unit cell of this section, colored in purple). This is based on the assumption that the minima and maxima of the surfaces lie only on the IBC. However, there are cases for which this assumption is indeed incorrect, so one should be very careful and scan the whole IBZ. In most cases however, the assumption is valid and only wavenumbers that lie in the IBC are those that are used in the Bloch Floquet analysis to calculate what is often called the band structure of the metamaterial (see Fig. 1.5).

The dispersion curves obtained from Bloch-Floquet analysis exhibit the following two important scaling properties:

- The dispersion curves scale proportionally in frequency with respect to the base material's wave speed. This means that when keeping the geometry and size of the unit cell unaltered, using a stiffer or less dense base material would bring the curves higher in the frequency axis.
- Both the wavevector k and the frequency ω scale inversely with the unit cell size: This implies that when keeping the geometry and base material of the unit cell unaltered, making the size of the unit cell bigger using a homothetic scaling would bring the curves lower in the frequency axis and lower in the wavenumber axis.

These two properties are of great importance, and an enriched continuum describing dynamical metamaterial response should have dispersion curves that exhibit the same scaling properties, as it was clearly explained in [99]. More details are given in chapter 3 where the reduced relaxed micromorphic model is introduced.

Something else worth noticing in Fig. 1.5, is that some curves start from the origin of the diagram (we call these acoustic curves) but there also curves that start from a higher point on the y-axis (we call these optic curves). The frequency of an optic curve when $k \to 0$ is called a cutoff frequency, or more simply, a cutoff.

Two other important properties of the dispersion curves worth mentioning are the following:

- The dispersion curves' optic modes cutoffs do not change when the wavevector changes direction, since they correspond to a frequency where $k = 0$.
- The acoustic modes can always be approximated linearly at a small range near the start of the origin of the dispersion diagram. This happens because at low frequencies the wavelength is very long, and the periodic structure appears more homogeneous to the wave, thus the metamaterial behaves as a Cauchy continuum.

These two properties are also important for an enriched continuum describing dynamical metamaterial response since its' dispersion curves must respect the same properties. In Fig. 1.5 we can notice an orange colored region for which no dispersion curve is present, the so-called band-gap. Here we are plotting the frequency vs. the real part of the wavenumber because we are interested in propagating waves. We notice that in the band-gap, for any frequency, there is no corresponding real wavenumber. In the band-gap region, the wavenumber becomes purely imaginary and the wave becomes an evanescent wave, decaying exponentially in space. The corresponding imaginary wavenumbers for each frequency in the band-gap, indicate the attenuation of the wave.

Since we are studying metamaterials using linear elasticity, where no energy conversion to heat is present (i.e. damping), the wave is not attenuated via damping phenomena. Attenuation is rather achieved through an energy distribution in microstructural components, and different mechanisms of distribution have been identified. A very short review is discussed in the following section.

1.3.1 Band-gap mechanisms

Many researchers in mechanical metamaterials have tried to identify different ways in which a band-gap can be formed. The two most typical band-gap mechanisms, i.e. the ways in which band-gaps are produced, are called "Bragg scattering" and "local resonance" [51]. In Bragg scattering, we can say that a band-gap appears as a result of destructive interference of the wave reflections from the periodic

inclusions within the lattice [6, 89]. In local resonance, resonators are embedded in the lattice, that hinder wave propagation around their resonance frequencies [52]. Moreover, a band gap can be generated by the combination of these two mechanisms [44, 72]. One other mechanism discovered more recently is called "Inertial amplification", in which effective inertia of the wave propagation medium is amplified via embedded amplification mechanisms [106]. This method is particularly promising for low frequency wave attenuation without the need for big lattice constants or big resonator masses, since it depends on the amplification of a small mass. A proof that mechanisms are different ways to produce band-gaps is usually given through a band structure plot using the imaginary part of the wavenumber, since the idea is that a different mechanism produces different attenuation. A more detailed discussion can be found in [105].

1.3.2 Limits of Bloch-Floquet analysis

As explained above, the main assumption of Bloch-Floquet analysis is that the material is extended to infinity (an infinite number of unit cells is used for its construction), therefore the metamaterial has no boundaries. However, the dispersion curves coming from Bloch-Floquet analysis are inevitably used as a design tool in the real world, where every metamaterial is inevitably a finite-sized metamaterial.
Then, we can state that a finite-sized metamaterial's response can be described accurately by Bloch-Floquet analysis (Bloch-Floquet dispersion curves and mode shapes), only if the finite size is big enough in order for the infinite size metamaterial assumption to be approximately true. From results we will show in later chapters, it will become clear that when a metamaterial is of finite size, boundary effects arise, and they become more and more dominant as the size of the structure decreases in size. Then the question arises, when can these boundary effects be neglected in relation to the structure's size? Or in simpler terms, how many unit cells must be used so that boundary effects play a negligible role in the response of a finite-sized metamaterial? In this limit, the response of the structure would only be governed by the Bloch-Floquet dispersion curves and mode shapes, i.e. the bulk material behavior. Usually, the answer given is that a very big number of unit cells must be used to represent a metamaterial extended to infinity. By using more unit cells, the boundary of the metamaterial scales linearly and the bulk scales quadratically, until in some point, theoretically, the ratio of boundary to bulk would tend to zero. Another, more interesting answer to the same question, will be given at the end of Chapter 6, in terms of metamaterial response using different unit cell "cuts" and metamaterial modeling using homogenisation and interface forces.

1.4 Homogenisation of metamaterials

Apart form understanding how metamaterials function, how band-gaps are formed and discovering new and exotic properties, researchers have been trying to model metamaterials as homogenised media with effective properties for a number of valid reasons.

First, in metamaterials, the unit cell size is usually smaller than the wavelength of the travelling wave, which allows us to interpret the periodic structure as an "effective medium". Moreover, the homogenisation process leads to effective parameters that allow us to identify the main metamaterial's exotic properties. Finally, the computational cost is another key motivation in favor of modeling metamaterials as homogeneous media. The usual way to model elastic metamaterials is through a finite element analysis, while modeling the exact microstructure with Cauchy elasticity. However, when one wants to model a large metamaterial, or a structure made out of many metamaterials connected with each other (a metastructure), the computational cost can quickly become unsustainable. Therefore homogenisation is proposed for the design needs of the future, since a homogeneous material will require less computational time, because its geometry needs significantly less finite elements to be described accurately.

Homogenisation of metamaterials has been widely employed both in statics and in dynamics of metamaterials. Here we will be limited to using a homogenised description of metamaterials in dynamics since the metamaterials under our investigation fall in the category of band-gap metamaterials. Regarding metamaterials' dynamic homogenisation, many different strategies have been proposed for obtaining an effective homogenised medium [49, 92, 96], but all strategies work towards the same goal: obtaining dispersion curves for the homogenised medium, which will be as close as possible to the band structure of the metamaterial coming from Bloch-Floquet analysis on the unit cell.

The strategy of our choice is using an enriched continuum, to "homogenise" our metamaterial, which

means we are posing that this new homogenised material, has new kinematic fields that carry extra degrees of freedom related to the movements of the microstructure (see Fig. 1.6). A more detailed explanation will be given in the Chapters 2 and 3. We will also see in the Chapter 4, why all of the dynamical homogenisation schemes need extra enrichment in order to catch the response of real finite-size specimens constructed from different unit cell "cuts".

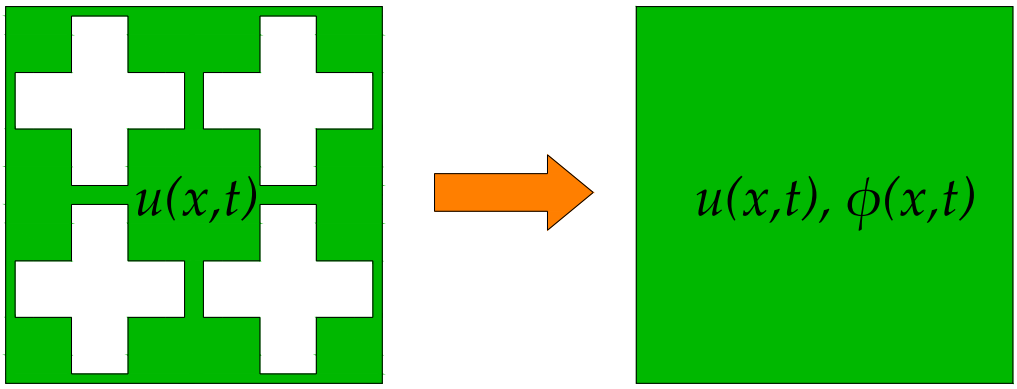

Figure 1.6: Microstructured metamaterial described by the kinematical field of the macroscopic displacement $u(x,t)$ (left) and homogenised enriched continuum describing the same metamaterial using the usual displacement field $u(x,t)$ and an extra kinematical field $\phi(x,t)$ (right).

Chapter 2

Cauchy, higher gradient and enriched continua

2.1 Introduction

A solid is essentially a very big collection of atoms, molecules or ions, where each atom, molecule or ion, interact with its adjacent through electromagnetic forces. However, when modeling solids in the macroscopic world, the main assumption one makes, is that the solid is homogeneous and can be treated as a continuum. In this way the interactions in the microscopic level are neglected. We will see in the following how this treatment only leaves us with a few engineering constants to calculate in order to describe material behaviour in the macroscopic world. Of course these engineering constants cannot be anything else than some sort of average of the interactions at the microscopic level.

There exist many theories that describe material behavior, such as linear elasticity, non-linear elasticity, linear viscoelasticity and many others. In this thesis we will limit ourselves to material behaviors appropriate for the modeling of metamaterials under dynamic loading and small strains, which will limit us to using Cauchy, higher gradient and Enriched continuum theories.

2.2 Cauchy elasticity

In 1660, Robert Hooke [35] was the first to discover that for many materials, the displacement under a load is proportional to the applied force. This discovery, that was published later in 1678, established the concept of linear elasticity upon the fact of direct proportionality between force and displacement, although the notion of stress and strain was still missing from the picture. In the following years, several researchers, including Leibniz, Bernoulli, and Euler, proposed an idea of internal tension/force per unit area, i.e. stress.

However, it was Augustin-Louis Cauchy [9] who formalized the concept of stress within the framework of a generalized three-dimensional theory. Cauchy demonstrated, using the tetrahedron argument, that we can describe the internal interactions of a continuum due to external loading, using a 3x3 symmetric matrix called stress (denoted with the Greek letter σ), that must transform as a tensor.

The two main assumptions of Cauchy's theory are the following:

- The only kinematical field is the displacement $u \in \mathbb{R}^3$.
- The stress σ in each point $x \in \mathbb{R}^3$ of the material, is a symmetric tensor that depends on the symmetric part of the gradient of the displacement $\operatorname{sym}\nabla u$ evaluated in the same material point x.

The Strain(W) and Kinetic(K) energy density of a Cauchy continuum are defined as

$$W(\operatorname{sym}\nabla u) \coloneqq \frac{1}{2}\langle \mathbb{C}_{\mathrm{e}}\ \operatorname{sym}\nabla u, \operatorname{sym}\nabla u\rangle\,, \tag{2.1}$$

$$K(\dot{u}) \coloneqq \frac{1}{2}\rho\,\langle \dot{u}, \dot{u}\rangle\,. \tag{2.2}$$

The associated Langrangian $\mathcal{L}$ and Action functional $\mathcal{A}$ can be defined respectively as

$$\mathcal{L}(\dot{u}, \operatorname{sym} \nabla u) \coloneqq K(\dot{u}) - W(\operatorname{sym} \nabla u)\,, \tag{2.3}$$

$$\mathcal{A} \coloneqq \iint\limits_{\Omega \times [0,T]} \mathcal{L}\left(\dot{u}, \operatorname{sym} \nabla u\right)\, \mathrm{d}x\, \mathrm{d}t\,, \tag{2.4}$$

and its first variation $\delta\mathcal{A}$ is taken with respect to the displacement u, which is the only independent kinematical field. We consider that $\delta\mathcal{A}$ is equal to the internal work W^{int} of the Cauchy continuum ($W^{int} = \delta\mathcal{A}$) and that the external work is given only by externally applied volume forces and boundary forces respectively, i.e.

$$W^{\text{ext}} = \int\limits_{\Omega} \langle f_V^{\text{ext}}, \delta u \rangle \, \mathrm{d}V + \int\limits_{\partial\Omega} \langle f_S^{\text{ext}}, \delta u \rangle \, \mathrm{d}s\,. \tag{2.5}$$

The principle of virtual work $W^{\text{int}} = W^{\text{ext}}$ thus implies the strong form of the balance equations governing Cauchy elasticity, in the absence of external body (volume) forces ($f_V^{\text{ext}} = 0$ and $f_S^{\text{ext}} = f^{\text{ext}}$)

$$\rho\, \ddot{u} = \operatorname{Div} \sigma\,, \tag{2.6}$$

with

$$\sigma = \mathbb{C}_{\text{e}} \operatorname{sym} \nabla u \tag{2.7}$$

where σ is the Cauchy stress and $\mathbb{C}_{\text{e}}$ is a fourth order elasticity tensor. The Dirichlet and Neumann boundary conditions are respectively

$$u = u^{\text{ext}}, \tag{2.8}$$

$$t = f^{\text{ext}} \tag{2.9}$$

where

$$t = \sigma \cdot n \tag{2.10}$$

is the Cauchy traction. The complete procedure of taking the first variation of our Action functional in the specific case of isotropic elastictiy can be found in Appendix A.

The number of independent coefficients of the elasticity tensor $\mathbb{C}_{\text{e}}$ depends on a number of factors. In three dimensions, a general fourth order tensor C_{jikl} with no symmetry contains $3^4 = 81$ independent coefficients. However, here we are dealing with an elasticity tensor (coupling stress to strain), where stress and strain are both symmetric tensors, which gives the elasticity tensor its minor symmetries ($6^2 = 36$ independent coefficients)

$$C_{ijkl} = C_{jikl} = C_{ijlk} \tag{2.11}$$

Also the fact that the Strain energy density is written in a quadratic form, gives the elasticity tensor its major symmetry

$$C_{ijkl} = C_{klij}\,. \tag{2.12}$$

Combining the effect of the minor and major symmetries reduces the number of independent coefficients to 21. For more details, see [38]. The number of independent coefficients can be further reduced depending on the class of symmetry of the material. The number of independent coefficients for different symmetry classes, in the 3D case can be seen in Table 2.1. For an in depth explanation, see [63]. Since we want to emphasize that a bulk Cauchy material shows no dispersion, and in this case showing or not showing dispersion is not a question of symmetry, we will proceed to show that a bulk isotropic Cauchy material shows no dispersion, but this of course holds for more anisotropic classes of symmetry. We also limit ourselves to the plain strain case, as this thesis is only concerned with results whose main assumption is that of plain strain. In the case of isotropy, $\mathbb{C}_{\text{e}}$ has only 2 independent coefficients [63].

These are the well known lame constants λ and μ. In planar linear elasticity their expression read

$$\lambda = \frac{E\nu}{(1+\nu)(1-\nu)} \tag{2.13}$$

and

$$\mu = G \tag{2.14}$$

Symmetry	**Independent Elastic Constants 3D**
Triclinic	21
Monoclinic	13
Orthotropic	9
Tetragonal	6
Transversely Isotropic	5
Cubic	3
Isotropic	2

Table 2.1: Number of independent elastic constants for different symmetries in 3D.

where $G = \frac{E}{2(1+\nu)}$ is the well known shear modulus, E is the Young's modulus and ν is the Poisson's ratio. Instead of using λ and μ, we can introduce the bulk modulus κ where $\kappa = \lambda + \mu$ in 2D. Therefore, our elasticity tensor is now a function of κ and μ instead of λ and μ. This allows for simpler positive definiteness conditions of the elasticity tensor. Additionally, we will use symbols κ_e and μ_e instead of κ and μ.

Since we want to study wave propagation in the infinite bulk medium, we are interested in the Equilibrium Equations (2.6) in contrast to the boundary conditions (2.8) and (2.9) which are of no interest here. We proceed by substituting equation (2.7) in equation (2.6), giving us a version of the Equilibrium Equations where the displacement is also visible by ∇u in the stress

$$\rho \ddot{u} - \mathrm{Div}\big[\mathbb{C}_\mathrm{e}\, \mathrm{sym}\, \nabla u\big] = 0\,. \tag{2.15}$$

We then substitute the displacement field with the plane wave ansatz under the plane strain hypothesis

$$u_j = U_j e^{i(k_1 x + k_2 y - \omega t)} \tag{2.16}$$

where u_j represents a generic component of the displacement vector, U_j is a scalar amplitude, $(k_1, k_2)^T = k(\sin\phi, \cos\phi)^T$ are the wavevector components with ϕ as the angle giving the direction of propagation, $k > 0$ is the wave vector length, t is time and ω is the frequency. Without any loss of generality, we assume $\phi = 0$, i.e. a wave traveling in $x-$direction.

After substitution of (2.16) in (2.15) and some manipulation, we end up with the linear homogeneous system

$$\begin{bmatrix} k^2(\kappa_e + \mu_e) - \rho\omega^2 & 0 \\ 0 & k^2\mu_e - \rho\omega^2 \end{bmatrix} \begin{bmatrix} U_1 \\ U_2 \end{bmatrix} = \begin{bmatrix} 0 \\ 0 \end{bmatrix}. \tag{2.17}$$

It is then easy to see that in order for this system to have a non trivial solution, the determinant of the matrix (called acoustic tensor)

$$\begin{bmatrix} k^2(\kappa_e + \mu_e) - \rho\omega^2 & 0 \\ 0 & k^2\mu_e - \rho\omega^2 \end{bmatrix} \tag{2.18}$$

needs to be zero. This provides us with a single algebraic equation

$$(k^2(\kappa_e + \mu_e) - \rho\omega^2)(k^2\mu_e - \rho\omega^2) = 0\,, \tag{2.19}$$

which is a polynomial in terms of wavenumber k and frequency ω and called the dispersion polynomial of isotropic Cauchy elasticity.

Extracting the dispersion relations, i.e. solving with respect to ω, we arrive at

$$\omega = k\sqrt{\frac{\mu_e}{\rho}} \tag{2.20}$$

describing pure shear waves, and

$$\omega = k\sqrt{\frac{\kappa_e + \mu_e}{\rho}} \tag{2.21}$$

describing pure pressure waves. There is always a second negative solution because the dispersion polynomial is a function of ω^2, but we are only interested in positive frequencies.

A proof of why these relations describe pure shear and pure pressure modes respectively comes from the calculation of the corresponding mode shapes, i.e. the eigenvectors of the acoustic tensor (2.18). Expressions (2.20) and (2.21) are in the form $\omega = f(k)$ and they constitute the eigenvalues of our linear homogeneous problem (2.17). For the calculation of the mode shapes, one has to plug back the eigenvalues into the linear homogeneous system and calculate the corresponding eigenvectors, which are precisely the mode shapes. Plugging back eigenvalue (2.21) into the system (2.17) we end up with a new system

$$\begin{bmatrix} 0 & 0 \\ 0 & -k^2\kappa_e \end{bmatrix} \begin{bmatrix} U_1 \\ U_2 \end{bmatrix} = \begin{bmatrix} 0 \\ 0 \end{bmatrix}. \tag{2.22}$$

The second equation of this system

$$-k^2\kappa_e U_2 = 0 \tag{2.23}$$

tells us that when we excite the mode that corresponds to this eigenvalue we substituted into our initial system, then the amplitude U_2, which acts in the $y-$direction, must be zero, while we have no restrictions on the amplitude U_1, hence the mode is a pure pressure mode in $x-$direction. If we follow the same procedure for our second eigenvalue, namely dispersion relation (2.20), we arrive at the the system

$$\begin{bmatrix} k^2\kappa_e & 0 \\ 0 & 0 \end{bmatrix} \begin{bmatrix} U_1 \\ U_2 \end{bmatrix} = \begin{bmatrix} 0 \\ 0 \end{bmatrix} \tag{2.24}$$

which now tells us that when we excite the mode that corresponds to eigenvalue (2.20), the amplitude U_1 must necessarily be zero, while no restrictions hold for amplitude U_2, therefore this mode is a pure shear mode.

We remark that, since matrix (2.18) encloses the information we need for the calculation of the dispersion relation, is therefore called the Acoustic Tensor. For any model, the matrix that comes from the same procedure, and whose determinant gives us the dispersion relations, is also called the Acoustic Tensor. It is important to notice that the size of the Acoustic Tensor is always $n \times n$ where n is the number of degrees of freedom in the model under consideration, here in 2D. The importance of this will be discussed later, when more continuum models will be presented. For Cauchy elasticity under the plain strain assumption, there are only two degrees of freedom, since displacement in the z-direction is prohibited, leading to an Acoustic Tensor of size 2×2.

Back to relations (2.20) and (2.21), these relations tell us if the medium is dispersive. A dispersive medium is one in which waves of different frequencies, travel with different phase velocities. Phase velocity is the speed at which a wave of a single frequency is travelling in the medium and is given by

$$v_{ph} = \frac{\omega}{k} \tag{2.25}$$

where u_{ph} is the phase velocity, ω is the frequency and k is the wave number. In order for a medium to be dispersive, its dispersion relations must be non-linear. Taking a quick look at equations (2.20) and (2.21), it is easy to see that they are linear i.e. phase velocity is the same for any frequency. The value of this phase velocity is given by the term which multiplies k in both relations. We also show in Fig. 2.1 the dispersion curves for an isotropic Cauchy continuum, made out of Titanium. For Titanium, the elastic constants take the values: $\rho = 4400\,[\mathrm{kg/m^3}]$, $\kappa_e = 116.7\,[\mathrm{GPa}]$ and $\mu_e = 41.8\,[\mathrm{GPa}]$.

Changing the anisotropy of the medium, would only lead to a phase velocity that is a function of the direction of propagation ϕ and additional material parameters depending on the symmetry class. However, no dispersion could arise, since the dispersion relations always remain linear. This means that a Cauchy bulk medium is in general non-dispersive. Cauchy elasticity can only describe dispersion, if dispersion is a result of the medium geometry's deviation from the infinite bulk medium [6, 37] or if we allow the material parameters itself to be frequency dependent [81]. Two notable examples of Cauchy elasticity describing dispersion that results from variations in the medium's geometry, is through a periodic microstructured medium (i.e. through the Bloch-Floquet theorem), or in the modeling of plates, where Lamb waves are generated through the scattering of the wave on the top and bottom of the plate, which mathematically translates as extra boundary conditions [37], leading to dispersive modes.

Once again though, we must stress, that when one wants to model a band-gap metamaterial using a homogenised description, Cauchy elasticity will never be sufficient, as the main characteristic of a ban-gap metamaterial (dispersion), is absent in a Cauchy bulk material. This is precisely the reason an enriched continuum is needed.

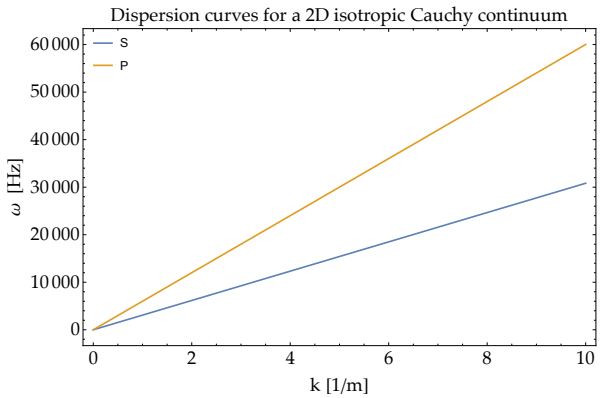

Figure 2.1: Dispersion curves for an isotropic Cauchy continuum made out of Titanium. The one pure shear mode is colored in blue while the one pure pressure mode is colored in yellow.

2.3 Enriched continuum theories: Motivation and History

Enriched continua, as the name suggests, are continua where the kinematics are enriched, i.e. more independent kinematical fields are assumed to exist other than the usual displacement field. This is done on the assumption that the underlying microstructures' movements need more degrees of freedom to be described when being homogenised, which does inevitably influence the behavior of the whole material (see Fig. 2.3).

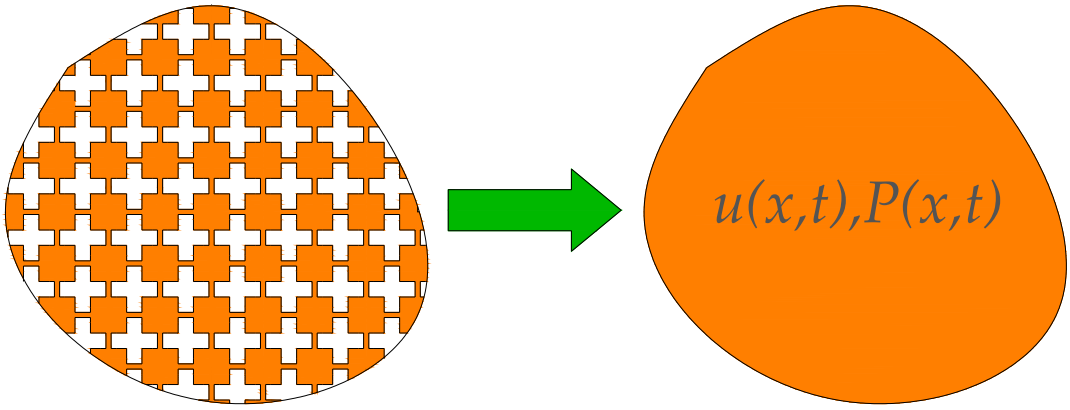

Figure 2.2: Microstructured material (left) and corresponding enriched continuum with extra kinematical field P (right)

It can be, that for a given material, the effects of the microstructure are not evident in the macroscopic scale. In this case Cauchy elasticity is sufficient, with notable examples being the behavior of macroscopically homogeneous metals like steel, titanium and iron. However, there are cases in which the opposite is true, and these are precisely the cases where enriched kinematics are needed. Most cases in need of an enriched continuum theory are materials that are heterogeneous even at large scales, and thus the effect of the microstructure plays a crucial role in their macroscopic description. Some examples include foam [70] and human bone [48, 102, 103].

The whole field of enriched continua started with the contribution of Piola [73], whose work was extended later by the Cosserat brothers in 1909 [12]. The Cosserat brothers proposed a micromorphic medium which was meant to describe rigid rotations of the microstructure, hence the extra kinematical field added was a skew-symmetric second order tensor. The work of the two brothers was not appreciated until the second half of the twentieth century when their work was extended by Mindlin [56, 57], Green and Rivlin [30], Toupin [95], Eringen [19, 20, 21] and Germain [25]. Mindlin and Eringen proposed the addition of a second order tensor in the kinematics, namely tensor P, which was named the micro-distortion or micro-deformation tensor, and in constrast to the Cosserat brother's tensor, this one would be a general one, meaning that it would add to the model 9 additional degrees of freedom, which are the 9 components of the 3×3 second order tensor. Through time this micro-deformation field was generalized to include micro-stretches, micro-strains, micro-shear, micro-distortions and micro-rotations. For more

information on the exact historic events, see [66].

Given the fact that metamaterials have a periodic microstructure by default, since they are nothing more than periodic structures which are heterogeneous even at large scales, it makes sense to model them using a homogenised description of an enriched continuum. In the following, we will thus list some well established enriched continua and discuss their potential to describe dynamical metamaterial behavior.

2.4 A short review of some enriched and higher gradient continua and their potential for band-gap metamaterial description as a function of their dispersion polynomial

Our scope here is to calculate dispersion curves for some higher order and enriched continua and showcase their potential for describing infinitely big metamaterials in the dynamic regime. In order to model finite-size metamaterials, as the title of the thesis suggests, one has to first understand the modeling of infinite size metamaterials. In this chapter, to avoid lengthy calculations, we will only use isotropic versions of these continuum models. Of course metamaterials are in most cases anisotropic, but our goal here is to just show that the potential for describing the dynamic response of infinitely big metamaterials ultimately depends on the dispersion polynomial (since approximating the band structure with dispersive modes coming from Bloch-Floquet analysis is the ultimate goal).

As we saw in the isotropic Cauchy case, the dispersion polynomial comes from taking the determinant of the Acoustic Tensor to be equal to zero. Adding more degrees of freedom to a model, makes the size of the Acoustic Tensor bigger, which means the calculation of the determinant causes more multiplications between the entries of the matrix. These entries, depending on the Equilibrium Equations of the model, will be functions of elastic parameters, the frequency ω (if a derivative with respect to time is present in the equilibrium equations) and the wavenumber k (if a derivative with respect to space is included in the equilibrium equations). It is then easy to understand that a bigger Acoustic Tensor usually means a dispersion polynomial of higher order, if we are comparing two models where the richer one has the same energy terms as the simpler one, plus some extra terms related to the extra degrees of freedom.

Of course one can describe dispersion without adding extra degrees of freedom, by adding higher gradients of the already existing kinematical fields increasing the order of k. One notable example is second gradient elasticity, for which we will calculate the dispersion relations in following section.

2.4.1 Second gradient elasticity

Second gradient elasticity, or Strain gradient elasticity, is based on the assumption that the material behavior depends not only on the classical strain but also on its gradient. In a reduced version of the isotropic 2D case with simplified curvature [82], the Kinetic (K) and Strain (W) energy density of the model take the form

$$K(\dot{u}, \nabla\dot{u}) \coloneqq \frac{1}{2}\rho \left\|\dot{u}\right\|^2 + \frac{\tau_e}{2}\left\|\operatorname{sym}\nabla\dot{u}\right\|^2, \tag{2.26}$$

$$\begin{aligned} W(\nabla u, \nabla\nabla u) \coloneqq{}& \mu_e \left\|\operatorname{sym}\nabla u\right\|^2 + \frac{\lambda_e}{2}\left\|\operatorname{tr}\,\nabla u\right\|^2 \\ &+ \frac{\mu {L_c}^2}{2}\left(\alpha_1\left\|\nabla \operatorname{dev}\operatorname{sym}\nabla u\right\|^2 + \alpha_2\left\|\nabla \operatorname{skew}\nabla u\right\|^2 + \frac{2\alpha_3}{9}\left\|\nabla\left(\operatorname{tr}\nabla u\mathbb{1}\right)\right\|^2\right) \end{aligned} \tag{2.27}$$

where μ_e and λ_e are the usual lame parameters, τ_e is a micro-inertia parameter and $\alpha_1, \alpha_2, \alpha_3$ are dimensionless parameters related to the rate of change of the strain. Using the principle of virtual work, one can arrive to the Equilibrium Equations and boundary conditions for strain gradient elasticity. We refrain here from showing the full procedure which can be found in [56], but we must remark that the procedure leads to a boundary condition defined as a "line load on sharp edges" which is one of the model's unique features. This boundary condition, coupled with the fact that the strain gradient is included in the strain energy, led to edge effects being one of the significant areas where second gradient elasticity is relevant. That is, modeling the behavior of materials near sharp edges, cracks, or discontinuities. These locations are where the Cauchy elasticity might fail, especially in cases involving stress concentrations.

The Equilibrium Equations for a second gradient continuum in the 2D isotropic case with simplified

curvature [82] read

$$\rho\ddot{u} = \mathrm{Div}\Big[\tau_e \,\mathrm{sym}\,\nabla\ddot{u} + 2\mu_e \,\mathrm{sym}\,\nabla u + \lambda_e \,\mathrm{tr}\,(\nabla u)\,\mathbb{1} - \mu {L_c}^2 \left(\alpha_1 \,\mathrm{dev}\,\mathrm{sym}\,(\Delta\nabla u) + \alpha_2 \,\mathrm{skew}\,(\Delta\nabla u) + \frac{2\alpha_3}{9}\,\mathrm{tr}\,(\Delta\nabla u)\,\mathbb{1}\right)\Big]. \tag{2.28}$$

Interested in the wave propagation capabilities of the model in the 2D isotropic case, we proceed by substituting the plane wave plane strain ansatz (2.16) in our displacement field, which after some manipulation provides us with the linear system

$$\begin{bmatrix} \frac{2}{9}k^4L_c^2(3\alpha_1+\alpha_3)\mu - \rho\omega^2 + k^2(\lambda_e+2\mu_e-\tau_e\omega^2) & 0 \\ 0 & \frac{1}{2}\left(k^4L_c^2(\alpha_1+\alpha_2)\mu - 2\rho\omega^2 + k^2\left(2\mu_e - \tau_e\omega^2\right)\right) \end{bmatrix} \begin{bmatrix} U_1 \\ U_2 \end{bmatrix} = \begin{bmatrix} 0 \\ 0 \end{bmatrix}. \tag{2.29}$$

Given the shape of the Acoustic Tensor, we have a clear split between the shear and pressure dispersion relations. For both shear and pressure waves, the dispersion polynomial is of the form

$$\psi_{1i}k^2 + \psi_{2i}k^4 - \left(\psi_{3i} + \psi_{4i}k^2\right)\omega^2 = 0 \tag{2.30}$$

where $i = \{s, p\}$ for shear or pressure respectively. The coefficients can be seen in Table 2.2. We notice

Coefficient	Expression
$\psi_1 p$	$\lambda_e + 2\mu_e$
$\psi_2 p$	$\frac{2}{9}\mu L_c^2(3\alpha 1 + \alpha 3)$
$\psi_3 p$	ρ
$\psi_4 p$	τ_e
$\psi_1 s$	μ_e
$\psi_2 s$	$\frac{1}{2}\mu L_c^2(\alpha 1 + \alpha 2)$
$\psi_3 s$	ρ
$\psi_4 s$	$\frac{\tau_e}{2}$

Table 2.2: The coefficients for the dispersion polynomial for shear or pressure waves for 2D isotropic Second Gradient Elasticity.

that the dispersion polynomial for shear or pressure curves is of the second order with respect to ω (or linear with respect to ω^2), which means that it produces only one curve respectively. Solving the dispersion polynomial with respect to ω, we arrive to the dispersion curves of second gradient isotropic elasticity in 2D

$$\omega_s = \frac{\sqrt{k^4L_c^2(\alpha_1+\alpha_2)\mu + 2k^2\mu_e}}{\sqrt{2\rho + k^2\tau_e}}, \qquad \omega_p = \frac{\sqrt{\frac{2}{9}k^4L_c^2(3\alpha_1+\alpha_3)\mu + k^2(\lambda_e+2\mu_e)}}{\sqrt{\rho + k^2\tau_e}} \tag{2.31}$$

where ω_s corresponds to the shear curve and ω_p to the pressure curve.

Asymptotes

The two dispersion curves in eq. (2.31) are both acoustic, since in the limit $k \to 0$, we can see that ω also goes to zero. For the asymptotes calculation, we take the limit $k \to +\infty$ in eq. (2.31) and we can see that ω also goes to plus infinity, implying that there are no horizontal asymptotes.

We can now understand that the one pressure mode and the one shear mode of 2D isotropic Second Gradient elasticity are two acoustic curves with no horizontal asymptotes. They are, however, dispersive, since the dispersion relations are not linear. In particular, we notice that the dispersion relations are both of the fourth order with respect to k. This would normally imply that each curve, shear or pressure, is allowed to change monotonicity one time, describing positive, zero and negative group velocity in an acoustic mode. We notice, however, that since there are no horizontal asymptotes, but the curves must rather tend to $+\infty$ for $k \to \infty$, this implies that we can, at most, have a saddle point (positive group velocity going to zero group velocity and back to positive), otherwise the curves could not tend to $+\infty$.

A plot of the dispersion curves can be seen in Fig.2.4.1 for the following values of parameters:
$\rho = 2000\,[\mathrm{kg/m^3}]\,,\ \mu_e = 1.15\,[\mathrm{MPa}]\,,\ \lambda_e = 2\,[\mathrm{MPa}], L_c = 0.2\,[\mathrm{m}]\,,\ \tau_e = 1\,[\mathrm{MPa}]\,,$
$\alpha_1 = 1\,[-]\,,\ \alpha_2 = 1\,[-]\,,\ \alpha_3 = 10\,[-]\,,\ \mu = 5\,[\mathrm{kPa}]\,.$

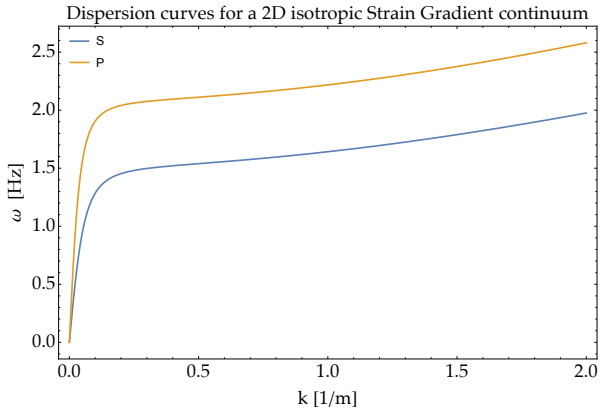

Figure 2.3: Dispersion curves for a 2D Second Gradient isotropic continuum. Shear modes are colored in blue while pressure modes are colored in yellow.

2.4.2 The micro-voids (or micro-dilatation) model

The micro-voids (or micro-dilatation) model was first proposed by Nunziato and Cowin [13, 68] for applications in Thermomechanics. The extra kinematics of the model, apart from the usual displacement u, is a microdistortion tensor P, that only carries one extra degree of freedom (the micro-motion field) along its diagonal. Therefore, the micro-distortion tensor for the micro-voids model takes the form

$$P = \begin{bmatrix} \zeta & 0 & 0 \\ 0 & \zeta & 0 \\ 0 & 0 & \zeta \end{bmatrix} = \zeta \mathbb{1}\,. \tag{2.32}$$

The reason behind the particular choice of the form of the micro-distortion tensor comes from the assumption that the micro-structure attached to the material can only expand or compress isotropically. The one extra degree of freedom $\zeta(x,t)$ is called the micro-motion field, it is dimensionless and it is an indicator of the micro-motions inside material particles. The Strain(W) and Kinetic(K) energy density of a micro-void continuum are defined as

$$W(\nabla u - \zeta\mathbb{1}, \zeta, \nabla\zeta) := \frac{1}{2}\langle \mathbb{C}_\mathrm{e}\ \mathrm{sym}\,(\nabla u - \zeta\mathbb{1})\,, \mathrm{sym}\,(\nabla u - \zeta\mathbb{1})\rangle + \frac{1}{2}\kappa_m\zeta^2 + \frac{\mu L_c^2}{2}\langle\nabla\zeta, \nabla\zeta\rangle, \tag{2.33}$$

$$K(\dot{u}, \dot{\zeta}) := \frac{1}{2}\rho\,\langle\dot{u}, \dot{u}\rangle + \frac{\eta}{2}\dot{\zeta}^2 \tag{2.34}$$

where $\mathbb{C}_\mathrm{e}$ is again an isotropic fourth order tensor with κ_e and μ_e as its only entries, κ_m is a constitutive parameter and L_c is a characteristic length. The characteristic length is usually something used in various enriched models, to show that the model is able to describe size effects. It is usually associated to the size of the unit cell and has dimensions of meters. The associated Langrangian $\mathcal{L}$ and Action functional $\mathcal{A}$ can be defined respectively as

$$\mathcal{L}(\dot{u}, \dot{\zeta}, \nabla u - \zeta\mathbb{1}, \zeta, \nabla\zeta) := K(\dot{u}, \dot{\zeta}) - W(\nabla u - \zeta\mathbb{1}, \zeta, \nabla\zeta)\,, \tag{2.35}$$

$$\mathcal{A} := \iint\limits_{\Omega\times[0,T]} \mathcal{L}\left(\dot{u}, \dot{\zeta}, \nabla u - \zeta\mathbb{1}, \zeta, \nabla\zeta\right)\,\mathrm{d}x\,\mathrm{d}t\,. \tag{2.36}$$

The first variation of the Action functional $\delta\mathcal{A}$ is taken with respect to both the displacement u and the micro-motion field ζ, which are the two independent kinematical fields. Thus we will arrive at two separate (but coupled) governing equations. We consider that $\delta\mathcal{A}$ is equal to the internal work W^{int} of the micro-voids continuum ($W^{int} = \delta\mathcal{A}$) and that the external work is given only by externally applied volume forces, boundary forces or double forces respectively, i.e.

$$W^{ext} = \int\limits_\Omega \langle f_V^{ext}, \delta u\rangle\,\mathrm{d}V + \int\limits_{\partial\Omega} \langle f_S^{ext}, \delta u\rangle\,\mathrm{d}s + \int\limits_{\partial\Omega} \langle \phi^{ext}, \delta\zeta\rangle\,\mathrm{d}s\,. \tag{2.37}$$

The principle of virtual work $W^{int} = W^{ext}$ thus implies the strong form governing equations for the micro-voids model in the absence of external body forces ($f_V^{ext} = 0$)

$$\rho\ddot{u} = \operatorname{Div}\sigma\,, \tag{2.38}$$

$$-\eta\ddot{\zeta} - \kappa_m\zeta + \operatorname{tr}(\sigma) + \mu L_c^2 \operatorname{Div}\nabla\zeta = 0 \tag{2.39}$$

where

$$\sigma = \mathbb{C}_{\mathrm{e}}\ \operatorname{sym}(\nabla u - \zeta\mathbb{1}) \tag{2.40}$$

and $\mathbb{C}_{\mathrm{e}}$ is again a fourth order isotropic elasticity tensor.

We now want to study wave propagation in the bulk micro-void medium. The procedure we follow is exactly the same as the one followed for the Cauchy bulk medium in Section 2.2. We assume a plane wave ansatz under the plane strain assumption for our kinematical fields:

$$u_j = U_j e^{i(k_1 x + k_2 y - \omega t)} \tag{2.41}$$

where u_j represents the generic component of the displacement and

$$\zeta = Z e^{i(k_1 x + k_2 y - \omega t)} \tag{2.42}$$

where Z is a scalar amplitude.
We substitute these into the Equilibrium Equations of the model and rewrite the equations in the form of a homogeneous linear system

$$\begin{bmatrix} k^2(\kappa_e+\mu_e)-\rho\omega^2 & 2ik\kappa_e & 0 \\ 2ik\kappa_e & \kappa_m - 4\kappa_e - k^2\mu L_c^2 + \eta\omega^2 & 0 \\ 0 & 0 & k^2(\mu_e)-\rho\omega^2 \end{bmatrix} \begin{bmatrix} U_1 \\ Z \\ U_2 \end{bmatrix} = \begin{bmatrix} 0 \\ 0 \\ 0 \end{bmatrix}. \tag{2.43}$$

It is then easy to see that in order for this system to have a non trivial solution, the determinant of the matrix

$$\begin{bmatrix} k^2(\kappa_e+\mu_e)-\rho\omega^2 & 2ik\kappa_e & 0 \\ 2ik\kappa_e & \kappa_m - 4\kappa_e - k^2\mu L_c^2 + \eta\omega^2 & 0 \\ 0 & 0 & k^2(\mu_e)-\rho\omega^2 \end{bmatrix} \tag{2.44}$$

needs to be zero. This matrix is the Acoustic Tensor of the micro-voids model and its size is 3×3 since the degrees of freedom the model has are three. Taking the determinant of the Acoustic Tensor equal to zero provides us with the dispersion polynomial of the micro-voids model

$$(k^2\mu_e - \rho\omega^2)(4k^2\kappa_e^2 + \big(k^2(\kappa_e+\mu_e)-\rho\omega^2)(-\kappa_m - 4\kappa_e - k^2\mu L_c^2 + \eta\omega^2)\big) = 0\,. \tag{2.45}$$

This can be rewritten in a more useful way as

$$\psi_1 k^4 - \psi_2 k^6 + (\psi_3 k^2 + \psi_4 k^4)\omega^2 - (\psi_5 + \psi_6 k^2)\omega^4 + \psi_7\omega^6 = 0\,. \tag{2.46}$$

where $\psi_1, \psi_2, ..., \psi_7$ are functions of the elastic constants reported in Table 2.3. Bringing the dispersion

Coefficient	Expression
ψ_1	$\mu_e\,(4\kappa_e\mu_e + k_m(\kappa_e+\mu_e))$
ψ_2	$\mu_e(\kappa_e+\mu_e)\mu {L_c}^2$
ψ_3	$\rho\,(8\kappa_e\mu_e + k_m(\kappa_e+2\mu_e))$
ψ_4	$\eta\mu_e(\kappa_e+\mu_e) + \rho(\kappa_e+2\mu_e)\mu {L_c}^2$
ψ_5	$\rho^2(k_m+4\kappa_e)$
ψ_6	$\rho\,\big(\eta(\kappa_e+2\mu_e) + \rho\mu {L_c}^2\big)$
ψ_7	$\rho^2\eta$

Table 2.3: The coefficients for the dispersion polynomial of the micro-voids model.

polynomial in the form of equation (2.46), makes it easier to see how many modes can be described by

the model. Firstly, the polynomial is of sixth order with respect to ω, which means solving it will give us six solutions of the form $\omega(k)$. However, because of symmetry arguments we are only interested in three. Thus we are left with three modes, one additional mode with respect to Cauchy elasticity. Calculating the mode shapes, similarly to the previous section, one can see that we have one shear mode and two pressure modes.

We remark here that it is possible to deduct, form the Acoustic Tensor's block shape, that we could have split the problem in two sub problems. One for shear and one for pressure waves, since from system (2.43) it is easy to see that the equation

$$\left(k^2(\mu_e) - \rho\omega^2\right) \cdot U_2 = 0 \tag{2.47}$$

is independent of the rest of the system and therefore describes shear waves by itself, producing a shear mode identical to Cauchy elasticity (see eq. (2.20)). Therefore, pressure waves dispersion curves can be calculated from the rest of the system, by taking the determinant of the matrix

$$\begin{bmatrix} k^2(\kappa_e + \mu_e) - \rho\omega^2 & 2ik\kappa_e \\ 2ik\kappa_e & \kappa_m - 4\kappa_e - k^2\mu L_c^2 + \eta\omega^2 \end{bmatrix} \tag{2.48}$$

equal to zero and calculating a dispersion polynomial for pressure waves by

$$\psi_{1p}k^2 + \psi_{2p}k^4 - (\psi_{3p} + \psi_{4p}k^2)\omega^2 + (\psi_{5p})\omega^4 = 0 \tag{2.49}$$

where the values of coefficients $\psi_{1p}, \psi_{2p}, ..., \psi_{5p}$ can be seen in Table 2.4 The solutions of dispersion

Coefficient	Expression
ψ_{1p}	$4\kappa_e\mu_e + k_m(\kappa_e + \mu_e)$
ψ_{2p}	$(\kappa_e + \mu_e)\mu {L_c}^2$
ψ_{3p}	$\rho\,(4\kappa_e + k_m)$
ψ_{4p}	$\eta(\kappa_e + \mu_e) + \rho\mu {L_c}^2$
ψ_{5p}	$\rho\eta$

Table 2.4: The coefficients for the dispersion polynomial of the micro-voids model for pressure waves.

polynomial (2.49) and dispersion relation (2.20) together, give the same dispersion curves as the problem we solved on the full Acoustic Tensor.

Nature of the modes: acoustic and optic

Taking wavenumber k to be equal to zero, the dispersion polynomial (2.46) becomes

$$-\psi_5\omega^4 + \psi_7\omega^6 = 0\,. \tag{2.50}$$

Similarly to solving the full dispersion polynomial, solving this with respect to ω gives us three solutions[1]

$$\omega = 0\,, \tag{2.51}$$

$$\omega = 0 \tag{2.52}$$

and

$$\omega = \sqrt{\frac{\psi_5}{\psi_7}}\,. \tag{2.53}$$

These expressions state that when $k = 0$, the first two modes are at $\omega = 0$ and the third one at $\omega = \sqrt{\frac{\psi_5}{\psi_7}}$. We notice that the first two modes are what we call acoustic modes, but the third one, whose first point is not at the origin of the dispersion diagram, but rather at a specific frequency, is called optic. That specific frequency $\omega = \sqrt{\frac{\psi_5}{\psi_7}}$ is what we call its cutoff frequency. In particular, using Table 2.3 the cutoff frequency here can be computed as

$$\omega = \sqrt{\frac{\psi_5}{\psi_7}} = \sqrt{\frac{\rho^2(k_m + 4\kappa_e)}{\rho^2\eta}} = \sqrt{\frac{(\kappa_m + 4\kappa_e)}{\eta}}. \tag{2.54}$$

[1]Only three are relevant because of symmetry arguments.

From the elastic constants present in the expression of the cutoff, only one exists in a Cauchy elastic medium: parameter κ_e, while the other two parameters (κ_m and η) are absent. Therefore, we note that the new cutoff owes its existence to the terms $\frac{\eta}{2}\dot{\zeta}^2$ and $\frac{1}{2}\kappa_m\zeta^2$ in the energy density (see Eq. (2.34)). Theses term, in turn, give us the terms $-\eta\ddot{\zeta}$ and $-\kappa_m\zeta$ in the Equilibrium Equations (2.39) respectively, which after the substitution of the plane strain plain wave ansatz, give us the terms $-\eta\omega^2$ and κ_m in the Acoustic Tensor. The first term is responsible for raising the order of the dispersion polynomial to the sixth order, allowing as to have three solutions instead of two for Cauchy elasticity, while the combination of the first and the second made the specific cutoff possible.

Therefore the enrichment of the Cauchy elasticity model with the micro-motion field, made the description of one optic mode possible. This, as we saw, is a direct consequence of choosing appropriate terms in the energy of the micro-voids model, so that the Equilibrium Equations and consequently the Acoustic Tensor, are of such a form, that they produce the specific dispersion polynomial which allows us to describe one extra optic mode. If we wish to describe more optic modes, further enrichment is needed.

Asymptotes

To calculate the asymptotes we consider the limit $k \to \infty$ in eq. (2.49) which only describes pressure waves, where only the terms with the highest order of k are important (since the dispersion relation of shear waves is identical to Cauchy elasticity, we know that it does not have a horizontal asymptote). This provides us with a reduced dispersion polynomial, whose solutions are the asymptotes. Thus we consider

$$\psi_{2p}k^4 - \psi_{4p}k^2\omega^2 + \psi_{5p}\omega^4 = 0\,. \tag{2.55}$$

However, taking the limit $k \to \infty$, the only solution found is $\omega = +\infty$ as well, which implies that none of the curves has a horizontal asymptote.

This can also be seen in Fig. 2.4.2, where the dispersion curves are plotted for the following values of parameters: $\rho = 4400\,[\mathrm{kg/m^3}]$, $\mu_e = 8.15\,[\mathrm{MPa}]$, $\kappa_e = 16\,[\mathrm{MPa}]$, $\kappa_m = 26\,[\mathrm{Pa}]$, $\eta = 3 \times 10^6\,[\mathrm{kg/m}]$, $\mu = 100\,[\mathrm{kPa}]$, $L_c = 1\,[\mathrm{m}]$.

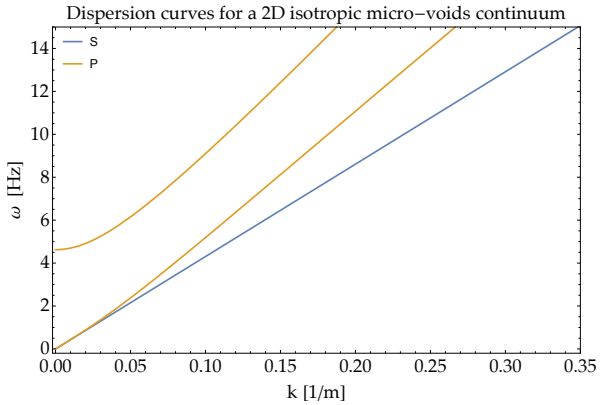

Figure 2.4: Dispersion curves for an isotropic micro-voids continuum. Shear modes are colored in blue while the pressure modes are colored in yellow.

Taking a quick look at eq. (2.49) we notice that similarly to the Strain Gradient case, the polynomial is of the 4th order with respect to k. Since we do not have horizontal asymptotes, this would imply that for any ω, we are allowed to have two distinct real k in the positive axis[2]. However, as mentioned before, when $k \to \infty$, $\omega \to +\infty$, so both curves must increase to infinity for increasing k. This implies that we can only describe zero group velocity in the cutoff of the optic pressure curve and possibly in the case of a saddle point in the acoustic pressure (before the cutoff of the pressure optic mode). At a certain point the acoustic will reach the cutoff of the optic, so from that point and afterwards, we always have two values of k for each ω, therefore the group velocity can only be positive.

[2]In general for a polynomial of the 4th order with respect to k, for any ω we must always have two solutions (two k). If in our graph (where we only plot real k), for a single ω, there exists only one k, this means that the other one is imaginary. It is the sum of real and imaginary k that must be equal to 2 (e.g. if no real k exists for a single ω, there exist two imaginary.

2.4.3 The Cosserat micropolar model

In the Cosserat micropolar model, the micro-deformation tensor A is assumed to be skew symmetric. Therefore, the assumption one can make is that the microstructure can only rotate, and hence the name micropolar. It was shown by R. Lakes that there are cases which Cosserat elasticity is able to describe natural porous bone, metallic foams and cellular materials [45, 47], where the author was able to determine and verify for consistency the Cosserat elasticity constants and to show how a Cosserat model obtains better results than Cauchy elasticity.

The kinetic(K) and Strain(W) energy density of the isotropic case of the Cosserat micropolar model can be written, as was shown in [27], in the following from

$$\begin{aligned} K &= \frac{1}{2}\rho\|\dot{u}\|^2 + \frac{1}{2}\rho\,\eta\,\tau_c^2\|\dot{A}\|^2, \\ W &= \mu_e\|\operatorname{sym}(\nabla u)\|^2 + \mu_c\|\operatorname{skew}(\nabla u - A)\|^2 + \frac{\lambda_e}{2}[\operatorname{tr}(\nabla u)]^2 \\ &\quad + \frac{\mu_e L_c^2}{2}\left[a_1\|\operatorname{dev}\operatorname{sym}\operatorname{Curl} A\|^2 + a_2\|\operatorname{skew}\operatorname{Curl} A\| + \frac{a_3}{3}\operatorname{tr}(\operatorname{Curl} A)^2\right] \end{aligned} \tag{2.56}$$

where μ_e, λ_e, μ_c, L_c and a_1, a_2, a_3 are the elastic moduli representing the parameters related to the meso-scale, the Cosserat couple modulus μ_c, the characteristic length L_c, and the three general isotropic curvature parameters (nondimensional weights), respectively, with $\eta\,\tau_c^2$ an inertia coefficient, $\eta > 0$ a non-dimensional weight parameter and τ_c the internal characteristic length. The well known Equilibrium Equations can then be written in the form

$$\begin{aligned} \rho\,\ddot{u} &= \operatorname{Div}\sigma, \\ \rho\,\eta\,\tau_c^2\ddot{A} &= -\operatorname{skew}\operatorname{Curl} m + \operatorname{skew}\sigma \end{aligned} \tag{2.57}$$

where the stress and moment are defined as

$$\sigma = 2\mu_e\operatorname{sym}\nabla u + 2\mu_c\operatorname{skew}\nabla u - A + \lambda_e\operatorname{tr}(\nabla u)\,\mathbb{1} \tag{2.58}$$

$$m = \mu_e L_c^2\left(a_1\operatorname{dev}\operatorname{sym}\operatorname{Curl} A + a_2\operatorname{skew}\operatorname{Curl} A + \frac{a_3}{3}\operatorname{tr}(\operatorname{Curl} A)\,\mathbb{1}\right). \tag{2.59}$$

Expressed only in terms of u and A, we arrive at

$$\rho\ddot{u} = \operatorname{Div}\left[2\mu_e\operatorname{sym}\nabla u + 2\mu_c\operatorname{skew}(\nabla u - A) + \lambda_e\operatorname{tr}(\nabla u)\mathbb{1}\right], \tag{2.60}$$

$$\rho\,\eta\,\tau_c^2\ddot{A} = -L_c^2\mu_e\operatorname{skew}\operatorname{Curl}\left[a_1\operatorname{dev}\operatorname{sym}\operatorname{Curl} A + a_2\operatorname{skew}\operatorname{Curl} A + \frac{a_3}{3}\operatorname{tr}(\operatorname{Curl} A)\mathbb{1}\right] + 2\mu_c\operatorname{skew}(\nabla u - A). \tag{2.61}$$

Starting from Equilibrium Equations (2.58), applying the usual procedure from previous sections, we end up with the following linear system of equations:

$$\begin{bmatrix} k^2(\lambda_e+2\mu_e)-\rho\omega^2 & 0 & 0 \\ 0 & k^2(\mu_c+\mu_e)-\rho\omega^2 & -2ik\mu_c \\ 0 & ik\mu_c & -2\mu_c - \frac{1}{4}k^2L_c^2\mu_e(\alpha 1+\alpha 2)+\rho\eta\tau_c^2\omega^2 \end{bmatrix}\begin{bmatrix} U_1 \\ U_2 \\ A_{12}\end{bmatrix} = \begin{bmatrix}0\\0\\0\end{bmatrix} \tag{2.62}$$

It is again apparent that we can split the problem described by system (2.62) in two separate problems, one for shear waves and one for pressure waves, similarly to the micro-voids case. Thus, system (2.62) can be divided in equation:

$$\left(k^2(\lambda_e+2\mu_e)-\rho\omega^2\right)U_1 = 0 \tag{2.63}$$

and subsystem

$$\begin{bmatrix} k^2(\mu_c+\mu_e)-\rho\omega^2 & -2ik\mu_c \\ ik\mu_c & -2\mu_c - \frac{1}{4}k^2L_c^2\mu_e(\alpha 1+\alpha 2)+\rho\eta\tau_c^2\omega^2 \end{bmatrix}\begin{bmatrix} U_2 \\ A_{12}\end{bmatrix} = \begin{bmatrix}0\\0\end{bmatrix}. \tag{2.64}$$

Equation (2.63) produces an identical non dispersive pressure mode with Cauchy elasticity (see eq. (2.21)). For Subsystem (2.64), looking for non-trivial solutions of the system, we have to take the determinant of matrix

$$\begin{bmatrix} k^2(\mu_c+\mu_e)-\rho\omega^2 & -2ik\mu_c \\ ik\mu_c & -2\mu_c - \frac{1}{4}k^2L_c^2\mu_e(\alpha 1+\alpha 2)+\rho\eta\tau_c^2\omega^2 \end{bmatrix} \tag{2.65}$$

equal to zero. This provides us with the dispersion polynomial of the shear modes of isotropic Cosserat elasticity

$$\chi_{1s}k^2 + \chi_{2s}k^4 - (\chi_{3s} + \chi_{4s}k^2)\omega^2 + \chi_{5s}\omega^4 = 0 \tag{2.66}$$

where $\chi_{1s}, \chi_{2s}, ..., \chi_{5s}$ are functions of the elastic constants reported in table 2.5. Solving with respect to

Coefficient	Expression
χ_{1s}	$2\mu_c\mu_e$
χ_{2s}	$\frac{1}{4}L_c^2\mu_e(\alpha 1 + \alpha 2)(\mu_c + \mu_e)$
χ_{3s}	$2\mu_c\rho$
χ_{4s}	$\frac{1}{4}L_c^2\mu_e\rho(\alpha 1 + \alpha 2) + (\mu_c + \mu_e)\rho\eta\tau_c^2$
χ_{5s}	$\rho^2\eta\tau_c^2$

Table 2.5: The coefficients for the dispersion polynomial of the Cosserat model for shear waves

ω provides us with our shear dispersion curves, which are both dispersive and have very long expressions so we refrain from showing them here.

Cutoffs

Since the pressure mode is identical to Cauchy elasticity, being an acoustic mode, it has no cutoff. For the shear modes, we can take the limit $k \to 0$ in the dispersion polynomial (2.66) which leads to

$$\chi_{3s}\omega^2 + \chi_{5s}\omega^4 = 0\,. \tag{2.67}$$

Solving with respect to ω gives two solutions (see Table 2.5:

$$\omega = 0 \tag{2.68}$$

and

$$\omega = \sqrt{\frac{2\mu_c}{\rho\,\eta\,\tau_c^2}}. \tag{2.69}$$

Again, one mode is acoustic and the other is optic.

Asymptotes

Following similar procedure to the micro-voids case, the two dispersive modes have no asymptotes (the polynomial has exactly the same shape as for the micro-voids model), and the same is true for the pressure mode since it is non-dispersive.

A plot of the dispersion curves can be seen in Fig. (2.4.3) for values of the parameters:
$\rho = 2000\,[\mathrm{kg/m^3}]\,,\ \mu_e = 1.15\,[\mathrm{MPa}]\,,\ \lambda_e = 2\,[\mathrm{MPa}]\,,\ \kappa_m = 24\,[\mathrm{Pa}]\,,\ \eta = 2\,[-]\,,$
$L_c = 0.01\,[\mathrm{m}]\,,\ \tau_c = 0.2\,[\mathrm{m}]\,,\ \alpha_1 = 101\,[-]\,,\ \alpha_2 = 20\,[-]\,,\ \mu_c = 0.1\,[\mathrm{kPa}]$.

Taking a quick look at eq. (2.66) we notice that similarly to the micro-voids case, the polynomial is of the 4th order with respect to k, but it now describes shear waves instead of pressure waves. Since we do not have horizontal asymptotes, this would imply that for any ω, we are allowed to have two distinct k in the positive axis. However, when $k \to \infty$, $\omega \to +\infty$, so both curves must increase to infinity for increasing wavenumber k. This implies that the acoustic shear curve can describe zero group velocity (in a possible a saddle point), but only before the cutoff of the shear optic mode. At a certain point, the acoustic will reach the cutoff of the optic, so from that point and afterwards, we always have two values of k for each ω, therefore the group velocity can only be positive.

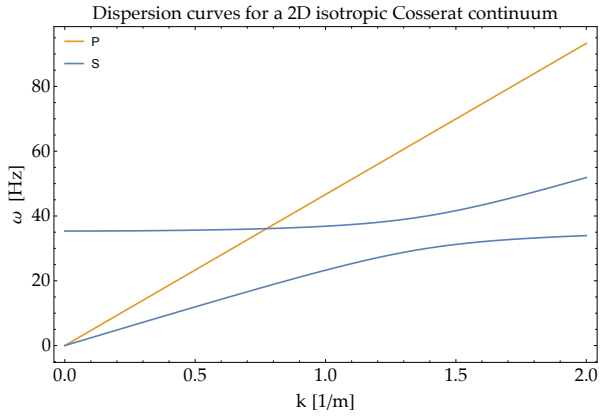

Figure 2.5: Dispersion curves for an isotropic Cosserat continuum. Shear modes are colored in blue while the pressure modes are colored in yellow.

2.5 The importance of horizontal asymptotes for the enriched continuum modeling of band-gap metamaterials

For each of the models studied in this Chapter, we calculated whether all of their dispersion curves have horizontal asymptotes. As mentioned earlier, the existence of a horizontal asymptote for a dispersion curve of an enriched continuum model guarantees that (with a good fitting) the curve stays confined to the frequency region in which it exists in Bloch-Floquet analysis. This implies that if a band-gap starts after the last point of this curve, this band-gap will not be invaded, since the curve will tend asymptotically to a point that is slightly beyond the start of the band-gap. Equivalently, if a curve has no horizontal asymptote, then it cannot stay confined to its associated Bloch-Floquet frequency region and if a band-gap starts after the last point of the curve, this band-gap will be invaded.

Something else worth mentioning is that in the case of a curve having no horizontal asymptote and when no change of monotonicity is possible, there is no option of invading a band-gap partially. Since the curve tends to infinity the whole band-gap must be invaded. In the case of a curve having a horizontal asymptote, if the fitting is perfect, then the curve does not invade the band-gap. If however, at the cost of having a better fitting at frequencies inside the IBZ, we can slightly invade the band-gap by manually choosing the asymptote to be a bit higher than the start of the band-gap.

An interesting question arises from the realization that horizontal asymptotes are necessary in enriched continuum models of band-gap metamaterials: Is there a criterion that must be fullfilled in order for all the curves of the model to have a horizontal asymptote?

If we want all the curves of the enriched model to have a horizontal asymptote, i.e. in the limit of $k \to \infty$, ω is finite, then we need a model with a dispersion polynomial where the highest order of k is multiplied by the highest order of ω.

As explained before, when $k \to \infty$, in the dispersion polynomial $p(\omega, k)$ only the terms with the highest orders of k are important which we call $\overline{p}(\omega)$. In this case, it implies that if the highest order of ω multiplies the highest order of k, then all curves have a horizontal asymptote, but they all tend to zero if this is the only contribution.

To make this more clear, let's imagine a random dispersion polynomial that respects this criterion

$$p(\omega, k) = \chi_1 + \chi_2 k^2 \omega^2 = 0\,. \tag{2.70}$$

When $k \to \infty$, we collect the highest coefficient k^2 and consider the reduced polynomial

$$\overline{p}(\omega) = \chi_2 \omega^2 = 0\,, \tag{2.71}$$

from which we can see that we have two identical solutions for ω: $\omega = 0$.

Since ω^2 is the highest order of ω, the two solutions correspond to the two curves that the model produces, hence all curves have an asymptote, but this asymptote is not any number, it is strictly zero, which is not something we want when modeling band-gap metamaterials. We would rather have an asymptote whose value we can manually change for the purposes of fitting the dispersion curves. This means that

instead of $\omega = 0$, we should have that $\omega = f_p$, where f_p is a function of the parameters of the model and its value is a positive real number.

If we want all asymptotes values to be positive real numbers, then there exists a necessary but not sufficient condition that the model's dispersion polynomial must respect. This condition is better explained through a table. The model's dispersion polynomial must have all the terms that are shown in Table 2.6 with a green tick (✓), that is, the last column of the table, which includes the terms that have the highest order of k and any power of ω including the 0_{th} (constant term). Note that for all examples discussed in this thesis and most models used in the literature, the dispersion polynomial only consists of expressions with even exponents for both k and ω.

–	k^0	k^2	...	k^n
ω^0	✗	★	★	✓
ω^2	✓	★	★	✓
...	✓	★	★	✓
ω^m	✓	★	★	✓

Table 2.6: Table of terms in powers of k and ω where m and n indicate the highest order of ω and k respectively. The ✓ indicates the terms of the dispersion polynomial $p(\omega, k)$ needed for the necessary but not sufficient condition. To have a polynomial whose roots can produce dispersion curves of a band-gap metamaterial we also need the constant term to be vanishing (shown with an ✗) in order to have acoustic curves, and finally the terms shown with a black tick (✓) in order to have cutoff frequencies. Terms shown with a ★ usually appear as a result of the way the dispersion polynomial is calculated through the determinant.

Descarte's rule [100] states that if the nonzero terms of a single-variable polynomial (here ω for $\overline{p}(\omega)$) with real-valued coefficients are ordered by descending variable exponent, then the number of positive roots of the polynomial is either equal to the number of sign changes between consecutive (nonzero) coefficients, or is less than it by an even number. In order to have the possibility of the number of positive real roots of the polynomial being equal to its highest order, terms of all orders must be included, which is the reason that all the terms of the last column of Table 2.6 are needed. This condition is necessary, but not sufficient. After it is met, Vieta's formulas and the polynomial's discriminant dictate the number of positive real roots.

In the remaining, for the models previously shown in this Chapter, we show that they do not respect this necessary but not sufficient condition.

2.5.1 Second gradient elasticity

Taking a look at the dispersion polynomial of Second Gradient elasticity for either shear or pressure waves (2.30), we can construct Table 2.7 (similarly to Table 2.6), from where we can see that there's a missing term, namely the $\omega^2 k^4$ term and therefore the dispersion polynomial does not respect the condition.

–	k^0	k^2	k^4
ω^0	✗	✓	✓
ω^2	✓	✓	✗

Table 2.7: Table of terms in powers of k and ω for the case of Second Gradient elasticity.

2.5.2 Micro-voids elasticity

For the dispersion polynomial of pressure curves (we saw that the shear mode is acoustic) of micro-voids elasticity (see eq. (2.49)), as can be seen in Table 2.8, there are two missing terms, namely the $\omega^2 k^4$ and $\omega^4 k^4$ terms.

–	k^0	k^2	k^4
ω^0	✗	✓	✓
ω^2	✓	✓	✗
ω^4	✓	✗	✗

Table 2.8: Table of terms in powers of k and ω for the case of Micro-voids elasticity.

2.5.3 Cosserat (micropolar) elasticity

Similarly to the pressure waves' dispersion polynomial of micro-voids elasticity, the shear polynomial of Cosserat elasticity (see eq. (2.66)) is missing the same exact terms (see Table 2.9).

$-$	k^0	k^2	k^4
ω^0	✗	✓	✓
ω^2	✓	✓	✗
ω^4	✓	✗	✗

Table 2.9: Table of terms in powers of k and ω for the case of Cosserat elasticity.

We witness that none of the three models respects the necessary but not sufficient condition, which is of course a direct consequence of the choice of terms in the Strain and Kinetic energy densities of each of the models.

2.6 Summary

In this chapter, we saw that for a given continuum model, the ability to describe metamaterials in the dynamic regime lies in the model's dispersion polynomial. The dispersion polynomial is a direct product of choosing appropriate terms in the Strain and Kinetic energy densities, and therefore the description of more dispersion curves or more dispersive curves will always require enrichment of the energy.

Using the 2D isotropic strain gradient model, we are able to describe two dispersive acoustic curves without horizontal asymptotes, and both of the curves can describe positive and zero group velocity. Zero group velocity can only be described in one point (possible saddle point) for each curve.

The 2D isotropic micro-voids model is able to describe one non-dispersive shear acoustic mode and two dispersive pressure modes (one acoustic and one optic). None of the three curves have horizontal asymptotes. The acoustic pressure mode can describe positive and zero group velocity before the cutoff of the optic mode by a possible saddle point of the acoustic mode and the cutoff itself. After the cutoff, both modes can only describe positive group velocity.

The 2D isotropic Cosserat model is able to describe one non-dispersive pressure acoustic mode and two dispersive shear modes (one acoustic and one optic). None of the three curves has horizontal asymptotes. The acoustic shear mode can describe positive and zero group velocity before the cutoff of the optic mode by a possible saddle point of the acoustic mode and the cutoff itself. After the cutoff, both modes can only describe positive group velocity.

Modeling a given band-gap metamaterial in a particular frequency range, means we need a model that produces the particular number of curves that the Bloch-Floquet dispersion curves show in that particular range. Moreover, for the correct description of the metamaterial, all of the curves below the band-gap must have a horizontal asymptote and the ability to describe dispersion. The models we saw in this Chapter produce dispersion curves without horizontal asymptotes, which makes the modeling of mechanical band-gap metamaterials very challenging. We will continue with a more enhanced model in the next chapter, i.e. the reduced relaxed micromorphic model, that is suitable for our applications.

At this point, we want to emphasize that the homogenized model one should use depends on the characteristics of the dispersion curves obtained from Bloch-Floquet analysis.

As an example, let's assume a simple case of an infinite mechanical metamaterial where we are only interested in the first six curves of the dispersion diagram. Let's also assume that for either the shear or the pressure modes, for a given ω we only need one solution in k, implying that shear or pressure curves do not intersect each other at any frequency range and all the six curves are increasing monotonically. This implies that we need a model that can describe six modes (three shear and three pressure) with every mode having a horizontal asymptote, and lastly, since curves do not intersect, the dispersion polynomial can be of the second order with respect to k. In summary, for either shear or pressure curves, we would need a dispersion polynomial $p(\omega, k)$ of third order with respect to ω^2 (to produce three modes) and linear with respect to k^2. A higher-order polynomial with respect to k could also be used here, but if a simpler model can describe the dispersion, then we shall always use that model.

If the dispersion polynomial for shear and pressure curves is of this order, this would imply that the dispersion of the metamaterial can be captured. However, we will see that this is only one condition that

must be respected. The other condition will be explained in Chapter 3 where the fitting procedure of the reduced relaxed micromorphic model will be introduced.

Chapter 3

The reduced relaxed micromorphic model

The reduced relaxed micromorphic model (in short: RRMM), as the name states, is a reduced version of the relaxed micromorphic model (RMM) [2, 26, 54, 64, 65, 66, 99], used in dynamic applications. The term "relaxed" is related to the fact that the curvature component in the strain energy term of the full model is represented by the Curl of the micro-distortion tensor P instead of its full gradient ∇P. We retrieve the reduced version of the relaxed micromorphic model used in this thesis by setting these curvature terms (those related to the Curl of the micro-distortion tensor P) to zero.

The main reason we use the reduced relaxed instead of the original relaxed micromorphic model for dynamic applications has been clearly explained in [99]: the horizontal asymptotes of the RMM are only four in total instead of six, which means that we must necessarily have two dispersion curves that diverge to infinity for increasing wavenumber. While it is possible to retrieve the two lost asymptotes with the addition of a mixed space-time derivative term Curl $\dot{P}$ in the energy, these two new asymptotes only allow for a simplified isotropic behavior due to the degenerative properties of curvature terms in 2D, while two asymptotes must coincide for any angle of incidence [99].

On the other side, for the reduced model, all six curves that can be described have horizontal asymptotes, which guarantees that the interval of frequencies that our model covers is limited as it is in the Bloch-Floquet analysis of the first six curves, but also, that using the appropriate parameter values, band-gap frequency regions will not be invaded. The reduced relaxed micromorphic model's ability to describe band-gap metamaterial behavior, and the reduced computational cost that it comes with when compared to the corresponding microstructured simulations, has already been proven in several instances [15, 17, 74, 75, 79, 80, 83, 84].

3.1 Strain and Kinetic Energy density, equilibrium equations and Boundary conditions

The Kinetic (K) and Strain (W) Energy density of the reduced relaxed micromorphic model can be defined respectively as

$$\begin{aligned} K(\dot{u}, \nabla\dot{u}, \dot{P}) \coloneqq & \frac{1}{2}\rho\,\langle \dot{u}, \dot{u}\rangle + \frac{1}{2}\langle \mathbb{J}_{\mathrm{m}}\,\mathrm{sym}\,\dot{P}, \mathrm{sym}\,\dot{P}\rangle + \frac{1}{2}\langle \mathbb{J}_{\mathrm{c}}\,\mathrm{skew}\,\dot{P}, \mathrm{skew}\,\dot{P}\rangle \\ & + \frac{1}{2}\langle \mathbb{T}_{\mathrm{e}}\,\mathrm{sym}\,\nabla\dot{u}, \mathrm{sym}\,\nabla\dot{u}\rangle + \frac{1}{2}\langle \mathbb{T}_{\mathrm{c}}\,\mathrm{skew}\,\nabla\dot{u}, \mathrm{skew}\,\nabla\dot{u}\rangle\,, \end{aligned} \tag{3.1}$$

$$\begin{aligned} W(\nabla u, P) \coloneqq & \frac{1}{2}\langle \mathbb{C}_{\mathrm{e}}\,\mathrm{sym}\,(\nabla u - P)\,, \mathrm{sym}\,(\nabla u - P)\rangle + \frac{1}{2}\langle \mathbb{C}_{\mathrm{c}}\,\mathrm{skew}\,(\nabla u - P)\,, \mathrm{skew}\,(\nabla u - P)\rangle \\ & + \frac{1}{2}\langle \mathbb{C}_{\mathrm{micro}}\,\mathrm{sym}\ P, \mathrm{sym}\ P\rangle\,. \end{aligned} \tag{3.2}$$

where $\mathbb{C}_{\mathrm{e}}, \mathbb{C}_{\mathrm{c}}, \mathbb{C}_{\mathrm{micro}}, \mathbb{J}_{\mathrm{m}}, \mathbb{J}_{\mathrm{c}}, \mathbb{T}_{\mathrm{e}}$ and $\mathbb{T}_{\mathrm{c}}$ are fourth order tensors of tetragonal symmetry whose particular form will be discussed in the next section. We can see that the Strain and Kinetic energy densities of the model are functions of the two kinematical fields: the macroscopic displacement $u \in \mathbb{R}^3$, and the

micro-distortion tensor $P \in \mathbb{R}^{3\times3}$.
In this case, P is a general second order tensor without any particular symmetries, and thus carries nine extra degrees of freedom. The exact physical meaning of the micro-distortion tensor P is in general an open question in the enriched continua community. As seen in the previous chapter, constraining P to be skew symmetric describes a microstructure that can only rotate, and constraining P to have a hydrostatic form describes a microstructure that can only expand and contract isotropically. If one wants to then translate a general second order tensor P in the same way, that would mean that the microstructure is able to deform freely. Nevertheless, the use of the micro-deformation tensor P is absolutely necessary if one wants to describe band-gap metamaterial behavior in a homogenised framework.

The associated Lagrangian $\mathcal{L}$ and Action functional $\mathcal{A}$ can be defined respectively as

$$\mathcal{L}(\dot{u}, \nabla\dot{u}, \dot{P}, \nabla u, P) \coloneqq K(\dot{u}, \nabla\dot{u}, \dot{P}) - W(\nabla u, P)\,, \tag{3.3}$$

$$\mathcal{A} \coloneqq \iint\limits_{\Omega\times[0,T]} \mathcal{L}\left(\dot{u}, \nabla\dot{u}, \dot{P}, \nabla u, P,\right) \mathrm{d}x\,\mathrm{d}t\,. \tag{3.4}$$

The first variation of the Action functional $\delta\mathcal{A}$ is taken with respect to the displacement u and the micro-distortion tensor P, which are the two independent kinematical fields. We consider that $\delta\mathcal{A}$ is equal to the internal work W^{int} of the reduced relaxed micromorphic continuum ($W^{\mathrm{int}} = \delta\mathcal{A}$) and assume that the external work is given only by externally applied boundary forces, i.e. $W^{\mathrm{ext}} = \int\limits_{\partial\Omega} \langle f^{\mathrm{ext}}, \delta u\rangle \,\mathrm{d}s$. The principle of virtual work $W^{\mathrm{int}} = W^{\mathrm{ext}}$ thus implies the strong form equations governing the reduced relaxed micromorphic model in the absence of external body forces by

$$\rho\ddot{u} - \operatorname{Div}\widehat{\sigma} = \operatorname{Div}\widetilde{\sigma}\,, \qquad\qquad \overline{\sigma} = \widetilde{\sigma} - s \tag{3.5}$$

where

$$\widetilde{\sigma} \coloneqq \mathbb{C}_{\mathrm{e}}\,\operatorname{sym}(\nabla u - P) + \mathbb{C}_{\mathrm{c}}\,\operatorname{skew}(\nabla u - P)\,, \qquad \widehat{\sigma} \coloneqq \mathbb{T}_{\mathrm{e}}\,\operatorname{sym}\nabla\ddot{u} + \mathbb{T}_{\mathrm{c}}\,\operatorname{skew}\nabla\ddot{u}\,, \tag{3.6}$$

$$s \coloneqq \mathbb{C}_{\mathrm{micro}}\,\operatorname{sym} P\,, \qquad \overline{\sigma} \coloneqq \mathbb{J}_{\mathrm{m}}\,\operatorname{sym}\ddot{P} + \mathbb{J}_{\mathrm{c}}\,\operatorname{skew}\ddot{P}\,. \tag{3.7}$$

The associated Neumann and Dirichlet boundary conditions are, respectively,

$$\widetilde{t} \coloneqq (\widetilde{\sigma} + \widehat{\sigma})\,n = f^{\mathrm{ext}} \tag{3.8}$$

and

$$u = u^{\mathrm{ext}} \tag{3.9}$$

where $\widetilde{t}$ is the generalized traction, n is the normal to the boundary, f^{ext} is any externally applied surface load and u^{ext} is any externally applied displacement.

3.2 Tetragonal symmetry and associated elastic tensors

All the infinitely extended metamaterials we are going to model in this thesis are characterized by their structural unit, the unit cell. The choice of unit cell is not unique, since the definition of a unit cell for a given lattice is "a section of the tiling that generates the whole tiling using only translations". Unit cells with different symmetry can be chosen, that can still produce the same infinite lattice if they are repeated periodically to infinity. However, even the repetition of the least symmetric unit cell one can identify, inevitably creates unit cells with the symmetry class of what is called the "maximal invariance group" [64]. For the periodic metamaterials in this thesis, the maximal invariance group is the tetragonal group, even if less symmetric unit cells can also be identified.

For this reason, we pose that the symmetry class of all our constitutive tensors should be the tetragonal symmetry class. We report here the structure of the 4th order micro inertia tensors $\mathbb{J}_{\mathrm{m}}$, $\mathbb{J}_{\mathrm{c}}$, $\mathbb{T}_{\mathrm{e}}$, $\mathbb{T}_{\mathrm{c}}$ and

of the 4th order elasticity tensors $\mathbb{C}_{\rm e}$, $\mathbb{C}_{\rm micro}$, $\mathbb{C}_{\rm c}$ for tetragonal symmetry in Voigt notation

$$\mathbb{C}_{\rm e} = \begin{bmatrix} \kappa_{\rm e}+\mu_{\rm e} & \kappa_{\rm e}-\mu_{\rm e} & \star & \dots & 0 \\ \kappa_{\rm e}-\mu_{\rm e} & \kappa_{\rm e}+\mu_{\rm e} & \star & \dots & 0 \\ \star & \star & \star & \dots & 0 \\ \vdots & \vdots & \vdots & \ddots & \\ 0 & 0 & 0 & & \mu_{\rm e}^* \end{bmatrix}, \qquad \mathbb{C}_{\rm micro} = \begin{bmatrix} \kappa_{\rm m}+\mu_{\rm m} & \kappa_{\rm m}-\mu_{\rm m} & \star & \dots & 0 \\ \kappa_{\rm m}-\mu_{\rm m} & \kappa_{\rm m}+\mu_{\rm m} & \star & \dots & 0 \\ \star & \star & \star & \dots & 0 \\ \vdots & \vdots & \vdots & \ddots & \\ 0 & 0 & 0 & & \mu_{\rm m}^* \end{bmatrix},$$

$$\mathbb{J}_{\rm m} = \rho L_{\rm c}^2 \begin{bmatrix} \kappa_\gamma+\gamma_1 & \kappa_\gamma-\gamma_1 & \star & \dots & 0 \\ \kappa_\gamma-\gamma_1 & \kappa_\gamma+\gamma_1 & \star & \dots & 0 \\ \star & \star & \star & \dots & 0 \\ \vdots & \vdots & \vdots & \ddots & \\ 0 & 0 & 0 & & \gamma_1^* \end{bmatrix}, \qquad \mathbb{T}_{\rm e} = \rho L_{\rm c}^2 \begin{bmatrix} \overline{\kappa}_\gamma+\overline{\gamma}_1 & \overline{\kappa}_\gamma-\overline{\gamma}_1 & \star & \dots & 0 \\ \overline{\kappa}_\gamma-\overline{\gamma}_1 & \overline{\kappa}_\gamma+\overline{\gamma}_1 & \star & \dots & 0 \\ \star & \star & \star & \dots & 0 \\ \vdots & \vdots & \vdots & \ddots & \\ 0 & 0 & 0 & & \overline{\gamma}_1^* \end{bmatrix}, \tag{3.10}$$

$$\mathbb{J}_{\rm c} = \rho L_{\rm c}^2 \begin{bmatrix} \star & 0 & 0 \\ 0 & \star & 0 \\ 0 & 0 & 4\,\gamma_2 \end{bmatrix}, \qquad \mathbb{T}_{\rm c} = \rho L_{\rm c}^2 \begin{bmatrix} \star & 0 & 0 \\ 0 & \star & 0 \\ 0 & 0 & 4\,\overline{\gamma}_2 \end{bmatrix}, \qquad \mathbb{C}_{\rm c} = \begin{bmatrix} \star & 0 & 0 \\ 0 & \star & 0 \\ 0 & 0 & 4\,\mu_{\rm c} \end{bmatrix}.$$

Only the in-plane components are reported since these are the only ones that play a role in the plane-strain simulations presented in the following chapters.

3.3 The Cauchy model as the *macroscopic scale* limit of the reduced relaxed micromorphic model

Every enriched continuum model used for the homogenised description of infinitely big metamaterials in the dynamic regime, must fall back to a Cauchy model when the frequency is very small and the wavelength is very big simultaneously, since the dispersion curves coming from Bloch-Floquet analysis can be approximated linearly close to the origin of the dispersion diagram. This happens because, in the dispersion diagram, at low frequencies the wavelength is very long, and the periodic structure appears more homogeneous to the wave, thus the metamaterial behavior can be well approximated with a Cauchy continuum. We can prove that the RRMM behaves like a Cauchy continuum at low frequencies and long wavelengths with the following procedure starting from the equilibrium equations

$$\begin{cases} \rho\ddot{u} - \operatorname{Div}\left[\mathbb{T}_{\rm e}\operatorname{sym}\nabla\ddot{u} + \mathbb{T}_{\rm c}\operatorname{skew}\nabla\ddot{u}\right] - \operatorname{Div}\left[\mathbb{C}_{\rm e}\operatorname{sym}(\nabla u - P) + \mathbb{C}_{\rm c}\operatorname{skew}(\nabla u - P)\right] = 0\,, \\ \mathbb{J}_{\rm m}\operatorname{sym}\ddot{P} + \mathbb{J}_{\rm c}\operatorname{skew}\ddot{P} - \mathbb{C}_{\rm e}\operatorname{sym}(\nabla u - P) - \mathbb{C}_{\rm c}\operatorname{skew}(\nabla u - P) + \mathbb{C}_{\rm micro}\operatorname{sym}P = 0\,. \end{cases} \tag{3.11}$$

We proceed by taking $L_c \to 0$. Taking $L_c \to 0$ is implying that the metamaterial has a tiny unit cell size (compared to the size of the specimen), and therefore the wave does not "see" the microstructure, i.e. the metamaterial appears homogeneous. This leads to the system

$$\begin{cases} \operatorname{Div}\left[\mathbb{C}_{\rm e}\operatorname{sym}(\nabla u - P) + \mathbb{C}_{\rm c}\operatorname{skew}(\nabla u - P)\right] = \rho\ddot{u}\,, \\ \mathbb{C}_{\rm e}\operatorname{sym}(\nabla u - P) + \mathbb{C}_{\rm c}\operatorname{skew}(\nabla u - P) - \mathbb{C}_{\rm micro}\operatorname{sym}P = 0\,. \end{cases} \tag{3.12}$$

From equation $(3.12)_2$ it is possible to calculate $\operatorname{skew}P$ and $\operatorname{sym}P$ and substitute them in equation $(3.12)_1$ to arrive at

$$\begin{cases} \operatorname{skew}P = \operatorname{skew}\nabla u\,. \\ \operatorname{sym}P = (\mathbb{C}_{\rm e} + \mathbb{C}_{\rm micro})^{-1}\mathbb{C}_{\rm e}\operatorname{sym}\nabla u\,, \\ \operatorname{Div}\left[\mathbb{C}_{\rm e}\operatorname{sym}\nabla u - \mathbb{C}_{\rm e}(\mathbb{C}_{\rm e} + \mathbb{C}_{\rm micro})^{-1}\mathbb{C}_{\rm e}\operatorname{sym}\nabla u\right] = \rho\ddot{u}\,, \end{cases} \tag{3.13}$$

Manipulating equation $(3.13)_3$ it is possible to write

$$\begin{aligned} &\operatorname{Div}\left[(\mathbb{C}_{\rm e} + \mathbb{C}_{\rm micro})(\mathbb{C}_{\rm e} + \mathbb{C}_{\rm micro})^{-1}\mathbb{C}_{\rm e}\operatorname{sym}\nabla u - \mathbb{C}_{\rm e}(\mathbb{C}_{\rm e} + \mathbb{C}_{\rm micro})^{-1}\mathbb{C}_{\rm e}\operatorname{sym}\nabla u\right] = \rho\ddot{u}\,, \\ \iff \qquad &\operatorname{Div}\left[\mathbb{C}_{\rm micro}(\mathbb{C}_{\rm e} + \mathbb{C}_{\rm micro})^{-1}\mathbb{C}_{\rm e}\operatorname{sym}\nabla u\right] = \operatorname{Div}\left[\mathbb{C}_{\rm Macro}\operatorname{sym}\nabla u\right] = \rho\ddot{u} \end{aligned} \tag{3.14}$$

where

$$\mathbb{C}_{\text{Macro}} = \mathbb{C}_{\text{micro}}(\mathbb{C}_{\text{e}} + \mathbb{C}_{\text{micro}})^{-1}\mathbb{C}_{\text{e}}\,. \tag{3.15}$$

Equation (3.14) is a Cauchy type equilibrium equation with stiffness tensor $\mathbb{C}_{\text{Macro}}$, which therefore proves our original statement.

3.4 Null Lagrangian in the micro-inertia contribution

As it has been proven in a recent contribution [18], it is possible to show the existence of a Null-Lagrangian in the mixed space time derivative kinetic part $\nabla\dot{u}$. While the corresponding tensors $\mathbb{T}_{\text{e}}$ and $\mathbb{T}_{\text{c}}$ depend on the 4 parameters $\overline{\kappa}_\gamma, \overline{\gamma}_1, \overline{\gamma}_1^*, \overline{\gamma}_2$ in the tetragonal case, the corresponding contribution $\operatorname{Div}\widehat{\sigma}$ (where $\widehat{\sigma} = \mathbb{T}_{\text{e}}\operatorname{sym}\nabla\ddot{u} + \mathbb{T}_{\text{c}}\operatorname{skew}\nabla\ddot{u}$) from the equilibrium equations, only depends on 3 independent parameters. Thus, one of the four micro-inertia parameters remains free, without any effect on the bulk material behavior (dispersion curves). Note that regarding boundary contribution still all 4 parameters play a role. More specifically [18], we have that computing $\operatorname{Div}\hat{\sigma}$ gives

$$\operatorname{Div}\hat{\sigma} = \begin{pmatrix}\hat{\sigma}_{11,1} + \hat{\sigma}_{12,2}\\ \hat{\sigma}_{21,2} + \hat{\sigma}_{22,2}\end{pmatrix} = \begin{pmatrix}(\overline{\kappa}_\gamma + \overline{\gamma}_1)\ddot{u}_{1,11} + (\overline{\kappa}_\gamma - \overline{\gamma}_1 + \overline{\gamma}_1^* - \overline{\gamma}_2)\ddot{u}_{2,12} + (\overline{\gamma}_1^* + \overline{\gamma}_2)\ddot{u}_{1,22}\\ (\overline{\gamma}_1^* + \overline{\gamma}_2)\ddot{u}_{2,11} + (\overline{\kappa}_\gamma - \overline{\gamma}_1 + \gamma_1^* - \overline{\gamma}_2)\ddot{u}_{1,12} + (\overline{\kappa}_\gamma + \overline{\gamma}_1)\ddot{u}_{2,22}\end{pmatrix}. \tag{3.16}$$

Focusing on this expression alone, it is evident that $\operatorname{Div}\hat{\sigma}$ stays invariant under the transformation

$$\begin{cases}\overline{\gamma}_{2f} = \overline{\gamma}_{2i} + \xi,\\ \overline{\kappa}_{\gamma f} = \overline{\kappa}_{\gamma i} + \xi,\\ \overline{\gamma}_{1f} = \overline{\gamma}_{1i} - \xi,\\ \overline{\gamma}_{1f}^* = \overline{\gamma}_{1i}^* - \xi\end{cases} \tag{3.17}$$

where f stands for final (after applying the transformation) and i stands for initial (before applying the transformation).

On the contrary, this transformation (3.17) modifies the boundary contribution of $\widehat{\sigma}$ in eq (3.8) by the term

$$(\widehat{\sigma_f} - \widehat{\sigma_i})\,n \tag{3.18}$$

where, again, f stands for final and i stands for initial. Practically this means two things:

- We can choose to make our model simpler without affecting the bulk material behavior by setting

$$\begin{cases}\overline{\gamma}_{2f} = \overline{\gamma}_{2i} + \xi\,,\\ \xi = -\overline{\gamma}_{2i}\,,\end{cases} \qquad \Longrightarrow \qquad \overline{\gamma}_{2f} = 0\,. \tag{3.19}$$

  This eliminates the term $\frac{1}{2}\langle\mathbb{T}_{\text{c}}\operatorname{skew}\nabla\dot{u}, \operatorname{skew}\nabla\dot{u}\rangle$ from the Kinetic energy density, while keeping the dispersion curves of the model unchanged and thus we have effectively reduced the number of parameters by one, easing significantly the fitting procedure that we will see at the end of this chapter.

- After the fitting procedure is done using Bloch-Floquet analysis, we can change the values of the micro inertia parameters in the tensors $\mathbb{T}_{\text{e}}$ and $\mathbb{T}_{\text{c}}$ incrementally, by varying ξ in the transformation (3.17), producing different versions of our model, where the bulk contribution is the same (i.e. dispersion curves), but the boundary contribution is different. As it has been shown in [18], this boundary contribution is significant only for small specimens, where it can may be used to capture some boundary effects.

Lastly, we note that in order for the tensors $\mathbb{T}_{\text{e}}$ and $\mathbb{T}_{\text{c}}$ to be positive-definite, i.e. all four parameters must always have a positive value, for the transformation (3.17) it must hold $\xi \in [-\min(\overline{\kappa}_{\gamma i}, \overline{\gamma}_{2i}), \max(\overline{\gamma}_{1i}, \overline{\gamma}_{1i}^*)]$.

3.5 Dispersion curves

We assume a plane-strain plane wave ansatz for the displacement u and the micro-distortion tensor P which are our two independent kinematical fields

$$v_j = \Psi_j e^{i(k_1 x + k_2 y - \omega t)} \tag{3.20}$$

where v_j represents the generic component of u or P, Ψ_j is a scalar amplitude, $(k_1, k_2)^T = k(\sin\phi, \cos\phi)^T$ are the wave vector components with ϕ as the angle giving the direction of propagation, k the wave vector length (or wavenumber), and ω is the frequency.

Substituting our ansatz (3.20) in the equilibrium equations (3.5), we obtain the homogeneous linear system

$$[AT]\,[\Psi] = 0 \tag{3.21}$$

where $AT(\omega, k, \phi)$ is the Acoustic Tensor of the reduced relaxed micromorphic model which depends on the frequency ω, the wave vector length k, the angle of propagation ϕ, and all the elastic parameters appearing in (3.10), while $\Psi \in \mathbb{C}^6$ is the vector of amplitudes. We notice that the size of the Acoustic Tensor is now 6×6, since the micro-distortion tensor P carries only four degrees of freedom because we are in plain strain, which means $P_{13} = P_{23} = P_{31} = P_{32} = 0$ and also $u_3 = 0$. The non-trivial solutions of the system (3.21) are obtained when AT is singular, i.e. when $\det AT = 0$, which provides us with the dispersion relations of the reduced relaxed micromorphic model.

The acoustic tensor can be written as follows

$$AT = \begin{pmatrix} A & B \\ C & D \end{pmatrix} \tag{3.22}$$

where $(A, B, C, D) \in \mathbb{C}^{3\times3}$.
Since $\det AT = \det(A) \det\left(D - CA^{-1}B\right)$ [58], it is clear that the determinant of AT becomes the product of the two independent factors ($\det A$ and $\det D$) if either $B = 0$ or $C = 0$. In order for this to happen, the reference system must be aligned with the direction of wave propagation, and both must be aligned with a symmetry axes of the material [99]. Then the determinant $\det AT = \det(A) \det(D)$ is the product of two independent factors. This means that when taking the determinant of the Acoustic Tensor equal to zero in order to calculate the dispersion relations, this two factors can be zero independently in order for the determinant of the Acoustic Tensor to be zero. These two independent factors can be associated with pure-pressure waves $\det(A)$ and pure-shear waves $\det(D)$[1]. For each of the two factors, the dispersion polynomial has the similar form

$$c_0 k^2 - \left(c_1 + c_2 k^2\right)\omega^2 + \left(c_3 + c_4 k^2\right)\omega^4 - \left(c_5 + c_6 k^2\right)\omega^6 = 0\,. \tag{3.23}$$

describing either shear or pressure waves and it can also be written in a form $k(\omega)$ by

$$k = \omega\sqrt{\frac{c_1 - c_3\omega^2 + c_5\omega^4}{c_0 - c_2\omega^2 + c_4\omega^4 - c_6\omega^6}}. \tag{3.24}$$

The expressions of coefficients $c_0, c_1, \ldots, c_6$ change with respect to the angle of incidence (here 0° and 45°) and with respect to shear or pressure waves. As it can be seen, the dispersion polynomial for either shear or pressure waves is of 6th order with respect to ω and symmetric with respect to the transformation $\omega \longleftrightarrow -\omega$ and thus 3rd order with respect to ω^2. As a result, the reduced relaxed micromorphic model can describe three shear and three pressure curves.

3.5.1 Reduced relaxed micromorphic cutoffs

For the analytical calculation of the cutoffs frequencies, we substitute $k = 0$ in our dispersion relation (3.23), which becomes

$$\begin{aligned} -c_1\omega^2 + c_3\omega^4 - c_5\omega^6 = 0 \qquad &\Longleftrightarrow \qquad \omega^2\left(\omega^4 - \frac{c_3}{c_5}\omega^2 + \frac{c_1}{c_5}\right) = 0 \\ &\Longleftrightarrow \qquad \omega_1^2 = 0, \quad \omega_{2,3}^2 = \frac{c_3 \pm \sqrt{c_3^2 - 4c_1c_5}}{2c_5}\,. \end{aligned} \tag{3.25}$$

Again, for evident symmetry considerations and without loss of generality, we will only consider the positive half of the solutions in terms of frequency ω. The coefficients c_1, c_3, c_5 depend on the elastic parameters $\mu_{\mathrm{m}}, \kappa_{\mathrm{m}}, \mu_{\mathrm{m}}^*, \mu_{\mathrm{c}}, \mu_{\mathrm{e}}, \kappa_{\mathrm{e}}, \mu_{\mathrm{e}}^*$, the micro-inertia parameters $\kappa_\gamma, \gamma_1, \gamma_1^*, \gamma_2$, the macroscopic apparent density ρ, and size of the unit cell L_{c} but are independent of the parameters of the micro-inertia tensors $\mathbb{T}_{\mathrm{e}}$ and $\mathbb{T}_{\mathrm{c}}$.

[1] The fact that $\det(A)$ is associated with pressure waves and $\det(D)$ with shear waves depends on our choice of the order of the amplitudes in $\Psi = (u_1, P_{11}, P_{22}, u_2, P_{12}, P_{21})^T$.

Since when $k \to 0$ one solution for ω is always $\omega = 0$ and the other two are the expressions reported above, this means that from the three modes that the model can describe for shear and pressure, one is acoustic and the other two are optic. The explicit expression (3.38) can be used for the fitting procedure of the RRMM as described in Section 3.7.

3.5.2 Reduced relaxed micromorphic asymptotes

We calculate the reduced relaxed micromorphic asymptotes by considering the limit $k \to \infty$ in eq. (3.23) where only the terms with the highest order of k are important. Thus, we arrive at

$$c_0 - c_2\omega^2 + c_4\omega^4 - c_6\omega^6 = 0 \quad \iff \quad \omega^6 - \frac{c_4}{c_6}\omega^4 + \frac{c_2}{c_6}\omega^2 - \frac{c_0}{c_6} = 0\,. \tag{3.26}$$

Contrary to the simple analytical expression of the cutoffs, simplifying and using the asymptotes' expressions is not an easy task, since we must solve a third-order polynomial in ω^2. However, we obtain three distinct real-valued roots implying that all three asymptotes are horizontal, which is what we want when fitting the RRMM dispersion curves with respect to those coming from Bloch-Floquet analysis.

Regarding the necessary but not sufficient condition mentioned in Section 2.5, for the RRMM we get Table 3.1. Our necessary but not sufficient condition is respected, but of course we always need extra

$-$	k^0	k^2
ω^0	0	✓
ω^2	✓	✓
ω^4	✓	✓
ω^6	✓	✓

Table 3.1: Table of terms in powers of k and ω for the case of the RRMM

analytic calculations to be sure that some asymptotes are not zero or that they do not coincide. As discussed in the previous chapter, a horizontal asymptote for each curve guarantees that the interval of frequencies that each curve covers is limited as the ones obtained form the Bloch-Floquet analysis. We would like for our curves to have their frequency asymptotes coinciding with the frequency corresponding to the last wavenumber at the end of the Irreducible Brillouin-Zone (IBZ) coming from the Bloch-Floquet analysis. However, this is not always possible, as it depends on the shape of the Bloch-Floquet curves we have to fit, and if the dispersion polynomial of our model is able to replicate them.

In general we prefer curves with high slope for low wavenumbers, that tend to become horizontal early, and stay horizontal for high wavenumbers. If this is not the case, depending on the dispersion of the curves, we can choose to fit the curve's asymptote slightly higher or lower, to have a better fitting inside the Brillouin zone or afterwards. However, if an asymptote is placed higher than the last fitted wavenumber, we achieve a better fitting inside the IBZ, but this implies that for the RRMM there exists solutions of higher wavenumber outside the IBZ for higher frequency than the fitted curve itself. If a band-gap should start after the last point of the curve, this implies that the curve is invading it. This is the main dilemma we have when the fitting procedure is done, for cases where the Bloch-Floquet dipsrsion curves do not have optimal shape for our model.

3.6 A link between the material properties and dimension of a unit cell and the RRMM: dimensional analysis

For the RRMM, according to dimensional analysis, all micro-inertia tensors must have dimensions of $\frac{\mathrm{kg}}{\mathrm{m}}$. Lets take for example the term $\frac{1}{2}\langle \mathbb{I}_{\mathrm{e}}\,\mathrm{sym}\,\nabla\dot{u}, \mathrm{sym}\,\nabla\dot{u}\rangle$ where $\mathrm{sym}\,\nabla\dot{u}$ has dimensions of $\frac{1}{s}$. This means that the scalar product has dimensions $\left[x \cdot \frac{1}{s} \cdot \frac{1}{s}\right]$ (we keep the dimensions of $\mathbb{I}_{\mathrm{e}}$ as an unknown x), which we know must be equal to $\frac{\mathrm{J}}{\mathrm{m}^3}$ (energy density). Thus

$$\frac{\mathrm{J}}{\mathrm{m}^3} = x \cdot \frac{1}{s^2} \qquad \Longrightarrow \qquad x = \frac{\mathrm{J}\cdot\mathrm{s}^2}{\mathrm{m}^3} = \frac{\mathrm{N}\cdot\mathrm{s}^2}{\mathrm{m}^2} = \frac{\mathrm{kg}\cdot\frac{\mathrm{m}}{\mathrm{s}^2}\cdot\mathrm{s}^2}{\mathrm{m}^2} = \frac{\mathrm{kg}}{\mathrm{m}} = \frac{\mathrm{kg}}{\mathrm{m}^3}\cdot\mathrm{m}^2. \tag{3.27}$$

We don't know any quantity with these dimensions. We know however, that this energy contribution represents an inertia-like contribution, so we can think about collecting a density parameter: $\left[\frac{\mathrm{kg}}{\mathrm{m}}\right] = \left[\frac{\mathrm{kg}\cdot\mathrm{m}^2}{\mathrm{m}^3}\right] = \rho \cdot \mathrm{L_c}^2$, where ρ and L_c^2 have dimensions of $\left[\mathrm{kg/m^3}\right]$ and $\left[\mathrm{m}^2\right]$ respectively.

We will also show in the following section how expressing the micro-intertia tensors as a function of a density and a length is also mandatory if one wants to be consistent with the scaling properties of the dispersion curves coming from Bloch-Floquet analysis.

3.6.1 Dependence on the density ρ and the size of the unit cell L_c

The dependence on the density and the size of the unit cell can work as tools in order to scale the RRMM dispersion curves according to some properties that the dispersion curves coming from Bloch-Floquet analysis have, as explained in Section 1.3. We will also report these properties here for clarity. For the dispersion curves coming from Bloch-Floquet analysis using an arbitrary unit cell, it holds:

- The dispersion curves scale proportionally in frequency ω with respect to the base material's wave speed. This means that when keeping the geometry and size of the unit cell unaltered, using a stiffer or less dense base material would bring the curves higher in the frequency axis without changing its shape.
- Both the wavevector k and the frequency ω scale inversely with the unit cell size This implies that while keeping the geometry and base material of the unit cell unaltered, making the size of the unit cell bigger using an isotropic scaling brings the curves lower in the frequency axis and lower in the wavenumber axis without changing its shape.

Consistency of the reduced relaxed micromorphic model with respect to a change in the unit cell's size

Starting with the second property, we want the dispersion curves of the reduced relaxed micromorphic model to scale in the same way the Bloch-Floquet dispersion curves do, for physical reasons, but also in order to be able to only fit the parameters of our model once, and being able to scale the curves if only the size of the unit cell is scaled but not the geometry. If an arbitrary unit cell of length L is scaled by a factor of 2, then the frequency ω will halve and so will the wavenumber k.

In order to obtain this behavior with the reduced relaxed micromorphic model, we must scale all the micro-inertia tensors $(\mathbb{J}_\mathrm{m}, \mathbb{J}_\mathrm{c}, \mathbb{T}_\mathrm{e}, \mathbb{T}_\mathrm{c})$ by the square of the size of the unit cell. A proof was already given in [99] for the relaxed micromorphic model, here we show the one for the reduced version of the model, which is simpler.

If we consider a change in the size of the unit cell by some arbitrary factor $t > 0$, this requires the scaling of the parameter L_c by the same factor t (since we set L_c to the size of the unit cell). Assuming that all the other material parameters used remain constant, we substitute $L_\mathrm{c} \to tL_\mathrm{c}$ in the dispersion polynomial (3.23) and obtain (see Appendix A for the coefficients of the polynomial)

$$c_0k^2 - c_1\omega^2 - t^2c_2k^2\omega^2 + t^2c_3\omega^4 + t^4c_4k^2\omega^4 - t^4c_5\omega^6 - t^6c_6k^2\omega^6 = 0\,. \tag{3.28}$$

We can now collect a factor $\frac{1}{t^2}$ and arrive at

$$\frac{1}{t^2}\left[c_0(tk)^2 - c_1(t\omega)^2 - c_2(tk)^2(t\omega)^2 + c_3(t\omega)^4 + c_4(tk)^2(t\omega)^4 - c_5(t\omega)^6 - c_6(tk)^2(t\omega)^6\right] = 0\,. \tag{3.29}$$

Comparing equations (3.23) and (3.29) we can see that their roots $\omega(k)$ are simply linearly scaled with respect the factor t. This result enables the choice of having L_c equal to the size of the unit cell and thus allows us to change the latter in the microstructured material considered without needing to repeat the whole fitting procedure and changing any other parameters.

In particular, scaling the size L_c of the unit cell by the factor $t > 0$ will change the frequency ω and wavenumber k by the factor $\frac{1}{t}$, i.e. the frequency and wavenumber decrease proportional to the size of the unit cell. This simple observation allows to perform the fitting procedure for the relaxed micromorphic model only once for each geometry and material of the unit cell: changing the size of the unit cell afterwards will result in an automatic adjustment without changing any of the material parameters

(except L_c). Note that the slopes at the origin of the dispersion curves do not change when changing the size of the unit cell while keeping the geometry fixed because both frequency ω and wavenumber k are scaled by the same factor $\frac{1}{t}$.

Consistency of the reduced relaxed micromorphic model with respect to a change in the unit cell's bulk material properties

The dispersive properties of a microstructured isotropic Cauchy material depend exclusively and linearly on the wave speeds of the bulk material once its geometry is fixed. It is well known that the dispersion relations can be always written as $\omega = kc_i$ with $i = \{p, s\}$, where c_p and c_s are the pressure and shear wave speeds, respectively, defined as

$$c_p := \sqrt{\frac{\kappa_M + \mu_M}{\rho}}, \qquad c_s := \sqrt{\frac{\mu_M}{\rho}}, \qquad k = \frac{\omega}{c_i}, \qquad i = \{p, s\}. \tag{3.30}$$

This implies that by scaling the elastic coefficients by a constant a and the density by another constant b, we have

$$\widetilde{c}_p := c_p\sqrt{\frac{a}{b}}, \qquad \widetilde{c}_s := c_s\sqrt{\frac{a}{b}}, \qquad k = \sqrt{\frac{b}{a}}\frac{\omega}{c_i}, \qquad i = \{p, s\}.$$

Therefore, the response of an effective model should also change accordingly. Thus, we observe that by multiplying all the reduced relaxed micromorphic elastic coefficients ($\mathbb{C}_e, \mathbb{C}_c, \mathbb{C}_{micro}$) by a constant a and the apparent density ρ by another constant b, we can rewrite equation (3.23) as

$$a^3c_0k^2 - a^2b\left(c_1 + c_2k^2\right)\omega^2 + ab^2\left(c_3 + c_4k^2\right)\omega^4 - b^3\left(c_5 + c_6k^2\right)\omega^6 = 0. \tag{3.31}$$

By collecting a^3 we obtain

$$a^3\left[c_0k^2 - \frac{b}{a}\left(c_1 + c_2k^2\right)\omega^2 + \frac{b^2}{a^2}\left(c_3 + c_4k^2\right)\omega^4 - \frac{b^3}{a^3}\left(c_5 + c_6k^2\right)\omega^6\right] = 0 \tag{3.32}$$

from which we can introduce a scaled frequency $\widetilde{\omega} = \omega\sqrt{\frac{b}{a}}$. We notice that solving the equation (3.32) for $\widetilde{\omega}$ is going to give us the same solutions of (3.23) which were for the unscaled material, and in order to obtain the new ones, i.e. the one of the scaled material, it is enough to use the relation $\omega = \widetilde{\omega}\sqrt{\frac{a}{b}}$. In summary, increasing the stiffness (a) or decreasing the density (b) of the base material will cause an overall shifting of the dispersion curves toward higher frequencies.

This is consistent with what is observed looking at the dispersion properties of a microstructured material's unit cell obtained via a Bloch-Floquet analysis. In the case for which $a = b$, the roots of equation (3.32) do not change at all. Thanks to this identification, we can now easily change the material constituting the unit cell (without changing the geometry) by scaling the material parameters accordingly without repeating the whole fitting process. In particular, all the cutoffs and asymptotes will be scaled by a quantity $\sqrt{\frac{a}{b}}$.

We explicitly remark again that scaling the macroscopic apparent density ρ of the unit cell by a factor $b > 0$ will change the frequency ω by the factor $\frac{1}{\sqrt{b}}$, i.e. the frequency is inversely proportional to the square root of the density of the unit cell. The wavenumber k is invariant under changing the macroscopic apparent density since the periodicity of the unit cell remains unaltered.

3.7 Identification procedure of the reduced relaxed micromorphic parameters

We will explain here how the identification procedure of the reduced relaxed micromorphic parameters is done for any single-phase unit cell that has tetragonal symmetry. We start by noting that the number of unknown parameters of the model is 16, namely: $\rho, \kappa_e, \mu_e, \mu_e^*, \kappa_m, \mu_m, \mu_m^*, \mu_c, \kappa_\gamma, \gamma_1, \gamma_1^*, \gamma_2, \overline{\kappa}_\gamma, \overline{\gamma}_1, \overline{\gamma}_1^*, \overline{\gamma}_2$. We will show how 8 of them are fixed on certain analytical properties the curves must fulfill, one parameter can be excluded due to reasons explained in Section 3.4 and the 7 remaining parameters are fitted through an error minimization procedure. We remark, that the ultimate goal of the identification procedure is to adequately replicate the Bloch-Floquet band structure of the unit cell under consideration, and thus

having a model that can capture the behavior of an infinite metamaterial composed of that specific unit cell.

The band structure includes wavevectors with angles of incidence ranging from 0° to 45°. Due to this, it makes sense that the fitting procedure should be done for all these angles, e.g. one could fix the parameters for an arbitrary angle of incidence, then check a second angle, see if the curve fitting is sufficient, change the parameters again, and so on and so forth, until the curves are accurate enough for all the angles. However, due to the symmetry class of the unit cell, and consequently, of all our material tensors, it is enough to apply the fitting procedure only for the 0° and 45° direction of propagation, and it must be done simultaneously for the two directions, as will be explained in the following section. This guarantees that the fitting will be accurate enough also for the in-between angles.

We start the identification procedure with the calculation of the macroscopic apparent density ρ. The macroscopic apparent density is calculated in a standard way: for any arbitrary unit cell, we calculate the percentage area (volume) that the material of the unit cell occupies with respect to its whole area (volume), and we multiply that by the density of the base material.

We proceed by calculating the macro parameters $\kappa_{\mathrm{M}}, \mu_{\mathrm{M}}, \mu^*_{\mathrm{M}}$, i.e. the values of tensor $\mathbb{C}_{\mathrm{Macro}}$ for the long-wavelength limit by evaluating the slopes of the Acoustic curves at the origin of the dispersion curves plot. For an anisotropic Cauchy material, the speed of the acoustic waves are

$$\begin{aligned} c_{\mathrm{p}} &= \sqrt{\frac{\kappa_{\mathrm{M}} + \mu_{\mathrm{M}}}{\rho}}\,, & c_{\mathrm{s}} &= \sqrt{\frac{\mu^*_{\mathrm{M}}}{\rho}}\,, \\ \overline{c}_{\mathrm{p}} &= \sqrt{\frac{\kappa_{\mathrm{M}} + \mu^*_{\mathrm{M}}}{\rho}}\,, & \overline{c}_{\mathrm{s}} &= \sqrt{\frac{\mu_{\mathrm{M}}}{\rho}}\,, \end{aligned} \tag{3.33}$$

where c_p, c_s are the speed of pressure and shear wave, respectively, for 0° of incidence, while $\overline{c}_p, \overline{c}_s$ describe an incidence angle of 45°. For the tetragonal class of symmetry we choose, it also holds

$$c_{\mathrm{p}}^2 + c_{\mathrm{s}}^2 = \frac{\kappa_{\mathrm{M}} + \mu_{\mathrm{M}} + \mu^*_{\mathrm{M}}}{\rho} = \overline{c}_{\mathrm{p}}^2 + \overline{c}_{\mathrm{s}}^2\,, \tag{3.34}$$

reducing the system of equations to just three independent quantities since density is already fixed. For the reduced relaxed micromorphic model, we fit these macro parameters by using the slope of the corresponding acoustic dispersion curves at $k = 0$ with

$$\mu_{\mathrm{M}} = \overline{c}_{\mathrm{s}}^2\,\rho\,, \qquad \mu^*_{\mathrm{M}} = c_{\mathrm{s}}^2\,\rho\,, \qquad \kappa_{\mathrm{M}} = \left(c_{\mathrm{p}}^2 - \overline{c}_{\mathrm{s}}^2\right)\rho = \left(\overline{c}_{\mathrm{p}}^2 - c_{\mathrm{s}}^2\right)\rho\,. \tag{3.35}$$

As a next step, we can always compute the parameters of the meso-scale depending on the micro-parameters and the macro-parameters, by manipulating eq. (3.15) as

$$\mathbb{C}_{\mathrm{e}} = \mathbb{C}_{\mathrm{micro}}\left(\mathbb{C}_{\mathrm{micro}} - \mathbb{C}_{\mathrm{Macro}}\right)^{-1}\mathbb{C}_{\mathrm{Macro}}\,. \tag{3.36}$$

For the tetragonal class of symmetry in 2D, relation (3.36) particularizes to

$$\mu_{\mathrm{e}} = \frac{\mu_{\mathrm{m}}\mu_{\mathrm{M}}}{\mu_{\mathrm{m}} - \mu_{\mathrm{M}}}\,, \qquad \kappa_{\mathrm{e}} = \frac{\kappa_{\mathrm{m}}\kappa_{\mathrm{M}}}{\kappa_{\mathrm{m}} - \kappa_{\mathrm{M}}}\,, \qquad \mu^*_{\mathrm{e}} = \frac{\mu^*_{\mathrm{m}}\mu^*_{\mathrm{M}}}{\mu^*_{\mathrm{m}} - \mu^*_{\mathrm{M}}}\,. \tag{3.37}$$

We note that one must be careful when using these relations, since the denominator of all fractions shows that the micro parameters must always be strictly bigger than the corresponding macro, otherwise the meso parameters either diverge to infinity or become negative. By calculating the density and the macro parameters, and then using relations (3.37) to express the meso parameters, we reduce the number of unknown variables to 12.

The next step in order to reduce the number of unknown parameters further, before proceeding to the error minimization step, is to use the analytical expressions of the cutoffs of the four optic curves. We remark that cutoffs values in Bloch-Floquet analysis remain constant for any angle of incidence, since they are frequencies at which $k = 0$. We can calculate the analytical expressions of the cutoffs from eq. (3.25) where the values of the coefficients can be found in Appendix A. Calculating them for the 0° or 45° direction of propagation (since the fitting must only be performed for these two angles) gives

$$\omega_r = \sqrt{\frac{\mu_c}{\rho L_c^2 \gamma_2}}\,, \qquad \omega_s = \sqrt{\frac{\mu_e + \mu_m}{\rho L_c^2 \gamma_1}}\,, \qquad \omega_{ss} = \sqrt{\frac{\mu^*_e + \mu^*_m}{\rho L_c^2 \gamma_1^*}}\,, \qquad \omega_p = \sqrt{\frac{\kappa_e + \kappa_m}{\rho L_c^2 \kappa_\gamma}}\,. \tag{3.38}$$

	0°	45°
Shear	$\omega_2 = \omega_{ss}$	$\omega_2 = \omega_s$
	$\omega_3 = \omega_r$	$\omega_3 = \omega_r$

	0°	45°
Pressure	$\omega_2 = \omega_s$	$\omega_2 = \omega_{ss}$
	$\omega_3 = \omega_p$	$\omega_3 = \omega_p$

Table 3.2: Cutoff expressions for the pressure waves (right) and for the shear waves (left).

We notice that ω_s and ω_{ss} change from pressure to shear and shear to pressure, respectively, when going from the direction of propagation of 0° to 45°. This means that for any unit cell we choose to fit, we must choose two modes to change polarization in the curves when going from 0° to 45°.

Relations (3.38) allow us to reduce the number of unknown parameters further, arriving to 8 unknown parameters overall. One additional reduction we can do, is take advantage of the Null-Lagrangian in the micro-inertia contribution of the model as explained in Section 3.4, and further reduce the number of unknown parameters to 7.

After this point, the values of the 7 remaining parameters, namely $\kappa_{\mathrm{m}}, \mu_{\mathrm{m}}, \mu^*_{\mathrm{m}}, \mu_c, \overline{\kappa}_\gamma, \overline{\gamma}_1, \overline{\gamma}^*_1$ are found through an error minimization procedure. This procedure is done using *Mathematica*® and its built in minimization function `Nminimize`. What is being minimized is the sum of the squares of the errors between the frequency of the dispersion curves of the RRMM and those coming from Bloch-Floquet analysis for all given wavenumbers.

In Chapter 2, we have talked about how the order of the dispersion polynomial with respect to ω and k was one important condition for the accurate description of the dispersion of a metamaterial. The other is the "freedom" one has during the fitting procedure. We have here arrived at the fitting loop with 7 parameters and we wish to simultaneously minimize the mean square error between the 0° and 45° dispersion curves of the model and those from Bloch-Floquet. The difficulty of this depends on the dependency of the parameters in each dispersion polynomial for 0° and 45°. This can be seen in Table 3.3.

We can clearly see that there are parameters influencing both the behavior of shear and pressure curves for a given direction of propagation, or the behavior of one polarisation (shear or pressure) for both 0° and 45°. In addition, we note that we have 12 different asymptotes to fit with the remaining 7 parameters. This means that the fitting procedure is not an easy task, but also that there are limits to what extent the dispersion curves can be fitted accurately. A case of full "freedom" would be one where curves of a single polarisation and a single direction depend on distinct parameters, but due to the nature of the procedure of dispersion curves calculation this is not possible.

	Shear	Pressure
0°	$\overline{\gamma_1}^*, \mu_c, \mu^*_m$	$\kappa_m, \overline{\gamma}_1, \overline{\kappa}_\gamma, \mu_m$
45°	$\overline{\gamma}_1, \mu_c, \mu_m$	$\kappa_m, \overline{\gamma_1}^*, \overline{\kappa}_\gamma, \mu^*_m$

Table 3.3: Dependence of dispersion curves on the parameters for pressure and shear at 0° and 45°.

Chapter 4

Modeling metamaterials of finite size: boundary effects as a consequence of the choice of unit cell "cut" for a locally resonant metamaterial

4.1 Introduction

In the previous chapter, we explained that in order to capture the dynamical response of an infinite microstructured metamaterial using a homogenised framework, one needs to use a model that is able to capture the dispersion of the metamaterial, since the dispersion curves for our homogenised model must coincide with those of the microstructured metamaterial obtained from Bloch-Floquet analysis.

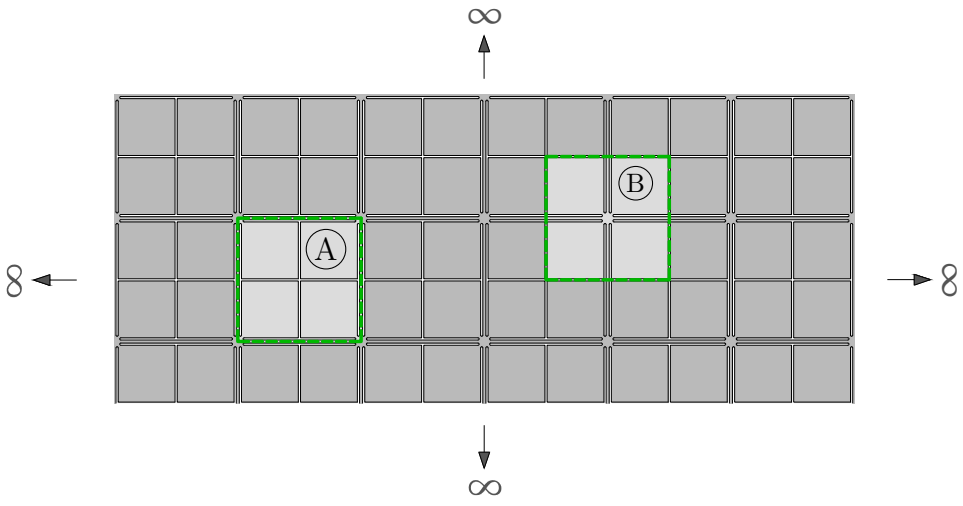

Figure 4.1: Infinitely big locally resonant metamaterial and identification of two possible unit cell "cuts": "cut" A (left) and "cut" B (right).

As already mentioned, the ability of the model to capture the dispersion relies firstly on the order of the dispersion polynomial, and secondly on the "freedom" of the curves (which parameters affect which curves). In this Chapter, we will attempt to go one step further by modeling a locally resonant metamaterial using the RRMM which we will show that has the ability to capture accurately the dispersion of this metamaterial. We will, however, see that the ability to capture the dispersion does not also necessarily mean an accurate description of finite-sized metamaterials.

4.2 Properties of the locally resonant acoustic metamaterial

The infinite locally resonant metamaterial we wish to model is made out of Titanium and can be seen in Fig. 4.1, where we can identify two tetragonal unit cell "cuts", "cut" A (left) and "cut" B (right). The two "cuts" are equivalent in the sense that their periodic tailing builds the same infinite metamaterial.

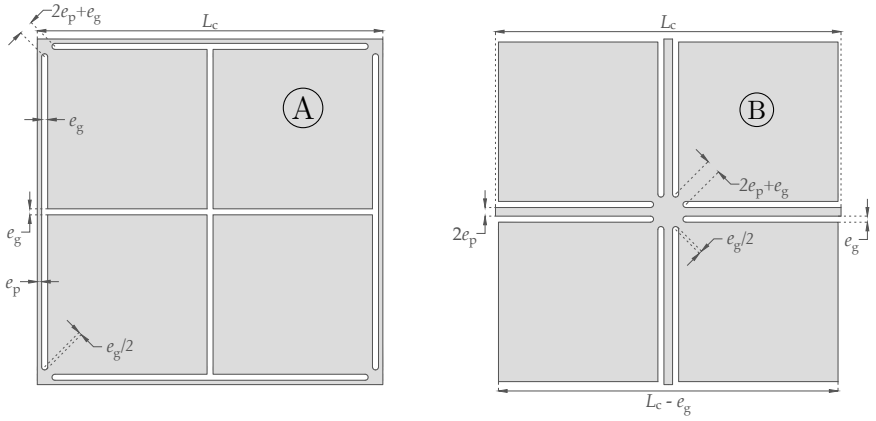

L_c [m]	e_g [mm]	e_p [mm]	ρ_{Ti} [kg/m^3]	κ_{Ti} [Pa]	μ_{Ti} [Pa]
0.02	0.35	0.25	4400	116.7×10^9	41.8×10^9

Figure 4.2: (Top left) unit cell "cut" A, (top right) unit cell "cut" B and (bottom) material and geometrical properties: the size of the unit cell is L_c, the density ρ_{Ti}, the bulk modulus κ_{Ti} and the shear modulus μ_{Ti}.

The dimensions of the "cuts" and the properties of the base material can be seen in Fig. 4.2 and the dispersion curves for 0° and 45° wave incidence can be seen in Fig. 4.3 where we notice a band-gap in the acoustic range, attributed to a local resonance mechanism (we can see the four local resonators clearly in both unit cell "cuts" in Fig. 4.2). For that particular reason, the unit cell possesses a very intricate geometry, which implies the huge computational cost that comes with modeling such materials using fully resolved microstructured simulations. As a result, we proceed by modeling our metamaterial using the RRMM.

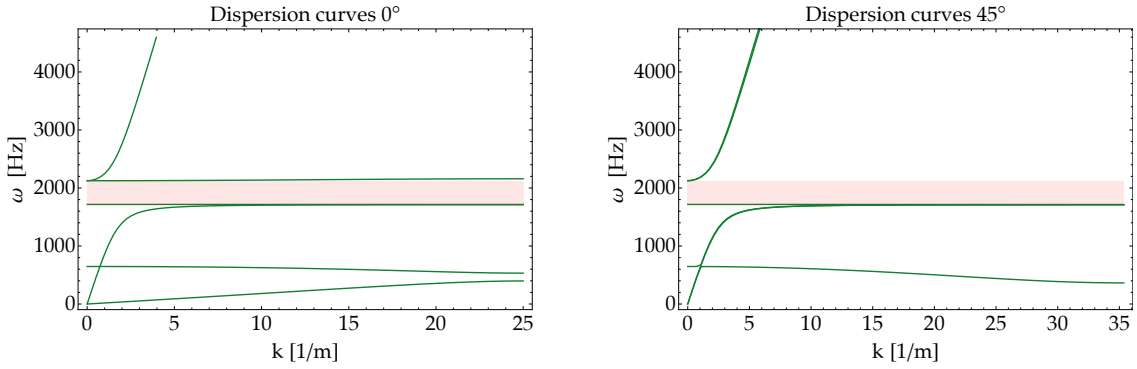

Figure 4.3: Dispersion curves for 0° (left) and 45° (right), obtained by performing Bloch-Floquet analysis on any of the two unit cell "cuts" in Fig. 4.2 by using *Comsol Multiphysics*®.

4.3 Parameter identification

The RRMM has been already introduced in Chapter 3 while in the same chapter, the parameter identification procedure has been explained in detail in Section 3.7. Wanting to model our metamaterial using the RRMM, our goal is to give to the parameters of the model such values, so that the RRMM dispersion curves for 0° and 45° are as close as possible to the dispersion curves from Bloch-Floquet analysis in Fig. 4.3.

According to Section 3.7, the parameters with an analytical expression are

$$\begin{aligned}
\rho &= \rho_{\mathrm{Ti}}\,\frac{A_{\mathrm{Ti}}}{A_{\mathrm{tot}}}\,, & \kappa_{\mathrm{e}} &= \frac{\kappa_{\mathrm{m}}\,\kappa_{\mathrm{M}}}{\kappa_{\mathrm{m}}-\kappa_{\mathrm{M}}}\,, & \mu_{\mathrm{e}} &= \frac{\mu_{\mathrm{m}}\,\mu_{\mathrm{M}}}{\mu_{\mathrm{m}}-\mu_{\mathrm{M}}}\,,\\
\mu_{\mathrm{e}}^{*} &= \frac{\mu_{\mathrm{m}}^{*}\,\mu_{\mathrm{M}}^{*}}{\mu_{\mathrm{m}}^{*}-\mu_{\mathrm{M}}^{*}}\,, & \kappa_{\gamma} &= \frac{\kappa_{\mathrm{e}}+\kappa_{\mathrm{m}}}{\rho\,L_{\mathrm{c}}^{2}\,\omega_{\mathrm{p}}^{2}} & \gamma_{1} &= \frac{\mu_{\mathrm{e}}+\mu_{\mathrm{m}}}{\rho\,L_{\mathrm{c}}^{2}\,\omega_{\mathrm{s}}^{2}}\,,\\
\gamma_{1}^{*} &= \frac{\mu_{\mathrm{e}}^{*}+\mu_{\mathrm{m}}^{*}}{\rho\,L_{\mathrm{c}}^{2}\,\omega_{\mathrm{ss}}^{2}}\,, & \gamma_{2} &= \frac{\mu_{\mathrm{c}}}{\rho\,L_{\mathrm{c}}^{2}\,\omega_{\mathrm{r}}^{2}}\,.
\end{aligned} \tag{4.1}$$

where A_{Ti} and A_{tot} are respectively the area of Titanium and the total area (including the voids) of the unit cell, ω_{p}, ω_{r}, ω_s, and ω_{ss} are the cutoff frequencies, namely the frequencies for a vanishing wavenumber $k=0$, κ_{M}, μ_{M}, and μ_{M}^{*} are the *Macro-parameters*, while L_{c} is the length of the side of the unit cell, i.e. $L_{\mathrm{c}}=0.02$ m.

As already remarked, the remaining 8 parameters κ_{m}, μ_{m}, μ_{m}^{*}, μ_{c}, $\overline{\kappa}_{\gamma}$, $\overline{\gamma}_1$, $\overline{\gamma}_1^{*}$, and $\overline{\gamma}_2$ are obtained by minimizing the error between the dispersion curves obtained via Bloch-Floquet analysis and the ones of the equivalent RRMM. Minimizing the error, one can arrive to the parameter values shown in Table 4.1. The dispersion curves of the RRMM, using these values are shown in Fig. 4.4 in comparison with those obtained via Bloch-Floquet analysis (same as Fig. 4.3).

L_{c} [m]	κ_{e} [Pa]	μ_{e} [Pa]	μ_{e}^{*} [Pa]
0.02	2.51×10^{9}	2.39×10^{9}	1.20×10^{6}
μ_{c} [Pa]	κ_{m} [Pa]	μ_{m} [Pa]	μ_{m}^{*} [Pa]
1.11×10^{4}	4.54×10^{9}	4.43×10^{9}	4.18×10^{10}
κ_{γ} [-]	γ_1 [-]	γ_1^{*} [-]	γ_2 [-]
1016.56	983.36	9234.89	0.02
$\overline{\kappa}_{\gamma}$ [-]	$\overline{\gamma}_1$ [-]	$\overline{\gamma}_1^{*}$ [-]	$\overline{\gamma}_2$ [-]
5.45	3.09	1.45×10^{-9}	1.87
κ_{M} [Pa]	μ_{M} [Pa]	μ_{M}^{*} [Pa]	ρ [kg/m^3]
1.62×10^{9}	1.55×10^{9}	1.20×10^{6}	3840.77

Table 4.1: Values of the elastic parameters, the micro-inertia parameters, the characteristic length L_{c}, and the apparent density ρ for the RRMM. In the last row we also report the macro parameters.

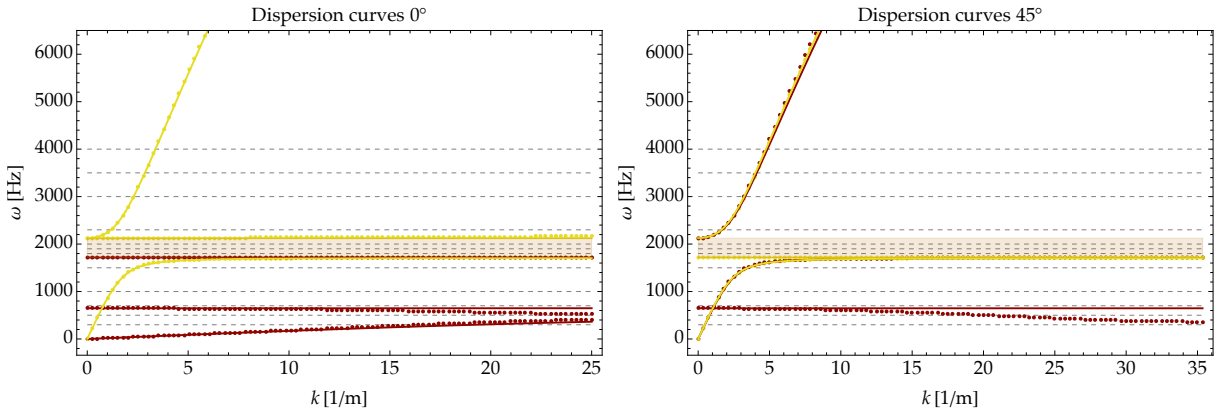

Figure 4.4: Dispersion curves for 0° (left), and for 45° (right). The dots correspond to the solution of the Bloch-Floquet analysis performed on any of the two unit cell "cuts" in Fig. 4.2 by using *Comsol Multiphysics*®, while the solid lines represent the analytical expression of the dispersion curves for the reduced relaxed micromorphic model. We mark shear modes in red and pressure modes in yellow. The dashed lines represent the frequencies used in the numerical simulations.

We can see that the dispersion curves of the RRMM coincide very accurately with those of the metamaterial, implying that now, with this very good agreement, we can proceed to run our numerical simulations of finite-sized specimens.

4.4 Numerical simulations

In this section, we present the set-up of the numerical simulations on a finite-size metamaterial both with a microstructured Cauchy model and the reduced relaxed micromorphic model.

4.4.1 Microstructured materials simulations set-up

All the 2D simulations presented here have been performed under a plane-strain assumption and with a *time-harmonic* ansatz. The two microstructured materials presented in this work have been built as a regular grid of finite-size (16×16 unit cells of side $L_c = 0.02$ m), whose building blocks are the unit cells made up of Titanium shown in Fig. 4.2. The resulting metamaterials are embedded between two slender homogeneous Cauchy plates made out of Titanium.

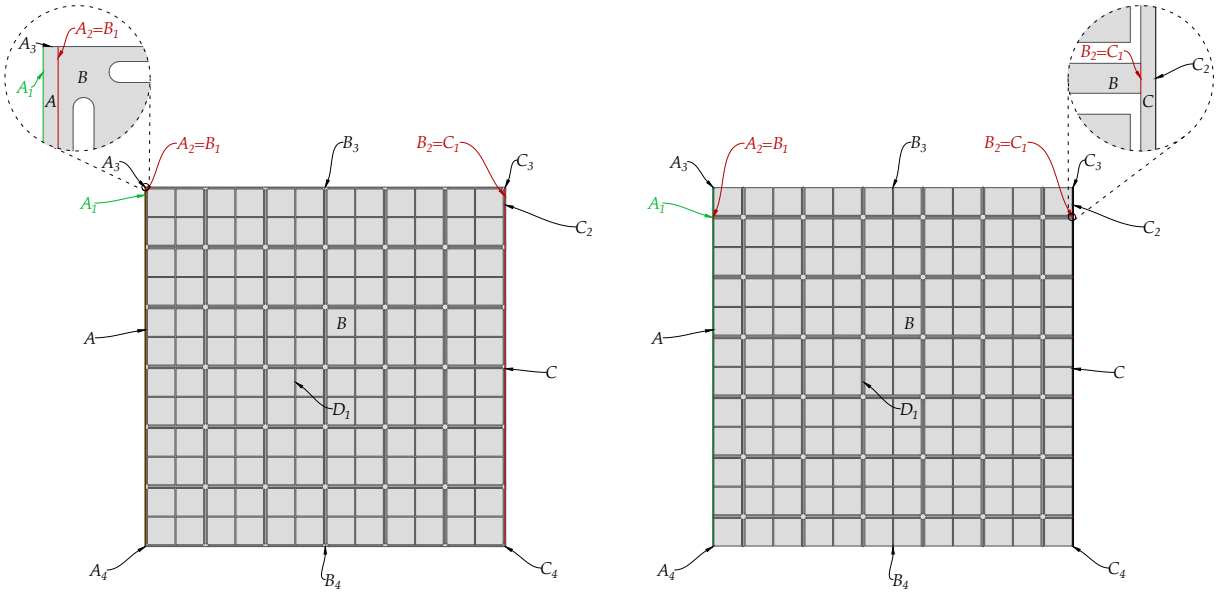

Figure 4.5: Schematic view of the geometry and the labeling of the boundaries and interfaces for (left) the microstructured material built out of the unit cell A and (right) the microstructured material built out of the unit cell B.

The following boundary and interface conditions have been enforced (see Fig. 4.5)

$$
\begin{array}{rcrlll}
u_x|_{A_1} = \overline{u} & \text{and} & u_y|_{A_1} \to \text{free} & \text{(prescribed disp. - green)} & \text{on} & A_1 \\
u|_{A_2} = u|_{B_1} & \text{and} & \sigma\, n|_{A_2} = \sigma\, n|_{B_1} & \text{(perfect contact - red)} & \text{on} & A_2 \equiv B_1 \\
u|_{B_2} = u|_{C_1} & \text{and} & \sigma\, n|_{B_2} = \sigma\, n|_{C_1} & \text{(perfect contact - red)} & \text{on} & B_2 \equiv C_1 \\
\sigma\, n = 0 & & & \text{(stress free - black)} & \text{on} & A_3, A_4, B_3, B_4, \\
 & & & & & C_2, C_3, C_4, D_1
\end{array}
\tag{4.2}
$$

where the magnitude of the harmonic prescribed displacement $\overline{u}$ is 1% of the size of the specimen. In particular, we set $\overline{u} = u_0\, e^{-i\omega t}$ with $u_0 = 3.2$ mm. The simulations have been performed by using the *Solid Mechanics* physics package of *Comsol Multiphysics*®. In order to ease the convergence of the analysis, we introduced a small amount of isotropic damping ($\eta = 0.002$).

4.4.2 Reduced relaxed micromorphic continuum simulations set-up

The microstructured material is here modeled with the reduced relaxed micromorphic model, which is characterised by the material parameters in Table 4.1. In addition, the following boundary and interface conditions have been enforced (see Fig. 4.6)

$$
\begin{array}{rcrlll}
u_x|_{A_1} = \overline{u} & \text{and} & u_y|_{A_1} \to \text{free} & \text{(prescribed disp. - green)} & \text{on} & A_1 \\
u|_{A_2} = u|_{B_1} & \text{and} & \sigma\, n|_{A_2} = \widetilde{\sigma}\, n|_{B_1} & \text{(perfect contact - red)} & \text{on} & A_2 \equiv B_1 \text{[1]} \\
u|_{B_2} = u|_{C_1} & \text{and} & \widetilde{\sigma}\, n|_{B_2} = \sigma\, n|_{C_1} & \text{(perfect contact - red)} & \text{on} & B_2 \equiv C_1 \\
\sigma\, n = 0 & & & \text{(stress free - black)} & \text{on} & A_3, A_4, C_2, C_3, C_4 \\
(\widetilde{\sigma} + \widehat{\sigma})\, n = 0 & & & \text{(stress free - black)} & \text{on} & B_3, B_4
\end{array}
\tag{4.3}
$$

where again, the magnitude of the prescribed harmonic displacement $\overline{u}$ is 1% of the size of the specimen. The effective homogeneous material modeled with the reduced relaxed micromorphic model is also embedded between two slender homogeneous Cauchy plates made out of Titanium. The simulations have been performed by using the *Weak Form PDE* physics package of *Comsol Multiphysics*®. This package requires the implementation of the expression of the Lagrangian of the model (3.3) and the appropriate boundary and interface conditions. To have a consistent comparison with the results from the microstructured material, we have introduced the same small amount of isotropic damping ($\eta = 0.002$) also in this case.

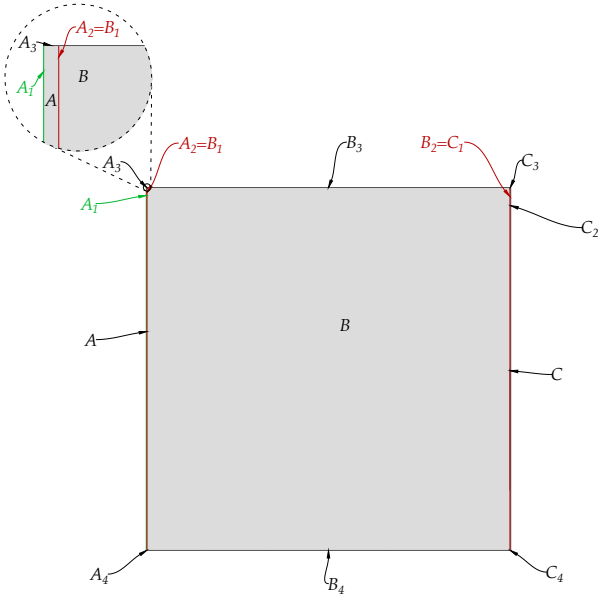

Figure 4.6: Schematic view of the geometry and the labeling of the boundaries and interfaces for the equivalent reduced relaxed micromorphic material.

4.5 Results and comparison

In this section, we show the results issued by the numerical simulations described in Section 4.4 for the values of frequencies highlighted in Figure 4.4 (dashed lines).

In Figs. 4.7 - 4.10 the structural response[2] for different frequencies is given for (left) the microstructured material built out of the unit cell "cut" A, (center) the equivalent reduced relaxed micromorphic material, and (right) the microstructured material built out of the unit cell "cut" B.

It can be inferred by direct inspection of these figures that "cut" B gives rise to a macroscopic response which is better captured by the reduced relaxed micromorphic model, except for the frequency $\omega = 3500$ Hz at which a structural resonant mode is predominant (see the right panel of the second row in Fig. 4.10). However, we can also notice that, except for some small regions close to the boundary (e.g. $\omega = 300$ and $\omega = 1000$ for "cut" A, where we can see a boundary effect of the size of half a unit cell at the top edge of the specimen), also the behaviour of "cut" A is captured at an acceptable level of agreement. Exceptions arise for the frequency $\omega = 500$ Hz and $\omega = 700$ Hz at which, respectively, microstructure related resonant modes might become predominant, or a boundary effect occurs that is able to propagate in the bulk.[3]

[1] These jump conditions can be also written in compact from as $[[u]] = 0$ and $[[t]]=0$ where $[[u]]$ represents the jump of displacement and $[[t]] = t^+ - t^- = \sigma n - (\widetilde{\sigma} + \widehat{\sigma})\, n$ is the jump of the generalized traction across the green interface.

[2] In these figures we show the dimensionless displacement field, i.e. norm of the displacement field at each point, divided by the assigned displacement $\overline{u}$.

[3] Microstructure related resonant modes are observed by direct inspection of the displacement field inside the unit cell for the microstructured simulation.

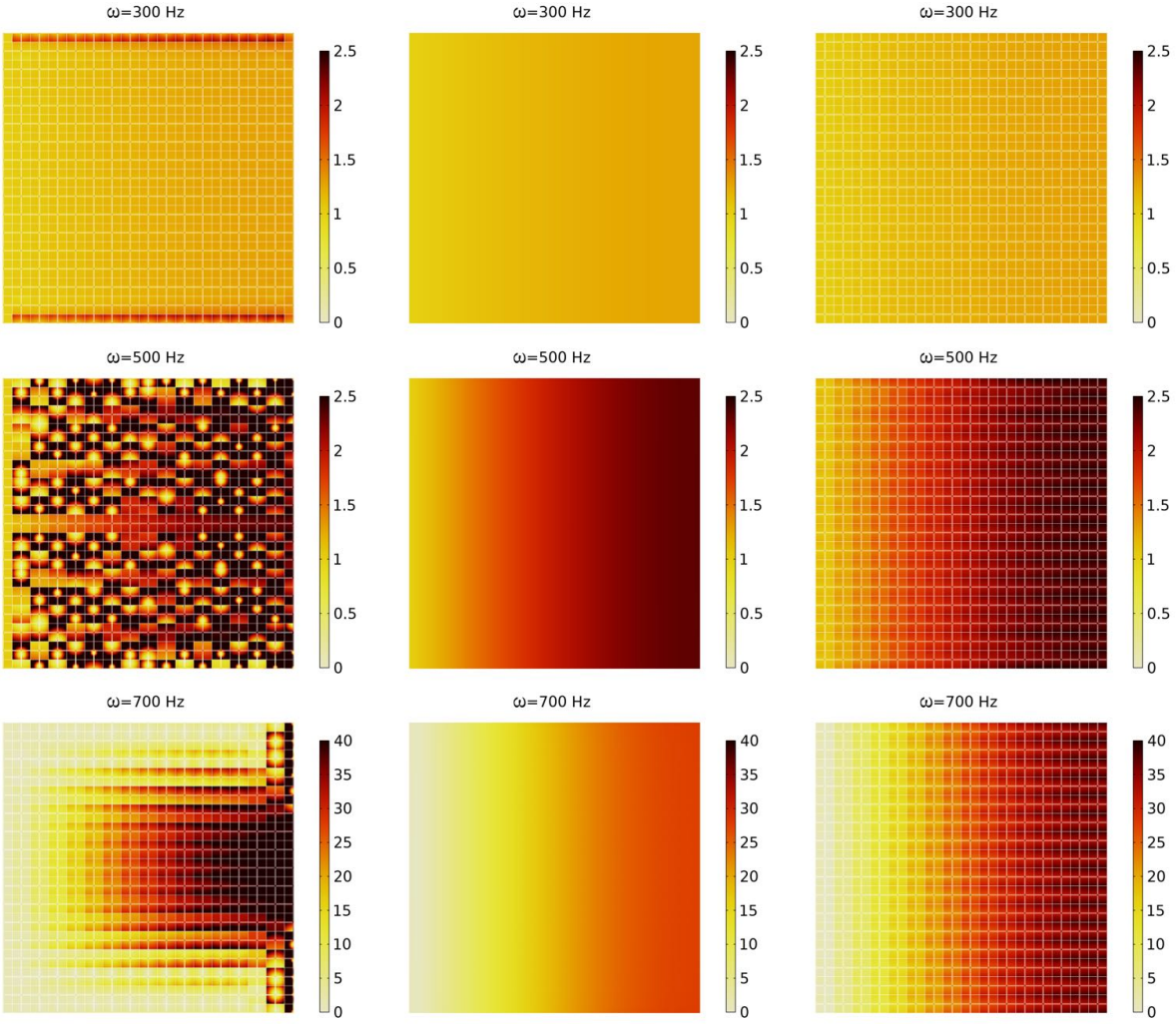

Figure 4.7: Norm of the displacement field $|u|$ divided by the amplitude of the assigned harmonic displacement $\overline{u}$ for 300, 500, and 700 Hz for (left) the microstructured material whose building block is "cut" A, (center) the equivalent reduced relaxed micromorphic material, and (right) the microstructured material whose building block is "cut" B.

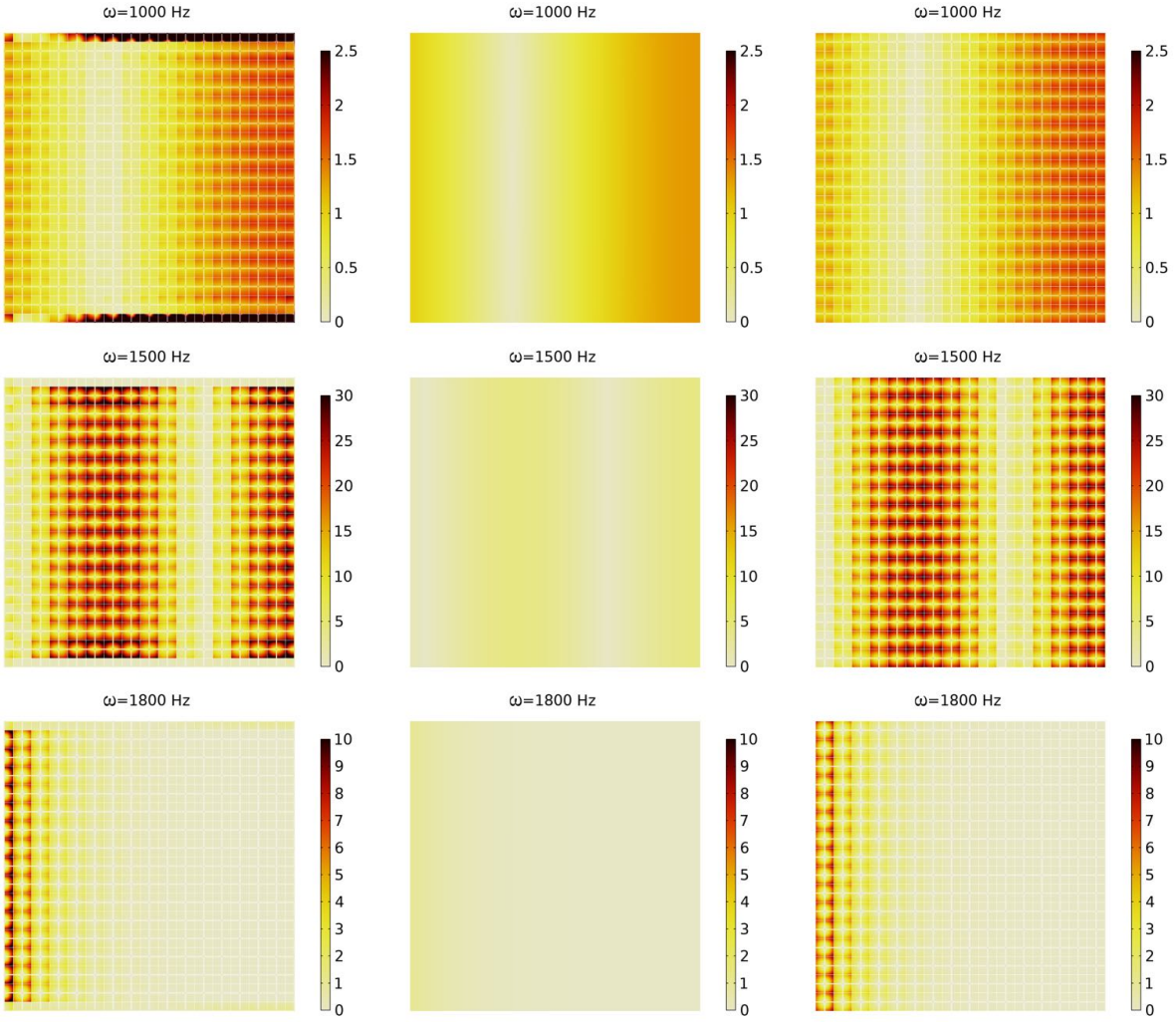

Figure 4.8: Norm of the displacement field $|u|$ divided by the amplitude of the assigned harmonic displacement $\overline{u}$ for 1000, 1500, and 1800 Hz for (left) the microstructured material whose building block is "cut" A, (center) the equivalent reduced relaxed micromorphic material, and (right) the microstructured material whose building block is "cut" B.

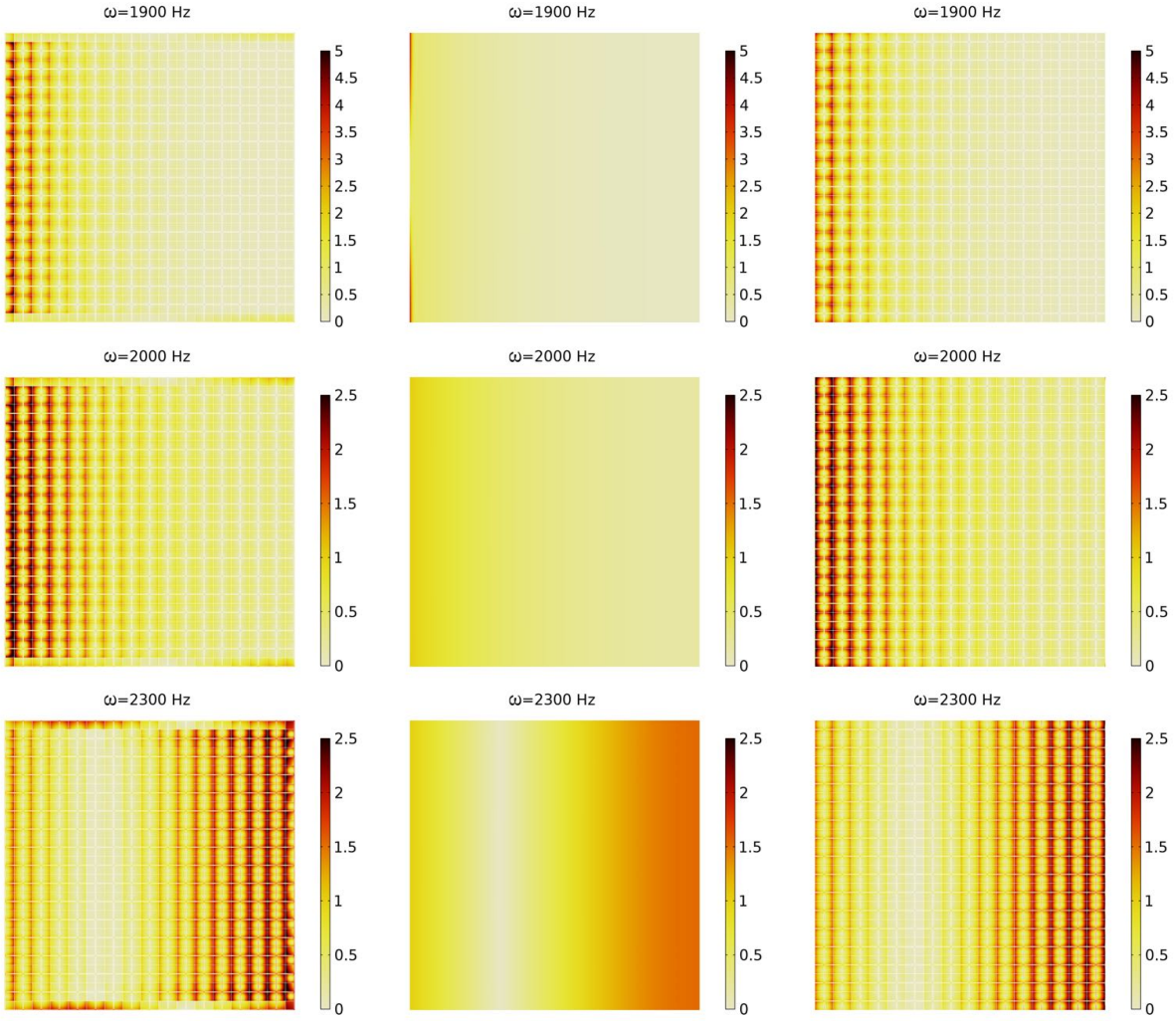

Figure 4.9: Norm of the displacement field $|u|$ divided by the amplitude of the assigned harmonic displacement $\overline{u}$ for 1900, 2000, and 2300 Hz for (left) the microstructured material whose building block is "cut" A, (center) the equivalent reduced relaxed micromorphic material, and (right) the microstructured material whose building block is "cut" B.

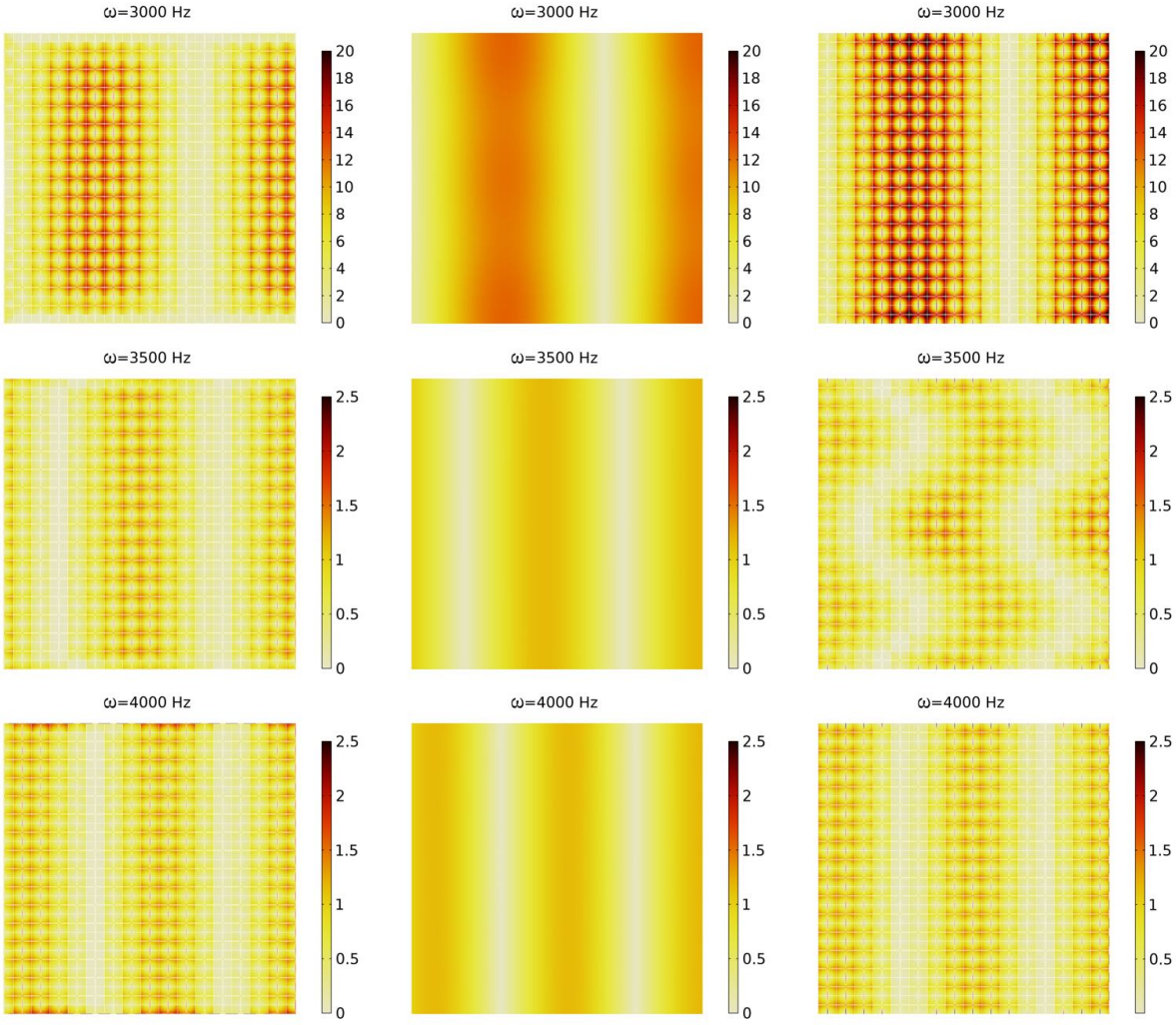

Figure 4.10: Norm of the displacement field $|u|$ divided by the amplitude of the assigned harmonic displacement $\overline{u}$ for 3000, 3500, and 4000 Hz for (left) the microstructured material whose building block is "cut" A, (center) the equivalent reduced relaxed micromorphic material, and (right) the microstructured material whose building block is "cut" B.

4.6 Discussion

In Figs. 4.11 - 4.13 we show a detail of the deformation close to the boundary for the simulations at which a disagreement with the reduced relaxed micromorphic model was detected in one of the two microstructured simulations. It seems to be the case that in all the simulations where the macroscopic response of the reduced relaxed micromorphic model deviates from the microstructured one, important bending of the structural elements constituting the unit cell occurs (we better describe this bending in the captions of Figures 4.11-4.13).

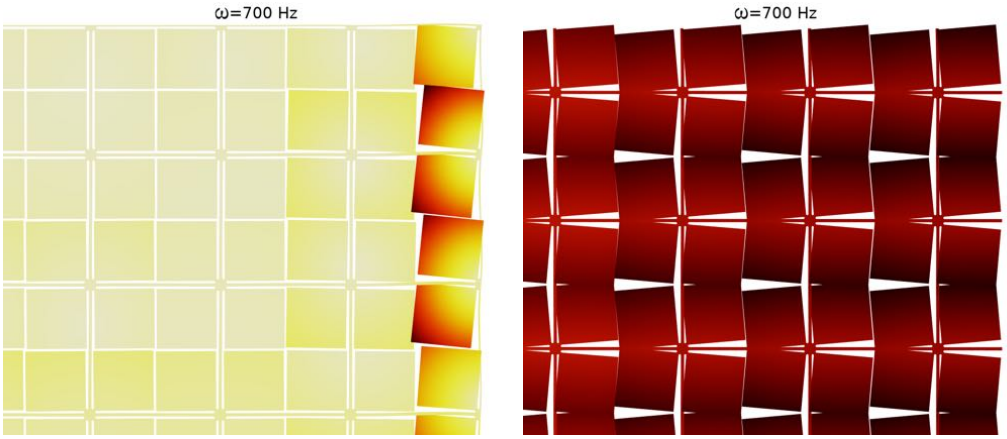

Figure 4.11: Detail of the deformation for $\omega = 700$ Hz for (left) the structure based on "cut" A and for (right) the structure based on "cut" B. It can be seen that "cut" A has a non-symmetric response that propagates along the vertical boundary, while "cut" B gives clearly rise to a symmetric response. More particularly, in the "symmetric response" (right) the internal resonators rotate of the same quantity at the top and at the bottom, so that the thin beams remain undeformed. In the "asymmetric response" (left) the rotations of top and bottom element do not compensate each other. This results in the bending of the thin beams inside the unit cell. To make the plot clearer, the homogeneous Cauchy bar at the end of the specimen has been removed from the plot.

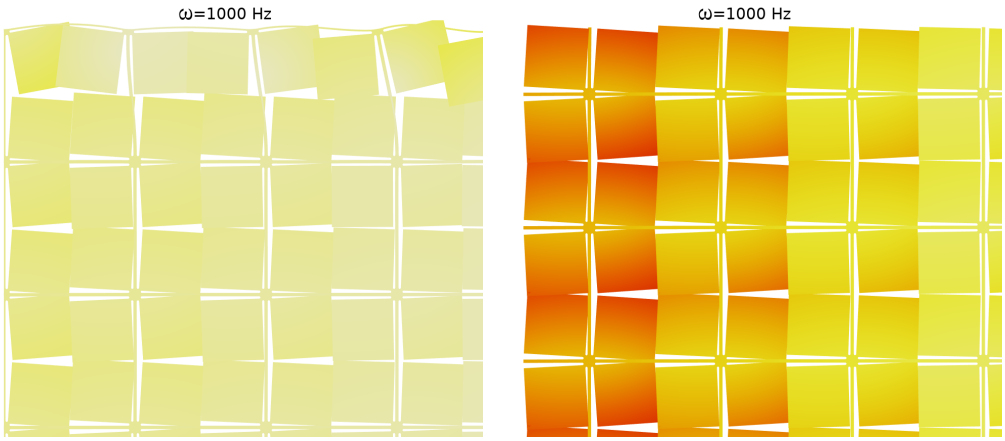

Figure 4.12: Detail of the deformation for $\omega = 1000$ Hz for (left) the structure based on "cut" A and for (right) the structure based on "cut" B. It can be seen that "cut" A has a localised non-symmetric response on the top left corner, while "cut" B gives clearly rise to a symmetric response. Also in this case the "non symmetric" response of the resonators implies bending of the thin beams inside the "cut", while the "symmetric response" leaves the thin beams undeformed. However, "cut" A recovers a symmetric response while moving away form the boundary. To make the plot clearer, the homogeneous Cauchy bar at the end of the specimen has been removed from the plot.

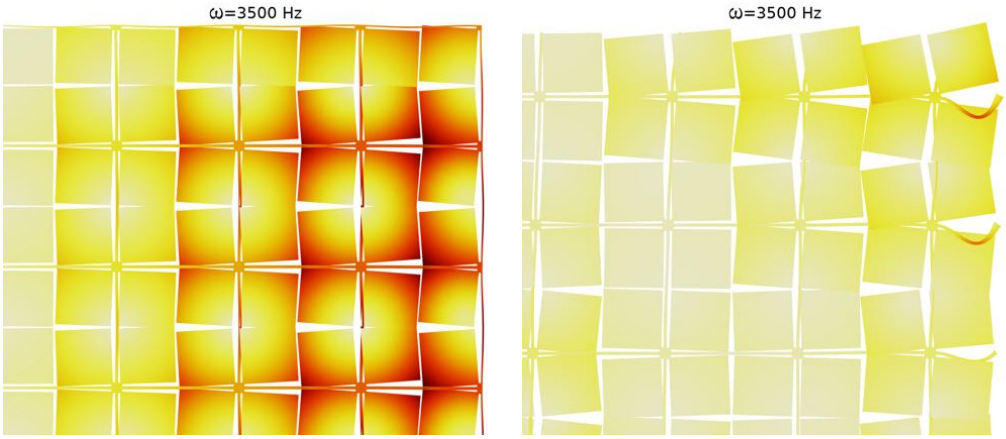

Figure 4.13: Detail of the deformation for $\omega = 3500$ Hz for (left) the structure based on "cut" A and for (right) the structure based on "cut" B. It can be seen that "cut" A has an overall symmetric response on the boundary, while "cut" B gives clearly rise to a prominent non-symmetric one. Once again the "non symmetric" response gives rise to pronounced bending of the internal thin beams, while the "symmetric response" leaves them almost undeformed. To make the plot clearer, the homogeneous Cauchy bar at the end of the specimen has been removed from the plot.

4.6.1 Effects of the size of the metastructure on the propagation of the boundary localization

In order to further investigate how these boundary effects persist while increasing the size of the domain we present here the results for an increasingly big metastructure domain for the frequencies $\omega = 500$ Hz and $\omega = 700$ Hz.

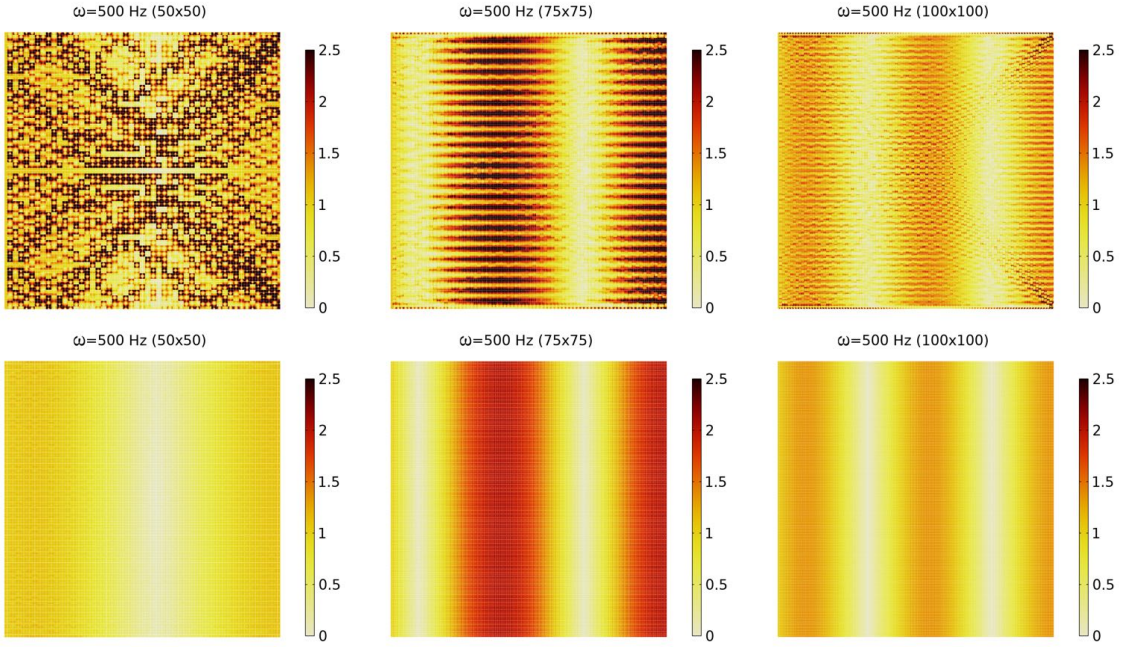

Figure 4.14: Norm of the displacement field $|u|$ divided by the amplitude of the assigned harmonic displacement $\overline{u}$ for 500 Hz for (top) the microstructured material whose building block is "cut" A, (bottom) the microstructured material whose building block is "cut" B, for a 50×50, 75×75, and 100×100 unit cells metastructure. "Cut" A shows an important boundary effect that propagates in the bulk material up to a 100×100 unit cells metastructure, while "cut" B does not show noticeable boundary effects regardless the size.

In Figs. 4.14 - 4.15, we show how the displacement field changes for a 50×50, a 75×75, and a 100×100 unit cells metastructure: in the top row we report the results for "cut" A while in the bottom row the one for "cut" B.

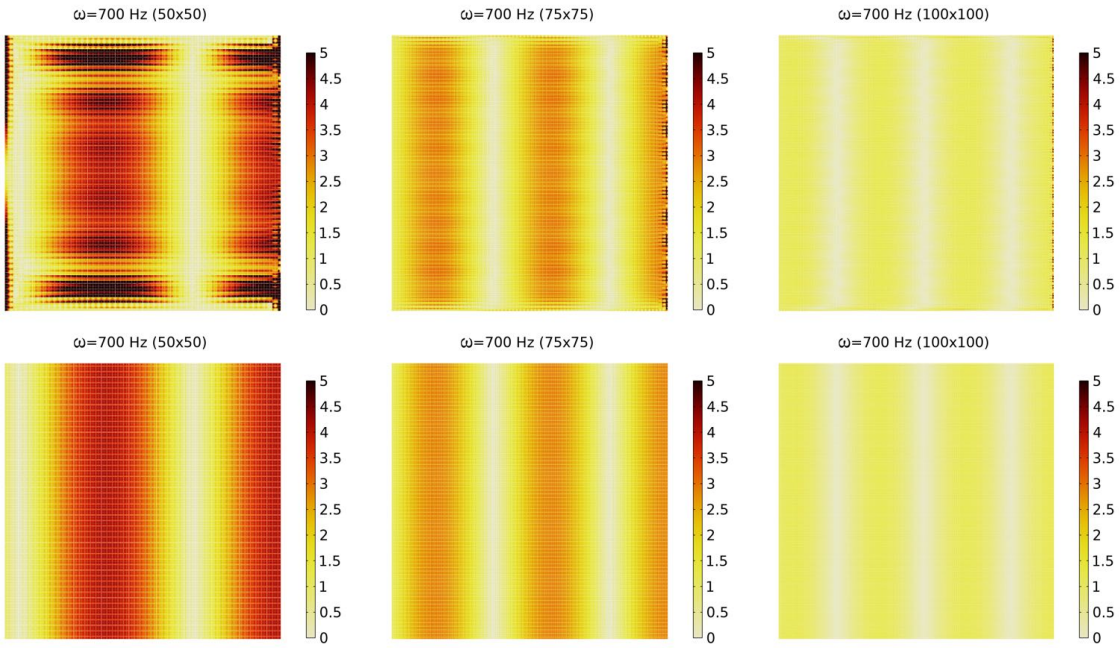

Figure 4.15: Norm of the displacement field $|u|$ divided by the amplitude of the assigned harmonic displacement $\overline{u}$ for 700 Hz for (top) the microstructured material whose building block is "cut" A, (bottom) the microstructured material whose building block is "cut" B, for a 50×50, 75×75, and 100×100 unit cells metastructures. "Cut" A shows an important boundary effect that propagates in the bulk material up to a 50×50 unit cells metastructure while it fades form 75×75. "Cut" B does not show noticeable boundary effects regardless the size.

For $\omega = 500$ Hz we can see how the boundary effects start to become negligible from a 100×100 unit cells metastructure, while before, their effect in the bulk is still relevant. On the contrary, for $\omega = 700$ Hz we can see how the boundary effects start to become negligible from a 75×75 unit cells metastructure, while in a 100×100 their effect is completely relegated to the boundaries and does not affect the bulk material.

4.7 Conclusions

The RRMM captures the behavior of both finite-size specimens accurately unless eigenfrequencies of the structure are activated, or "cut" related boundary effects appear that either stay confined on the boundary, or propagate in the bulk. That is, the RRMM captures accurately the "bulk" behavior of all the specimens. It is evident, that given the frequency and the "cut" in consideration, there are instances where the finite-size metamaterial does not have a big enough size in order for the "infinite metamaterial assumption" to hold. At that point the boundary effects would be negligible.

Since it is possible that for a given application, the size of the metamaterial has not yet reached this critical size where boundary effects can be neglected, this raises the question of how could these boundary effects be considered in a homogenised framework. Addressing this issue is absolutely critical for achieving even greater accuracy and reliability in modeling microstructured materials and will be addressed in the next chapter.

Chapter 5

Interface forces method for describing boundary effects using enriched continua: application of the method on a locally resonant metamaterial

5.1 Introduction

As we saw in the previous chapter, when modeling metamaterials in the real world, that boundary effects arise as a result of finite-size. As soon as a metamaterial is of finite-size, the "infinite metamaterial assumption" only holds approximately, if enough unit cells are used for its construction, so that boundary effects can be neglected. As discussed in previous chapter, boundary effects are directly related to the unit cell "cut" one uses to construct the finite-size metamaterial, as the geometry of the "cut" inevitably dictates the boundary of the finite-size metamaterial. On one hand, the bulk properties can be considered identical for same size finite specimens constructed from different "cuts", since all "cuts" can build the same infinite medium that corresponds to the same dispersion curves in Bloch-Floquet analysis. On the other hand, it is not rare that a boundary effect can propagate in the "bulk" of the material causing the response to deviate from that of the infinite medium (see for example Fig. 4.7 at 700 Hz for "cut" A (left panel)). It is also possible that the boundary effect remains confined on the boundary (see for example Fig. 4.8 at 1000 Hz for "cut" A (left panel)). In both cases, when using a homogenised framework, we would like to have a method of enriching our homogenised model in order to capture these boundary effects, since we would like to have a more accurate description of finite-sized problems.

When constructing an $m \times n$ metamaterial from a certain unit cell "cut", the boundary properties will be governed by the choice of "cut" while the "bulk" properties will be governed by the Bloch-Floquet dispersion curves and mode shapes of the corresponding infinitely big metamaterial. When changing the "cut", theoretically, only the boundary properties should change, while the "bulk" properties stay the same, since all "cuts" will build the same infinite metamaterial. If we imagine two $m \times n$ finite-sized metamaterials constructed from two different unit cell "cuts"(e.g. cuts A and B of previous chapter), it is always true that the boundary of the resulting metamaterial is different in each case but also that the bulk is different, in the sense that you never find the same geometry in the same place. However, as explained before, since the "bulk" properties stay the same, i.e. dispersion curves, we can approximate the bulk in each case as the same, while the boundary as different.

From this point of view, when modeling metamaterials composed of different "cuts" using a homogenised framework, it would make sense to think of the boundary of the homogenised metamaterial as a surface where boundary effects are activated. Equivalently, if the microstrucutred metamaterial is then connected to another material, then the boundary between the two, when the metamaterial is modeled as an enriched continuum, can be thought of as an interface where the boundary effect is activated. For many interfaces there are already existing models in the literature we discuss in the next section.

5.2 Material interfaces: from microscopic towards macroscopic interfaces

In the context of mechanical problems, various interface models can be categorized depending on the quantities that may suffer a jump across the interface itself:

- **Perfect interface model**: continuity of both displacement and traction is prescribed across the interface [15, 17, 39, 75].
- **Cohesive interface model**: continuity of traction is respected on the interface but the displacement can suffer a jump [7, 28, 39, 98].
- **Elastic interface model**: continuity of displacement is respected on the interface but the traction can suffer a jump [32, 39, 59, 62].
- **General interface model**: a jump of both displacement and traction is prescribed on the interface [39].

Up to this day, interface models have been used in the modeling of a number of phenomena such as adhesives and their fracture [41, 93, 104], crack growth [50, 53, 85], damage [1, 3, 42], surface effects between matrix and inclusion in nano-materials and composites [39, 86], grain boundary microcracking [29, 71, 90]. We point out that interface methods have been used to model size effects in nanomaterials in the context of periodic homogenisation [39] or in composites with fibers [33], but only to model the interphase between the matrix and the inclusion in the RVE of the composite an thus, as stated before, only at the microscopic level. This means that, usually, the discontinuity of the material properties is considered at the scale of the unit cell (e.g. the microscopic interface that separates two different materials inside the unit cell). These macroscopic material interfaces are then taken into account in the homogenisation procedure to show that the obtained homogenised (infinite-size) continuum exhibits different macroscopic bulk properties if one considers different interface properties at the microscopic level.

The viewpoint adopted here is quite different, since we are stating that, when considering finite-size (macroscopic) metamaterials' specimens, also the macroscopic specimen's boundaries should be treated as material interfaces carrying their own material properties [74]. In particular, the macroscopic interfaces considered in this thesis will be treated as (macroscopic) elastic interfaces across which the displacement field remains continuous, while the traction may suffer a jump. Indeed this choice is justified by the type of metamaterials that we want to describe through our homogenised model. If we imagine a single-phase microstructured metamaterial conneted to a homogeneous material it is true that the interface between the two materials might have empty spaces (due to the microstructured nature of the metamaterial), and we know that a cohesive interface is usually used for the modeling of interfaces with cracks and damage [1, 3, 42, 50, 53, 85] (where holes are present in our material). However in our case, the two materials are strongly bonded and no crack propagation is intended. Therefore, when the metamaterial is modeled using a homogenised model, the macroscopic displacement must be continuous at the interface, while the traction is allowed to suffer a jump.

The macroscopic interfaces occurring in the problem we studied in last chapter are highlighted in Fig. 4.6 with a red (RRM/Cauchy interface) or a black (free RRM interface) color. When considering the red interface connecting the RRM continuum to the Cauchy plate, we want that this interface models the transition from the metamaterial in Fig. 4.5 to the Cauchy continuum (interface $A2 = B1$ and $B2 = C1$). On the one hand, given the type of connections shown in Fig. 4.5, under the hypothesis that there are no defects in the solid-solid connections between the metamaterial and the Cauchy plate, it is natural to consider that at the macroscopic (homogenised) level one should impose continuity of the macroscopic displacement across the red line in Fig. 4.6. On the other hand, it is also evident that if one would also impose the continuity of traction across the red line in Fig. 4.6, then the RRMM would not be able to discriminate between the 2 different cases presented in Fig. 4.5, since the homogenised solution imposing $[[u]] = 0$ and $[[t]] = 0$ is unique.

It becomes thus clear that, in order to discriminate between the 2 different cases in Fig. 4.5, the homogenised counterpart must account for the possibility of a jump of the traction along the red lines. Across these lines, the equations expressing perfect contact in (4.3), should then be modified to

$$[[u]] = 0 \qquad \text{and} \qquad [[t]] = f^{\text{int}} \tag{5.1}$$

where f^{int} is an interface force that takes different expressions depending on the type of metamaterial/Cauchy connection which is considered in the "real" system (e.g. one of the different metamaterial/Cauchy connections given in Fig. 4.5). The black interface in Fig. 4.6 is a particular limiting case of the red interface just described. The black line represents a free RRM interface, corresponding to a free interface in Fig. 4.5 (i.e. $B3$ and $B4$), in the sense that a RRM continuum is present on one side of the interface, while no other material is present on the other side. In this particular case no condition must be imposed on the macroscopic displacement of the RRM continuum which can of course be arbitrary. On the other hand, the generalized traction that can arise at this black interface might not be vanishing, so that the fourth condition in (4.3) should be modified to

$$\mathrm{t} := (\widetilde{\sigma} + \widehat{\sigma})\, n = f^{\text{int}} \tag{5.2}$$

where f^{int} is a macroscopic interface force that might take different (in general non-vanishing) values depending on the structure of the "real" metamaterial close to that interface (which depends on which "cut" we use to construct the metamaterial from the two shown in Fig. 4.5). It becomes apparent that when considering a homogenised (macrosopic) model as the RRMM for the description of the heterogeneous materials which have different properties close to the free microscopic interface, then the associated homogenised (macroscopic) interface does not have, in general, a vanishing generalized traction. This is due to the fact that small layers of the metamaterial across the free interface can create some stress concentrations which are entirely related to the specific properties of the underlying microstructure close to the free interface (boundary effects). Such stress concentrations, (typically of the order of 1/2 to 1 unit cell when considering a free interface) are concentrated close to the free interface and might be very different depending on the unit cell "cut". These different responses must be accounted for at the homogenised level through the interface force $f^{\text{interface}}$.

5.3 Interface forces for modeling a locally resonant acoustic metamaterial using the RRMM

In the context of modeling metamaterials as homogenised media, the concept of considering macroscopic interface forces is practically disregarded in the literature. This concept of macroscopic interface force has been introduced in [74] for the first time. However, given the novelty of the concept many challenges remain open and must be addressed with targeted case studies so as to unveil the specific properties that such interface forces should have and to draw some general conclusions.

We wish to study the properties of interface forces in the context of RRM elasticity for the case study presented in Chapter 4. As we have stated in the end of previous chapter, introducing a method to capture boundary effects (in this case the method of interface forces) is an absolute priority if one wants to extend the use of homogenised models from a purely infinite-size framework to the study of realistic finite-sized structures.

Regarding boundary effects seen in the dynamic response of metamaterials, we know that they depend on the frequency under consideration, the geometry of the unit cell "cut" and on the loading conditions in the test under consideration. Indeed, what we (in mechanical metamaterials) call boundary effects, has already been observed in a similar sense in electronic crystals. In electronic crystals, (similar to our case) an electronic band structure is calculated using the Bloch-Floquet theorem, which then describes the electron states in the crystal. This energy band structure plays a major role in determining the physical properties of the crystal and which physical processes may happen in the crystal [76]. Here the "infinite metamaterial" assumption translates to an "infinite crystal" assumption. However, real world crystals, like real world metamaterials, are always finite-sized. It was then proven that new electronic states can be formed near the surfaces of the finite-sized crystal, thus named surface states [88, 94]. The authors of [76] have succesfully used the theory of periodic Sturm-Liouville equations to calculate finite band structures of 1D crystals. Usually, this band structure is calculated using a boundary value problem (a partial differential equation coupled with boundary conditions that express the finite size). However, the results in [76] only concern one-dimensional electronic, phononic and photonic crystals. Regarding the calculation of a finite-size band structure in two dimensions, to the knowledge of the author, no work exists in which a finite-size band structure is calculated, given an arbitrary unit cell "cut" and a number of unit cells in each of the two spatial directions.

An alternative path is usually taken, where metamaterials are specifically designed so that they show topological edge states. After the 2016 Physics Nobel prize in topological phases of matter, a whole

new field emerged called topological insulators [60], from which topological metamaterials eventually emerged (see [67] for mechanical metamaterials). Usually, through certain procedures that involve a bulk Hamiltonian and some calculations of topological invariants, it is possible to show that topological edge states might exist in a system [14], and sometimes even for which boundary terminations [8]. It is not still clear however, if this procedure can be done for all the possible "cuts" and all the possible unit cell shapes and more than that, it is well known that not all boundary/edge effects are topological. There exists yet, no general expression describing an arbitrary surface state/boundary effect for an arbitrary frequency, unit cell "cut" and loading.

The core idea of interface forces, that any boundary effect can be seen as an activated force per unit area on the respective boundary, offers an interesting separation of information, where the information are separated in bulk (band structure coming from Bloch-Floquet analysis) and boundary information (applied interface forces). If such an idea is posed, then one should show at some point, that these forces, for any "cut" and any loading, depend on some physical quantities. Such task, i.e. coming up with a general analytic relation for an arbitrary "cut" and excitation involving physical quantities, given the previously mentioned literature, is highly challenging, and given the plethora of loading conditions and unit cell "cuts", might even be impossible to achieve . However, one can imagine that such task could be achievable for specific metamaterials and specific excitations. In this thesis, we will discuss later in this Chapter, the idea that an edge effect might be associated to a low shear stiffness of the unit cell "cut", thus trying to associate a physical quantity to the edge effect and we will show how the same edge effect might remain invariant to some specific parameters related to the number of unit cells used, thus trying to exclude some physical quantities from the picture.

In this section, we will describe in more detail the specific form that such interface forces should take so that the RRMM can be safely used to describe the two different metamaterial's specimens of Fig. 4.5.

For the tests presented in last Chapter 4, introduced in Fig. 4.5 (Fig. 4.6 for its RRM counterpart), we consider the following traction jump conditions across the red lines in Fig. 4.6 separating the RRM continuum from the Cauchy plates

$$t_{\text{Cauchy}_{i_n}} = \alpha_{i_n}\, t_{\text{RRMM}_{i_n}} + \beta_{i_n} \tag{5.3}$$

where $i = L, R$ for left or right interface respectively and $n = x, y$ for x or y component of the tractions respectively, α_{i_n} is a dimensionless coefficient and β_{i_n} is a surface force.

Jump condition (5.3) can be rewritten setting $\gamma = (\alpha - 1)$, so that

$$t_{\text{Cauchy}_{i_n}} = t_{RRMM_{i_n}} + \gamma_{i_n}\, t_{\text{RRMM}_{i_n}} + \beta_{i_n} \tag{5.4}$$

or

$$[[t]] = \gamma_{i_n}\, t_{\text{RRMM}_{i_n}} + \beta_{i_n}. \tag{5.5}$$

With reference to eq. (5.1) this means that we are setting the interface force to be

$$f_{i_n}^{\text{interface}} = (\alpha_{i_n} - 1) t_{\text{RRMM}_{i_n}} + \beta_{i_n}. \tag{5.6}$$

In other words, we are setting that the interface force which is stemming from the heterogeneity of the underlying microstructure close to the Cauchy/RRM interface is a linear function of the RRM traction $t_{\text{RRMM}} = (\widetilde{\sigma} + \widehat{\sigma})\, n$. We thus note, that here the jump of the traction at the interface takes the simple form of a linear function of the RRM traction.

However, depending on the frequency under consideration and the nature of the boundary effect, the expression can be modified and the jump of traction could take more complex forms, e.g. α and β must be functions of the x or y coordinates along the interface, instead of being constants.

For the black interfaces in Fig. 4.6 we assume no special general form, so that eq. (5.2) remains the same. We remark however, that this expression, for an arbitrary frequency, could also become dependent on the x or y coordinates.

5.4 Results and discussion

We will here present results that show that interface forces can be effective in capturing boundary effects that either remain confined on the boundary (we will here call those "pure boundary effects" or "edge effects"), propagate in the bulk, or are more general boundary effects related to the finite-size of the structure.

5.4.1 Interface forces in the case of edge effects: the frequency of 1000 Hz

We start with the case of 1000 Hz, where an edge effect was evident on the top free boundary of the microstructured metamaterial in Fig. 4.8 for the case of the finite-size metamaterial made out of "cut" A (we will name this metamaterial A for simplicity). We wish to capture that edge effect using the method of interface forces. For the corresponding case of the finite-size metamaterial made out of "cut" B (we will also name this metamaterial B for simplicity), the RRMM was accurate enough, but interface forces can improve the response even more, accounting for the boundary effects which caused the response to be less accurate initially. Such effects are not clearly visible like the case of edge effects, but are still related to the finite-size of the structure, and hence to the choice of unit cell "cut".

Metamaterial A

In Figure 5.1[1] we can see the structural response of the RRMM with ($f \neq 0$), and without interface forces ($f = 0$), in comparison to metamaterial A, and a detail of the deformed shaped of the top right corner of the specimen can be seen in Fig. 5.2.

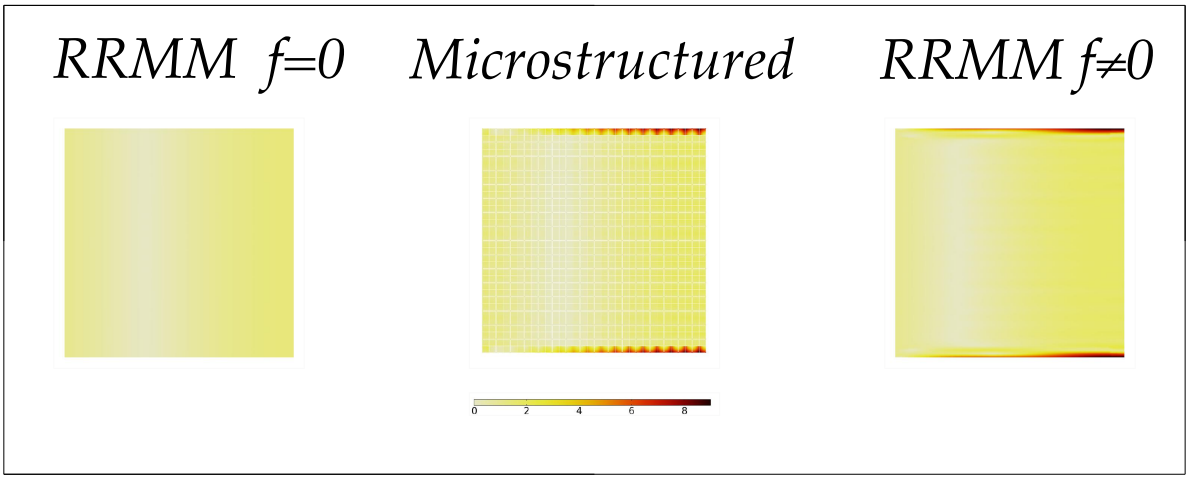

Figure 5.1: Norm of the displacement field $|u|$ divided by the amplitude of the assigned harmonic displacement $\overline{u}$ at 1000 Hz for (left) the RRMM without interface forces ($f = 0$), (center) metamaterial A and (right) the RRMM with ($f \neq 0$).

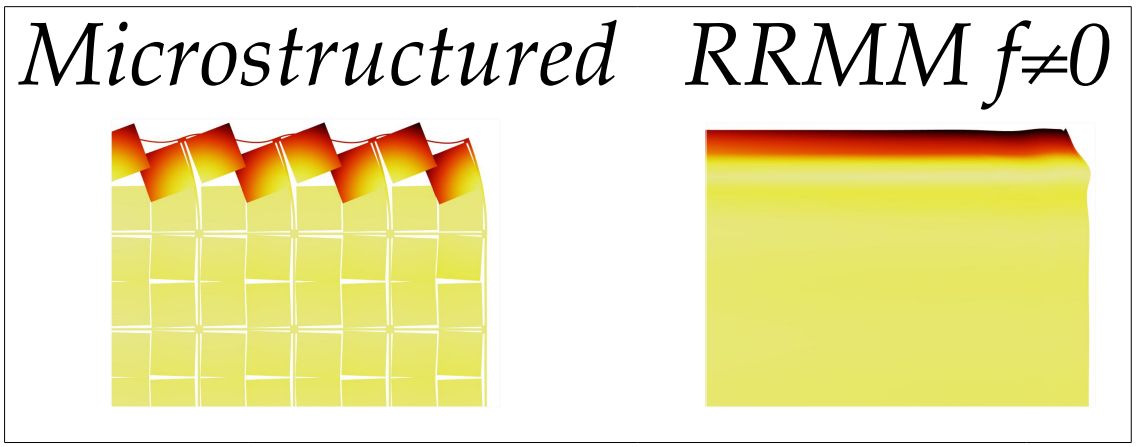

Figure 5.2: Detail of the deformed shape of the top right corner of the specimen at 1000 Hz, for (left) the microstructured specimen and (right) the RRMM with ($f \neq 0$).

[1]The scale of the dimensionless displacement field used here is different than the one in Fig. 4.8. In Fig. 4.8, we wanted to highlight the difference of the displacement on the edge and hence we used a lower scale, whereas in the current case we want the natural scale in order to calibrate the interface force accurately.

For the case of the RRMM with $f \neq 0$, interface forces were used on the top and bottom boundaries (black boundaries $B3$ and $B4$ in Fig. 4.6) and on the right RRMM/Cauchy interface (red boundary $B2 = C1$ in 4.6). Since the problem is symmetric, the force used on boundary $B3$ will have the same $x-$component as the one used on $B4$ and the same y-component but with opposite sign. We will therefore only state the expression of the interface force on the top boundary $B3$, if one is used, for all cases shown below. For the right interface, an interface force was only used on the Cauchy/RRM interface in the $x-$direction, which particularises the general expression of eq. (5.6) to

$$f_{R_x}^{interface} = (\alpha_{R_x} - 1) t_{RRMM_{R_x}} + \beta_{R_x} \tag{5.7}$$

where $\alpha_{R_x} = 1$ and $\beta_{R_x} = -2 \cdot 10^7$. Regarding the surface force used on the top free boundary (black boundary $B3$ in Fig. 4.6), whose general expression is given by eq. (5.2), particularising for this specific case, the interface force had to be a coordinate dependent function of the type

$$f^{\text{int}} = 2.47 \cdot 10^7 \cdot e^{-\frac{x^2}{0.0128}}. \tag{5.8}$$

A question naturally arising is how does one arrive to the appropriate interface force that produces the correct response (i.e. represents accurately the boundary effect)? The RRMM, being an enriched continuum used in a homogenised framework, captures the response of the metamaterial in an averaging sense, meaning that not every little detail of the displacement of the microstructural components can be captured, but rather, the overall macroscopic displacement field in an average sense. Given this, the appropriate interface force should do exactly that. This implies that we can change the interface force appropriately by direct inspection of the displacement field and deformed shape, until the response is accurate enough.

Moreover, if one has arrived to the correct solution using an enriched continuum coupled with the method of interface forces, the traction on the "homogenised" interfaces should also be an average of the microstructured traction on the same interface, since it is a function of the displacement. This can be used in the opposite way in some cases, meaning, that if one inspects the microstructured traction at a given boundary, and calculates an "average" of this traction, then this should correspond to the traction that we should have calculated when we already arrived at the accurate response when inspecting the dislplacement field. This implies that one could arrive at the correct interface force by trial and error, so that the traction on the interface in the case of modeling the metamaterial using an enriched continuum, becomes an average of the microstructured traction. If this average was achieved for all interfaces in the homogenised problem, then the displacement field should be the same as the one we arrived at before, only by direct inspection of the displacement field. However, since the calculation of this average is an open problem in the enriched continua community, and since we might be also dealing with too small specimens, calculating an average of the traction can become challenging, so calculating the appropriate interface force via direct inspection of the displacement field is usually more versatile here.

Nevertheless, we point out that which of the two strategies should be used, to arrive to the correct interface force more efficiently depends on the specific case. When talking about the fact that an average of the tractions in the RRMM case, should lead to the correct solution, we can think of it as an interpolation of the microstructured traction. An example is the the traction on the top free boundary of the specimen for the case under consideration. We know that on the top boundary (in the microstructured case), since we have no assigned displacement, the traction must be zero. We can therefore only calculate the traction really close to this boundary, by moving inside the material by a very small distance. Thus we move one quarter of a unit cell down from the top free boundary, and calculate the $x-$component of the traction on a horizontal line, for both metamaterial A and the corresponding RRMM with $f \neq 0$. The results are shown in Fig. 5.3.

The average sense in which the RRMM should capture the traction is here very evident.

Metamaterial B

In the case of metamaterial B, as mentioned before, the response of the RRMM was already accurate, but we can make it even more precise by capturing boundary effects using interface forces. In Figure 5.4 we can see the structural response of the RRMM with $f \neq 0$ and without interface forces ($f = 0$), in comparison to metamaterial B. In the case of $f \neq 0$, an interface force was only needed on the right Cauchy/RRMM interface, which particularises the general expression of eq. (5.6), to

$$f_{R_x}^{\text{int}} = (\alpha_{R_x} - 1) t_{\text{RRMM}_{R_x}} + \beta_{R_x} \tag{5.9}$$

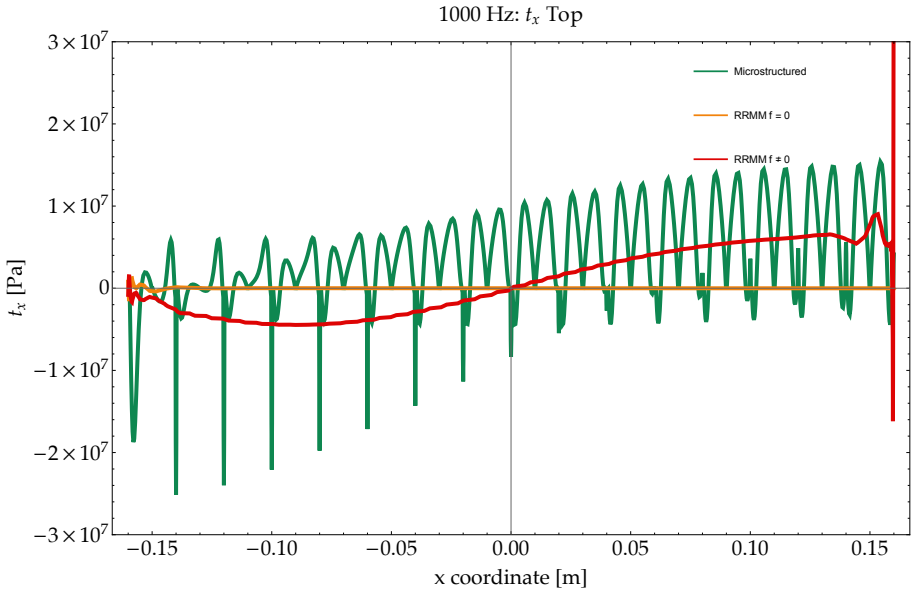

Figure 5.3: x-component of the traction, for the microstructured specimen (green line), the RRMM without interface forces ($f = 0$) (orange line) and the RRMM with interface forces ($f \neq 0$) (red line).

where $\alpha_{R_x} = 1$ and $\beta_{R_x} = -2 \cdot 10^7$.

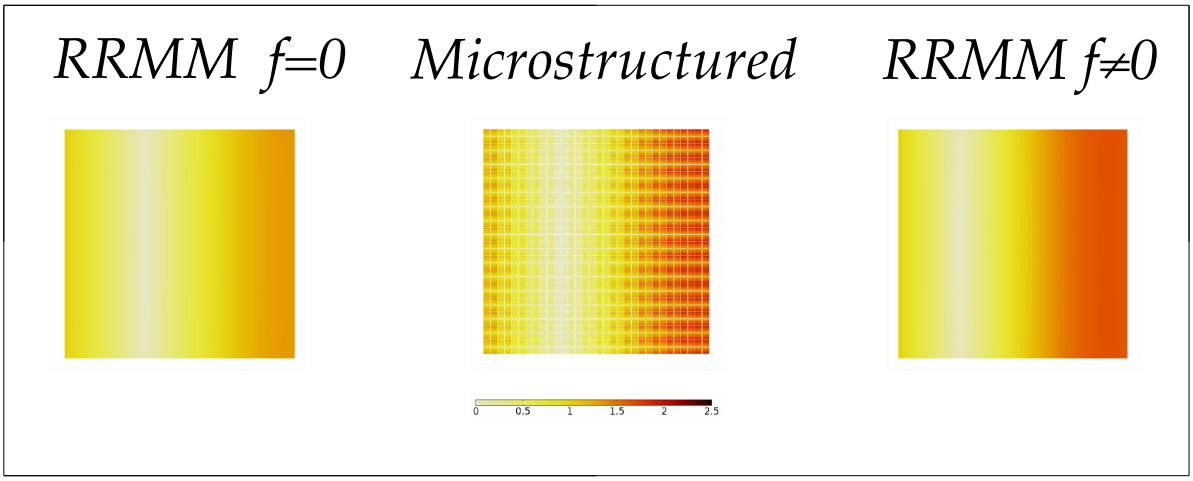

Figure 5.4: Norm of the displacement field $|u|$ divided by the amplitude of the assigned harmonic displacement $\overline{u}$ at 1000 Hz for (left) the RRMM without interface forces ($f = 0$), (center) metamaterial B and (right) the RRMM with $f \neq 0$.

5.4.2 Interface forces in the case of edge effects: the frequency of 1500 Hz

At 1500 Hz, another edge effect was evident on the top free boundary of metamaterial A in Fig. 4.8. We aim to capture that edge effect again, using the method of interface forces. For the corresponding case of metamaterial B, the RRMM was not accurate enough in capturing the response, therefore interface forces are once again used to capture an accurate enough finite-sized response.

Metamaterial A

In Figure 5.5 we can see the structural response of the RRMM with ($f \neq 0$) and without interface forces ($f = 0$), in comparison to metamaterial A. To capture the response of metamaterial A, for the case of the RRMM with $f \neq 0$, an interface force was used on the Cauchy/RRM right interface (red boundary $B2 = C1$ in 4.6) in the $x-$direction, so that the usual expression of eq. (5.6) is modified such that $\alpha_{R_x} = 1$

and β_{R_x} becomes piece-wise constant $y-$coordinate dependent

$$\beta_{R_x} = \begin{cases} -4 \cdot 10^8 & \text{if} \quad y \in \left[0.15 \text{ [m]}, 0.16 \text{ [m]}\right]^2, \\ 3 \cdot 10^8 & \text{if} \quad y \in \left[-0.16 \text{ [m]}, 0.15 \text{ [m]}\right]. \end{cases} \tag{5.10}$$

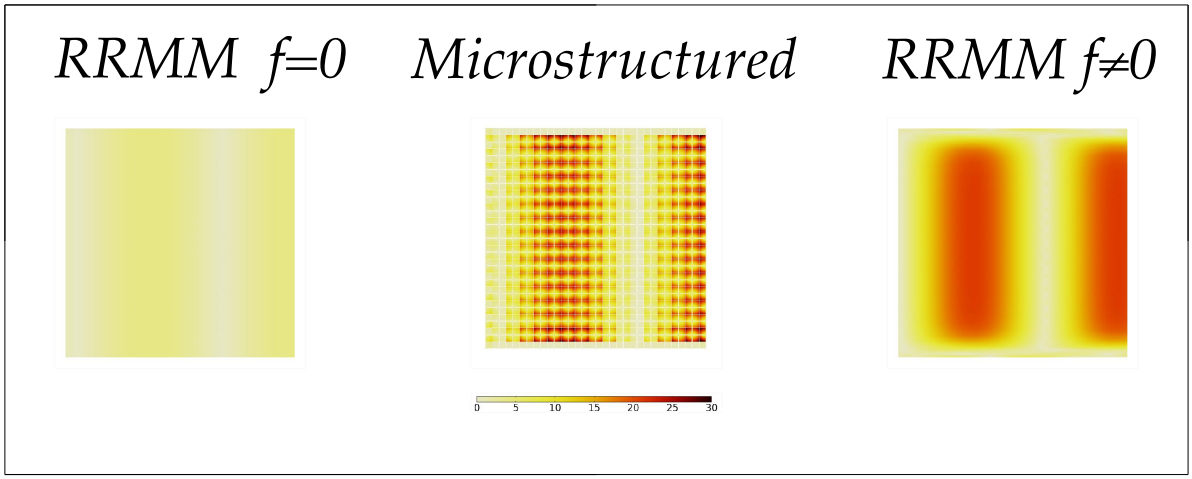

Figure 5.5: Norm of the displacement field $|u|$ divided by the amplitude of the assigned harmonic displacement $\overline{u}$ at 1500 Hz for (left) the RRMM without interface forces ($f = 0$), (center) metamaterial A and (right) the RRMM with $f \neq 0$.

Metamaterial B

In Figure 5.6 we can see the structural response of the RRMM with $f \neq 0$ and without interface forces ($f = 0$), in comparison to metamaterial B. To capture the response of metamaterial B, for the case of the RRMM with $f \neq 0$, an interface force was used on the Cauchy/RRM right interface (red boundary $B2 = C1$ in Fig. 4.6) in the $x-$direction, so that for eq. (5.6), we have $\alpha_{R_x} = 1$ and $\beta_{R_x} = 3 \cdot 10^8$.

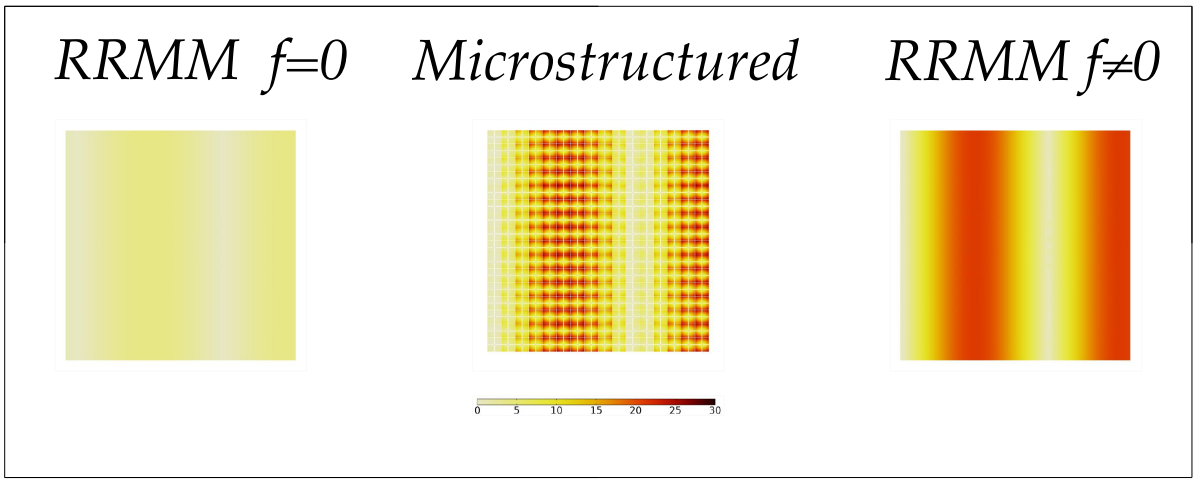

Figure 5.6: Norm of the displacement field $|u|$ divided by the amplitude of the assigned harmonic displacement $\overline{u}$ at 1500 Hz for (left) the RRMM without interface forces ($f = 0$), (center) metamaterial B and (right) the RRMM with $f \neq 0$.

[2] We assume that the center of the metastructure is at the coordinates $(0, 0)$, therefore the right interface's y-coordinates can be $y \in [-0.16, +0.16]$.

5.4.3 Interface forces in the case of boundary effects that propagate in the bulk: the frequency of 700 Hz

At 700 Hz and metamaterial A, in Fig. 4.7 we can see a boundary effect propagating in the bulk of the material which the RRMM is unable to catch. In the same figure, for metamaterial B the RRMM captures the response in a good extent, but we can still enhance the accuracy by the use of interface forces. The use of interface forces enhances the accuracy since it adds missing information to the picture regarding finite-size effects.

Metamaterial A

In Figure 5.7 we can see the structural response of the RRMM with $f \neq 0$ and without interface forces ($f = 0$), in comparison to metamaterial A. For the case of the RRMM with $f \neq 0$, an interface force was used on the Cauchy/RRM right interface (red boundary $B2 = C1$ in 4.6) in the $x-$direction so that the usual expression of eq. (5.6) is modified so that both α_{R_x} and β_{R_x} become dependent on the $y-$coordinate. We have

$$f^{\text{int}}_{R_x} = (\alpha_{R_x} - 1) t_{\text{RRMM}_{R_x}} + \beta_{R_x} \tag{5.11}$$

where this time

$$\alpha_{R_x} = \begin{cases} 0.01 & \text{if} \quad y \in \left[0.11\ [\text{m}], 0.16\ [\text{m}]\right], \\ 1 & \text{if} \quad y \in \left[-0.16\ [\text{m}], 0.11\ [\text{m}]\right] \end{cases} \tag{5.12}$$

and β_{R_x} takes the form

$$\beta_{R_x} = 4 \cdot 10^7 \cdot e^{-\frac{y^2}{0.005}}. \tag{5.13}$$

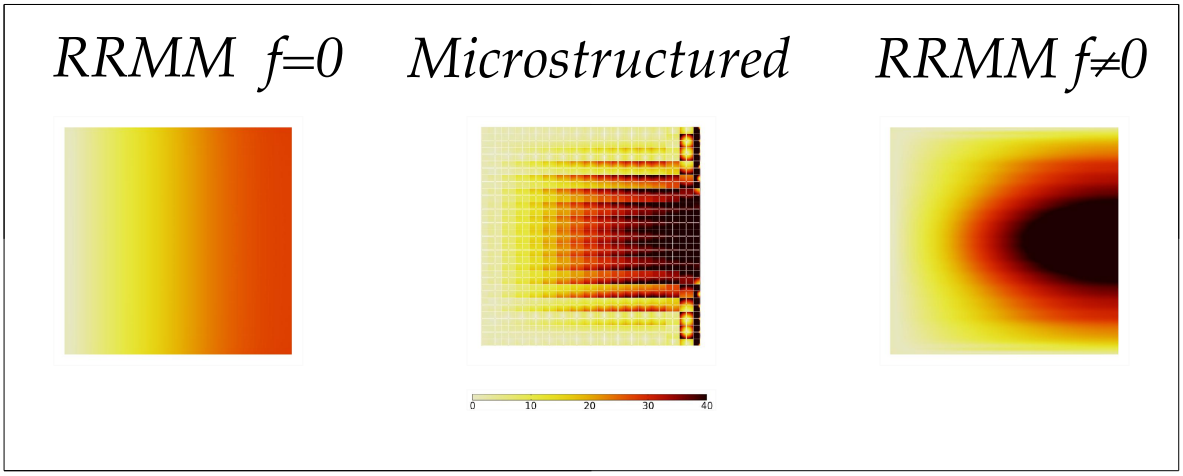

Figure 5.7: Norm of the displacement field $|u|$ divided by the amplitude of the assigned harmonic displacement $\overline{u}$ at 700 Hz for (left) the RRMM without interface forces ($f = 0$), (center) metamaterial A and (right) the RRMM with $f \neq 0$.

Metamaterial B

In Figure 5.8 we can see the structural response of the RRMM with $f \neq 0$ and without interface forces ($f = 0$), in comparison to metamaterial B. For the case of the RRMM with $f \neq 0$, an interface force was used on the Cauchy/RRM right interface (red boundary $B2 = C1$ in Fig. 4.6) in the $x-$direction so that for the usual expression of eq. (5.6) we have that $\alpha_{R_x} = 1$ and $\beta_{R_x} = 1.1 \cdot 10^8$.

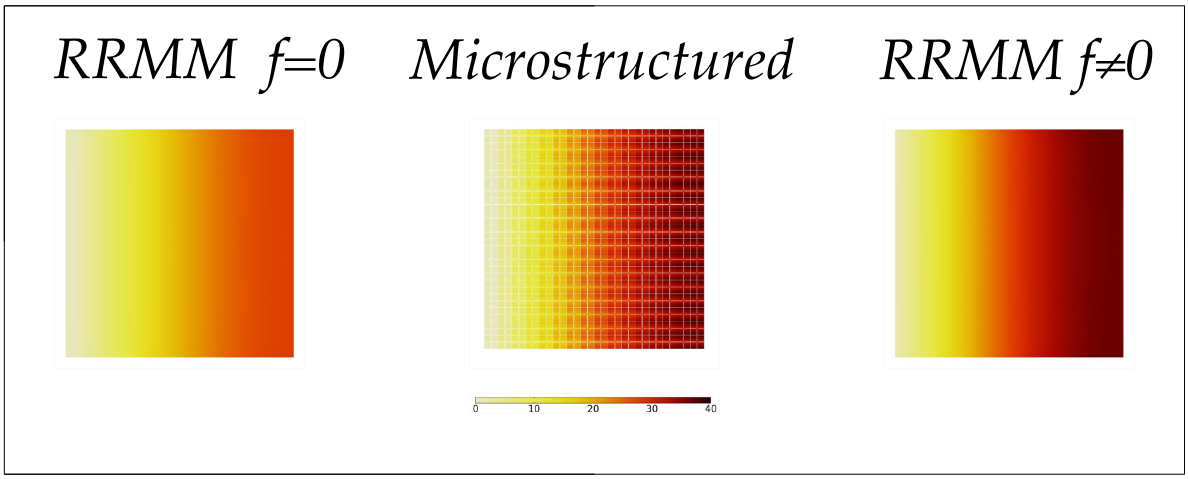

Figure 5.8: Norm of the displacement field $|u|$ divided by the amplitude of the assigned harmonic displacement $\overline{u}$ at 700 Hz for (left) the RRMM without interface forces ($f = 0$), (center) metamaterial B and (right) the RRMM with $f \neq 0$.

5.5 Edge effects: edge tests, dependence on the number of unit cells in the $y-$direction and scalability of interface forces

Out of the three different boundary effects we identified in this chapter, the one that appears the most is the edge effect where the top and bottom edges of the metamaterial deform more than the bulk. This effect appeared, specifically for metamaterial A, in many different frequencies, namely: 300 Hz, 1000 Hz, 1800 Hz and 2300 Hz (see Figures 4.7–4.9). Although, in these cases, the boundary effect is not always identical, we can always observe that it is of half a unit cell size and it takes place at the top and bottom edges of the specimen. We remark, that we are always doing a pressure test (i.e. we are sending a compressional wave), but the edges of the specimen in the case of metamaterial A appear to be responding to a shear-type test (see Fig.5.2).

Looking at the geometry of "cut" A in Fig. 4.2, and paying particular attention to its mass distribution, one can understand that this "cut" possesses very low shear stiffness. It is reasonable to hypothesize that this property of the unit cell "cut" may be correlated with the edge effect observed in our simulations. Based on this hypothesis, could we maybe predict the edge effect by only performing a shear-type test on the edge of the specimen, where we apply suitable boundary conditions on the bottom boundary (we will call this an edge test)? Should this be achievable, significant implications emerge:

- We would have effectively associated some properties of the microstructure with the edge effect itself.
- To predict the existence of an edge effect we would only need an edge test and not a microstrcutured simulation of the whole finite-sized specimen.
- For capturing edge effects using the RRMM and interface forces, it would suffice to perform only the edge test. This test could then be used to retrieve the expression of the interface force that is activated from this particular boundary effect within the RRM simulation.

5.5.1 Edge tests

In order to achieve what has been previously described, we choose our edge test to be the same physical test we have seen throughout this and the previous chapter but, in order to represent the edge, we use a 16×1 specimen, again embedded between two Cauchy plates of matching height. We then proceed to search for these boundary conditions that must be applied at the bottom edge in order to reproduce the edge effect. More specifically, with reference to the schematic view in Fig. 5.9, we apply

$u_x = \overline{u}$ and $u_y = 0$ prescribed displacement - green

$u^- = u^+$ and $(\sigma n)^- = (\sigma n)^+$ perfect contact (continuity of displacement and traction) - red

$$\begin{aligned} &\sigma n = 0 && \text{stress free - black} \\ &u_x = u_{BC_x} \quad \text{and} \quad u_y = u_{BC_y} && \text{edge test boundary conditions - blue} \end{aligned} \tag{5.14}$$

where similarly to the previous chapter $\overline{u} = u_0\, e^{-i\omega t}$ with $u_0 = 3.2$ mm and now u_{BC_x} and u_{BC_y} correspond to either free or fixed ($u = 0$) boundary conditions.

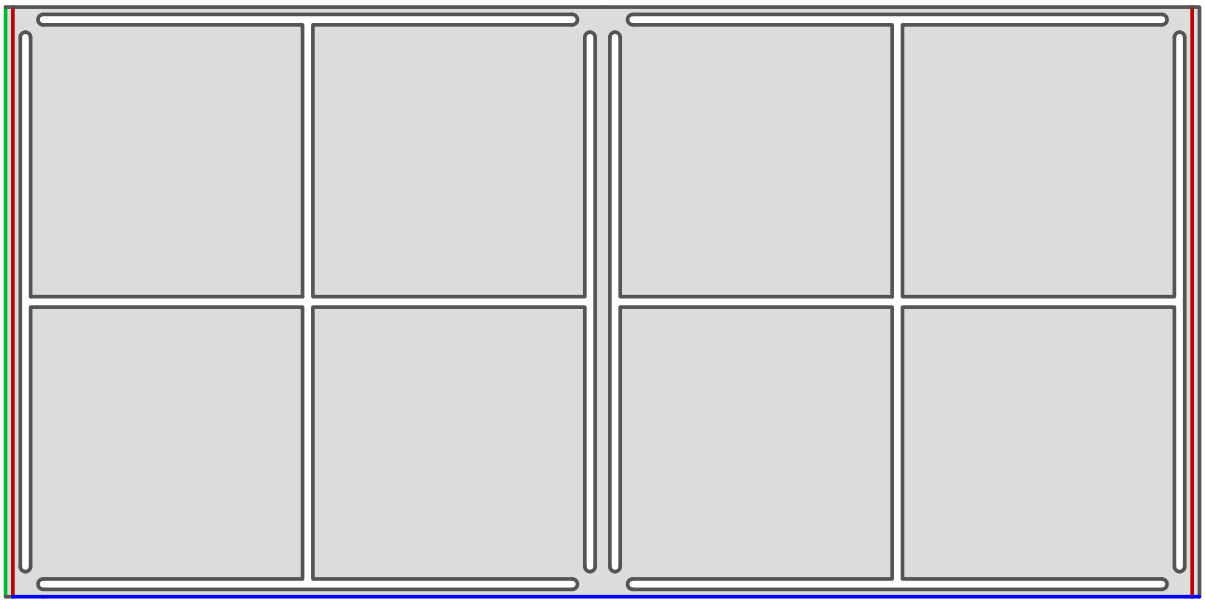

Figure 5.9: Schematic view of the geometry of the edge test. A 2×1 metamaterial is presented for easier identification of the boundary conditions while the edge test was performed using a 16×1 specimen.

Edge test with $u_{BC_x} = 0$ and u_{BC_y} free

Our first guess is that since we observe a shearing effect on the edge, setting $u_{BC_x} = 0$ and letting u_{BC_y} to be free, seems appropriate. We compare the results of the edge test with the upper half of the 16×16 specimen for the frequency of 1000 Hz in Figure 4.8. Since our test in Chapter 4 is symmetric, our results will also hold for the bottom edge of the metastructure.

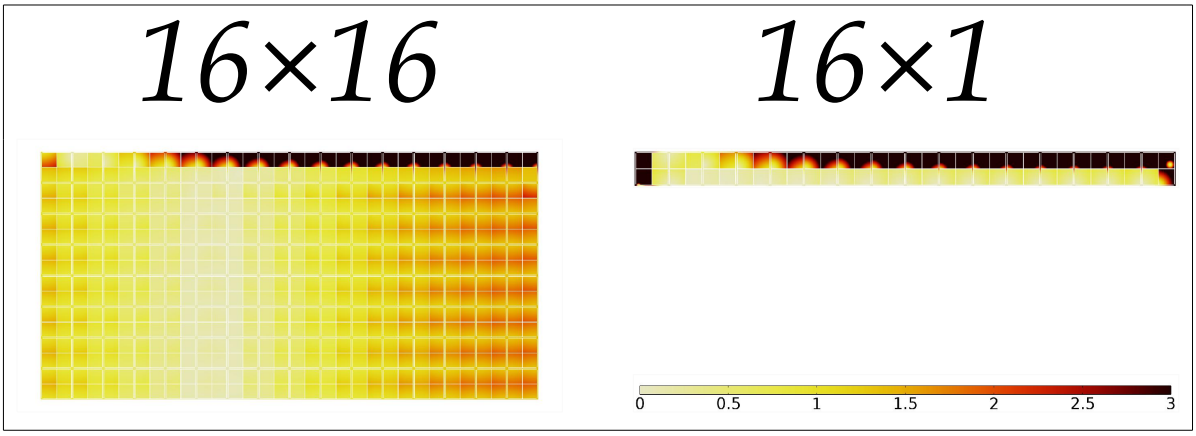

Figure 5.10: Dimensionless displacement field at 1000 Hz for (left) the 16×16 metamaterial A (only top half is shown due to the symmetry of the problem) and (right) the corresponding edge test with $u_{BC_x} = 0$ and u_{BC_y} free.

The comparison can be seen in Fig. 5.10, where we can see that the edge effect appears in the edge test, but we have areas where the displacement is overestimated (left- and right-hand side of the specimen) and areas where it is underestimated (bottom half row of unit cells). Due to this agreement issues we cannot use this edge test for retrieving the expression of the appropriate interface force, but we could perhaps use it for identification of a possible edge effect given a choice of "cut". To check this, we try

the same exact edge test using cut B and see if the response is comparable to the one of the edge of the corresponding 16×16 specimen. The results are shown in Fig. 5.11, where we observe that the response

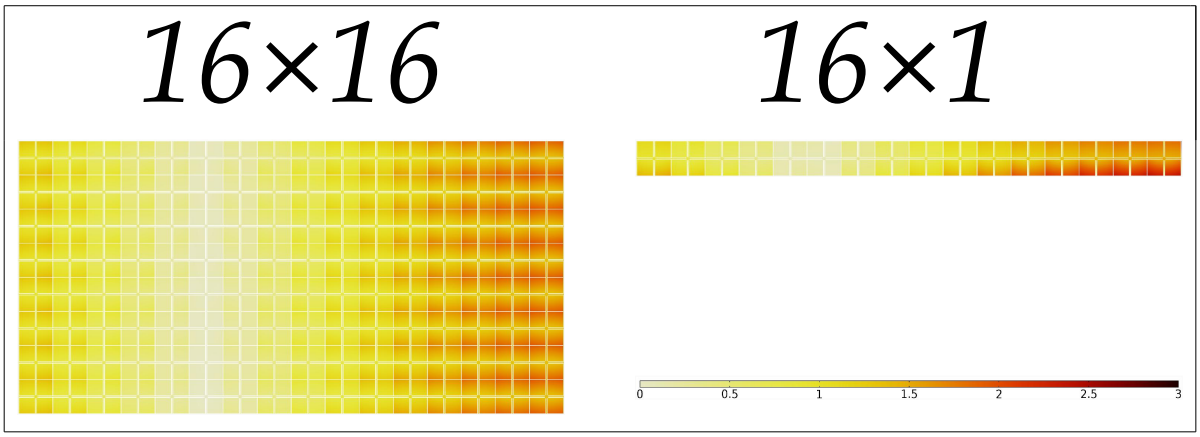

Figure 5.11: Dimensionless displacement field at 1000 Hz for (left) the 16×16 metamaterial B (only top half is shown due to the symmetry of the problem) and (right) the corresponding edge test with $u_{BC_x} = 0$ and u_{BC_y} free.

between edge test and edge of the corresponding 16×16 specimen is comparable, in the sense that there is no edge effect in both cases. The specific edge test looks promising for use in the identification of edge effects, and a first step towards the generalisation of the idea of an edge test for edge effect prediction, but as already remarked, we need a more accurate test if we want to use it to retrieve an expression of the corresponding interface force. We therefore continue to vary the boundary conditions until greater accuracy is achieved.

Edge test with $u_{BC_x} = u_{BC_y} = 0$

Our second guess is to also set the $y-$component of the displacement to zero. We compare the results of the edge test with the upper half of the 16×16 specimen for the frequency of 1000 Hz in Figure 4.8.

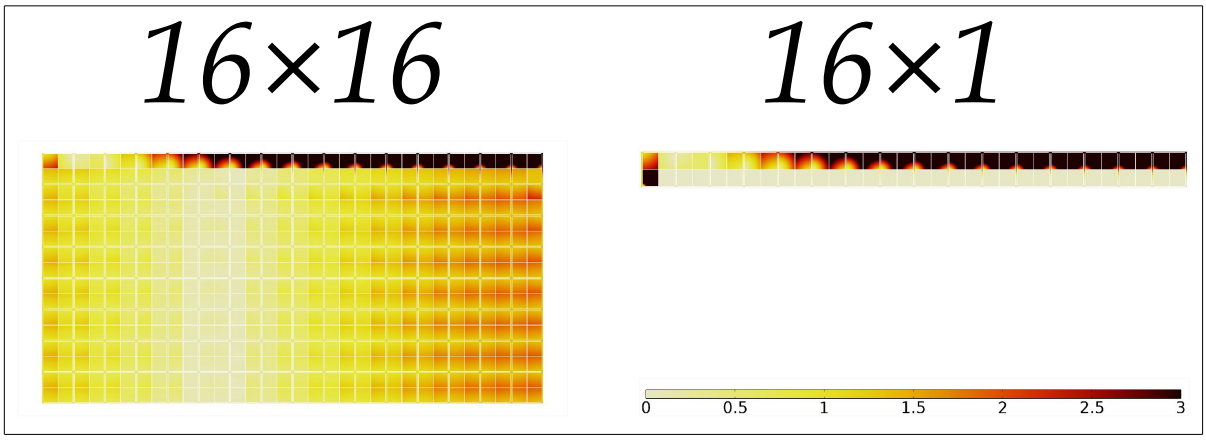

Figure 5.12: Dimensionless displacement field at 1000 Hz for (left) the 16×16 metamaterial A (only top half is shown due to the symmetry of the problem) and (right) the corresponding edge test with $u_{BC_x} = u_{BC_y} = 0$.

The comparison can be seen in Fig. 5.12, where we can see that the edge test is a good approximation similar to the last case (see Fig. 5.10) but still, we have areas where the displacement is both overestimated and underestimated. This implies that, again, this particular edge test can not be used for retrieval of an interface force.

Edge test with $u_{BC_y} = 0$ and u_{BC_x} free

Lastly, we set the $y-$component of the displacement to zero while letting the $x-$component free and compare the results of the edge test with the upper half of the 16×16 specimen for the frequency of 1000 Hz in Figure 4.8. We note that when taking a look at Fig. 5.9 and eq. (5.14), we see that the bottom part of the left Cauchy plate is free. Only here, since we are not constraining u_{BC_x} to be zero, we choose to extend our edge test boundary conditions to that part of the boundary of the plate as well.

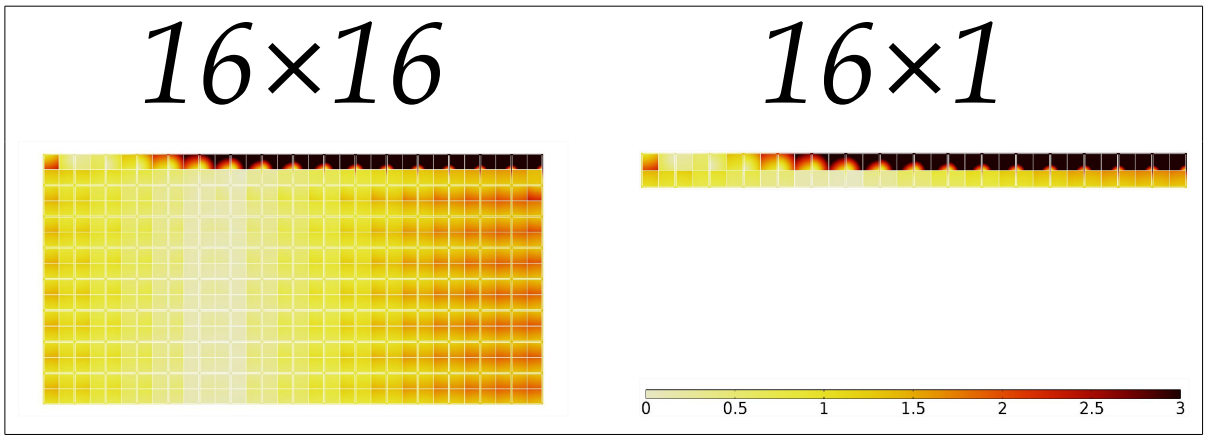

Figure 5.13: Dimensionless displacement field at 1000 Hz for (left) the 16×16 metamaterial A (only top half is shown due to the symmetry of the problem) and (right) the corresponding edge test with $u_{BC_y} = 0$ and u_{BC_x} free.

The comparison can be seen in Fig. 5.13. We observe that there is now both a very good qualitative and a quantitative agreement in the displacement field.

The results shown here for 1000 Hz translate in the same way for the rest of the frequencies where edge tests took place. For the four frequencies mentioned at the start of the section, we can reproduce the edge effect appearing on a 16×16 by doing an edge test on a 16×1, if we apply the same excitation, plus the boundary condition $u_{BC_y} = 0$ on the bottom boundary.

At first glance this result looks to be the edge test we were looking for, but taking a second look at the edge test and the boundary condition applied ($u_{BC_y} = 0$), we realise that this boundary condition is actually nothing more than a symmetry condition. This means that while we thought we were solving an edge test, we were actually solving an identical test to the one of the previous chapter, but instead of a 16×16 metamaterial, we now have a 16×2 specimen.

While this realisation renders the term "edge test" less meaningful in this case, it raises another, perhaps equally interesting question. If the same edge effect appears for a 16×16 and a 16×2, does it also appear for in-between (or higher) values of the number of unit cells used in the $y-$ direction? We wish to investigate this question in the remainder of this chapter.[3]

5.5.2 Dependence of the edge effect on the number of unit cells in the $y-$direction: scalability of interface forces

We wish to approach this problem, by starting from a 16×2, progressively adding more unit cells in the $y-$direction, until we reach the 16×16 size. We here show results for all the four frequencies and the cases of 16×4, 16×6, 16×8, 16×10, 16×12 and 16×14, but we note that also the rest of cases were checked (16×3, 16×5,..., 16×15), giving similar results.

The frequency of 300 Hz

Interestingly, we observe that the edge effect is not affected by the number of unit cells in the $y-$direction, cf. Fig. 5.14.

[3]For the particular case of a 16×1 where no boundary conditions are imposed on the bottom boundary, the edge effect does not appear. Only when two unit cells are used in the $y-$direction, the edge effect starts taking place.

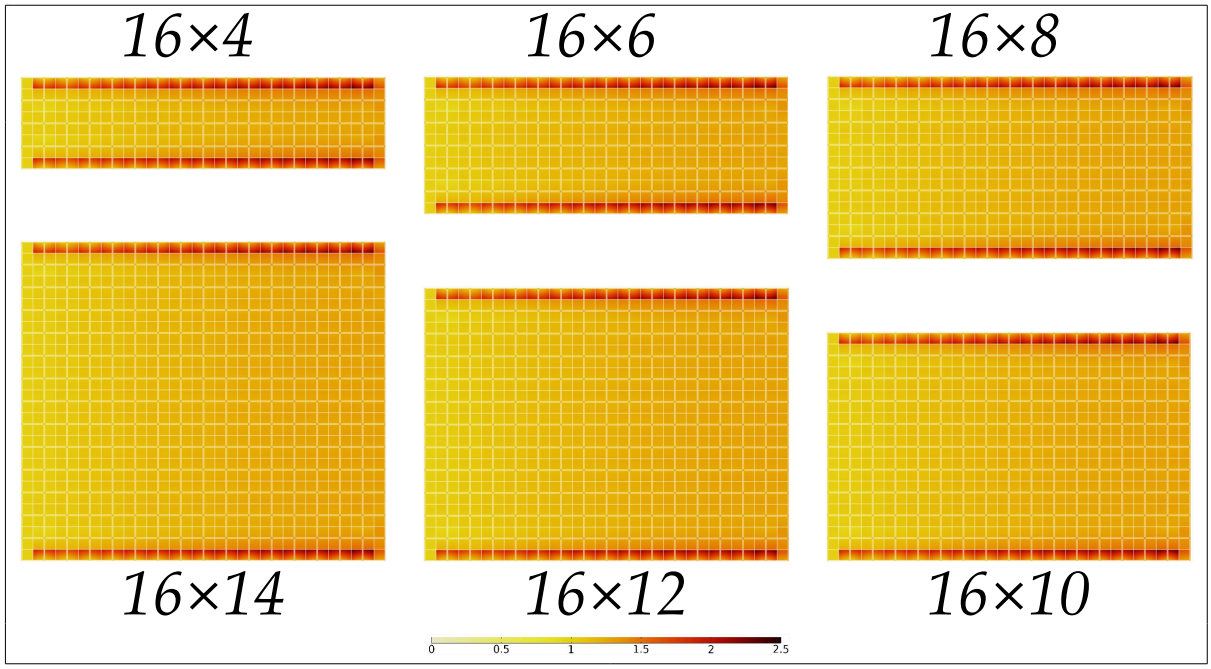

Figure 5.14: Progressively increasing the number of unit cells used in the $y-$direction at the frequency of 300 Hz.

The frequency of 1000 Hz

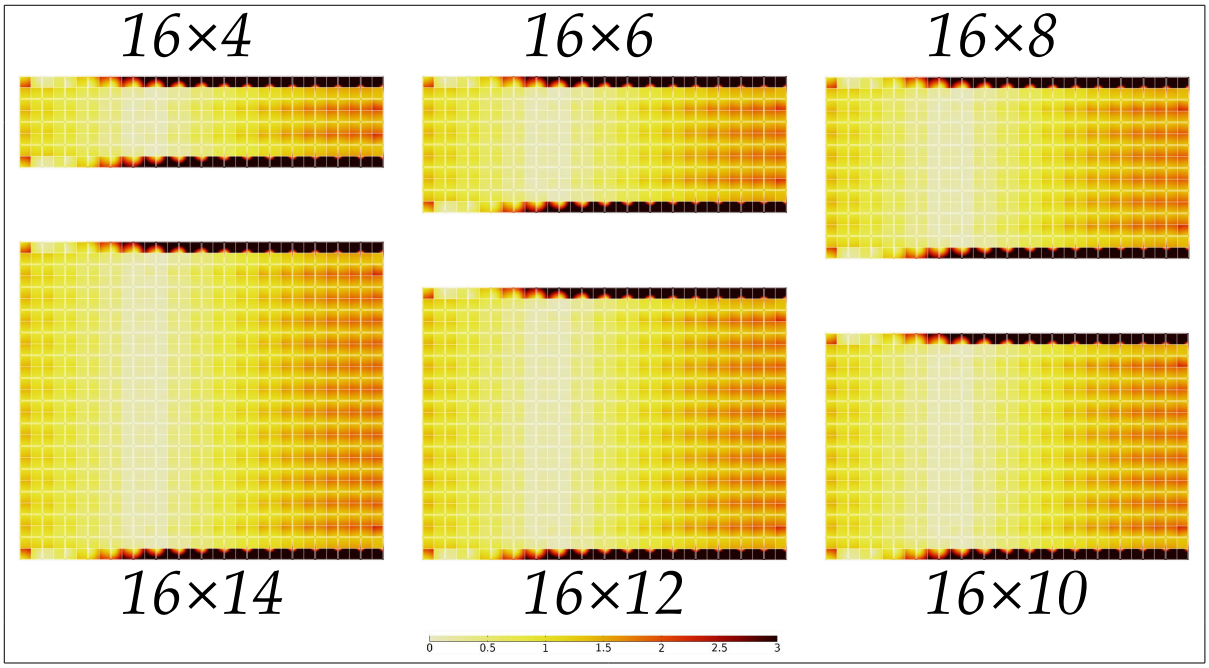

Figure 5.15: Progressively increasing the number of unit cells used in the $y-$direction at the frequency of 1000 Hz.

Similarly, we observe that the edge effect is not affected by the number of unit cells in the $y-$direction, cf. Fig. 5.15.

The frequency of 1800 Hz

We again observe that the edge effect is not affected by the number of unit cells in the $y-$direction, cf. Fig. 5.16.

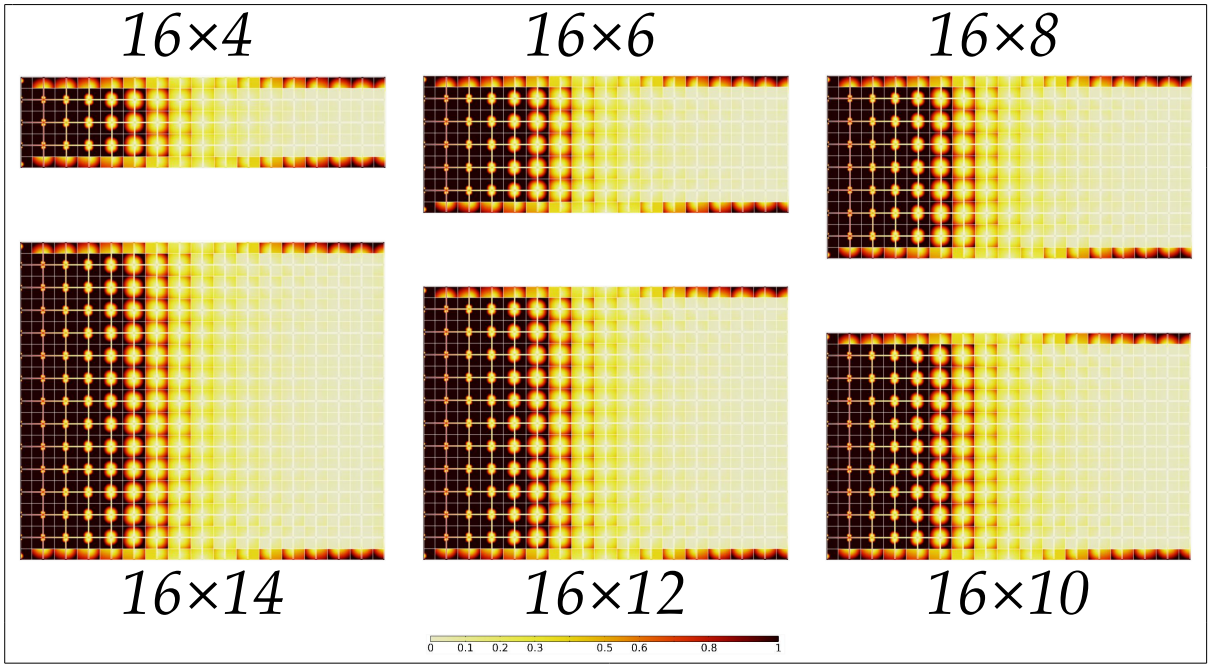

Figure 5.16: Progressively increasing the number of unit cells used in the $y-$direction at the frequency of 1800 Hz.

The frequency of 2300 Hz

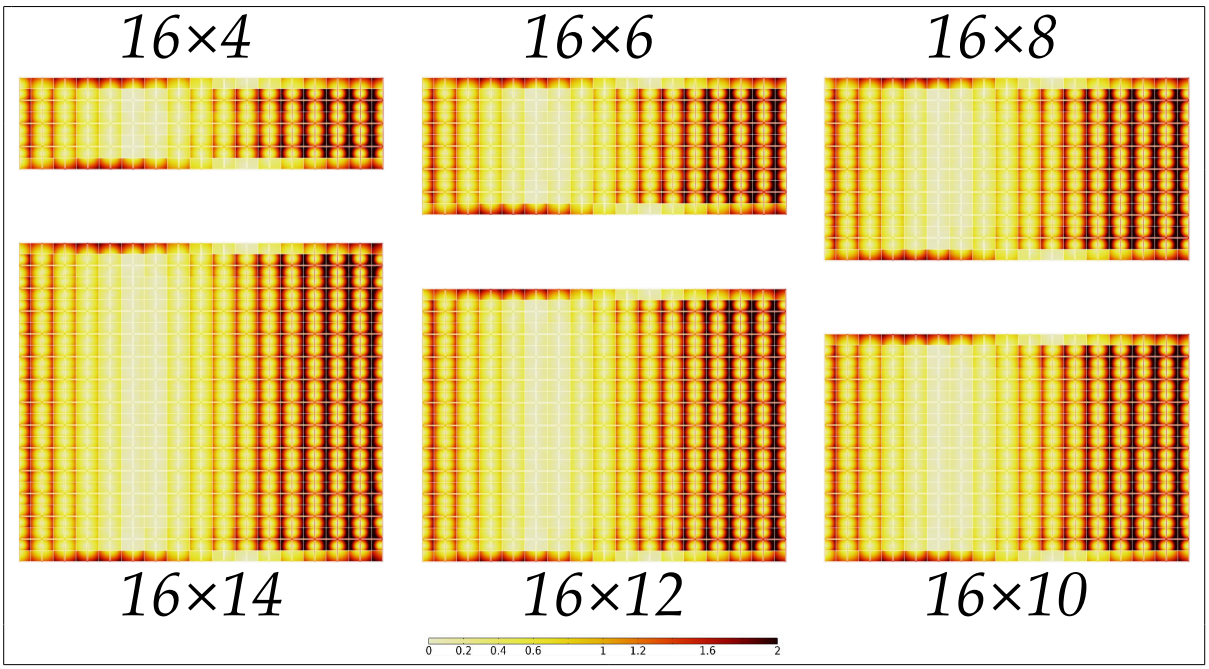

Figure 5.17: Progressively increasing the number of unit cells used in the $y-$direction at the frequency of 2300 Hz.

Once again, we observe that the edge effect is not affected by the number of unit cells in the $y-$direction, cf. Fig. 5.17.

We conclude that for this unit cell "cut" and these loading conditions, any edge effect is not affected by the number of unit cells in the range of 2 to 16 unit cells. This also means, that the corresponding interface force that is activated in the corresponding RRM simulation on the top and bottom boundaries is always the same, if the number of unit cells in the $x-$direction is 16 and the number of unit cells in the $y-$direction is between 2 and 16. This implies that for our initial test we could have calibrated

the interface force on the top and bottom "free" boundaries, on a 16×2 instead of a 16×16 saving computation time. This can be seen in Fig. 5.18 where for the frequency of 1000 Hz, we can see that for different size specimens but same interface force[4], we always arrive at the identical displacement field that captures the edge effect accurately.

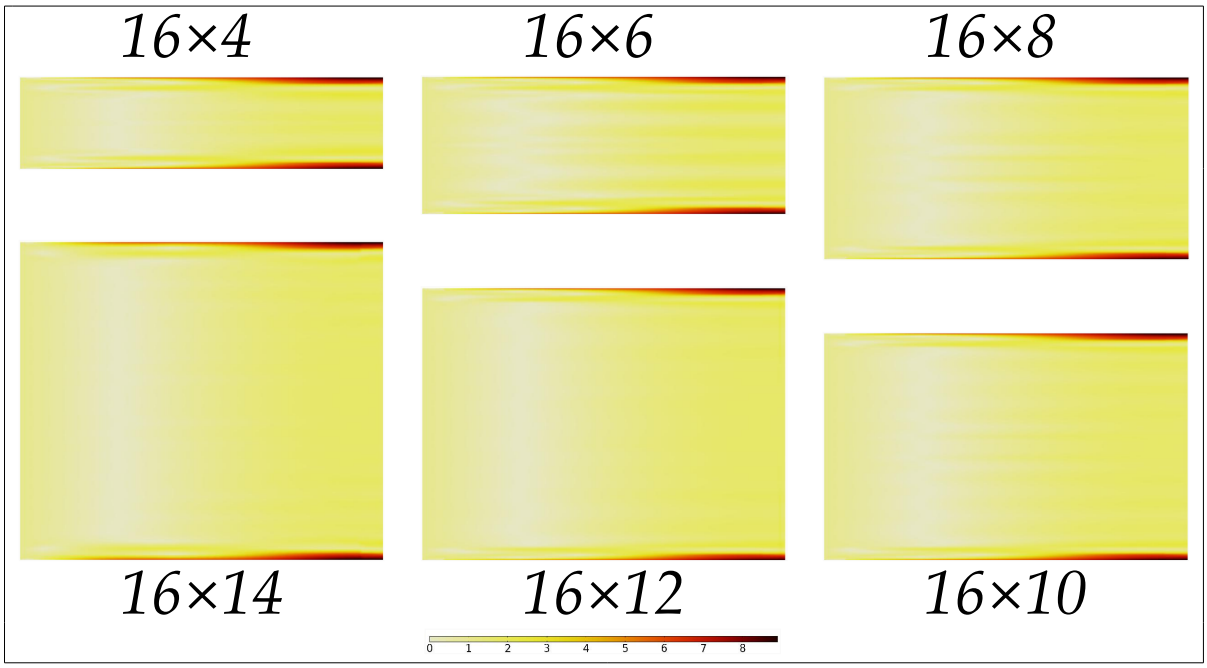

Figure 5.18: Progressively bigger metamaterials, modeled with the RRMM and the same expression of interface forces for all sizes, for the frequency of 1000 Hz.

Here we must point out, that the fact that the interface force could be calibrated on a 16×2, we couldn't have known until our investigation on the dependence of the edge effects on the number of unit cells in the $y-$direction was concluded. Therefore, if we want to apply this reasoning on other metamaterials, more investigation is needed in order to understand if this feature (i.e. the edge effect not being affected from the number of unit cells in the $y-$direction) is a feature of this particular metamaterial or polarisation direction, or if this is a general feature of edge effects.

Additionally, based on the findings of this section, another question that follows naturally is if the edge effect stays invariant with respect to any number of unit cells in the $y-$direction. For this we have conducted the same test performed multiple times in this and the previous chapter but we change the number of unit cells in the $y-$direction to be twice, four and eight times those in the $x-$direction, that is, 16×32, 16×64 and 16×128, respectively. We note that we repeated the test for all four frequencies discussed before but here we only show results for the frequency of 1000 Hz, since the results where similar in all cases. Furthermore, as already discussed, the problem is symmetric and the bottom edge effect is identical to the top but mirrored, we only show the upper half of the specimen. The results are shown in Fig. 5.19.

We observe that the edge effect stays invariant with respect to the number of unit cells in the $y-$direction for the sizes under consideration. We anticipate that as long as the specimen is of finite size, when changing the number of unit cells in the $y-$direction, the edge effect will persist but it will become more and more negligible for the rest of the specimen as the number of unit cells increases and unless structural eigenfrequencies are activated.

[4]The expression of the interface force in all cases is the one in Section 5.4.1 for metamaterial A.

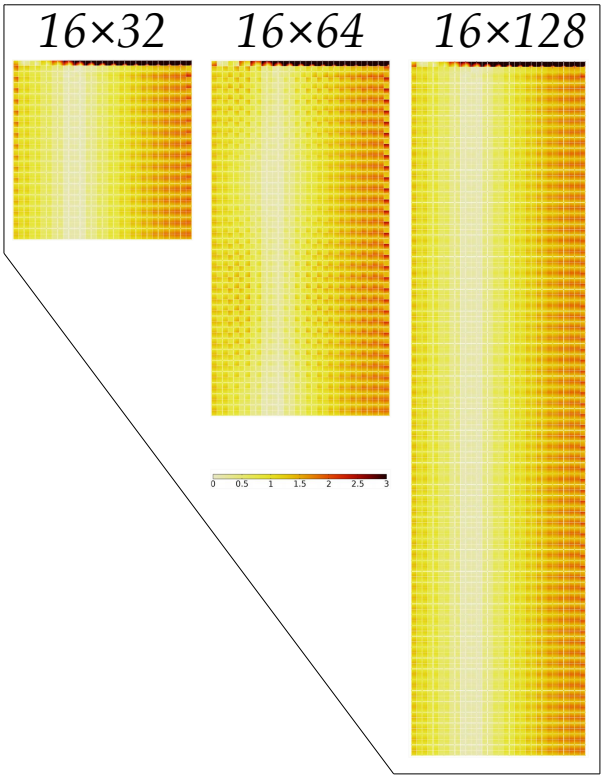

Figure 5.19: Dimensionless displacement field at 1000 Hz for the metamaterial A with 16×32, 16×64 and 16×128 unit cells.

5.6 Discussion

We have seen multiple cases in which interface forces were used to improve the accuracy of the RRMM's response by capturing neglected boundary effects. In these cases we showed that interface forces made the response more accurate by capturing edge effects, boundary effects that propagate in the bulk, and more general boundary effects related to the finite-size of the structure. We showed what expressions these interface forces take in order for the solution's accuracy to be improved.

We emphasize that, as explained in this chapter, one can arrive to these expressions in two ways. The first way is by a direct inspection of the displacement field and the deformation i.e. using an appropriate force, checking if the response is captured, change the force and check again, until a satisfactory result. The second way is again by trial and error, but this time by direct inspection of the tractions on the interfaces. The tractions on an interface in the homogenised simulation should correspond to an "average" of the corresponding tractions in the microstructured simulation. We explained that this average is an open problem in the literature but we can think of it as an interpolation.

Regarding edge effects, we showed that in the cases under consideration, they remain invariant to a change of the number of unit cells in the $y-$direction, which means that also the corresponding interface forces remain invariant as long as other boundary effects, in particular effects that propagate in the bulk, are not triggered. We also defined edge tests, based on the idea that while the structure is under a compression test, the edge is experiencing a shear-type test, owing to the transfer of shear stiffness from the unit cell to the row of unit cells (i.e. the edge) and we discussed these tests' potential for edge effect prediction. Results seem promising regarding the prediction of edge effects, but more investigation is needed for different "cuts" and different loading conditions. The mechanism of how the shear stiffness gets transferred from the unit cell to the edge might reveal the wanted physical quantities on which the edge effects depends on, and inevitably those that the surface force in the case of the enriched model depends on.

Chapter 6

Modeling a finite-size labyrinthine metamaterial using the RRMM and interface forces

6.1 Introduction

In the previous chapter, the RRMM coupled with the method of interface forces were used to capture the response of a 16×16 locally resonant metamaterial in some cases where boundary effects took place. In this Chapter, we wish to go one step further and model the behavior of even smaller specimens, for a metamaterial that only needs a small number of unit cells in order to attenuate a wave in the band-gap region.

6.2 Labyrinthine metamaterial, unit cell "cuts" and finite size specimens

The Labyrinthine unit cell shown in Fig. 6.1, designed by our group, presents wide band-gap behavior in the acoustic range as shown in Fig. 6.4 (black dots), and was already tested experimentally in [34]. The dimensions and properties of the base material of the unit cell are also reported in Fig. 6.1.

It was found, both experimentally and by corresponding microstructured simulations, that for the case of a pressure wave, only three unit cells are enough to attenuate waves in the band-gap. Thus, in [34], three different 3×2 metamaterial-specimens were 3D printed, each from a different unit cell "cut", and tested both computationally and experimentally, showing that the choice of unit cell "cut" can have a huge impact on the attenuative properties of the metamaterial.

The periodic repetition in space, of the unit cell presented in Fig. 6.1, creates the infinite metamaterial shown in Fig. 6.3 (top). In this infinite metamaterial, one can identify three more unit cell "cuts" shown in Fig. 6.3 (bottom). We name these "cuts" A, B, Γ and Δ, as shown in Fig. 6.3. We note that while A and B are of tetragonal symmetry, Γ and Δ are orthotropic. Nevertheless, as explained in Chapter 3, they all correspond to the maximal invariance group (in this case the tetragonal group), which represents the symmetry of the infinitely big metamaterial.

Here, we recreate similar tests as in [34], but in a computational setting, in 2D, and we choose to use one more unit cell "cut" which implies one more finite-size specimen. We model our metamaterials using fully resolved microstructured simulations and corresponding RRM simulations for comparison, and show the importance of interface forces regarding the homogenised modeling of small metamaterial specimens. The four finite-size specimens of 3×2 size are shown in Fig. 6.2, where it can be seen that the metamaterials are once again embedded between two Cauchy plates. We will call these four specimens, metamaterials A, B, Γ and Δ.

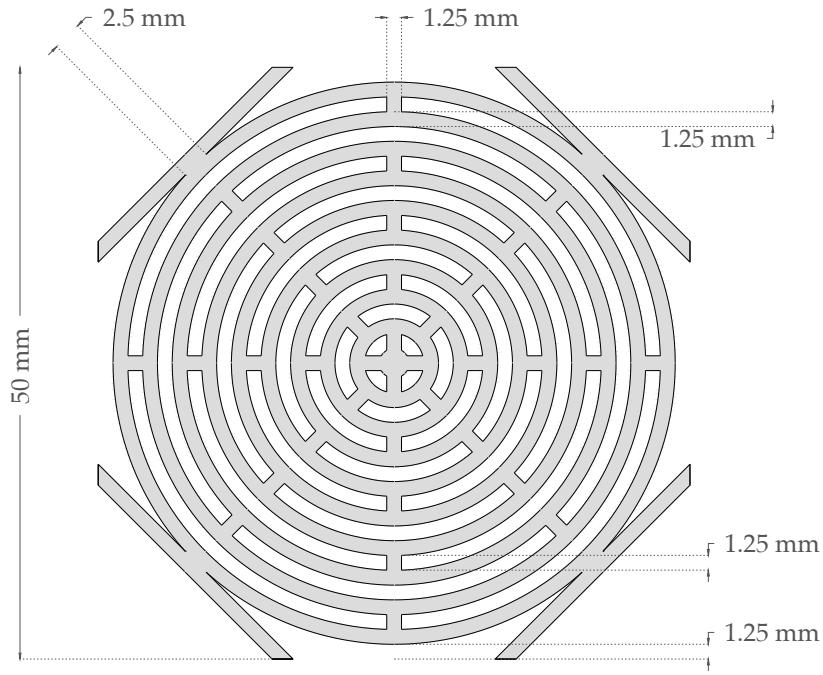

L_c [m]	ρ_{poly} [kg/m^3]	E_{poly} [Pa]	ν_{poly} [-]
0.05	1220	1.45×10^9	0.4

Figure 6.1: Unit cell and material properties of the metamaterial studied in this chapter. The base material is Polyethylene currently used in 3D printing.

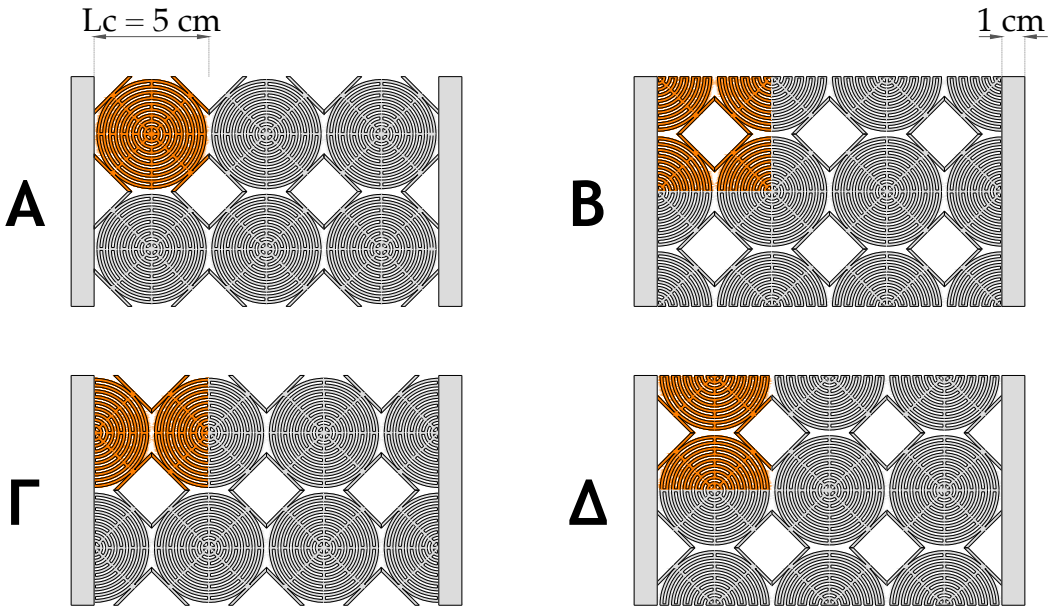

Figure 6.2: The four 3x2 specimens, each constructed from one of the four unit cell cuts of Fig. 6.3. The specimens are embedded between two Cauchy plates made out of the same material (Polyethylene). For simplicity we keep the nomenclature A, B, Γ, Δ, also to indicate these different macroscopic finite-sized specimens.

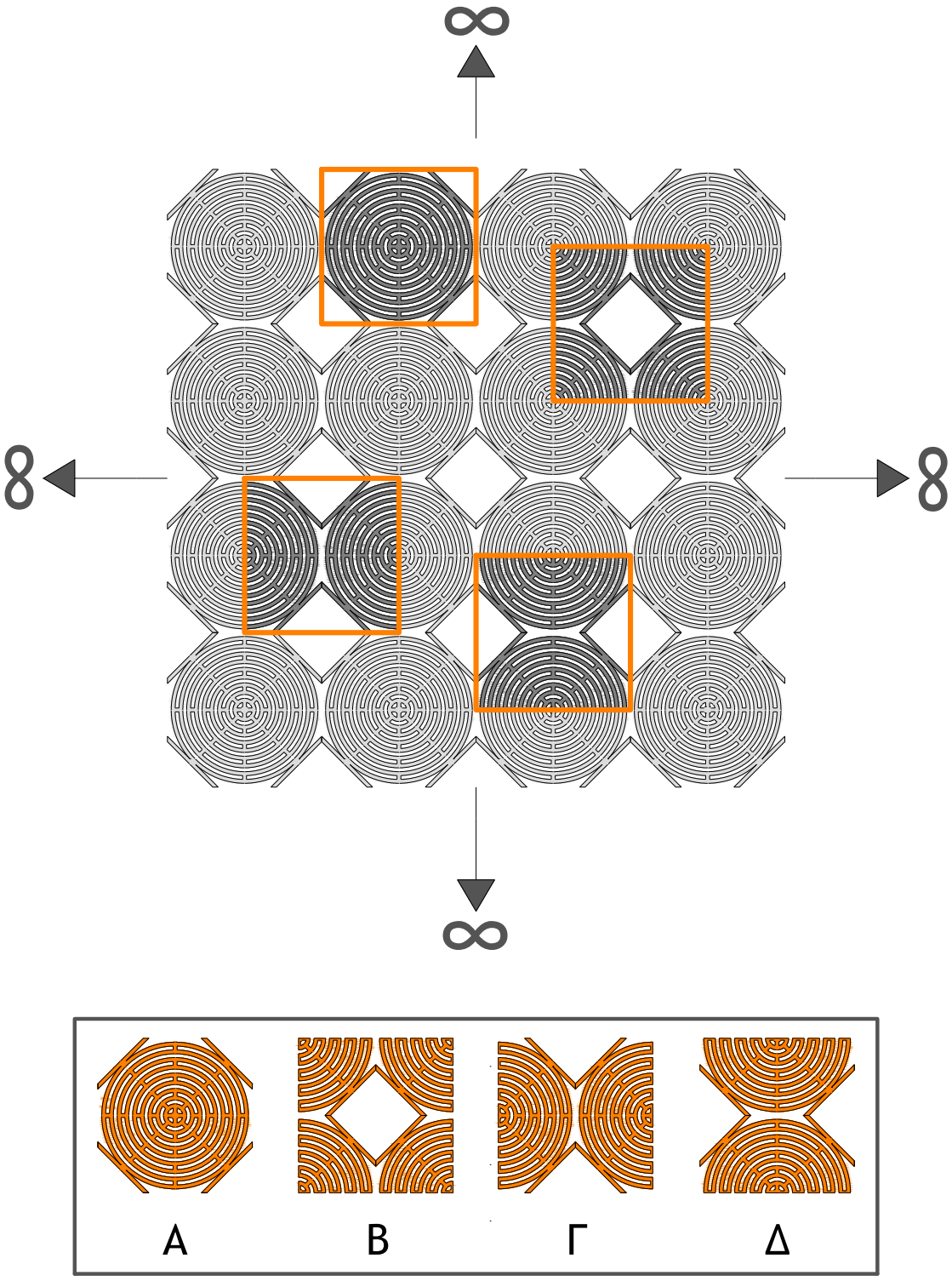

Figure 6.3: Infinite size periodic metamaterial (top) and the four unit cell cuts of the labyrinthine metamaterial used in our simulations (bottom). Cells A and B are of tetragonal symmetry and cells Γ and Δ are of orthotropic symmetry.

6.2.1 Identification of the RRMM parameters and dispersion curves fitting

The Equilibrium Equations, boundary conditions and the parameter identification procedure of the RRMM have been already explained in Chapter 3. As has been already explained, the ultimate goal of the parameter identification procedure given a specific metamaterial, is to give to the parameters of the RRMM such values, so that the dispersion curves of the RMMM are as close as possible to those coming from Bloch-Floquet analysis. In the case of infinite Labyrinthine metamaterial we study in this Chapter, the Bloch-Floquet dispersion curves for the labyrinthine metamaterial, and the corresponding dispersion curves for the RRMM after the parameter identification procedure, are shown in Fig.6.4. We also report here the values of those parameters (see Table 6.1).

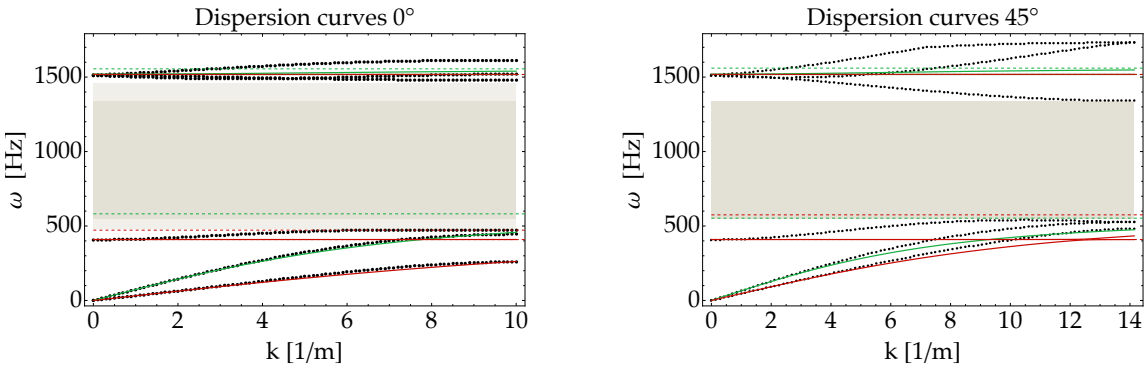

Figure 6.4: Dispersion curves for 0° (left), and for 45° (right). The dots correspond to the solution of the standard Bloch-Floquet analysis performed on unit cell A or B in Fig. 6.3 by using *Comsol Multiphysics*®, while the solid lines represent the analytical expression of the dispersion curves for the RRMM. Shear curves are colored with red and pressure curves with green. The dashed lines represent the asymptotes of the dispersion curves of the RRMM.

L_c [m]	κ_e [Pa]	μ_e [Pa]	μ_e^* [Pa]
0.05	2.56×10^6	1.18×10^6	5.38×10^5
μ_c [Pa]	κ_m [Pa]	μ_m [Pa]	μ_m^* [Pa]
243.1	5.81×10^6	5.13×10^8	5.13×10^8
κ_γ [-]	γ_1 [-]	γ_1^* [-]	γ_2 [-]
2.68	165	164.84	0.001
$\overline{\kappa}_\gamma$ [-]	$\overline{\gamma}_1$ [-]	$\overline{\gamma}_1^*$ [-]	[−]
3.53	2.63	1.78	-
κ_{Macro} [Pa]	μ_{Macro} [Pa]	μ^*_{Macro} [Pa]	ρ [kg/m^3]
$1.78.\ \times10^6$	1.17×10^6	5.37×10^5	540.7

Table 6.1: Values of the elastic parameters, the micro-inertia parameters, the size of the unit cell L_c, and the apparent density ρ for the reduced relaxed micromorphic model calibrated on the metamaterial whose building block is any of the four unit cells in Fig. 6.3. In the last row, we give the associated *macro-parameters*, i.e. the corresponding long-wavelength limit Cauchy material coefficients [64, 79].

6.3 Full-microstructured and reduced-relaxed-micromorphic finite element simulations for selected benchmark tests

We present here the benchmark tests that have been chosen to unveil the importance of the concept of interface forces for the homogenised modeling of finite-size metamaterials. We present the setting-up of

the numerical simulations on a finite-size metamaterial both with a microstructured Cauchy model (full detail of the unit-cells microstructure is coded in the numerical simulations) and the reduced relaxed micromorphic model (a homogeneous domain is used in the numerical simulations in which the constitutive laws are those of the reduced relaxed micromoprhic model and are eventually enriched with the concept of interface forces). For both the microstructured and the micromorphic simulations, we will take advantage of the symmetry of the problem, allowing us to reduce the computational time by simulating half of the structure while applying the appropriate symmetry conditions on the cut boundaries[1].

6.3.1 Full-Microstructured simulations set-up

As previously discussed in this thesis, the full-microstructured simulations take into account the detailed specimen's geometry, and the metamaterial's behavior is simply given by classical Cauchy elasticity. This process is typically computationally expensive due to the complex interior geometry of larger specimens, but it is manageable here because of the low number of unit cells used and the 2D setting. All the 2D simulations presented here have been performed under a plane-strain assumption and with a *time-harmonic* ansatz. The four microstructured materials presented in this work have been built as a regular grid of finite-size (3×2 unit cells of size $L_c = 0.05$ m each) as can be seen in Fig. 6.2. Their building blocks are the unit cells made up of Polyethylene shown in Fig. 6.3. The resulting metamaterials are in perfect contact on the left and right side with homogeneous Cauchy plates also made up of Polyethylene. The thickness of the plates is set to be 1 cm.

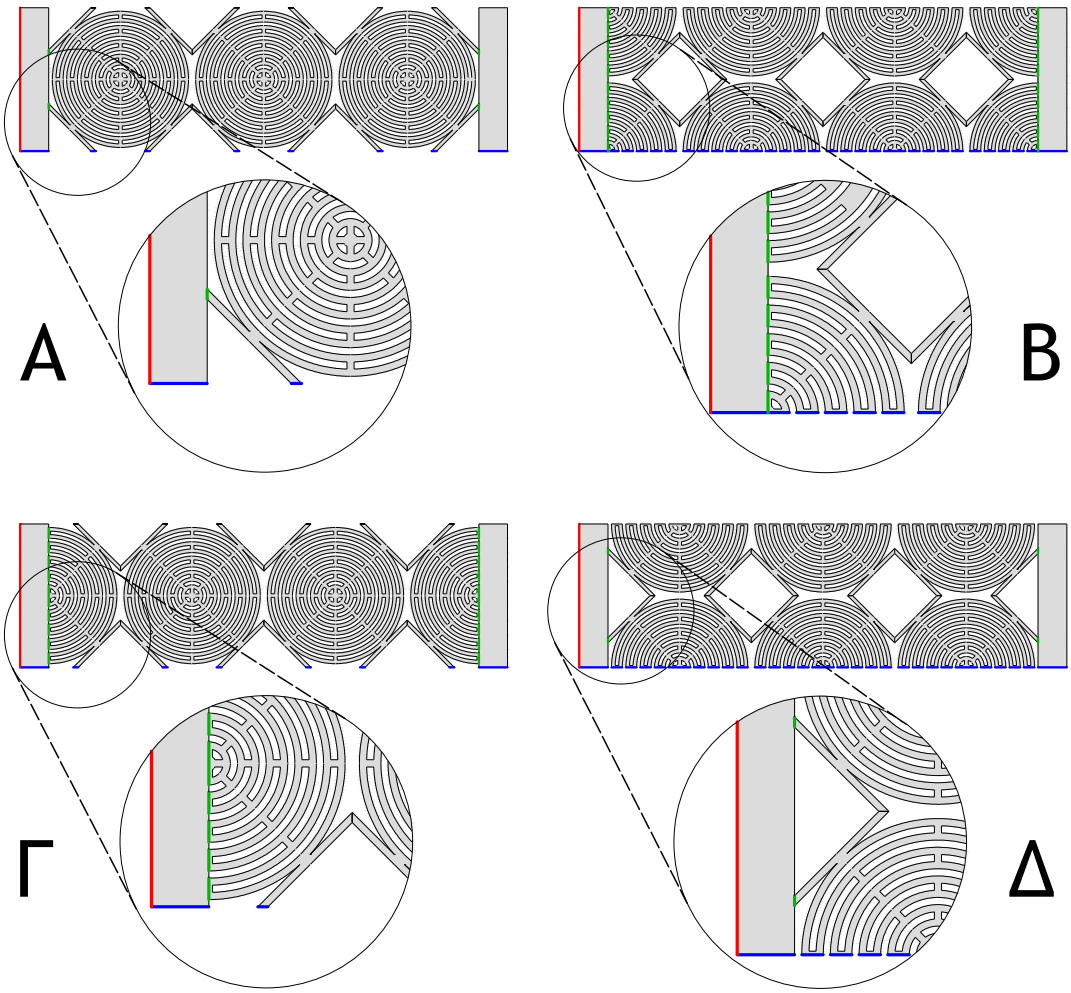

Figure 6.5: Schematic view of the geometry and the labeling of the boundaries and interfaces for the four microstructured specimens: A (top left), B (top right), Γ (bottom left) and Δ (bottom right).

The following boundary and interface conditions have been enforced on the relevant boundaries (see

[1] In all cases of this thesis, where half of the structure was simulated, the appropriate symmetry conditions were calculated according to Curie's symmetry principle, as explained in Appendix A.2

Fig. 6.5 to identify the different interfaces):

$$
\begin{aligned}
&\sigma n = \overline{F} && && \text{prescribed force - red} \\
&u^- = u^+ && \text{and} \quad (\sigma n)^- = (\sigma n)^+ && \text{perfect contact (continuity of displacement and traction) - green}^2 \\
&\sigma n = 0 && && \text{stress free - black} \\
&u_y = 0 && && \text{symmetry - blue}
\end{aligned} \tag{6.1}
$$

where σ is the classical Cauchy stress tensor, n is the outward unit normal to the interface and the expression of the externally applied force per unit area is: $\overline{F} = 10\widehat{e_1} + 0\widehat{e_2}$ [N/m^2].[3] This problem thus corresponds to a compression test along the horizontal direction, mimicking, in a 2D setting, the experimental testing performed in [34]. The simulations have been performed by using the *Solid Mechanics* physics package of *Comsol Multiphysics*®. In order to ease the numerical convergence of the analysis, and also to represent appropriately the material damping of Polyethylene, we introduced some damping using an isotropic loss factor with a value of $\eta = 0.1$ in all our calculations.[4]

6.3.2 Reduced-relaxed-micromorphic simulations set-up

The microstructured metamaterial is here modeled with the RRMM, which is characterised by the material parameters in Table 6.1. This means that the microstructured (heterogeneous) domains in Fig. 6.2 are replaced with a homogeneous domain of the same size (see Fig. 6.6) whose constitutive behavior is set to be that of a reduced relaxed micromorphic continuum (i.e. governing equations (3.5) hold in this bulk domain with the kinematic variables u and P).

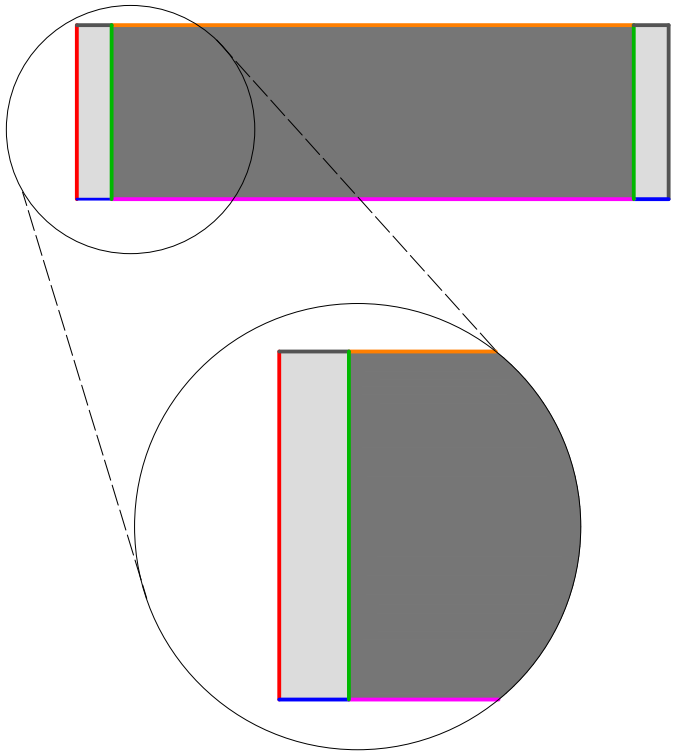

Figure 6.6: Schematic view of the geometry and the labeling of the boundaries and interfaces for the equivalent reduced relaxed micromorphic modeling of the considered metamaterial's specimens: Reduced relaxed micromorphic governing equations (3.5) are enforced in the darker gray bulk region, while classical isotropic Cauchy governing equations $\mathrm{Div}\,\sigma = \rho\ddot{u}$ are enforced in the two thin plates (lighter gray region). The enforced boundary and interface conditions are detailed in Eqs. (6.2).

In addition, the following boundary and interface conditions have been enforced (see Fig. 6.6 for the

[2] these jump conditions can be written in a more compact form as $[[u]] = 0$ and $[[t]] = 0$, $t = \sigma n$ being the Cauchy traction on each side.

[3] The value of the externally applied load is compatible with the experimental one used in [34].

[4] This value of the damping has been found to be realistic when comparing numerical simulations to experimental tests [34].

definition of the different interfaces):

$$
\begin{aligned}
\sigma\, n &= \overline{F} && && \text{prescribed force - red (Cauchy)} \\
\sigma\, n &= 0 && && \text{stress free - black (Cauchy)} \\
u_y &= 0 && && \text{symmetry - blue (Cauchy)} \\
(\widetilde{\sigma} + \widehat{\sigma})\, n &= 0 && && \text{stress free - orange (RRMM)} \\
u_y &= 0 && \text{and} \quad P_{12} = P_{21} = 0 && \text{symmetry - magenta (RRMM)} \\
u_{Cauchy} &= u_{\text{RRMM}} && \text{and} \quad \sigma\, n = (\widetilde{\sigma} + \widehat{\sigma})\, n && \text{perfect contact - green (Cauchy/RRMM interface)}^{5}
\end{aligned}
\tag{6.2}
$$

where, again σ is the well known Cauchy stress tensor, the enriched stress tensors $\widetilde{\sigma}$ and $\widehat{\sigma}$ are given in eq. (3.6), the expression of the applied force per unit area is: $\overline{F} = 10\widehat{e_1} + 0\widehat{e_2}$ [N/m^2] and the symmetry conditions are calculated according to Appendix A.2. The effective homogeneous material modeled with the reduced relaxed micromorphic model is also embedded between two slender homogeneous Cauchy plates made out of Polyethylene. The simulations have been performed by using the *Weak Form PDE* physics package of *Comsol Multiphysics*®. This package requires the implementation of the expression of the Lagrangian (3.3) and the appropriate boundary and interface conditions. To have a consistent comparison with the results from the microstructured simulations, we have introduced the same damping value of the isotropic loss factor ($\eta = 0.1$) also in this case.

6.3.3 Interface forces ansatz

Before showing the results of the simulations, we once again state the "ansatz" of our interface forces. From those results, it will become clear that the RRMM is in need of enrichment if one wants to describe the response of all four finite-size metamaterials. In the RRM simulations (see Fig. 6.6), for all interfaces colored in green we assume an interface force that depending on the value of α_{i_n} may or may not be a linear function of the RRM traction on the interface

$$
f_{i_n}^{\text{interface}} = (\alpha_{i_n} - 1) t_{(\text{RRMM})_{i_n}} + \beta_{i_n}. \tag{5.6}
$$

where $i = L, R$ for left or right interface respectively and $n = x, y$ for x or y component of the tractions respectively, α_{i_n} is a dimensionless coefficient and β_{i_n} is a surface force.

For all "free" interfaces colored in orange, the interface force f^{int} can have any form so that the RRM traction on the "free" boundary becomes

$$
\mathrm{t} := (\widetilde{\sigma} + \widehat{\sigma})\, n = f^{\text{interface}}. \tag{5.2}
$$

6.3.4 Reduced Relaxed Micromorphic Model with and without interface forces vs Microstructured and long-wavelength limit Cauchy simulations

We present here the results of the previously discussed simulations, stressing the importance of the concept of interface forces when a homogenised model like the RRMM has to be used for the modeling of finite-sized metamaterials' structures.

To this aim, we consider the comparison between the RRM simulations and the microstructured ones for the A, B, Γ, Δ "cuts" of different frequencies. When the solution of the RRMM does not match the microstructured solution, we calibrate the corresponding interface forces arising at the interfaces between the RRM domain (corresponding to the metamaterial) and the Cauchy plates (see eq. (5.6)), until the RRM solution matches the microstructured one. We also provide a comparison with a simulation in which the metamaterial domain is modeled through a homogeneous Cauchy continuum of tetragonal symmetry, which is the long-wavelength limit of the RRMM. The Equilibirum Equations and boundary conditions for the macro-Cauchy model, are those reported in Chapter 2 regarding Cauchy elasticity (eqs. (2.7), (2.8) and (2.9)), but the Elasticity tensor is the one reported in eq. (3.15), where the values of the macro parameters are given in Table 6.1. By including the macro-Cauchy model in the comparison, we are able to stress the fact that in order for interface forces to be effectively used as an enrichment to the boundary conditions in order to capture boundary effects, the dispersion of the metamaterial must first be captured. This will become more clear after the results are shown. The frequencies chosen are reported in Fig. 6.7 with reference to the dispersion curves.

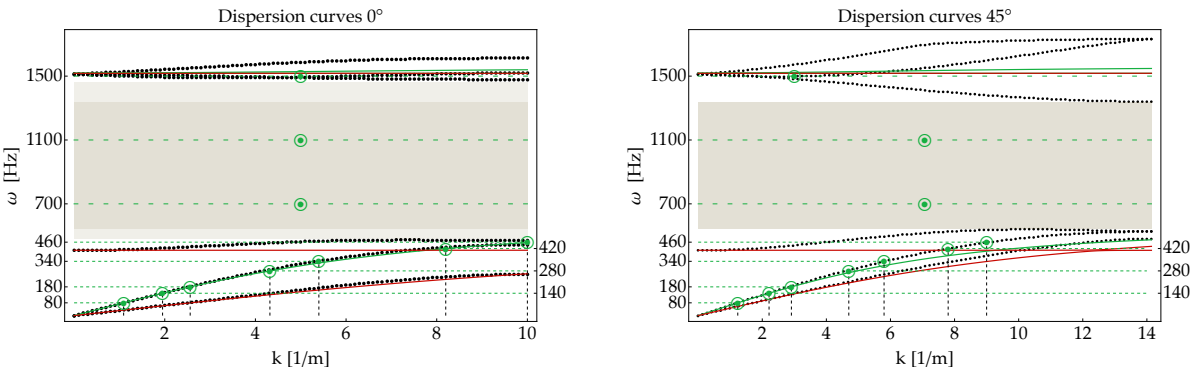

Figure 6.7: Dispersion curves for 0° (left), and for 45° (right).The dots correspond to the solution of the standard Bloch-Floquet analysis performed on unit cell A or B in Fig. 6.3 by using *Comsol Multiphysics*®, while the solid lines represent the analytical expression of the dispersion curves for the RRRM. Shear curves are colored with red and pressure curves with green. Green circular points indicate the frequencies and corresponding wavenumbers for which our finite size RRM simulations were implemented (the points in the band-gap show only the frequency used, since there exists no corresponding real wavenumber).

Frequency (Hz)	**Wavelength (cm)**
80	91
140	51
180	39
280	23
340	18.5
420	12
460	10
700	band-gap
1100	band-gap
1500	no propagation

Table 6.2: Wavelengths at which a pressure wave propagates in the infinite metamaterial of Fig. 6.3 at the considered frequencies. The size of the specimen (without the bars) is 15 cm.

The wavelength for which a wave propagates inside the metamaterial at the considered frequencies is summarized in Table 6.2. Regarding the procedure of calculating coefficients α_{i_n} and forces β_{i_n}, we must add that they are calculated by direct inspection and comparison of the RRM and corresponding microstructured displacement fields. We first run a parametric sweep for the α_{i_x} coefficients, compare the displacement field with that of the microstructured metamaterial and check which values make the response more accurate. Then, if the Cauchy plates on the left and right hand side of the metamaterial in the microstructured simulation experience bending, also the α_{i_y} coefficients must be taken into account. We apply the same procedure (running a parametric sweep and inspecting the displacement field) until the response is accurate. Furthermore, forces β_{i_x} and β_{i_y} can be used as an extra tool if the response is hard to capture. Moreover, if edge effects appear on the top boundary of the microstructured simulation, an interface force must be activated on the top "free" RRM boundary in the corresponding RRM simulation.

In the following, we also look at the tractions on the Cauchy/RRM interfaces, that could potentially be used as an alternative method to calculate coefficients α_{i_n} and forces β_{i_n} that lead to the correct response. A method based on the "average" of the tractions is indeed a promising method for bigger specimens where the calculation of "average" traction is more meaningful.

[5] These jump conditions can be also written in compact from as $[[u]] = 0$ and $[[t]]=0$ where $[[u]]$ represents the jump of displacement and $[[t]] = t^+ - t^- = \sigma n - (\widetilde{\sigma} + \widehat{\sigma})\ n$ is the jump of the generalized traction across the green interface.

Frequency: 80 Hz

We start analyzing the homogenised Cauchy and RRM simulations and the corresponding comparison to the microstructured ones for the frequency of 80 Hz. This frequency is relatively low and corresponds to a macro Cauchy-like non-dispersive behavior (see the first point in Fig. 6.7).

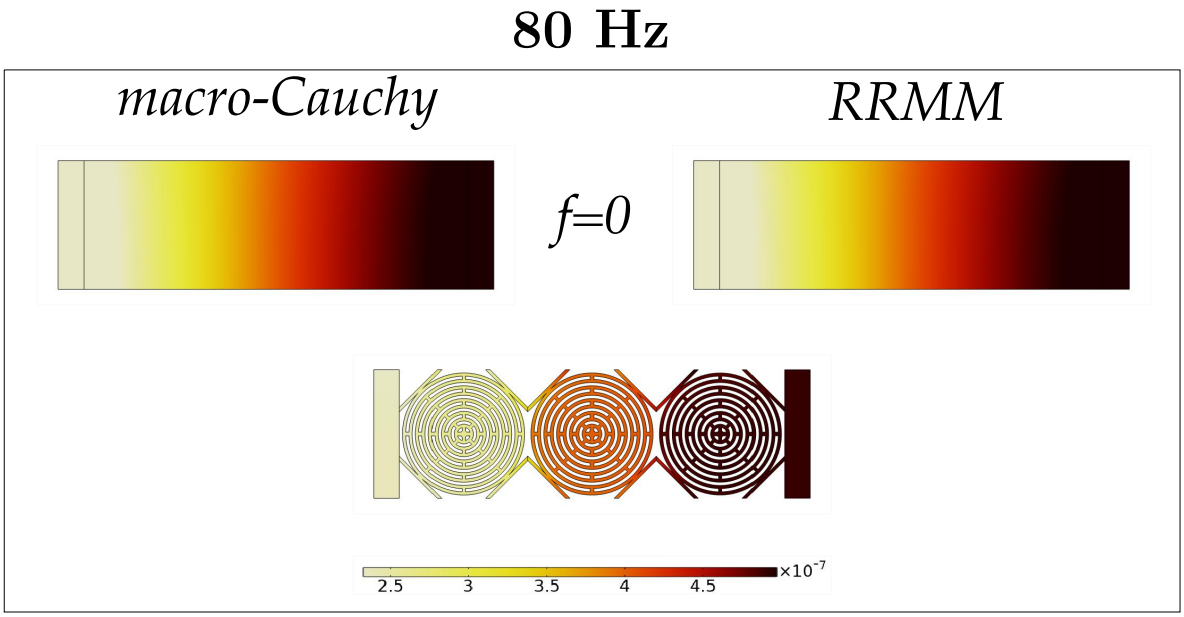

Figure 6.8: Comparison of the displacement field of the metamaterial specimen A with the macro-Cauchy and the RRMM when $f = 0$ at 80 Hz.

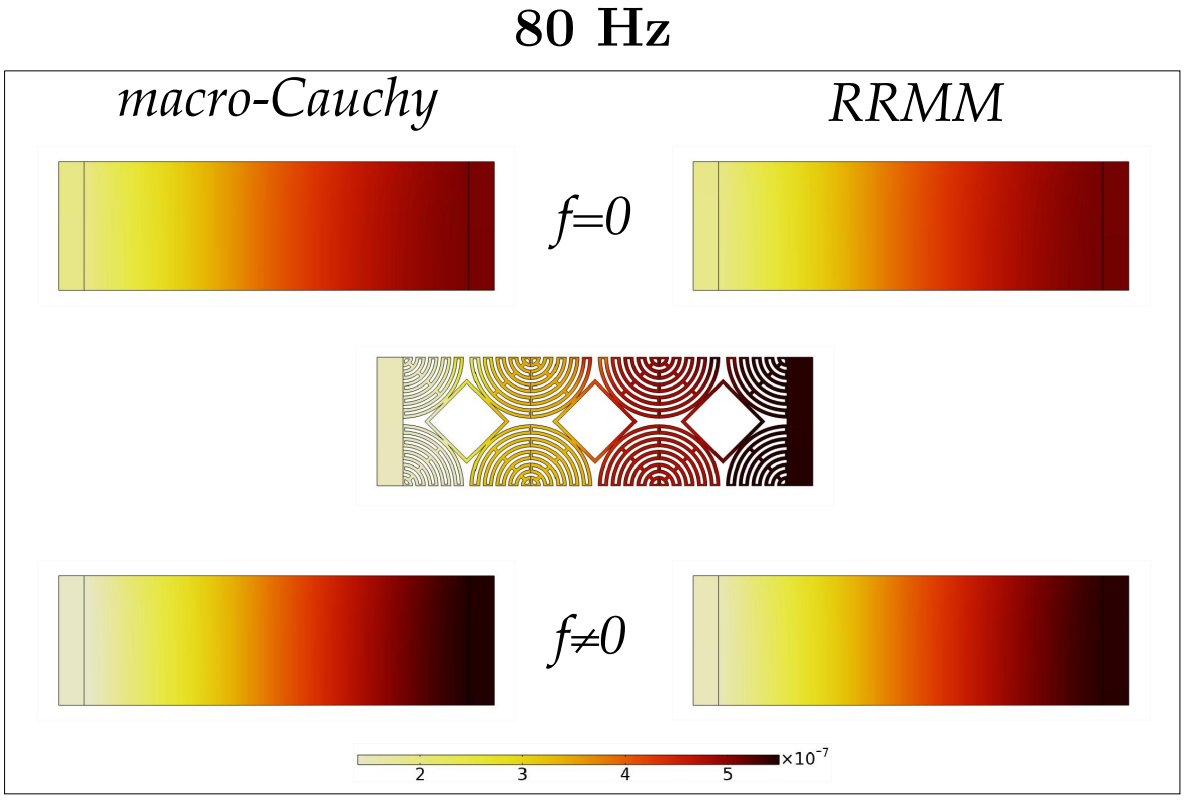

Figure 6.9: Comparison of the displacement field of the metamaterial specimen B with the macro-Cauchy and the RRMM when $f = 0$ and $f \neq 0$ at 80 Hz. When $f \neq 0$ for the macro RRMM, we have: $\alpha_{L_x} = 0.9$, $\beta_{L_x} = 0$, $\alpha_{L_y} = 1$, $\beta_{L_y} = 0$, $\alpha_{R_x} = 0.6$, $\beta_{R_x} = 0$, $\alpha_{R_y} = 1$ and $\beta_{R_y} = 0$, while for the macro Cauchy: $\alpha_{L_x} = 0.87$, $\beta_{L_x} = 0$, $\alpha_{L_y} = 1$, $\beta_{L_y} = 0$, $\alpha_{R_x} = 0.5$, $\beta_{R_x} = 0$, $\alpha_{R_y} = 1$ and $\beta_{R_y} = 0$.

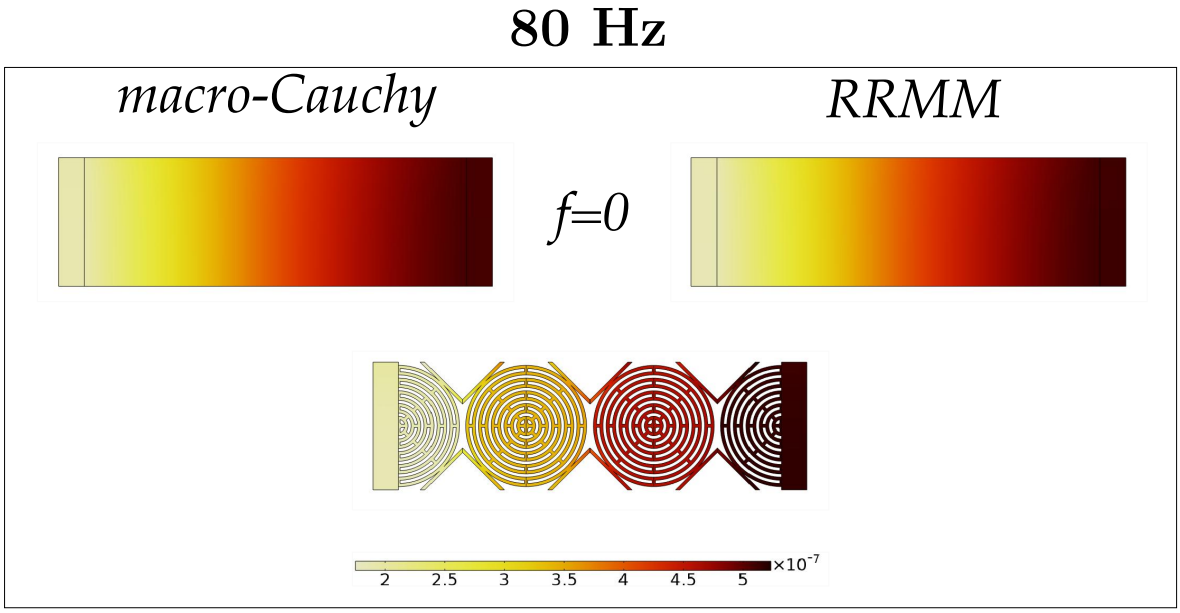

Figure 6.10: Comparison of the displacement field of the metamaterial specimen Γ with the macro-Cauchy and the RRMM when $f = 0$ at 80 Hz.

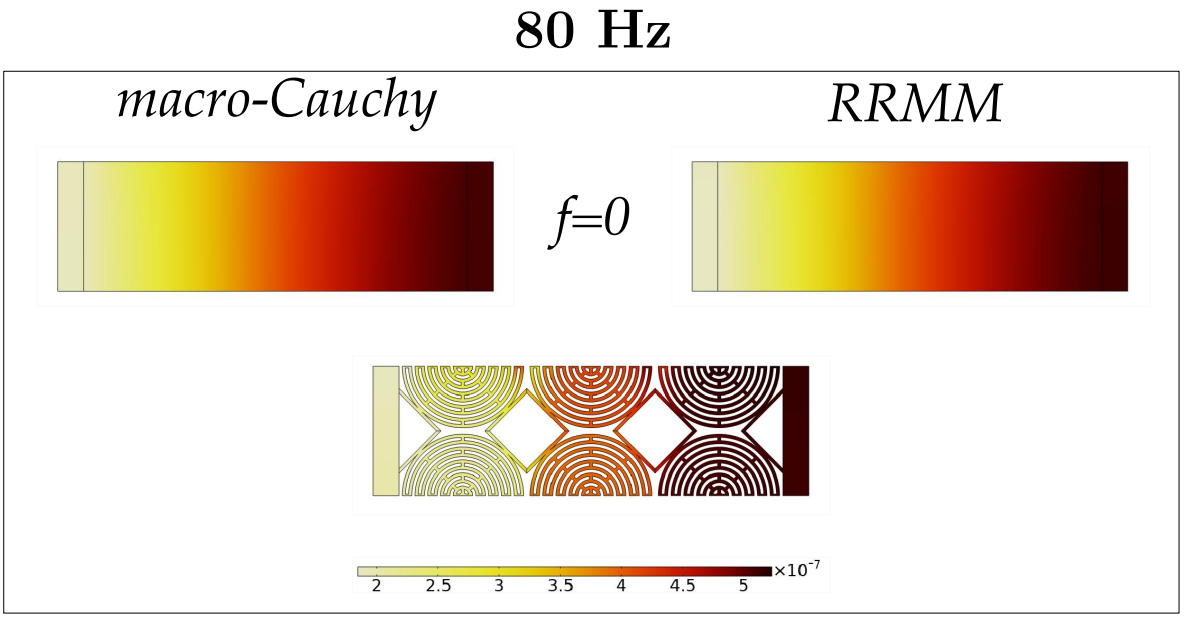

Figure 6.11: Comparison of the displacement field of the metamaterial specimen Δ with the macro-Cauchy and the RRMM when $f = 0$ at 80 Hz.

Figures 6.8, 6.9, 6.10 and 6.11 show that at the frequency of 80 Hz the RRM solution is almost coinciding with the long-wavelength limit Cauchy solution. This is related to the fact that the behavior of the dispersion curves is still linear at the considered lower frequency (see Fig. 6.7). However, it is evident that, even at this lower frequency, boundary effects may play a non-negligible role. Indeed, while for the "cuts" A, Δ and Γ there is no need to introduce non-vanishing interface forces, "cut" B needs a non-vanishing interface force to recover the correct solution (see Fig. 6.9).

However, also for the B case for which interface forces are necessary to recover the correct solution, it can be recognized that the correction brought by triggering $f^{\text{interface}} \neq 0$ is quite small when compared to the corrections which are found for higher frequencies (see Fig. 6.9 with $f = 0$ and $f \neq 0$). The fact that the interface force is bringing either a small correction or no correction at all is related to the fact that at this low frequency the wavelength is quite larger than the size of the specimen (see Table 6.2).

This implies that for such large wavelength boundary effects are overall quite small or mostly negligible.

We have seen that at the considered frequency of 80 Hz both the RRMM and the macro-Cauchy model give good results when suitable interface forces are introduced. This can also be seen when looking at the tractions that arise at the Cauchy-plates/metamaterial interfaces, as shown in Fig. 6.12.

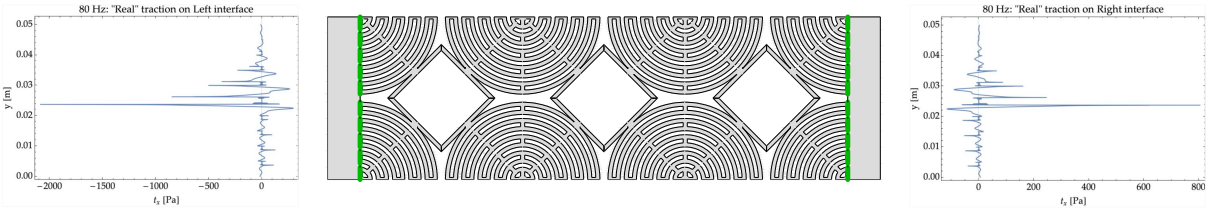

Figure 6.12: Sketch of the tractions on the Cauchy side of the Cauchy plate/metamaterial interfaces at 80 Hz. The two plots on the two sides of the specimen represent the traction fields on the Cauchy-plate sides along the green lines highlighted in the picture. Similar patters can be observed for all other "cuts" and for other frequencies.

Fig. 6.12 shows the microstructured tractions arising at the Cauchy-plates/metamaterial interfaces (on the Cauchy side), for "cut" B. Completely analogous considerations are valid for all other "cuts". As a first rough measure, we can compute the "mean" value of this traction[6] and compare it to the corresponding RRM and macro-Cauchy tractions. This comparison is shown in Fig. 6.13, where we can see that there is practically no difference between the RRM and macro-Cauchy tractions both on the left and right interface.

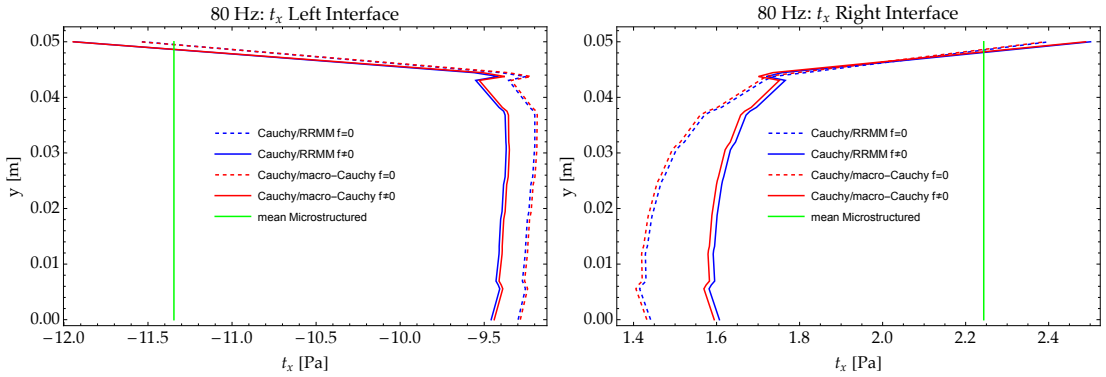

Figure 6.13: Tractions on the Cauchy side of the Cauchy plate/metamaterial interfaces (left and right) for the RRMM and for the macro-Cauchy when $f = 0$ and $f \neq 0$. The tractions shown here are those relative to "cut" B. Analogous reasoning holds true for all other "cuts".

It can also be inferred that the homogenised (both RRMM and macro-Cauchy) tractions become "closer" to the mean traction calculated starting from the microstructured solution as soon as "interface" forces are triggered. This is a good indication that the homogenised framework including the concept of interface forces is a mandatory step if homogenised models have to be used for finite-size metamaterials modeling. However, we can see that the homogenised (both RRMM and macro-Cauchy) traction does not exactly coincide with the "mean" of the microstructured traction which has been evaluated for comparison. This is due to the fact that the "averaging" of the interface microstructured traction (the one shown in Fig. 6.12) is an operation whose exact definition is an open challenge in the homogenisation community. Practically no work exists which try to incorporate the effect of microscopic heterogeneous boundaries into the existing homogenisation procedures. Given the complexity of the considered metamaterials and interfaces, a rigorous definition of such average interface microstructured tractions could be impossible to be fully achieved.

We also note that while Fig. 6.13 shows the x-component of the tractions at the Cauchy-plate/metamaterial interface, completely analogous conclusions should hold for the y-component. However, for the considered interfaces, given the direction of the excitation we chose to use the more meaningful component of the tractions for our comparison.

[6]The "mean" is calculated with a standard procedure: The traction t_x has a specific value on every point on the Cauchy-plate/metamaterial interface. We sum all these values together and we divide by the number of points. This gives us a number that represents the "average" value of the traction t_x on the interface.

Frequency: 140 Hz

We continue analyzing the homogenised Cauchy and RRM simulations and the corresponding comparison to the microstructured ones for the frequency of 140 Hz. This frequency is relatively low and still corresponds to a macro Cauchy-like non-dispersive behavior (see the second point in Fig. 6.7).

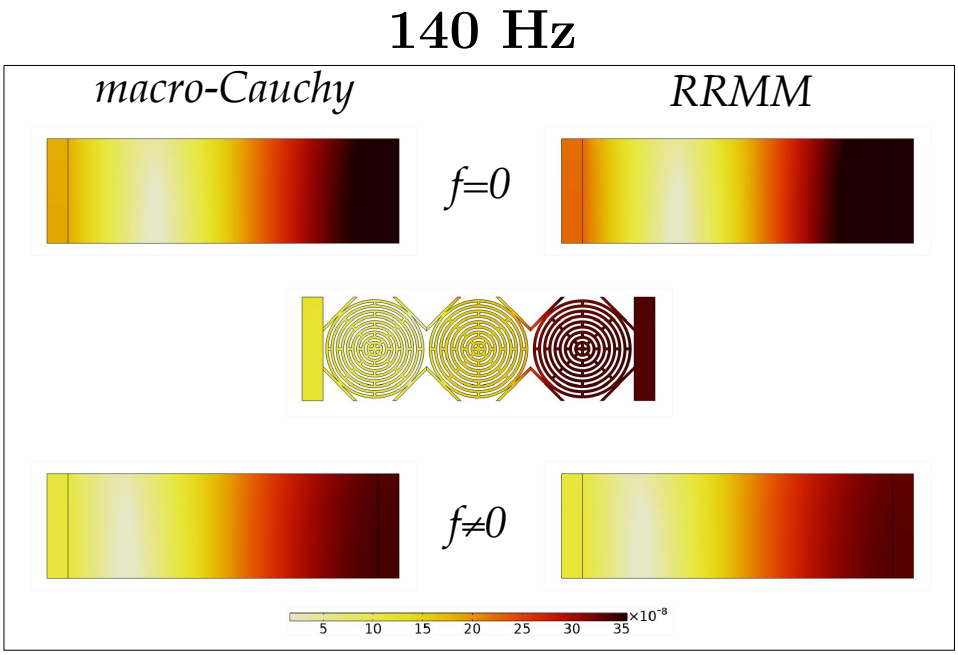

Figure 6.14: Comparison of the displacement field of the metamaterial specimen A with the macro-Cauchy and the RRMM when $f = 0$ and $f \neq 0$ at 140 Hz. When $f \neq 0$ for the RRMM, we have: $\alpha_{L_x} = 1.05$, $\beta_{L_x} = 0$, $\alpha_{L_y} = 1$, $\beta_{L_y} = 0$, $\alpha_{R_x} = 5$, $\beta_{R_x} = 0$, $\alpha_{R_y} = 1$ and $\beta_{R_y} = 0$, while for the macro Cauchy: $\alpha_{L_x} = 0.99$, $\beta_{L_x} = 0$, $\alpha_{L_y} = 1$, $\beta_{L_y} = 0$, $\alpha_{R_x} = 3$, $\beta_{R_x} = 0$, $\alpha_{R_y} = 1$ and $\beta_{R_y} = 0$.

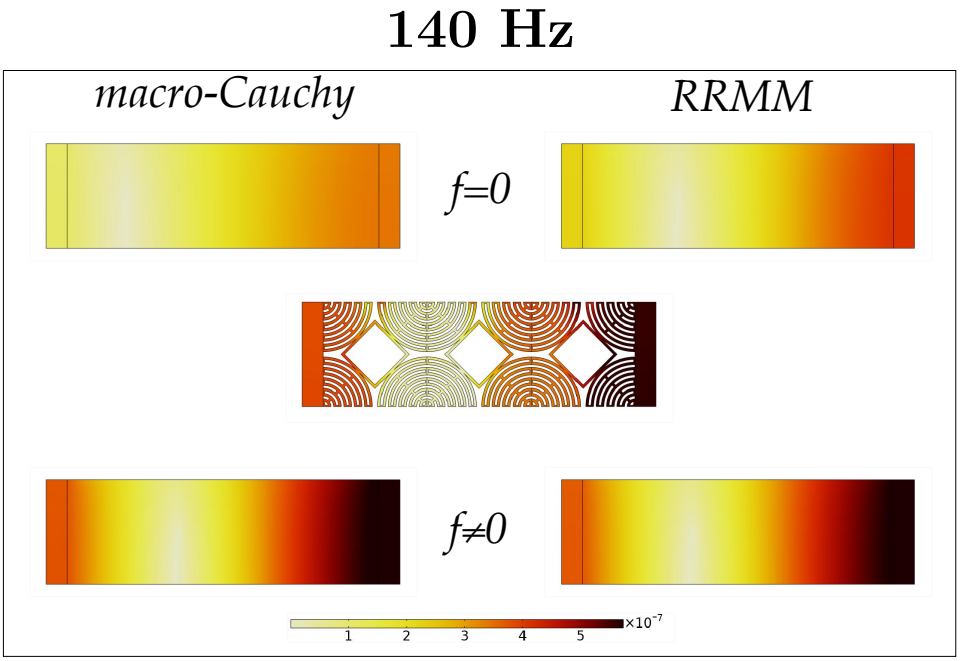

Figure 6.15: Comparison of the displacement field of the metamaterial specimen B with the macro-Cauchy and the RRMM when $f = 0$ and $f \neq 0$ at 140 Hz. When $f \neq 0$ for the RRMM, we have: $\alpha_{L_x} = 0.8$, $\beta_{L_x} = 0$, $\alpha_{L_y} = 1$, $\beta_{L_y} = 0$, $\alpha_{R_x} = 0.75$, $\beta_{R_x} = 0$, $\alpha_{R_y} = 1$ and $\beta_{R_y} = 0$, while for the macro Cauchy: $\alpha_{L_x} = 0.75$, $\beta_{L_x} = 0$, $\alpha_{L_y} = 1$, $\beta_{L_y} = 0$, $\alpha_{R_x} = 0.65$, $\beta_{R_x} = 0$, $\alpha_{R_y} = 1$ and $\beta_{R_y} = 0$.

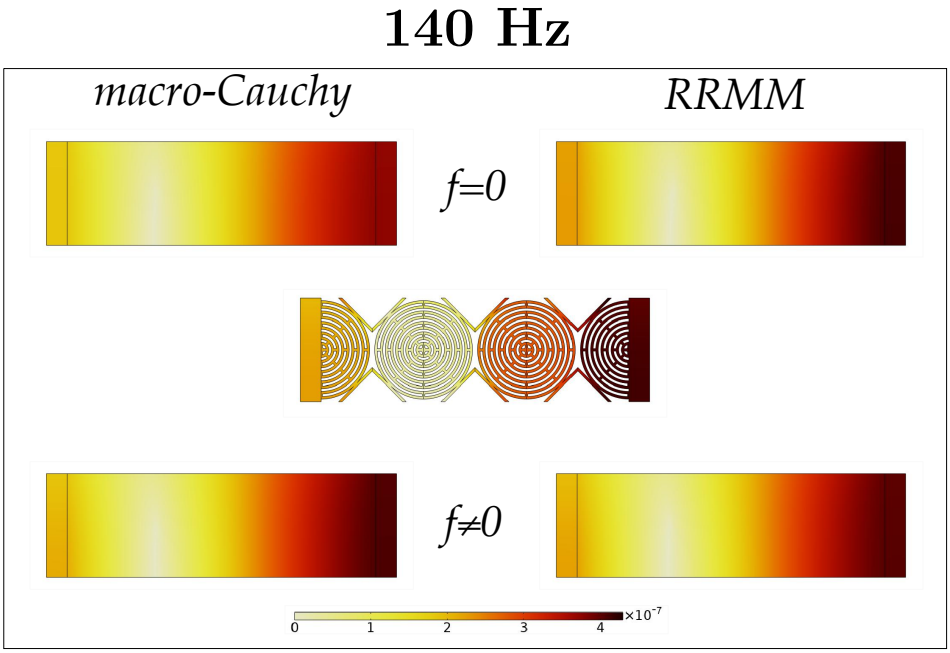

Figure 6.16: Comparison of the displacement field of the metamaterial specimen Γ with the macro-Cauchy and the RRMM when $f = 0$ and $f \neq 0$ at 140 Hz. When $f \neq 0$ for the RRMM, we have: $\alpha_{L_x} = 1$, $\beta_{L_x} = 0$, $\alpha_{L_y} = 1$, $\beta_{L_y} = -18$, $\alpha_{R_x} = 1.1$, $\beta_{R_x} = 0$, $\alpha_{R_y} = 1$ and $\beta_{R_y} = 0$, while for the macro Cauchy: $\alpha_{L_x} = 0.93$, $\beta_{L_x} = 0$, $\alpha_{L_y} = 1$, $\beta_{L_y} = -18$, $\alpha_{R_x} = 0.5$, $\beta_{R_x} = 0$, $\alpha_{R_y} = 1$ and $\beta_{R_y} = 0$.

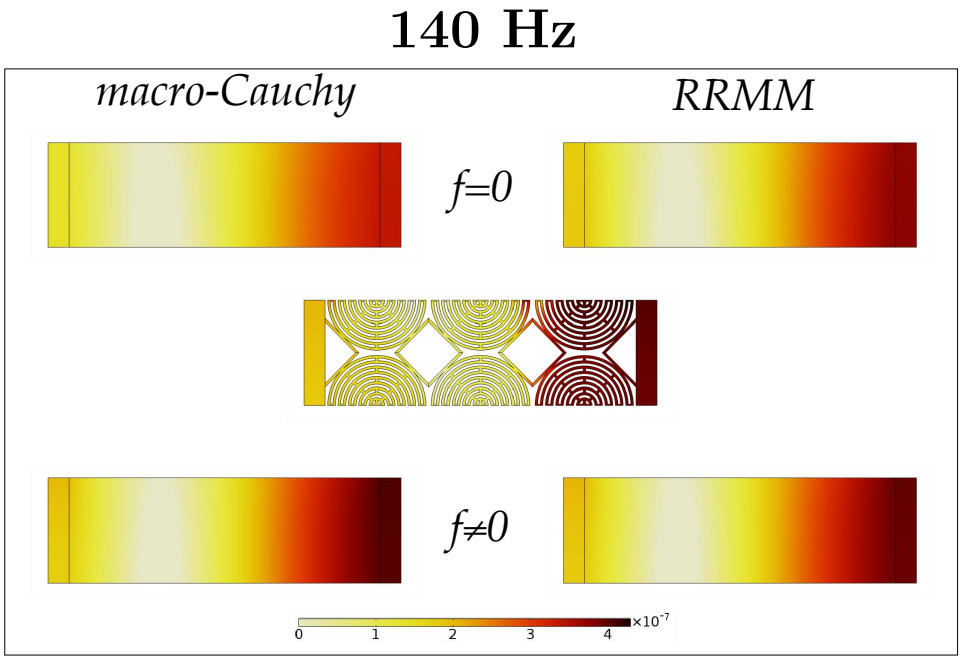

Figure 6.17: Comparison of the displacement field of the metamaterial specimen Δ with the macro-Cauchy and the RRMM when $f = 0$ and $f \neq 0$ at 140 Hz. When $f \neq 0$ for the RRMM, we have: $\alpha_{L_x} = 0.96$, $\beta_{L_x} = 0$, $\alpha_{L_y} = 1$, $\beta_{L_y} = 20$, $\alpha_{R_x} = 1.01$, $\beta_{R_x} = 0$, $\alpha_{R_y} = 1$ and $\beta_{R_y} = 5$, while for the macro Cauchy: $\alpha_{L_x} = 0.89$, $\beta_{L_x} = 0$, $\alpha_{L_y} = 1$, $\beta_{L_y} = 20$, $\alpha_{R_x} = 0.9$, $\beta_{R_x} = 0$, $\alpha_{R_y} = 1$ and $\beta_{R_y} = 5$.

Figures 6.14, 6.15, 6.16 and 6.17 show that at the frequency of 140 Hz both the RRM and the long-wavelength limit (macro-Cauchy) model can recover well the microstructured solution as far as suitable interface forces to discriminate between the 4 different cuts are calibrated. Indeed boundary effects are clearly more important here than for the frequency of 80 Hz, since the solution is very different for the 4 considered cuts, while this strong difference between the different cuts was not present at lower frequencies. It is clear that at this higher frequency the wavelength decreases to an extent that the

different connections between the Cauchy plate and the metamaterial start to macroscopically affect the travelling wave. This means that interface effects are more important than the bulk behavior at the considered frequency and specimen's size. This must be necessarily accounted for via the introduction of suitable interface forces when considering the homogenised modeling of the considered benchmark test. Completely analogous conclusions can be drawn here for the interface forces as those presented

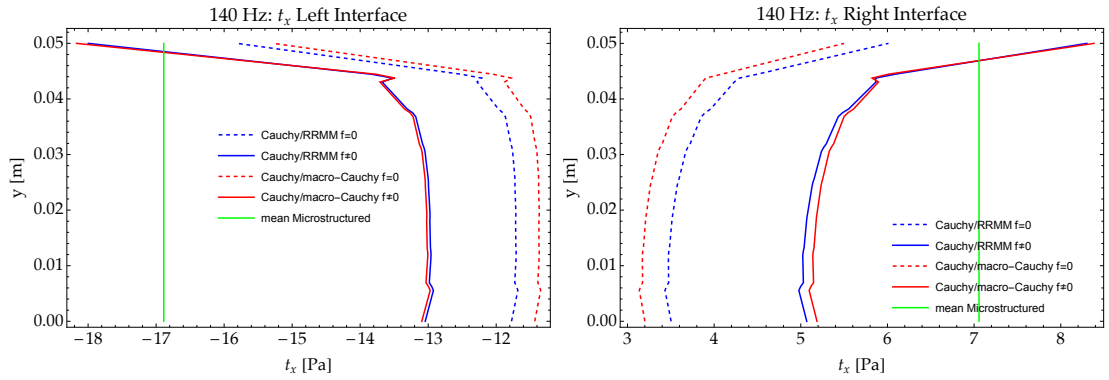

Figure 6.18: Tractions on the Cauchy side of the Cauchy plate/metamaterial interfaces (left and right) for the RRMM and for the macro-Cauchy when $f = 0$ and $f \neq 0$. The tractions shown here are those relative to "cut" B. Analogous reasoning holds true for all other "cuts".

for a frequency of 80 Hz. This means that both the RRMM and the macro-Cauchy interface forces get "closer" to the microstructured traction's average as soon as triggering interface forces. At the current frequency of 140 Hz (see Fig. 6.18)[7] the two solutions are equally good after the introduction of suitable interface forces since the dispersion is still small in this low frequency.

Frequency: 180 Hz

We continue analyzing the homogenised Cauchy and RRM simulations and the corresponding comparison to the microstructured ones for the frequency of 180 Hz. This frequency is still relatively low and but we notice dispersive behavior (see the third point in Fig. 6.7) indicating a noticeable difference between the homogenised Cauchy and RRMM.

For the frequency of 180 Hz similar considerations hold than for the lower frequencies. Since 180Hz lies in the quasi-linear domain, both the RRMM and the Cauchy model can recover the microstructured solution as soon as suitable interface forces are considered. This is related to the fact that the acoustic pressure dispersion curve is still quasi linear corresponding to this frequency. Important differences of the solution can be observed at this frequency when changing the specimen's "cut". This implies that interface forces must be introduced to recover all the cases. We note that according to Table 6.2, for this frequency, the wavelength of the pressure wave in the metamaterial is approaching the limit where it is twice the size of the metamaterial specimen. From this limit and for progressively smaller wavelengths (i.e. higher frequencies since the curve is monotonically increasing), the wave will always "see" the structure, which implies greater wave-microstructure interaction and hence more pronounced boundary effects. Fig. 6.23 shows that also in this case the Cauchy and the RRM tractions are comparable after introducing suitable interface forces.

[7] The traction comparison is again done for the case of "cut" B as is done for every other case. The reason for choosing this "cut" is that it is one of the "cuts" with the most surface area on the Cauchy plate/metamaterial interface and therefore the mean traction calculation is more meaningful.

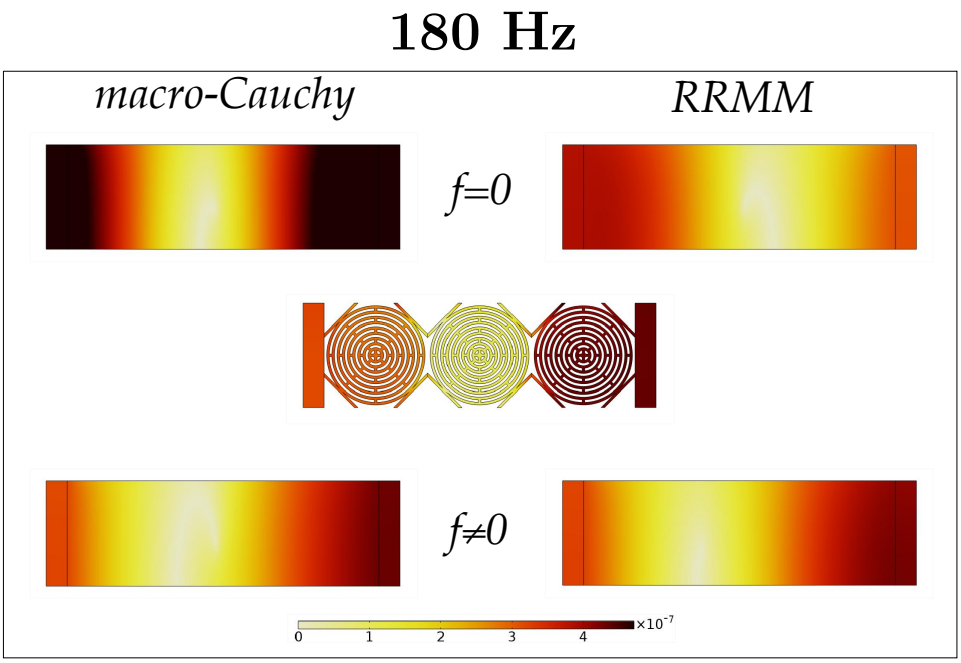

Figure 6.19: Comparison of the displacement field of the metamaterial specimen A with the macro-Cauchy and the RRMM when $f = 0$ and $f \neq 0$ at 180 Hz. When $f \neq 0$ for the RRMM, we have: $\alpha_{L_x} = 1.3$, $\beta_{L_x} = 0$, $\alpha_{L_y} = 1$, $\beta_{L_y} = 0$, $\alpha_{R_x} = 9$, $\beta_{R_x} = 0$, $\alpha_{R_y} = 1$ and $\beta_{R_y} = 0$, while for the macro Cauchy: $\alpha_{L_x} = 0.835$, $\beta_{L_x} = 0$, $\alpha_{L_y} = 1$, $\beta_{L_y} = 0$, $\alpha_{R_x} = 1$, $\beta_{R_x} = 0$, $\alpha_{R_y} = 1$ and $\beta_{R_y} = 0$.

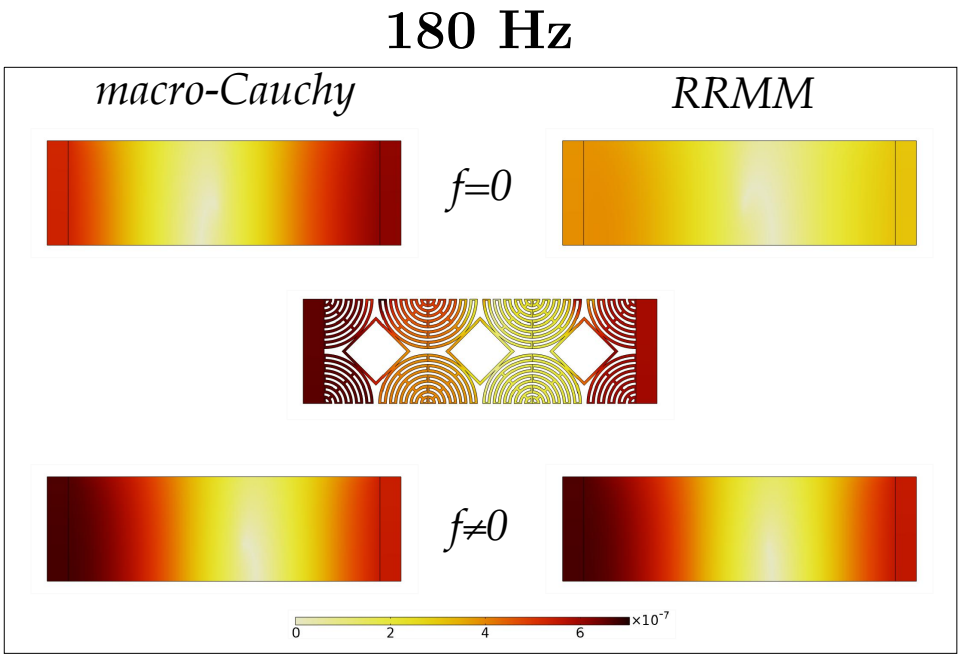

Figure 6.20: Comparison of the displacement field of the metamaterial specimen B with the macro-Cauchy and the RRMM when $f = 0$ and $f \neq 0$ at 180 Hz. When $f \neq 0$ for the RRMM, we have: $\alpha_{L_x} = 0.85$, $\beta_{L_x} = 0$, $\alpha_{L_y} = 1$, $\beta_{L_y} = 0$, $\alpha_{R_x} = 0.65$, $\beta_{R_x} = 0$, $\alpha_{R_y} = 1$ and $\beta_{R_y} = 0$, while for the macro Cauchy: $\alpha_{L_x} = 0.97$, $\beta_{L_x} = 0$, $\alpha_{L_y} = 1$, $\beta_{L_y} = 0$, $\alpha_{R_x} = 0.6$, $\beta_{R_x} = 0$, $\alpha_{R_y} = 1$ and $\beta_{R_y} = 0$.

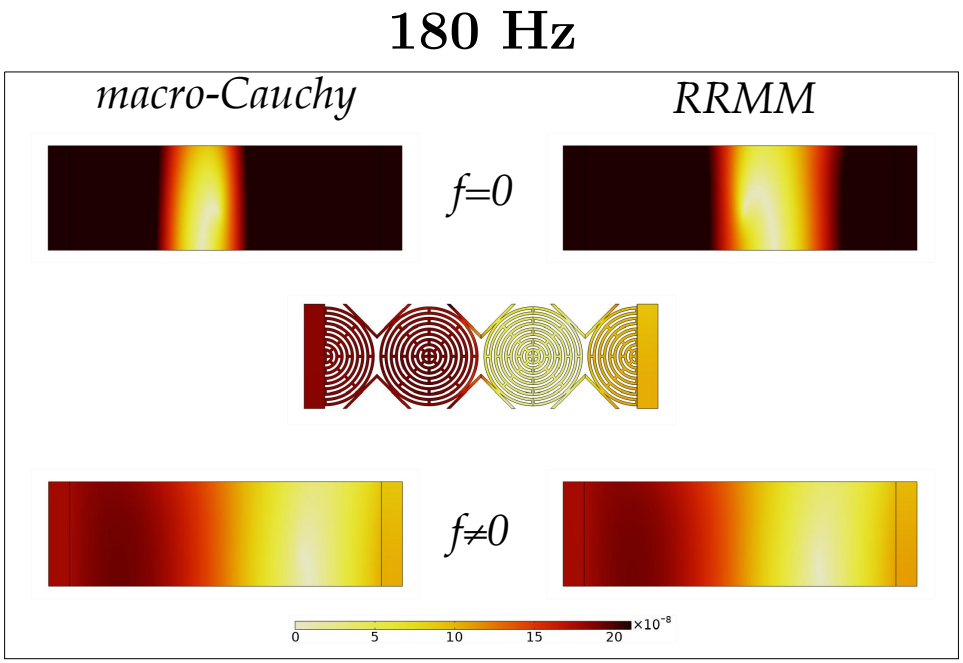

Figure 6.21: Comparison of the displacement field of the metamaterial specimen Γ with the macro-Cauchy and the RRMM when $f = 0$ and $f \neq 0$ at 180 Hz. When $f \neq 0$ for the RRMM, we have: $\alpha_{L_x} = -4.2$, $\beta_{L_x} = 0$, $\alpha_{L_y} = 1$, $\beta_{L_y} = -3$, $\alpha_{R_x} = 0.27$, $\beta_{R_x} = 0$, $\alpha_{R_y} = 1$ and $\beta_{R_y} = -8$, while for the macro Cauchy: $\alpha_{L_x} = -3.87$, $\beta_{L_x} = 0$, $\alpha_{L_y} = 1$, $\beta_{L_y} = -3$, $\alpha_{R_x} = 0.25$, $\beta_{R_x} = 0$, $\alpha_{R_y} = 1$ and $\beta_{R_y} = -8$.

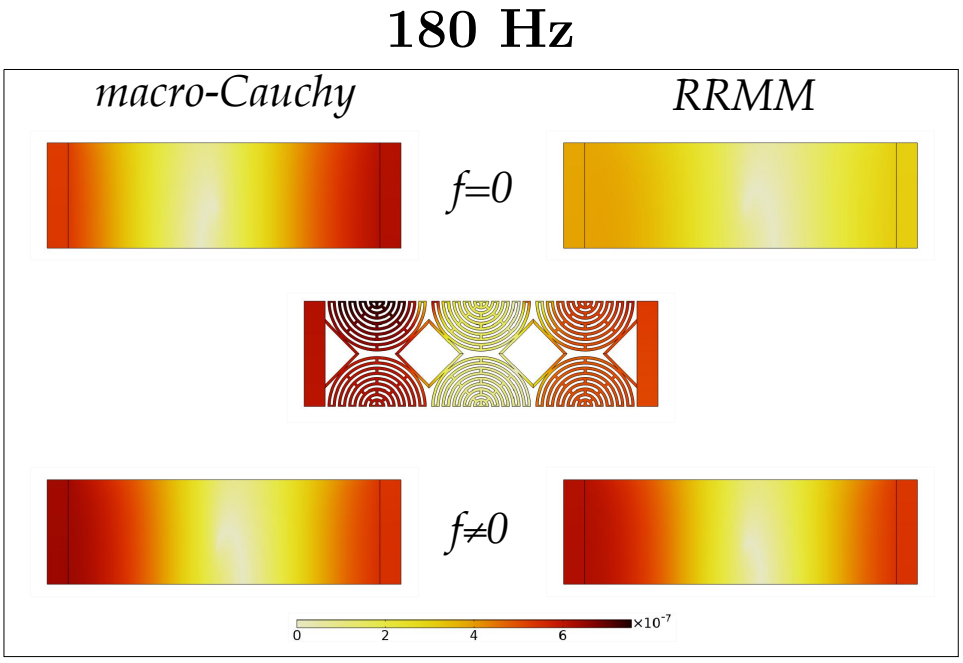

Figure 6.22: Comparison of the displacement field of the metamaterial specimen Δ with the macro-Cauchy and the RRMM when $f = 0$ and $f \neq 0$ at 180 Hz. When $f \neq 0$ for the RRMM, we have: $\alpha_{L_x} = 0.89$, $\beta_{L_x} = 0$, $\alpha_{L_y} = 1$, $\beta_{L_y} = 0$, $\alpha_{R_x} = 1$, $\beta_{R_x} = 0$, $\alpha_{R_y} = 1$ and $\beta_{R_y} = 0$, while for the macro Cauchy: $\alpha_{L_x} = 0.65$, $\beta_{L_x} = 0$, $\alpha_{L_y} = 1$, $\beta_{L_y} = 0$, $\alpha_{R_x} = 1$, $\beta_{R_x} = 0$, $\alpha_{R_y} = 1$ and $\beta_{R_y} = 0$.

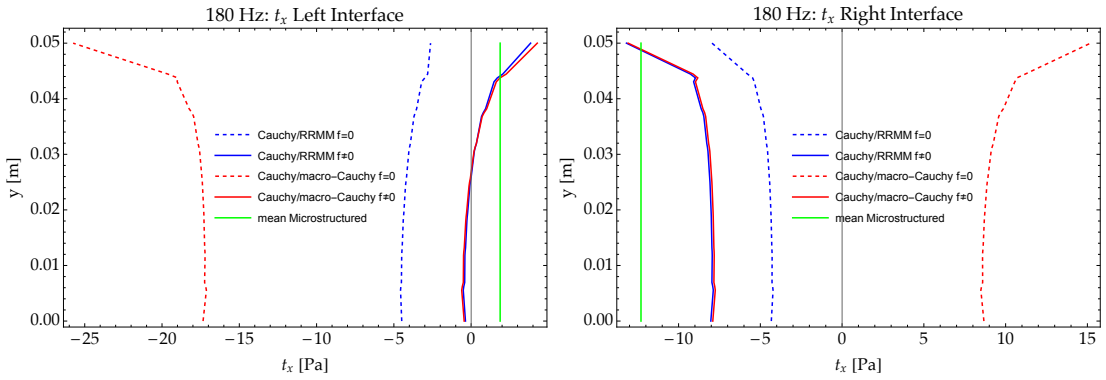

Figure 6.23: Tractions on the Cauchy side of the Cauchy plate/metamaterial interfaces (left and right) for the RRMM and for the macro-Cauchy when $f = 0$ and $f \neq 0$. The tractions shown here are those relative to "cut" B. Analogous reasoning holds true for all other "cuts".

Frequency: 420 Hz

We continue analyzing the homogenised Cauchy and RRM simulations and the corresponding comparison to the microstructured ones for the frequency of 420 Hz. This frequency shows strong dispersive behavior (see the sixth point in Fig. 6.7) and is close to the band-gap. The two missing frequencies 280 Hz and 340 Hz are discussed later in Section 6.3.5.

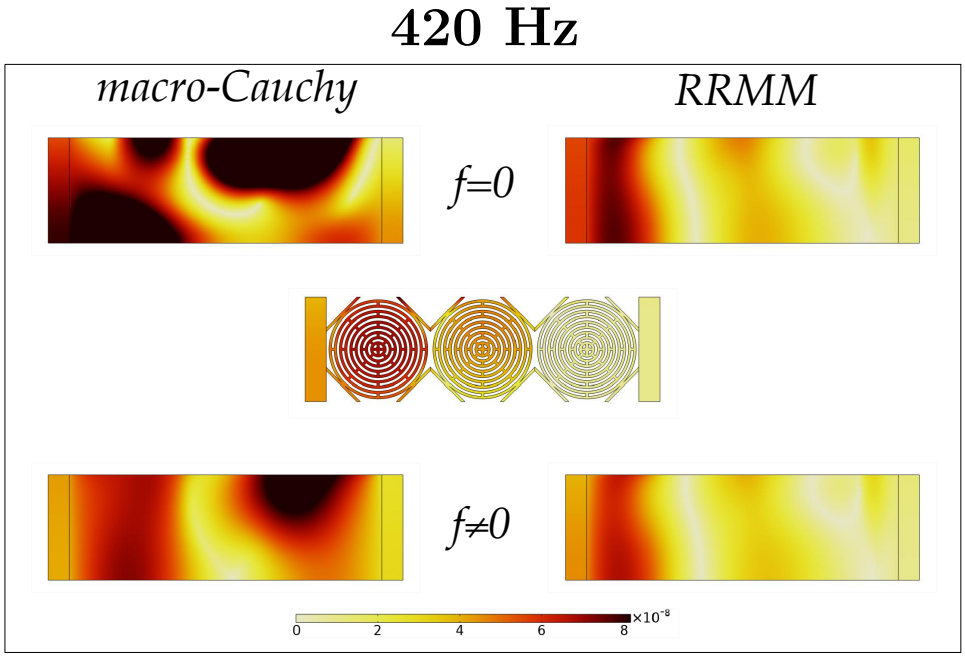

Figure 6.24: Comparison of the displacement field of the metamaterial specimen A with the macro-Cauchy and the RRMM when $f = 0$ and $f \neq 0$ at 420 Hz. When $f \neq 0$ for the RRMM, we have: $\alpha_{L_x} = 1.3$, $\beta_{L_x} = 0$, $\alpha_{L_y} = 1$, $\beta_{L_y} = 2$, $\alpha_{R_x} = 0.8$, $\beta_{R_x} = 0$, $\alpha_{R_y} = 1$ and $\beta_{R_y} = 0$, while for the macro Cauchy: $\alpha_{L_x} = 1$, $\beta_{L_x} = 0$, $\alpha_{L_y} = 1$, $\beta_{L_y} = 0$, $\alpha_{R_x} = -0.4$, $\beta_{R_x} = 0$, $\alpha_{R_y} = 1$ and $\beta_{R_y} = 0$.

For the frequency of 420 Hz the dispersion curves start showing a strong dispersive behavior (see Fig. 6.7). This implies that, while the RRMM gives good results when introducing the suitable interface forces, the long-wavelength limit Cauchy model is not able anymore to recover the correct behavior even when interface forces are triggered. The long-wavelength limit Cauchy model gives rise to unphysical responses which are due to the fact that dispersion cannot be described in the framework of Cauchy linear-elasticity.

Here, we can observe that the initial (without interface forces correction) tractions for the Cauchy model are not only quantitatively less close to the mean microstructured traction than the RRM one, but we can also start seeing a qualitative deviation of the macro-Cauchy initial traction. This is because a correct description of the bulk response becomes more and more important at higher frequencies where dispersion

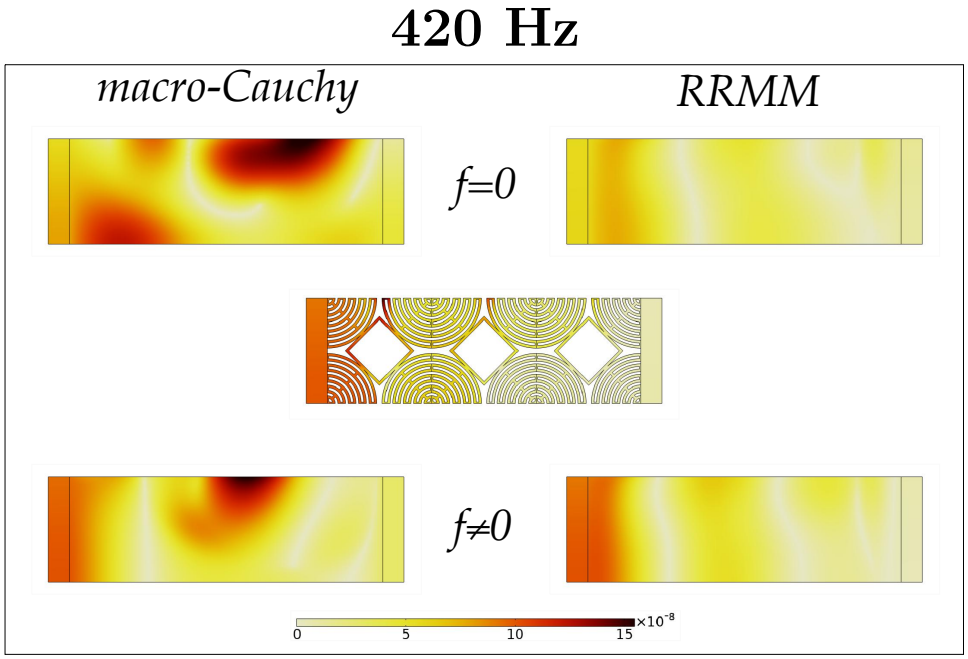

Figure 6.25: Comparison of the displacement field of the metamaterial specimen B with the macro-Cauchy and the RRMM when $f = 0$ and $f \neq 0$ at 420 Hz. When $f \neq 0$ for the RRMM, we have: $\alpha_{L_x} = 0.5$, $\beta_{L_x} = 0$, $\alpha_{L_y} = 1$, $\beta_{L_y} = 5$, $\alpha_{R_x} = 1.1$, $\beta_{R_x} = 0$, $\alpha_{R_y} = 1$ and $\beta_{R_y} = -5$, while for the macro Cauchy: $\alpha_{L_x} = -1$, $\beta_{L_x} = 0$, $\alpha_{L_y} = 1$, $\beta_{L_y} = 0$, $\alpha_{R_x} = 0.3$, $\beta_{R_x} = 0$, $\alpha_{R_y} = 1$ and $\beta_{R_y} = 0$.

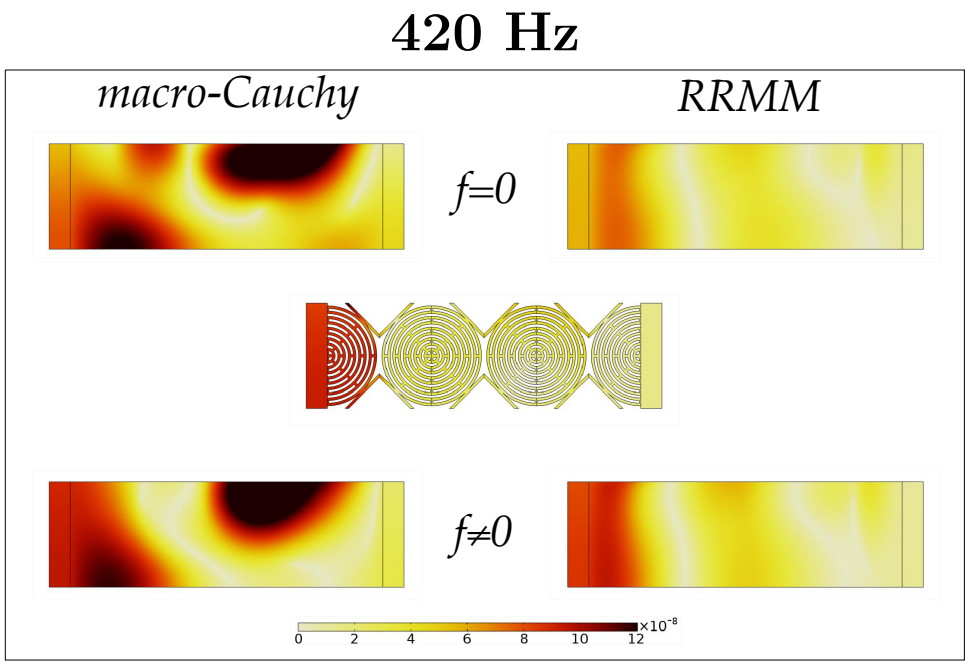

Figure 6.26: Comparison of the displacement field of the metamaterial specimen Γ with the macro-Cauchy and the RRMM when $f = 0$ and $f \neq 0$ at 420 Hz. When $f \neq 0$ for the RRMM, we have: $\alpha_{L_x} = 0.6$, $\beta_{L_x} = 0$, $\alpha_{L_y} = 1$, $\beta_{L_y} = 2$, $\alpha_{R_x} = 1.4$, $\beta_{R_x} = 0$, $\alpha_{R_y} = 1$ and $\beta_{R_y} = -5$, while for the macro Cauchy: $\alpha_{L_x} = 0.5$, $\beta_{L_x} = 0$, $\alpha_{L_y} = 1$, $\beta_{L_y} = 0$, $\alpha_{R_x} = 0.3$, $\beta_{R_x} = 0$, $\alpha_{R_y} = 1$ and $\beta_{R_y} = 0$.

becomes higher. Moreover, we can see that while the corrected RRM and macro-Cauchy tractions with interface forces are comparable on the left interface, the RRM one is by far better on the right interface. We thus see how the RRM response starts having better performances as soon as frequency increases. We note that according to Table 6.2, the wavelength is already smaller than twice the size of the structure and therefore comparable to the size of the unit cell. Nevertheless, the RRMM is still able to recover a good solution as soon as considering suitable interface forces.

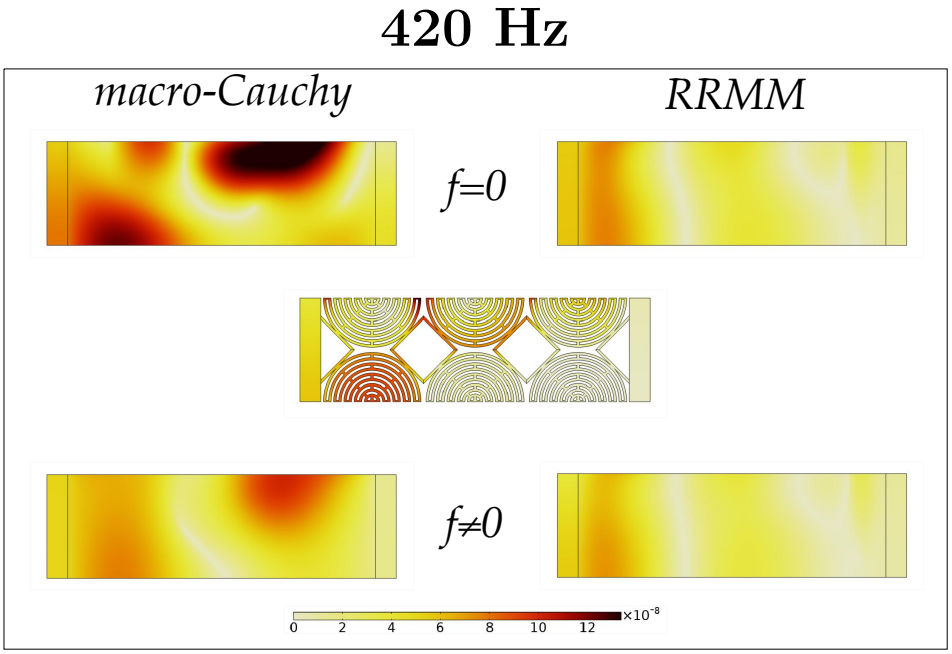

Figure 6.27: Comparison of the displacement field of the metamaterial specimen Δ with the macro-Cauchy and the RRMM when $f = 0$ and $f \neq 0$ at 420 Hz. When $f \neq 0$ for the RRMM, we have: $\alpha_{L_x} = 1.2$, $\beta_{L_x} = 0$, $\alpha_{L_y} = 1$, $\beta_{L_y} = 10$, $\alpha_{R_x} = 0.8$, $\beta_{R_x} = 0$, $\alpha_{R_y} = 1$ and $\beta_{R_y} = 0$, while for the macro Cauchy: $\alpha_{L_x} = 1$, $\beta_{L_x} = 0$, $\alpha_{L_y} = 1$, $\beta_{L_y} = 0$, $\alpha_{R_x} = -0.2$, $\beta_{R_x} = 0$, $\alpha_{R_y} = 1$ and $\beta_{R_y} = 0$.

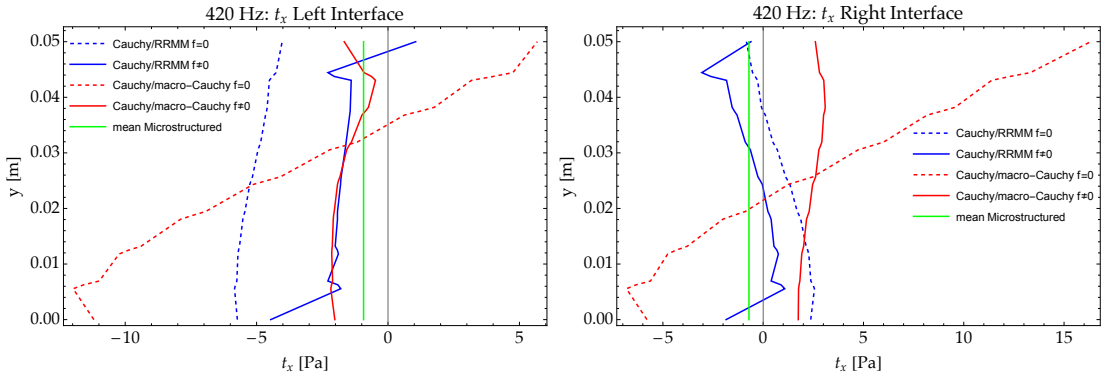

Figure 6.28: Tractions on the Cauchy side of the Cauchy plate/metamaterial interfaces (left and right) for the RRMM and for the macro-Cauchy when $f = 0$ and $f \neq 0$. The tractions shown here are those relative to "cut" B. Analogous reasoning holds true for all other "cuts".

Frequency: 460 Hz

We continue analyzing the homogenised Cauchy and RRM simulations and the corresponding comparison to the microstructured ones for the frequency of 460 Hz. This frequency shows strong dispersive behavior (see the seventh point in Fig. 6.7) and is directly below the band-gap. For the frequency of 460 Hz considerations analogous to the frequency of 420 Hz hold.

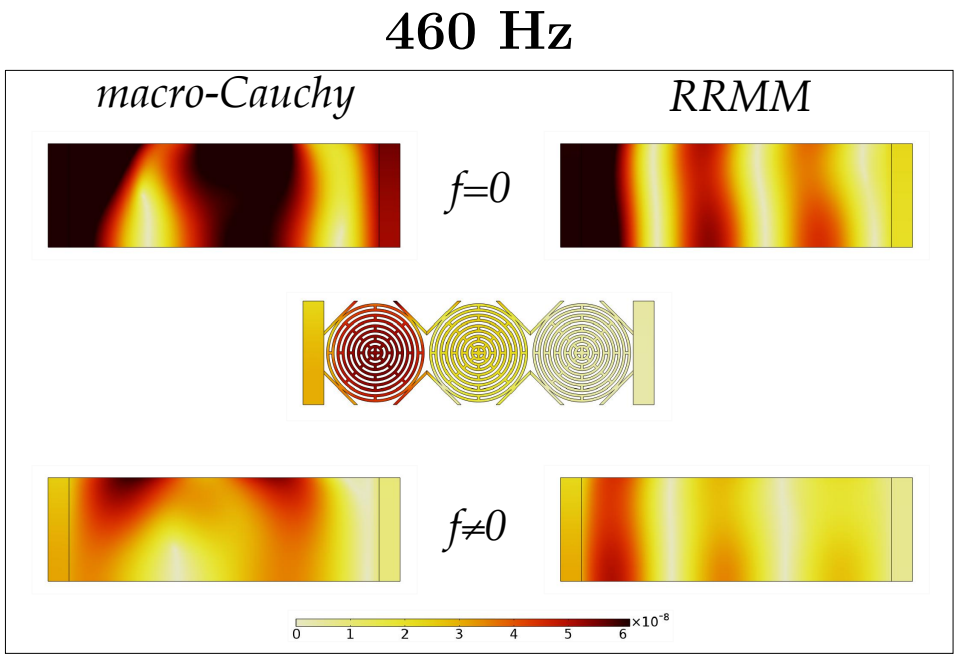

Figure 6.29: Comparison of the displacement field of the metamaterial specimen A with the macro-Cauchy and the RRMM when $f = 0$ and $f \neq 0$ at 460 Hz. When $f \neq 0$ for the RRMM, we have: $\alpha_{L_x} = 2$, $\beta_{L_x} = 0$, $\alpha_{L_y} = 1$, $\beta_{L_y} = 4$, $\alpha_{R_x} = -0.4$, $\beta_{R_x} = 0$, $\alpha_{R_y} = 1$ and $\beta_{R_y} = 0$, while for the macro Cauchy: $\alpha_{L_x} = 1.9$, $\beta_{L_x} = 0$, $\alpha_{L_y} = 1$, $\beta_{L_y} = 10$, $\alpha_{R_x} = 0.2$, $\beta_{R_x} = 0$, $\alpha_{R_y} = 1$ and $\beta_{R_y} = 0$.

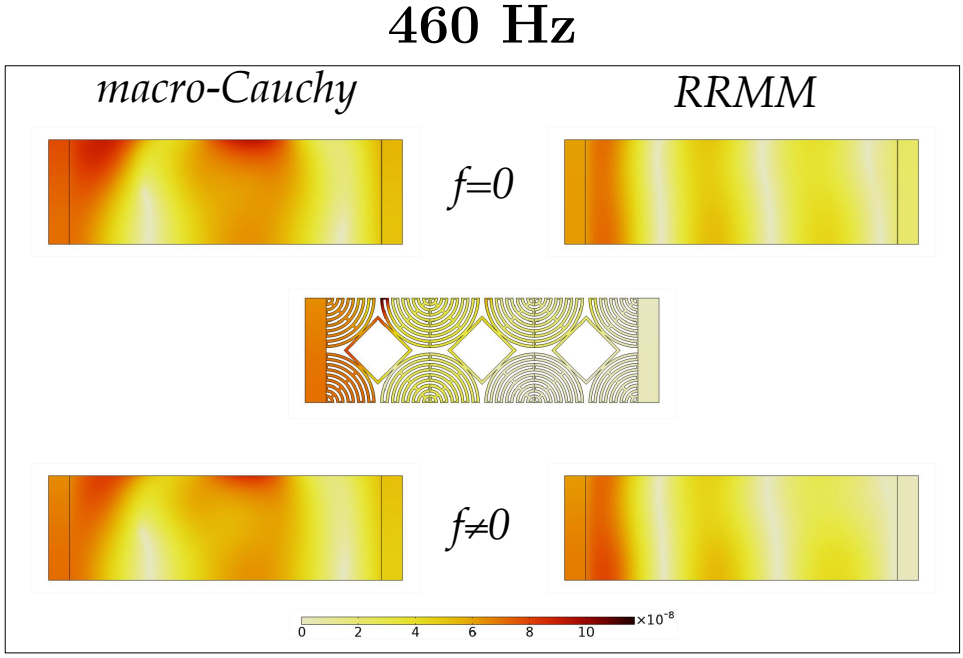

Figure 6.30: Comparison of the displacement field of the metamaterial specimen B with the macro-Cauchy and the RRMM when $f = 0$ and $f \neq 0$ at 460 Hz. When $f \neq 0$ for the RRMM, we have: $\alpha_{L_x} = 0.8$, $\beta_{L_x} = 0$, $\alpha_{L_y} = 1$, $\beta_{L_y} = 3$, $\alpha_{R_x} = 0.1$, $\beta_{R_x} = 0$, $\alpha_{R_y} = 1$ and $\beta_{R_y} = 0$, while for the macro Cauchy: $\alpha_{L_x} = 1.2$, $\beta_{L_x} = 0$, $\alpha_{L_y} = 1$, $\beta_{L_y} = 10$, $\alpha_{R_x} = 1$, $\beta_{R_x} = 0$, $\alpha_{R_y} = 1$ and $\beta_{R_y} = 0$.

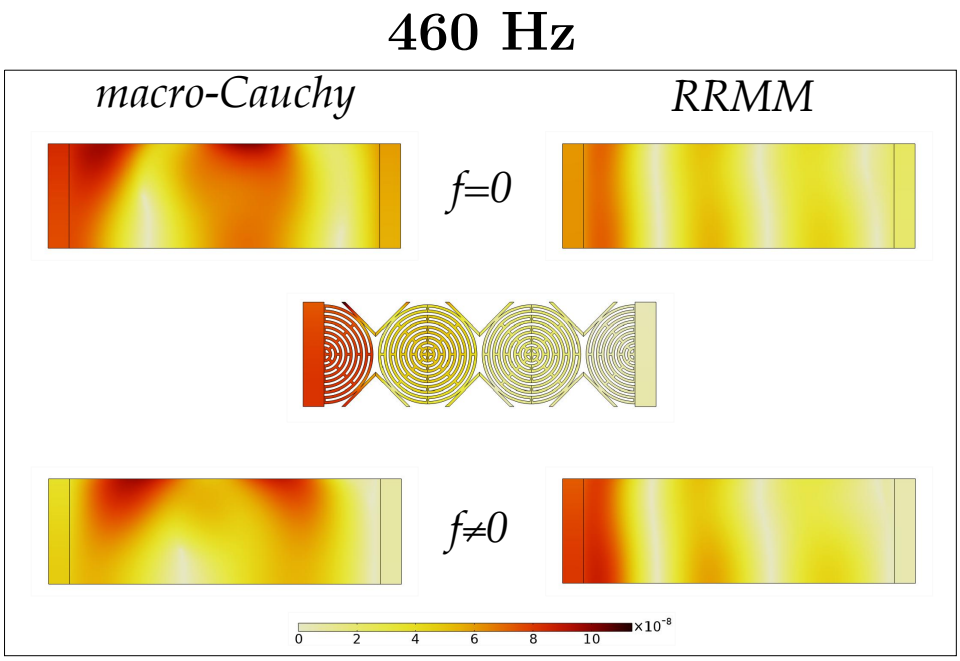

Figure 6.31: Comparison of the displacement field of the metamaterial specimen Γ with the macro-Cauchy and the RRMM when $f = 0$ and $f \neq 0$ at 460 Hz. When $f \neq 0$ for the RRMM, we have: $\alpha_{L_x} = 0.55$, $\beta_{L_x} = 0$, $\alpha_{L_y} = 1$, $\beta_{L_y} = 4$, $\alpha_{R_x} = 0.2$, $\beta_{R_x} = 0$, $\alpha_{R_y} = 1$ and $\beta_{R_y} = 0$, while for the macro Cauchy: $\alpha_{L_x} = 1.1$, $\beta_{L_x} = 0$, $\alpha_{L_y} = 1$, $\beta_{L_y} = 10$, $\alpha_{R_x} = 1$, $\beta_{R_x} = 0$, $\alpha_{R_y} = 1$ and $\beta_{R_y} = 0$.

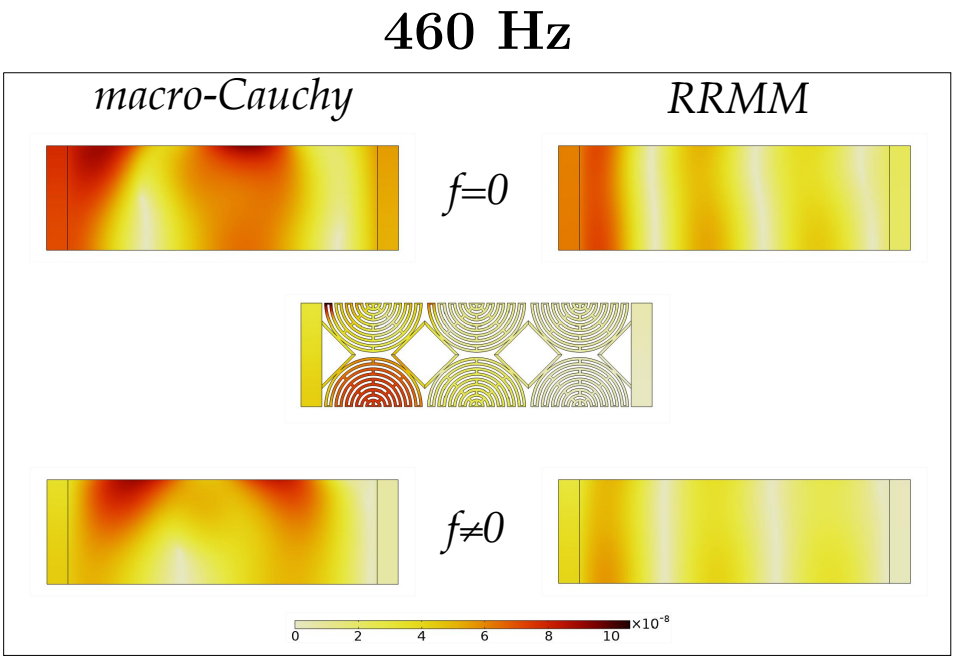

Figure 6.32: Comparison of the displacement field of the metamaterial specimen Δ with the macro-Cauchy and the RRMM when $f = 0$ and $f \neq 0$ at 460 Hz. When $f \neq 0$ for the RRMM, we have: $\alpha_{L_x} = 1.7$, $\beta_{L_x} = 0$, $\alpha_{L_y} = 1$, $\beta_{L_y} = 6$, $\alpha_{R_x} = 0.1$, $\beta_{R_x} = 0$, $\alpha_{R_y} = 1$ and $\beta_{R_y} = 0$, while for the macro Cauchy: $\alpha_{L_x} = 1$, $\beta_{L_x} = 0$, $\alpha_{L_y} = 1$, $\beta_{L_y} = 10$, $\alpha_{R_x} = 0.1$, $\beta_{R_x} = 0$, $\alpha_{R_y} = 1$ and $\beta_{R_y} = -8$.

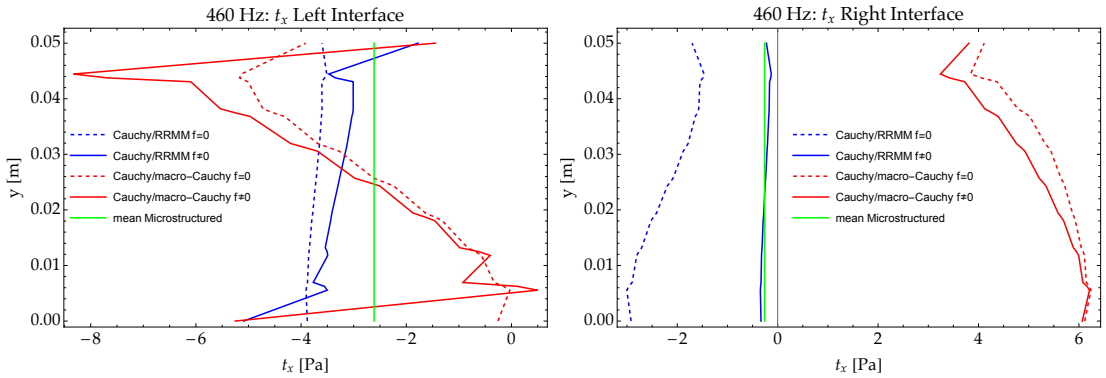

Figure 6.33: Tractions on the Cauchy side of the Cauchy plate/metamaterial interfaces (left and right) for the RRMM and for the macro-Cauchy when $f = 0$ and $f \neq 0$. The tractions shown here are those relative to "cut" B. Analogous reasoning holds true for all other "cuts".

At the present frequency it becomes more and more evident how the RRMM outperforms with respect to the macro-Cauchy as soon as suitable interface forces are introduced. All the considerations done for the frequency of 420 Hz also apply here. The wavelength associated to the present frequency is closer to the size of the unit cell than the previous case.

Frequency: 700 Hz

We continue analyzing the homogenised Cauchy and RRM simulations and the corresponding comparison to the microstructured ones for the frequency of 700 Hz. This frequency is in the lower part of the band-gap (see the eighth point in Fig. 6.7).

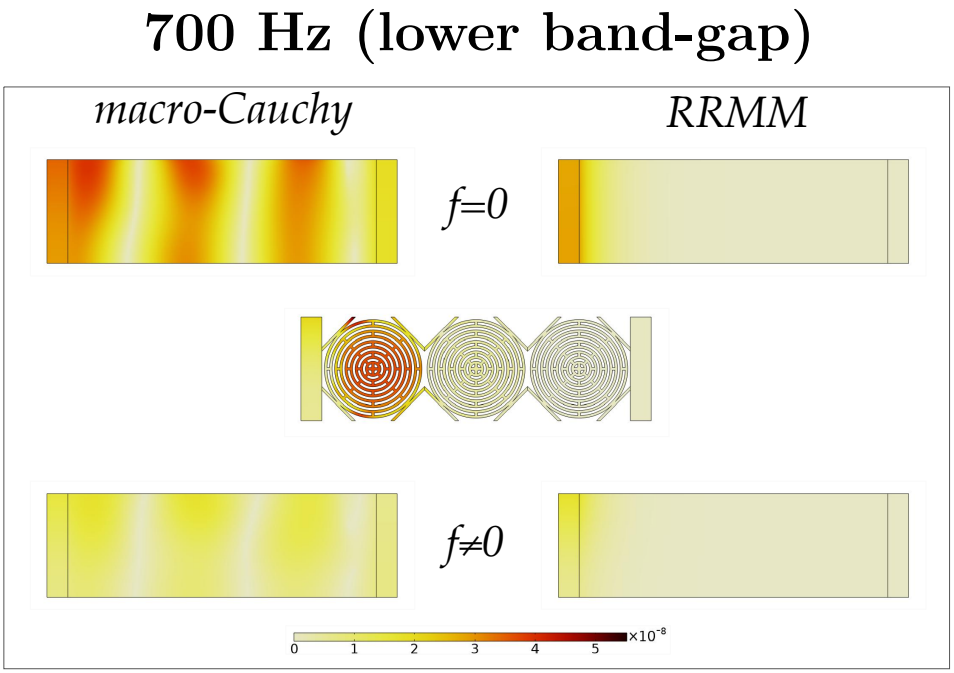

Figure 6.34: Comparison of the displacement field of the metamaterial specimen A with the macro-Cauchy and the RRMM when $f = 0$ and $f \neq 0$ at 700 Hz. When $f \neq 0$ for the RRMM, we have: $\alpha_{L_x} = 6$, $\beta_{L_x} = 0$, $\alpha_{L_y} = 1$, $\beta_{L_y} = 5$, $\alpha_{R_x} = 1$, $\beta_{R_x} = 0$, $\alpha_{R_y} = 1$ and $\beta_{R_y} = 0$, while for the macro Cauchy: $\alpha_{L_x} = 5$, $\beta_{L_x} = 0$, $\alpha_{L_y} = 1$, $\beta_{L_y} = 0$, $\alpha_{R_x} = 1$, $\beta_{R_x} = 0$, $\alpha_{R_y} = 1$ and $\beta_{R_y} = 0$.

The frequency of 700 Hz is located in the band-gap region of the considered metamaterial. In this case boundary effects are limited to the interface close to the surface where the external load is applied (left interface). Since wave propagation is not allowed through the metamaterial's bulk, the deformation is concentrated at the level of the first unit cell. Depending on the unit cell's "cut", the solution is quite different and macroscopic bending of the left Cauchy plate can occur as a consequence of a heterogeneous

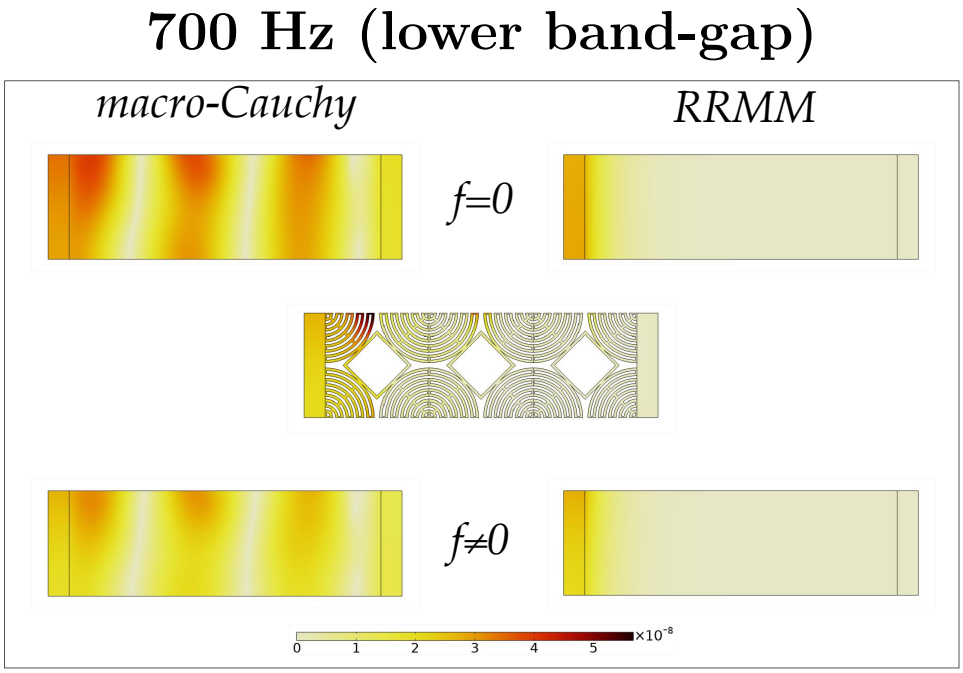

Figure 6.35: Comparison of the displacement field of the metamaterial specimen B with the macro-Cauchy and the RRMM when $f = 0$ and $f \neq 0$ at 700 Hz. When $f \neq 0$ for the RRMM, we have: $\alpha_{L_x} = 1.6$, $\beta_{L_x} = 0$, $\alpha_{L_y} = 1$, $\beta_{L_y} = -2$, $\alpha_{R_x} = 1$, $\beta_{R_x} = 0$, $\alpha_{R_y} = 1$ and $\beta_{R_y} = 0$, while for the macro Cauchy: $\alpha_{L_x} = 2$, $\beta_{L_x} = 0$, $\alpha_{L_y} = 1$, $\beta_{L_y} = 1$, $\alpha_{R_x} = 1$, $\beta_{R_x} = 0$, $\alpha_{R_y} = 1$ and $\beta_{R_y} = 0$.

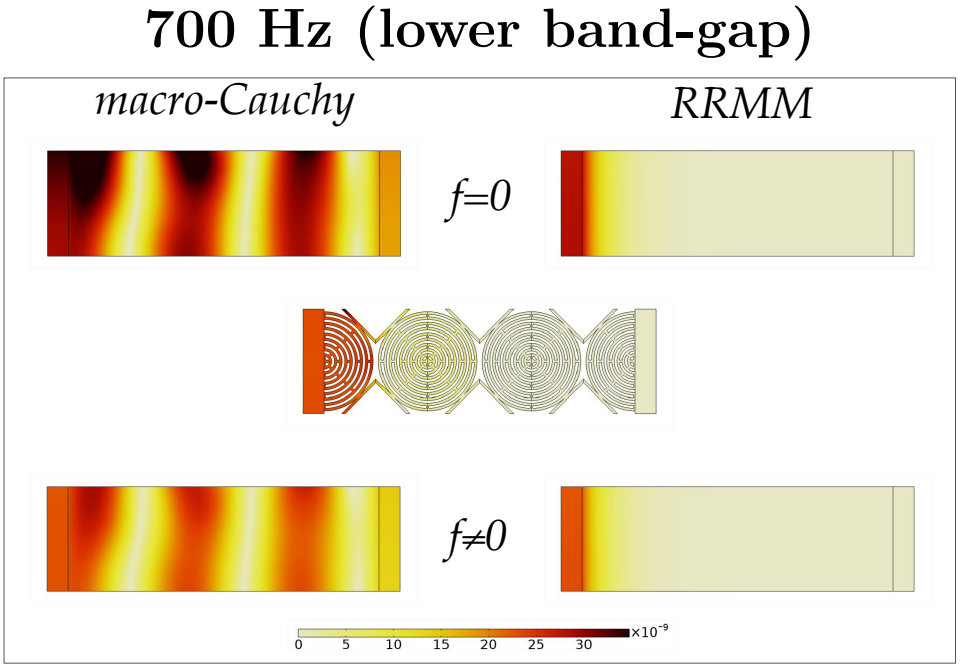

Figure 6.36: Comparison of the displacement field of the metamaterial specimen Γ with the macro-Cauchy and the RRMM when $f = 0$ and $f \neq 0$ at 700 Hz. When $f \neq 0$ for the RRMM, we have: $\alpha_{L_x} = 1.7$, $\beta_{L_x} = 0$, $\alpha_{L_y} = 1$, $\beta_{L_y} = 0$, $\alpha_{R_x} = 1$, $\beta_{R_x} = 0$, $\alpha_{R_y} = 1$ and $\beta_{R_y} = 0$, while for the macro Cauchy: $\alpha_{L_x} = 2$, $\beta_{L_x} = 0$, $\alpha_{L_y} = 1$, $\beta_{L_y} = 5$, $\alpha_{R_x} = 1$, $\beta_{R_x} = 0$, $\alpha_{R_y} = 1$ and $\beta_{R_y} = 0$.

micro-deformation field of the unit cells belonging to the first cell's layer close to the left interface. The RRMM can correctly describe the band-gap behavior of the considered specimen for all 4 "cuts", as soon as suitable interface forces are introduced.

On the other hand the long-wavelength limit Cauchy model fails to recover the correct solution also when triggering interface forces. This is due to the fact that Cauchy models are not able to describe band-gap

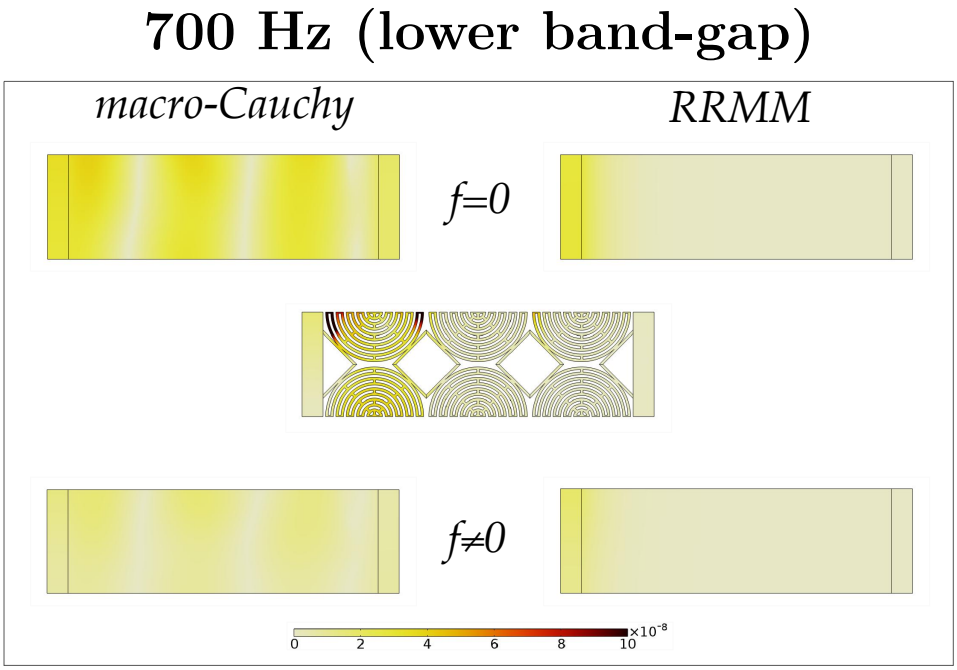

Figure 6.37: Comparison of the displacement field of the metamaterial specimen Δ with the macro-Cauchy and the RRMM when $f = 0$ and $f \neq 0$ at 700 Hz. When $f \neq 0$ for the RRMM, we have: $\alpha_{L_x} = 4$, $\beta_{L_x} = 0$, $\alpha_{L_y} = 1$, $\beta_{L_y} = 2$, $\alpha_{R_x} = 1$, $\beta_{R_x} = 0$, $\alpha_{R_y} = 1$ and $\beta_{R_y} = 0$, while for the macro Cauchy: $\alpha_{L_x} = 5.5$, $\beta_{L_x} = 0$, $\alpha_{L_y} = 1$, $\beta_{L_y} = 0$, $\alpha_{R_x} = 1$, $\beta_{R_x} = 0$, $\alpha_{R_y} = 1$ and $\beta_{R_y} = 0$.

behaviors.

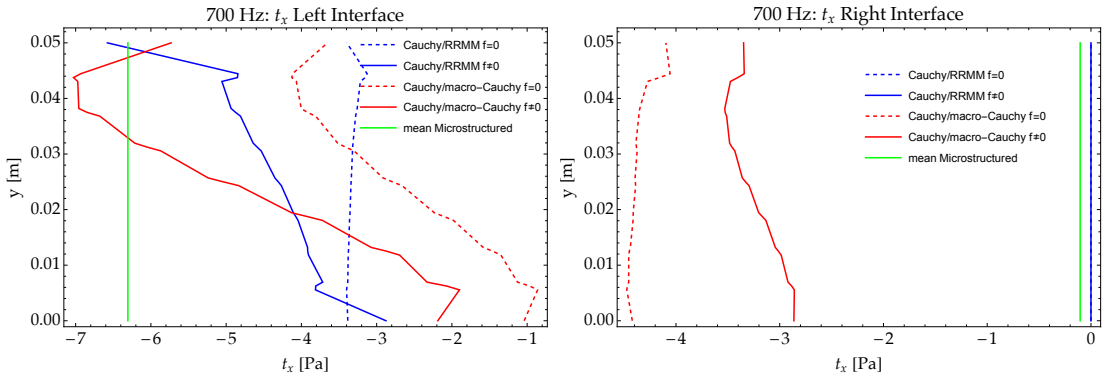

Figure 6.38: Tractions on the Cauchy side of the Cauchy plate/metamaterial interfaces (left and right) for the RRMM and for the macro-Cauchy when $f = 0$ and $f \neq 0$. The tractions shown here are those relative to "cut" B. Analogous reasoning holds true for all other "cuts".

Frequency: 1100 Hz

We continue analyzing the homogenised Cauchy and RRM simulations and the corresponding comparison to the microstructured ones for the frequency of 1100 Hz. This frequency is in the middle of the band-gap (see the ninth point in Fig. 6.7). Considerations similar to the frequency of 700 Hz hold for the present frequency of 1100 Hz.

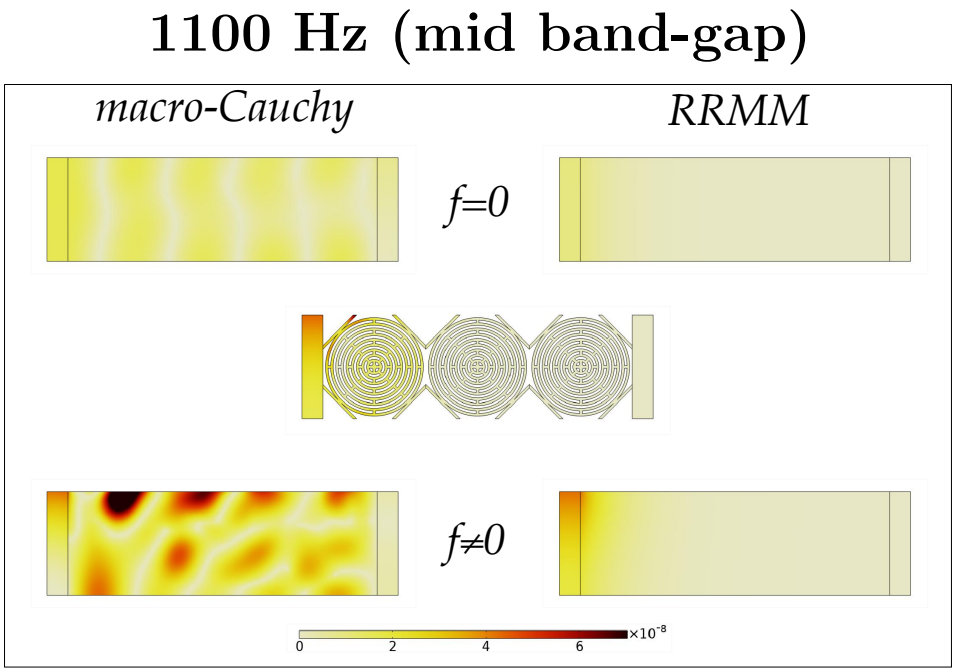

Figure 6.39: Comparison of the displacement field of the metamaterial specimen A with the macro-Cauchy and the RRMM when $f = 0$ and $f \neq 0$ at 1100 Hz. When $f \neq 0$ for the RRMM, we have: $\alpha_{L_x} = -0.5$, $\beta_{L_x} = 0$, $\alpha_{L_y} = 1$, $\beta_{L_y} = -7$, $\alpha_{R_x} = 1$, $\beta_{R_x} = 0$, $\alpha_{R_y} = 1$ and $\beta_{R_y} = 0$, while for the macro Cauchy: $\alpha_{L_x} = 1$, $\beta_{L_x} = 0$, $\alpha_{L_y} = 1$, $\beta_{L_y} = -50$, $\alpha_{R_x} = 1$, $\beta_{R_x} = 0$, $\alpha_{R_y} = 1$ and $\beta_{R_y} = 0$.

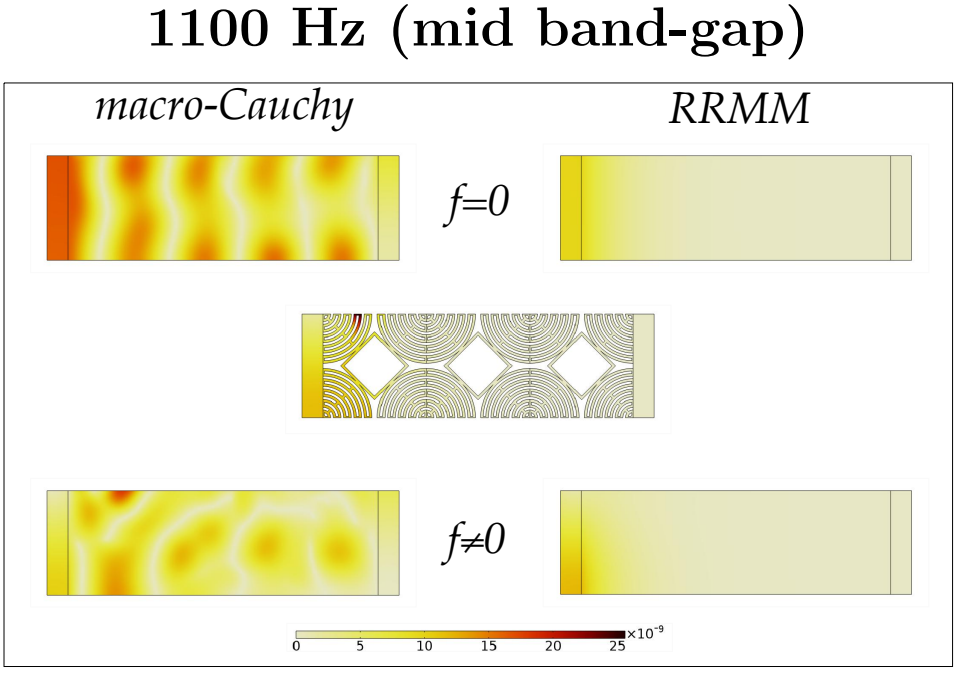

Figure 6.40: Comparison of the displacement field of the metamaterial specimen B with the macro-Cauchy and the RRMM when $f = 0$ and $f \neq 0$ at 1100 Hz. When $f \neq 0$ for the RRMM, we have: $\alpha_{L_x} = 1.5$, $\beta_{L_x} = 0$, $\alpha_{L_y} = 1$, $\beta_{L_y} = -8$, $\alpha_{R_x} = 1$, $\beta_{R_x} = 0$, $\alpha_{R_y} = 1$ and $\beta_{R_y} = 0$, while for the macro Cauchy: $\alpha_{L_x} = 1$, $\beta_{L_x} = 6$, $\alpha_{L_y} = 1$, $\beta_{L_y} = 12$, $\alpha_{R_x} = 1$, $\beta_{R_x} = 0$, $\alpha_{R_y} = 1$ and $\beta_{R_y} = 0$.

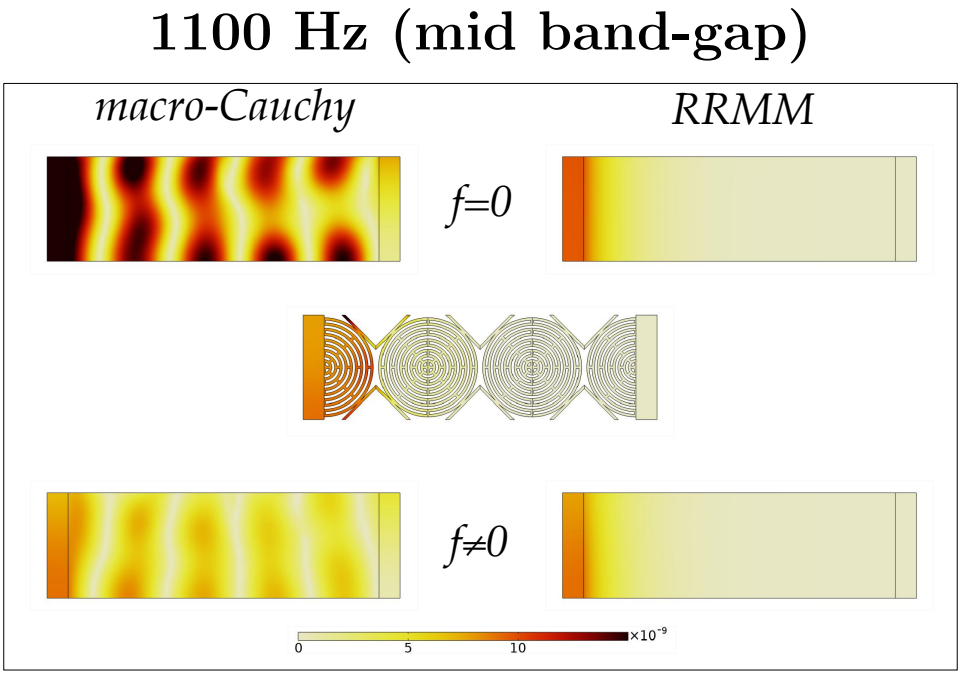

Figure 6.41: Comparison of the displacement field of the metamaterial specimen Γ with the macro-Cauchy and the RRMM when $f = 0$ and $f \neq 0$ at 1100 Hz. When $f \neq 0$ for the RRMM, we have: $\alpha_{L_x} = 1.3$, $\beta_{L_x} = 0$, $\alpha_{L_y} = 1$, $\beta_{L_y} = -1$, $\alpha_{R_x} = 1$, $\beta_{R_x} = 0$, $\alpha_{R_y} = 1$ and $\beta_{R_y} = 0$, while for the macro Cauchy: $\alpha_{L_x} = 1$, $\beta_{L_x} = 5$, $\alpha_{L_y} = 1$, $\beta_{L_y} = 3$, $\alpha_{R_x} = 1$, $\beta_{R_x} = 0$, $\alpha_{R_y} = 1$ and $\beta_{R_y} = 0$.

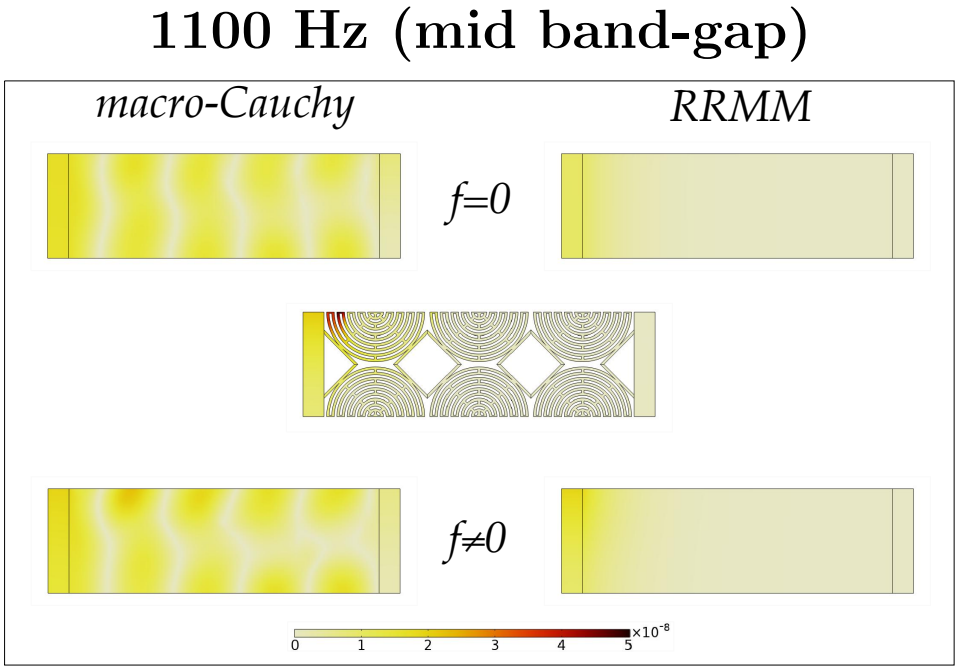

Figure 6.42: Comparison of the displacement field of the metamaterial specimen Δ with the macro-Cauchy and the RRMM when $f = 0$ and $f \neq 0$ at 1100 Hz. When $f \neq 0$ for the RRMM, we have: $\alpha_{L_x} = 0.4$, $\beta_{L_x} = 0$, $\alpha_{L_y} = 1$, $\beta_{L_y} = 2$, $\alpha_{R_x} = 1$, $\beta_{R_x} = 0$, $\alpha_{R_y} = 1$ and $\beta_{R_y} = 0$, while for the macro Cauchy: $\alpha_{L_x} = 1$, $\beta_{L_x} = 0$, $\alpha_{L_y} = 1$, $\beta_{L_y} = -5$, $\alpha_{R_x} = 1$, $\beta_{R_x} = 0$, $\alpha_{R_y} = 1$ and $\beta_{R_y} = 0$.

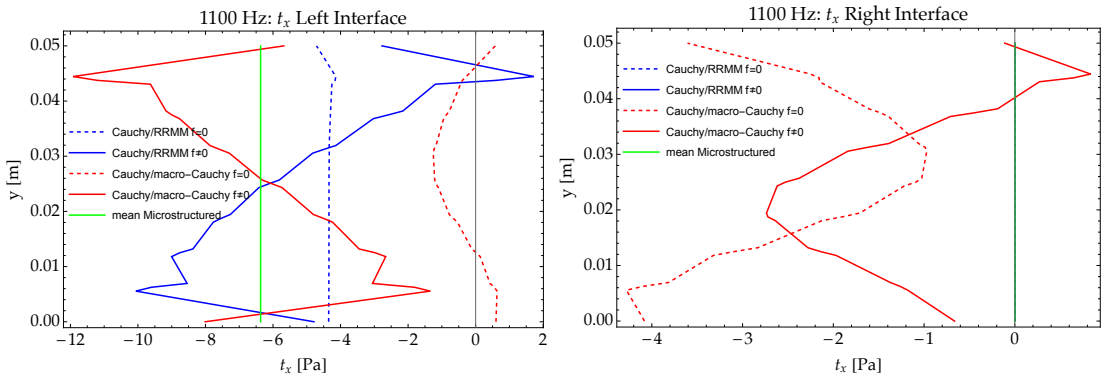

Figure 6.43: Tractions on the Cauchy side of the Cauchy plate/metamaterial interfaces (left and right) for the RRMM and for the macro-Cauchy when $f = 0$ and $f \neq 0$. The tractions shown here are those relative to "cut" B. Analogous reasoning holds true for all other "cuts".

Frequency: 1500 Hz

We continue analyzing the homogenised Cauchy and RRM simulations and the corresponding comparison to the microstructured ones for the frequency of 1500 Hz. This frequency is in the upper limit of the band-gap (see the tenth point in Fig. 6.7).

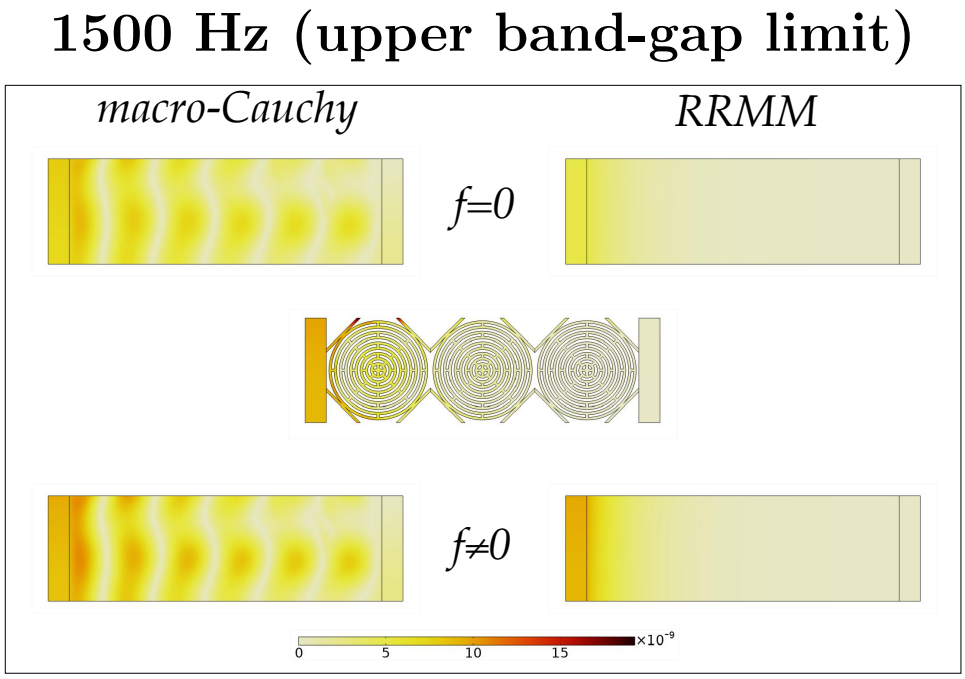

Figure 6.44: Comparison of the displacement field of the metamaterial specimen A with the macro-Cauchy and the RRMM when $f = 0$ and $f \neq 0$ at 1500 Hz. When $f \neq 0$ for the RRMM, we have: $\alpha_{L_x} = -0.01$, $\beta_{L_x} = 0$, $\alpha_{L_y} = 1$, $\beta_{L_y} = 0.5$, $\alpha_{R_x} = 1$, $\beta_{R_x} = 0$, $\alpha_{R_y} = 1$ and $\beta_{R_y} = 0$, while for the macro Cauchy: $\alpha_{L_x} = 1$, $\beta_{L_x} = -2$, $\alpha_{L_y} = 1$, $\beta_{L_y} = 0$, $\alpha_{R_x} = 1$, $\beta_{R_x} = 0$, $\alpha_{R_y} = 1$ and $\beta_{R_y} = 0$.

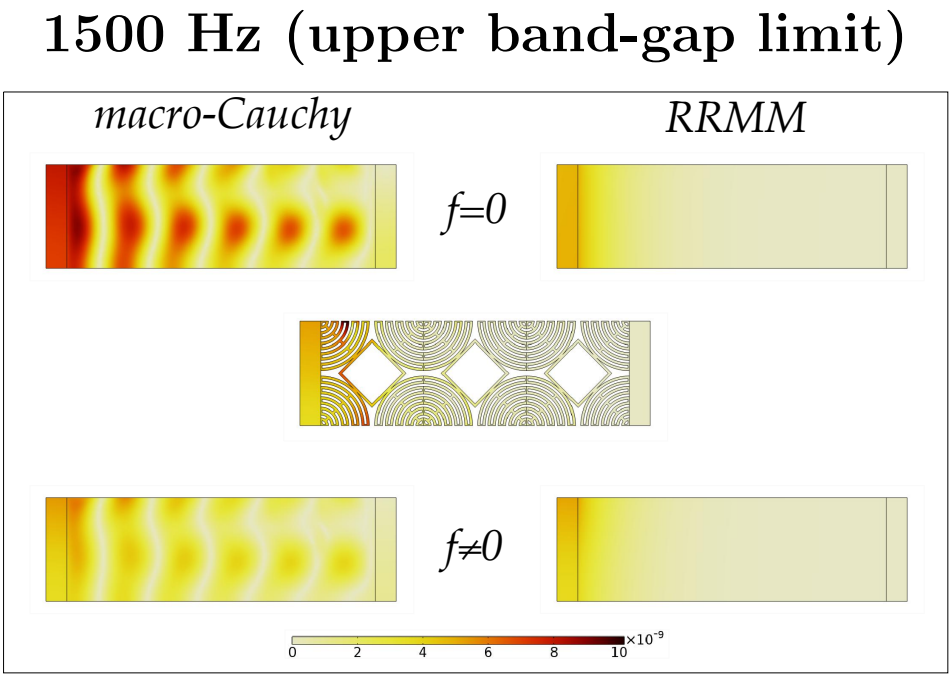

Figure 6.45: Comparison of the displacement field of the metamaterial specimen B with the macro-Cauchy and the RRMM when $f = 0$ and $f \neq 0$ at 1500 Hz. When $f \neq 0$ for the RRMM, we have: $\alpha_{L_x} = 1.3$, $\beta_{L_x} = 0$, $\alpha_{L_y} = 1$, $\beta_{L_y} = 3$, $\alpha_{R_x} = 1$, $\beta_{R_x} = 0$, $\alpha_{R_y} = 1$ and $\beta_{R_y} = 0$, while for the macro Cauchy: $\alpha_{L_x} = 1$, $\beta_{L_x} = 4.2$, $\alpha_{L_y} = 1$, $\beta_{L_y} = 1.1$, $\alpha_{R_x} = 1$, $\beta_{R_x} = 0$, $\alpha_{R_y} = 1$ and $\beta_{R_y} = 0$.

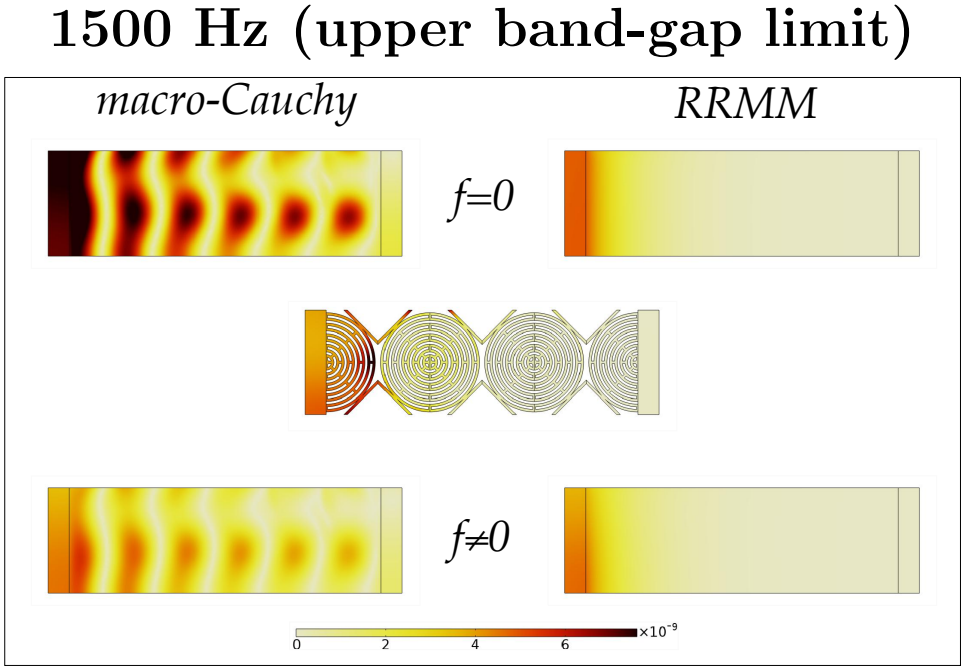

Figure 6.46: Comparison of the displacement field of the metamaterial specimen Γ with the macro-Cauchy and the RRMM when $f = 0$ and $f \neq 0$ at 1500 Hz. When $f \neq 0$ for the RRMM, we have: $\alpha_{L_x} = 1.3$, $\beta_{L_x} = 0$, $\alpha_{L_y} = 1$, $\beta_{L_y} = -2$, $\alpha_{R_x} = 1$, $\beta_{R_x} = 0$, $\alpha_{R_y} = 1$ and $\beta_{R_y} = 0$, while for the macro Cauchy: $\alpha_{L_x} = 1$, $\beta_{L_x} = 4.4$, $\alpha_{L_y} = 1$, $\beta_{L_y} = -1.4$, $\alpha_{R_x} = 1$, $\beta_{R_x} = 0$, $\alpha_{R_y} = 1$ and $\beta_{R_y} = 0$.

Considerations similar to the frequency of 700 Hz and 1100 Hz hold here.

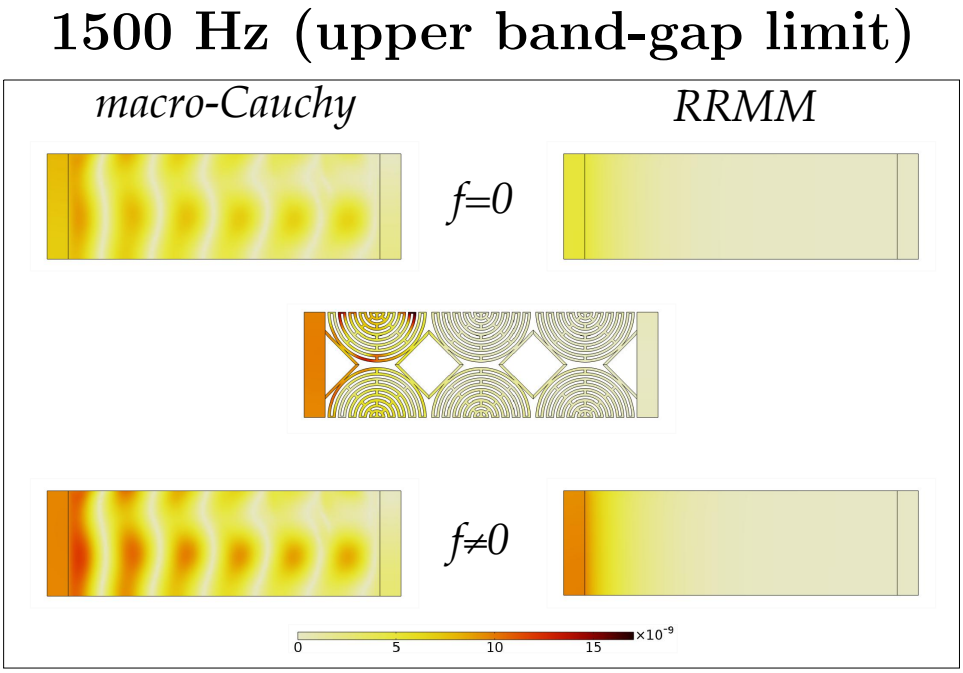

Figure 6.47: Comparison of the displacement field of the metamaterial specimen Δ with the macro-Cauchy and the RRMM when $f = 0$ and $f \neq 0$ at 1500 Hz. When $f \neq 0$ for the RRMM, we have: $\alpha_{L_x} = -0.05$, $\beta_{L_x} = 0$, $\alpha_{L_y} = 1$, $\beta_{L_y} = 0$, $\alpha_{R_x} = 1$, $\beta_{R_x} = 0$, $\alpha_{R_y} = 1$ and $\beta_{R_y} = 0$, while for the macro Cauchy: $\alpha_{L_x} = 1$, $\beta_{L_x} = -3$, $\alpha_{L_y} = 1$, $\beta_{L_y} = -1$, $\alpha_{R_x} = 1$, $\beta_{R_x} = 0$, $\alpha_{R_y} = 1$ and $\beta_{R_y} = 0$.

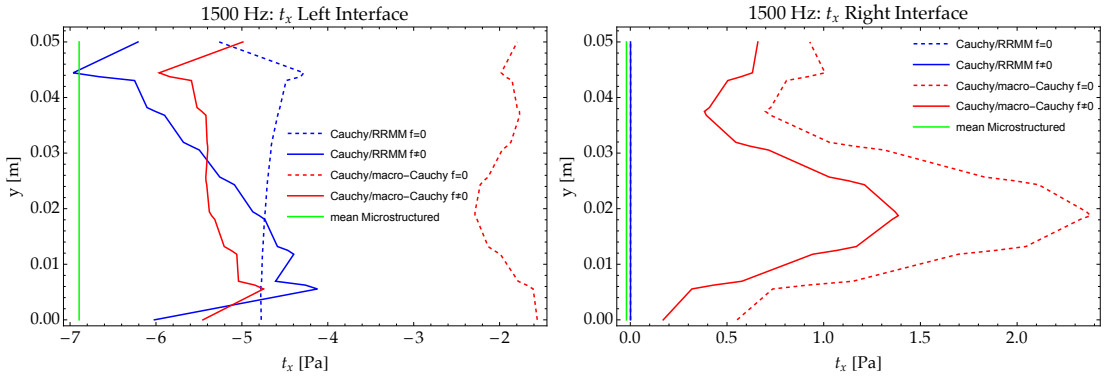

Figure 6.48: Tractions on the Cauchy side of the Cauchy plate/metamaterial interfaces (left and right) for the RRMM and for the macro-Cauchy when $f = 0$ and $f \neq 0$. The tractions shown here are those relative to "cut" B. Analogous reasoning holds true for all other "cuts".

6.3.5 "Problematic" region

This region extends from 200 to 400 Hz with the upper half being worse (300-400 Hz). Here the four cuts have massive differences. In this frequency interval, the wavelength gets smaller (around 2 times the size of the specimen at the start of the region and around the size of the specimen at the end of the "problematic" frequency interval),interacts with the microstructure, and these boundary effects are now governing the whole response of the 3×2 specimen. We expect that in this frequency interval structural resonances of the entire specimen can be easily triggered. As a consequence, the interface forces arising at the Cauchy-plates metamaterial's interfaces could experience strong oscillations making expression (5.6) for the macroscopic interface force insufficient to capture such complex interface behavior. We expect that the RRMM would be only able to catch the four different metamaterial's responses with very exotic expressions of interface forces. In this frequency region the pressure mode is very dispersive, so we avoid using the macro-Cauchy, since it does not have the ability to capture the dispersion.

Frequency: 280 Hz

At this frequency the pressure mode shows very dispersive behavior (see the fourth point in Fig. 6.7).

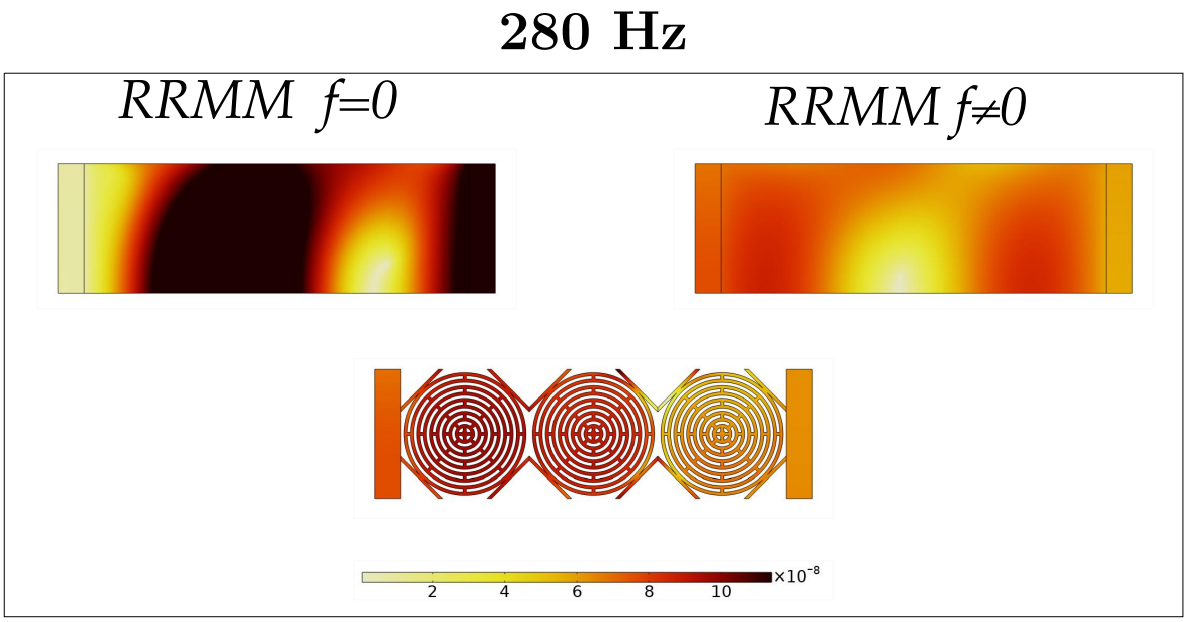

Figure 6.49: Comparison of the displacement field of the metamaterial specimen A with the RRMM when $f = 0$ and $f \neq 0$ at 280 Hz. When $f \neq 0$ for the RRMM, we have: $\alpha_{L_x} = 3$, $\beta_{L_x} = 0$, $\alpha_{L_y} = 1$, $\beta_{L_y} = 0$, $\alpha_{R_x} = -0.7$, $\beta_{R_x} = 0$, $\alpha_{R_y} = 1$ and $\beta_{R_y} = 0$.

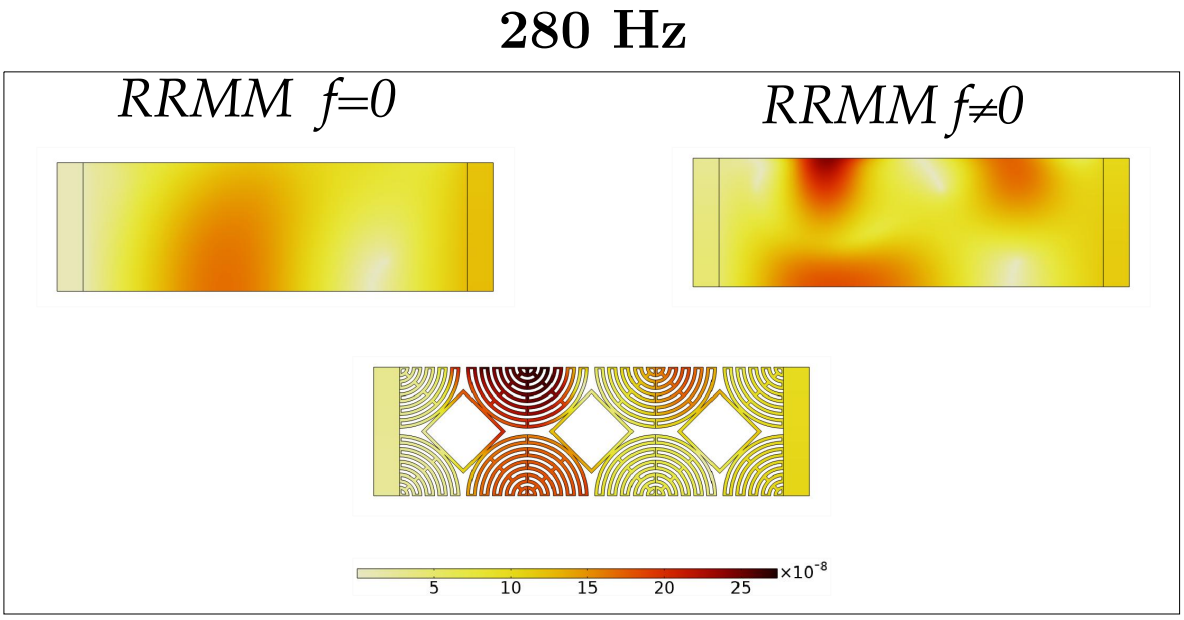

Figure 6.50: Comparison of the displacement field of the metamaterial specimen B with the RRMM when $f = 0$ and $f \neq 0$ at 280 Hz. When $f \neq 0$ for the RRMM, we have: $\alpha_{L_x} = 1.1$, $\beta_{L_x} = 0$, $\alpha_{L_y} = 1$, $\beta_{L_y} = 0$, $\alpha_{R_x} = 2$, $\beta_{R_x} = 0$, $\alpha_{R_y} = 1$ and $\beta_{R_y} = 0$. An interface force was used on the top "free" RRMM boundary with the expression: $f^{int} = -16.67 \cdot e^{\frac{-(x+0.0035)^2}{0.0002}} - 1.67 \cdot e^{\frac{-(x-0.045)^2}{0.0002}}$. Moreover, only here, we apply an additional boundary load an all three boundaries by taking advantage of a null-Lagrangian property of the RRMM as explained in [18]: The micro-inertia parameters of the RRMM can change in a specific way so that the bulk behavior (dispersion curves) remains invariant, but the boundary contribution varies. In this particular case, the value of $\overline{\gamma}_2$ in front of a new contribution $\langle \mathbb{T}_c \text{ skew } \nabla \dot{u}, \text{skew } \nabla \dot{u} \rangle$ is now set to 1.52541 $\frac{\text{kg}}{\text{m}}$ and the rest micro-inertia parameters' values change accordingly [18].

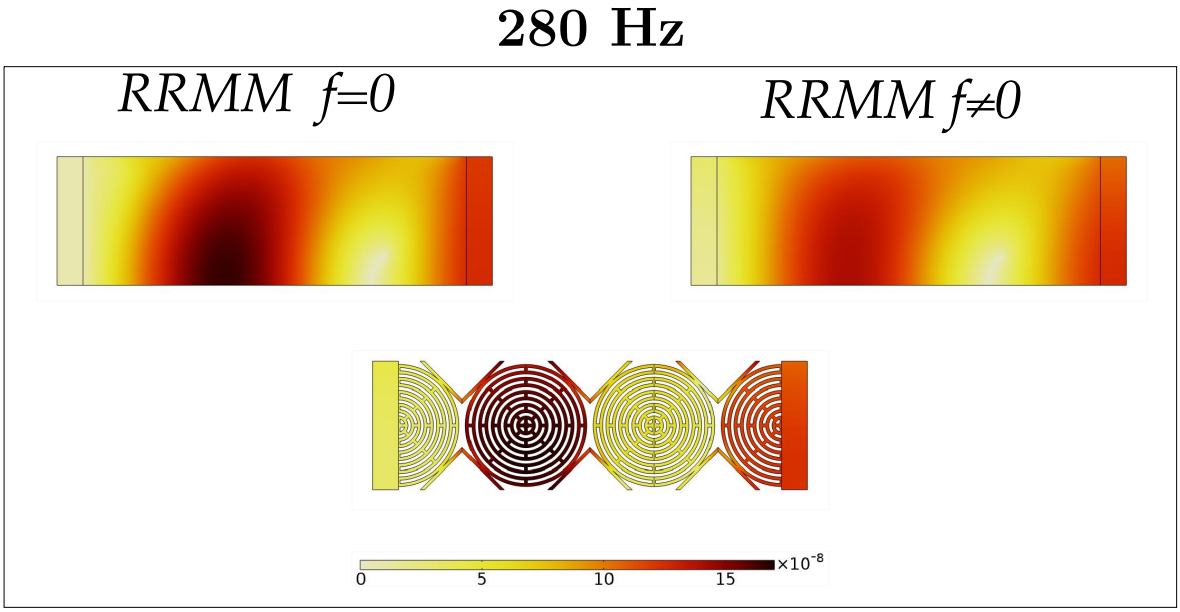

Figure 6.51: Comparison of the displacement field of the metamaterial specimen Γ with the RRMM when $f = 0$ and $f \neq 0$ at 280 Hz. When $f \neq 0$ for the RRMM, we have: $\alpha_{L_x} = 1.1$, $\beta_{L_x} = 0$, $\alpha_{L_y} = 1$, $\beta_{L_y} = -10$, $\alpha_{R_x} = 1.51$, $\beta_{R_x} = 0$, $\alpha_{R_y} = 1$ and $\beta_{R_y} = 10$.

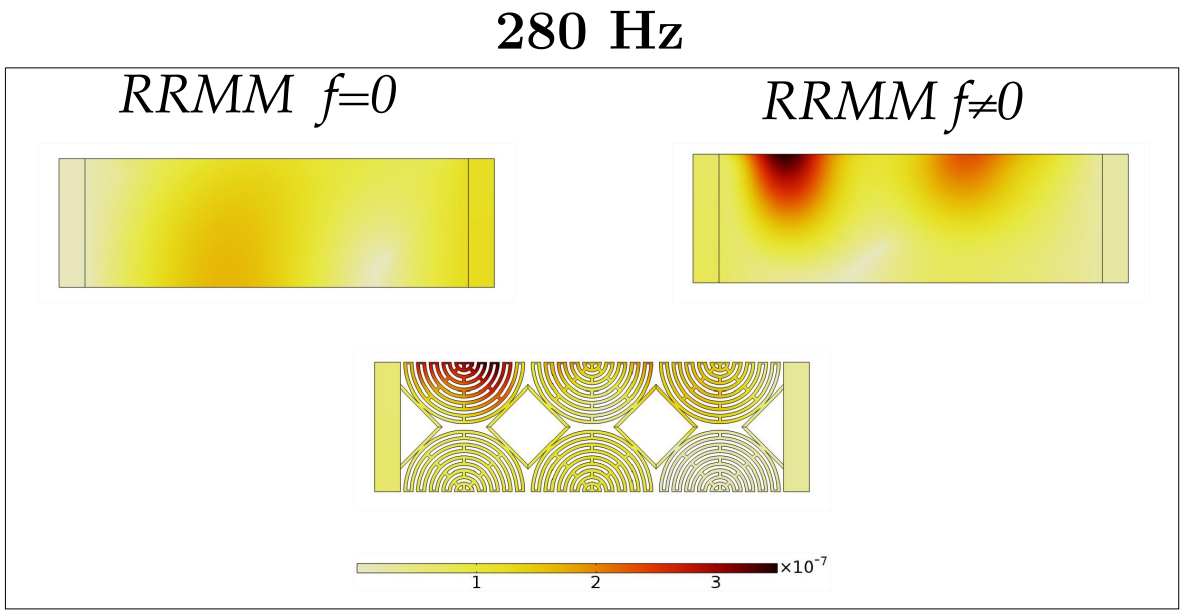

Figure 6.52: Comparison of the displacement field of the metamaterial specimen Δ with the RRMM when $f = 0$ and $f \neq 0$ at 280 Hz. When $f \neq 0$ for the RRMM, we have: $\alpha_{L_x} = 2.7$, $\beta_{L_x} = 0$, $\alpha_{L_y} = 1$, $\beta_{L_y} = -30$, $\alpha_{R_x} = -0.2$, $\beta_{R_x} = 0$, $\alpha_{R_y} = 1$ and $\beta_{R_y} = 0$. An interface force was used on the top "free" RRMM boundary with the expression: $f^{int} = -29.4 \cdot e^{\frac{-(x+0.05)^2}{0.0002}} - 13.3 \cdot e^{\frac{-(x-0.02)^2}{0.0002}}$.

Frequency: 340 Hz

At this frequency the pressure mode shows very dispersive behavior (see the fifth point in Fig. 6.7).

Figs. 6.49 - 6.56 show that in this frequency interval the wavelength is comparable to the size of the specimen, therefore more complex expressions of $f^{\text{interface}}$ would be needed compared to linear ones (5.6). Indeed, we see that interface forces of the form (5.6) improve the solutions for all "cuts", but sometimes some details of the microstructured ("real") solution are not entirely captured. When the frequency increases again, approaching the band-gap region (see Fig. 6.24, expression (5.6) is again sufficient to catch the overall solution. This is due to the fact that even if the wavelength gets smaller, we are indeed

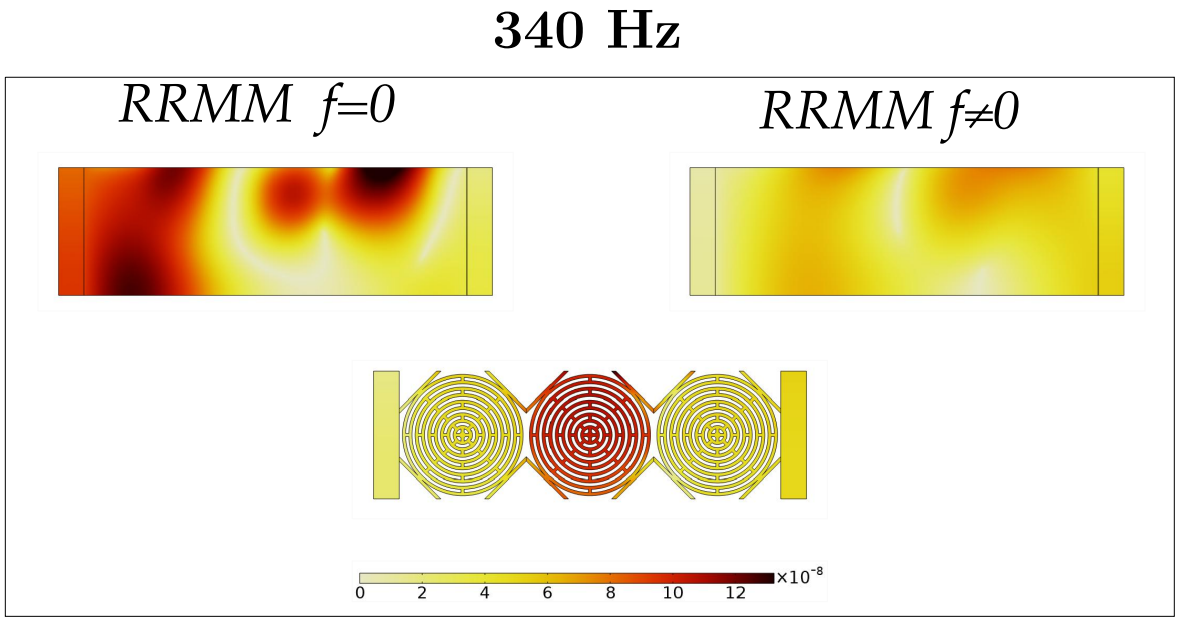

Figure 6.53: Comparison of the displacement field of the metamaterial specimen A with the RRMM when $f = 0$ and $f \neq 0$ at 340 Hz. When $f \neq 0$ for the RRMM, we have: $\alpha_{L_x} = 2$, $\beta_{L_x} = 0$, $\alpha_{L_y} = 1$, $\beta_{L_y} = 0$, $\alpha_{R_x} = -2$, $\beta_{R_x} = 0$, $\alpha_{R_y} = 1$ and $\beta_{R_y} = 0$.

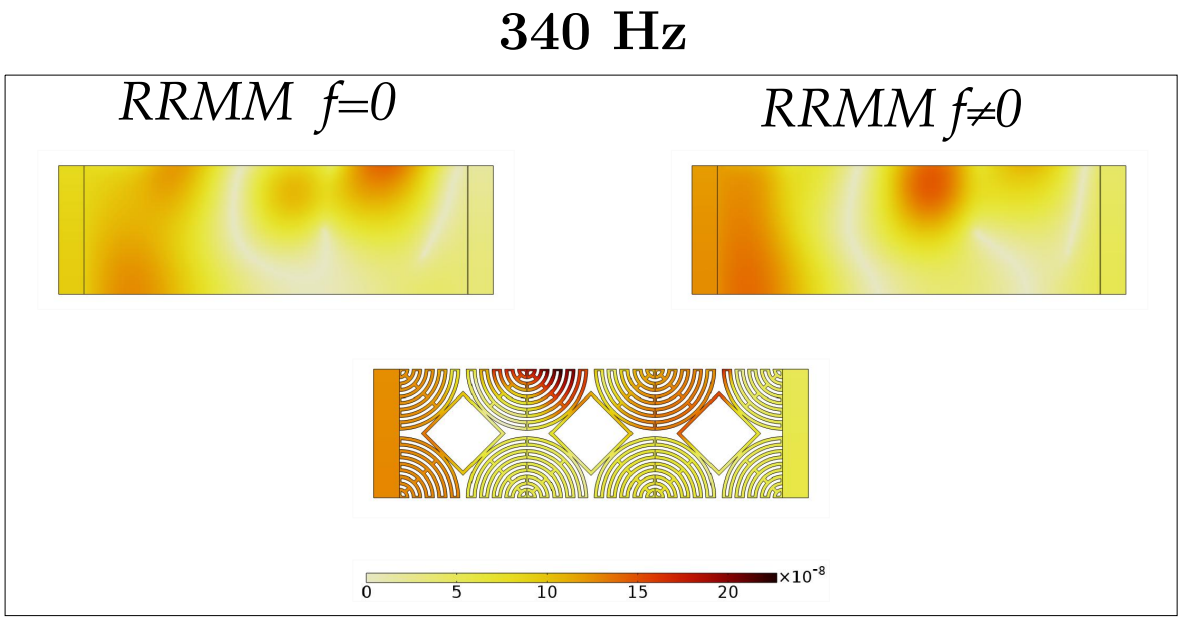

Figure 6.54: Comparison of the displacement field of the metamaterial specimen B with the RRMM when $f = 0$ and $f \neq 0$ at 340 Hz. When $f \neq 0$ for the RRMM, we have: $\alpha_{L_x} = 0.8$, $\beta_{L_x} = 0$, $\alpha_{L_y} = 1$, $\beta_{L_y} = 0$, $\alpha_{R_x} = 0.6$, $\beta_{R_x} = 0$, $\alpha_{R_y} = 1$ and $\beta_{R_y} = 0$.

approaching the band-gap region, so instead of having more pronounced boundary effects, we have more significant destructive interference of the waves, since we are approaching the band-gap. These findings point out to the general result that macroscopic interface effects can be predominant as soon as the wavelength is comparable to the specimen's size or smaller, and the frequency is not close to a band-gap region. Particular attention should be payed to all those cases in which one wants to use homogenised models for these frequencies.

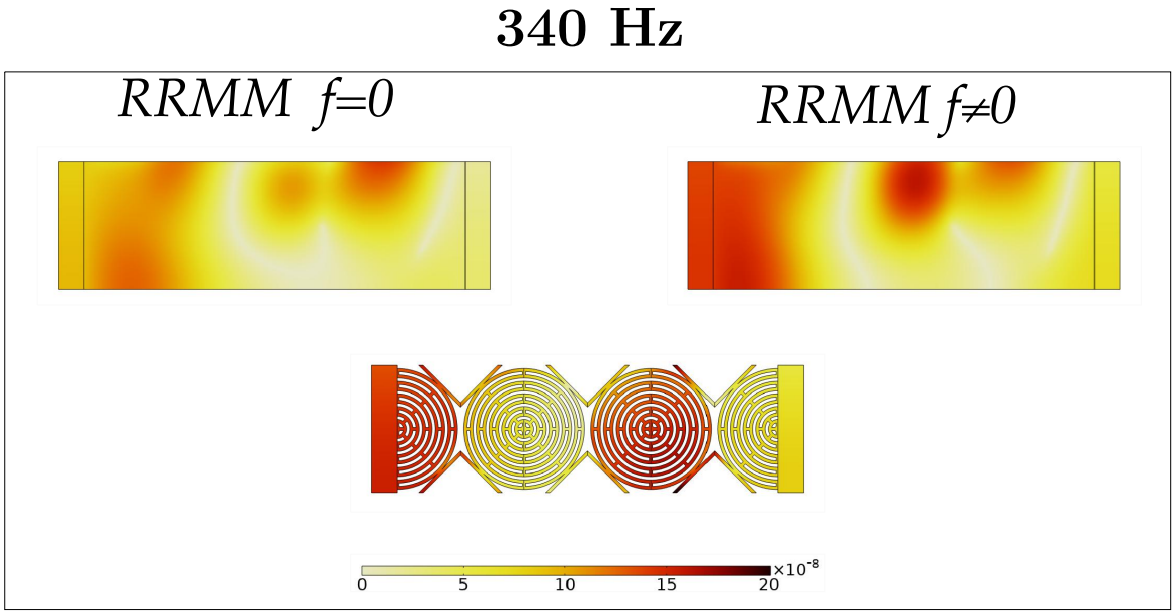

Figure 6.55: Comparison of the displacement field of the metamaterial specimen Γ with the RRMM when $f = 0$ and $f \neq 0$ at 340 Hz. When $f \neq 0$ for the RRMM, we have: $\alpha_{L_x} = 0.6$, $\beta_{L_x} = 0$, $\alpha_{L_y} = 1$, $\beta_{L_y} = 0$, $\alpha_{R_x} = 1$, $\beta_{R_x} = 0$, $\alpha_{R_y} = 1$ and $\beta_{R_y} = 0$.

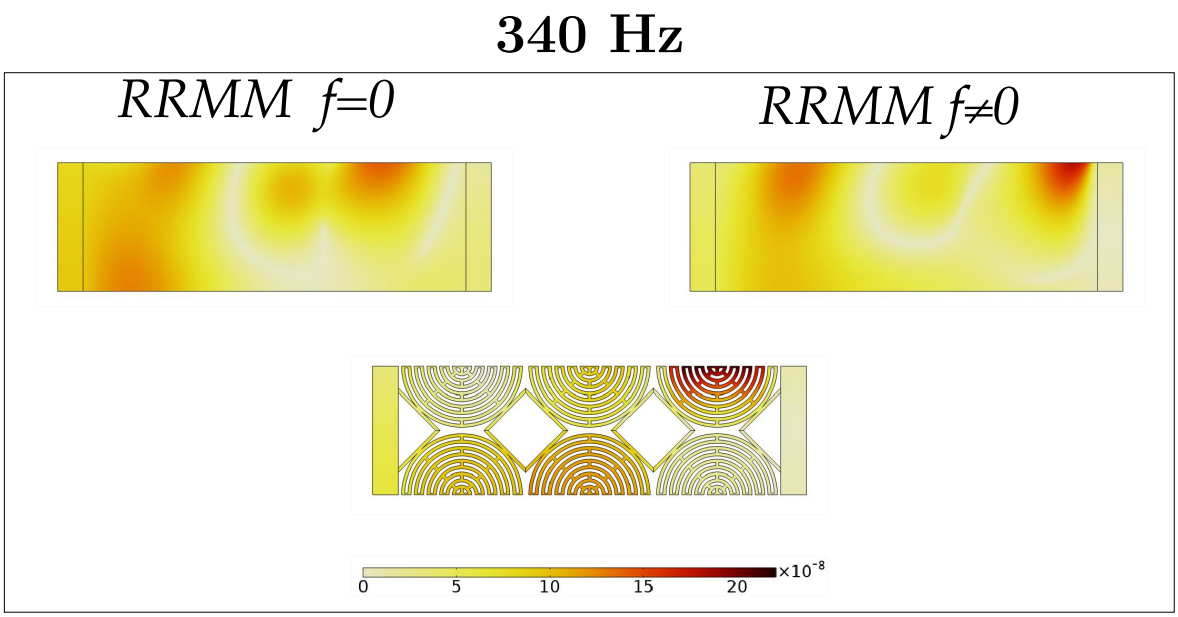

Figure 6.56: Comparison of the displacement field of the metamaterial specimen Δ with the RRMM when $f = 0$ and $f \neq 0$ at 340 Hz. When $f \neq 0$ for the RRMM, we have: $\alpha_{L_x} = 1.3$, $\beta_{L_x} = 0$, $\alpha_{L_y} = 1$, $\beta_{L_y} = 0$, $\alpha_{R_x} = 1$, $\beta_{R_x} = 0$, $\alpha_{R_y} = 1$ and $\beta_{R_y} = 0$. An interface force was used on the top "free" RRMM boundary with the expression: $f^{int} = -50 \cdot e^{\frac{-(x-0.08)^2}{0.0002}}$.

6.3.6 Independent tests using bigger specimens: limits of Bloch-Floquet analysis

Since the analyzed 3x2 specimens have vastly different displacement field solutions, we wish to increase the size of the structures in steps, to understand how much it needs to be increased in order for the four specimens to have a similar displacement field, i.e. what is the size of the specimens to consider boundary effects (and thus the need for interface forces in the RRM setting) as negligible. We proceed with this task but we change the excitation to a displacement instead of a force. We present here the results for specimens of size 3x2, 9x6, 15x10, 30x20 and 45x30 for the frequency of 200 Hz and all the four "cuts".

3x2 cells, L_{specimen}=15 cm, wavelength λ=35 cm

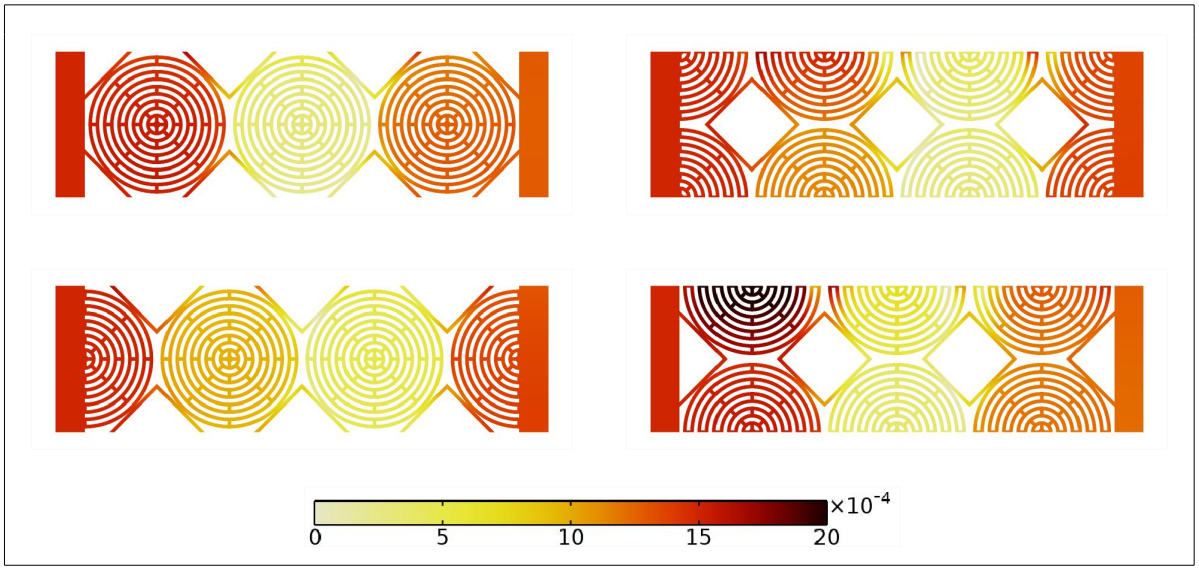

Figure 6.57: Displacement field for the four original 3x2 specimens at the frequency of 200 Hz. Specimen made out of cut A(Top Left), cut B(Top Right), cut Γ(Bottom Left) and cut Δ(Bottom Right).

9x6 cells, L_{specimen}=45 cm, wavelength λ=35 cm

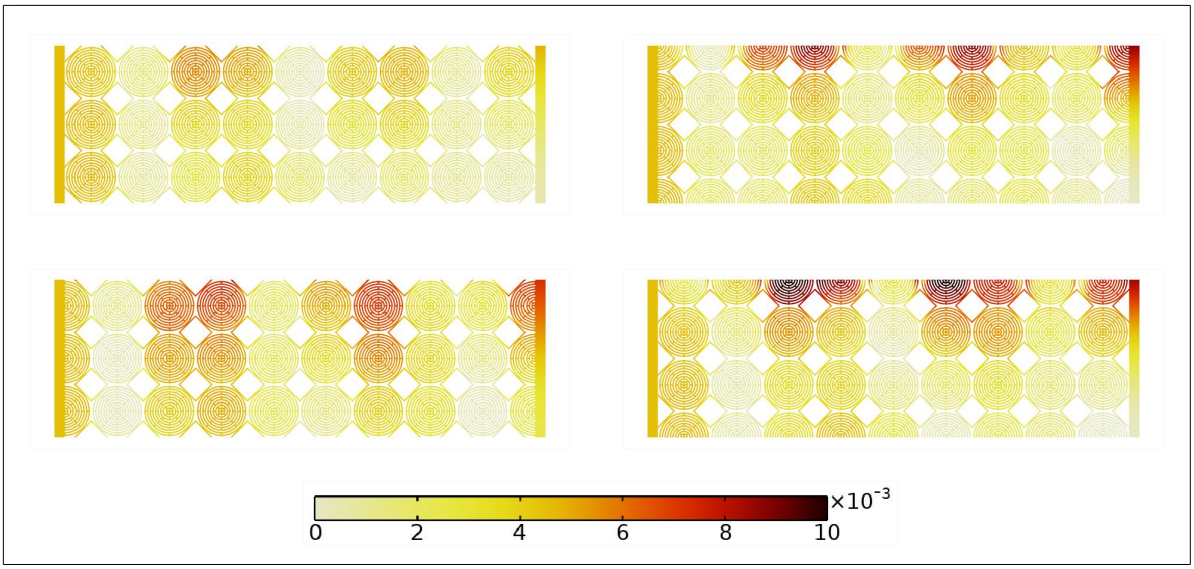

Figure 6.58: Displacement field for the four 9x6 specimens at the frequency of 200 Hz. Specimen made out of cut A(Top Left), cut B(Top Right), cut Γ(Bottom Left) and cut Δ(Bottom Right).

The specimens have 9 times more unit cell than the original samples but they are too small to ignore boundary effects.

15x10 cells, L_{specimen}=75 cm, wavelength λ=35 cm

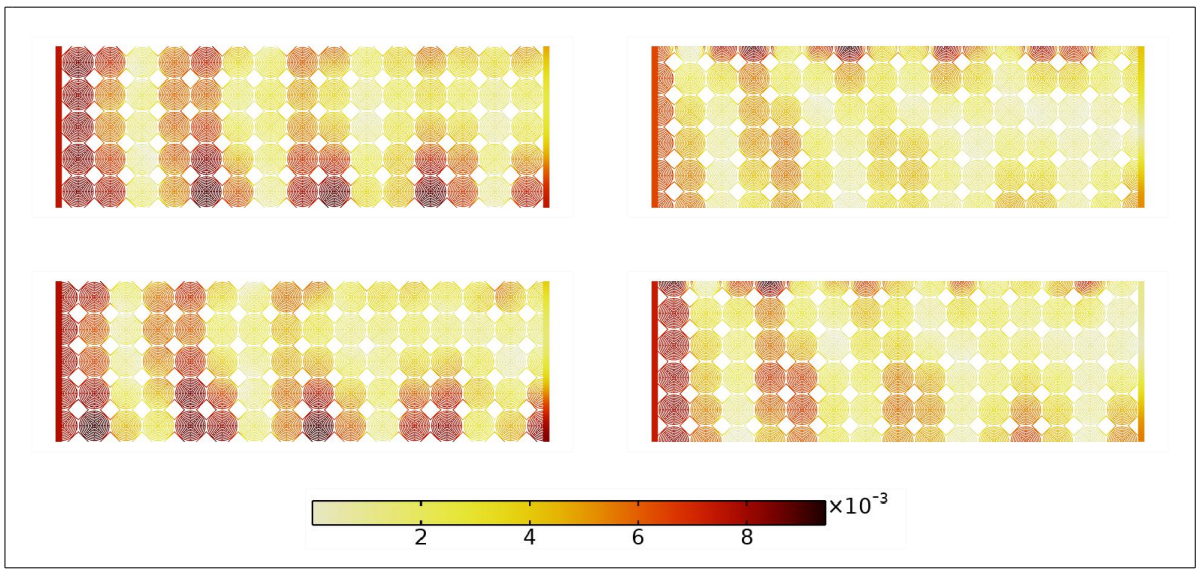

Figure 6.59: Displacement field for the four 15x10 specimens at the frequency of 200 Hz. Specimen made out of cut A(Top Left), cut B(Top Right), cut Γ(Bottom Left) and cut Δ(Bottom Right).

Even with a sample consisting of 150 unit-cells overall, boundary effects still produce significant differences between the different "cuts" that are prominent also in the bulk of the material. The specimen is still too small to ignore boundary effects.

30x20 cells, L_{specimen}=150 cm, wavelength λ=35 cm

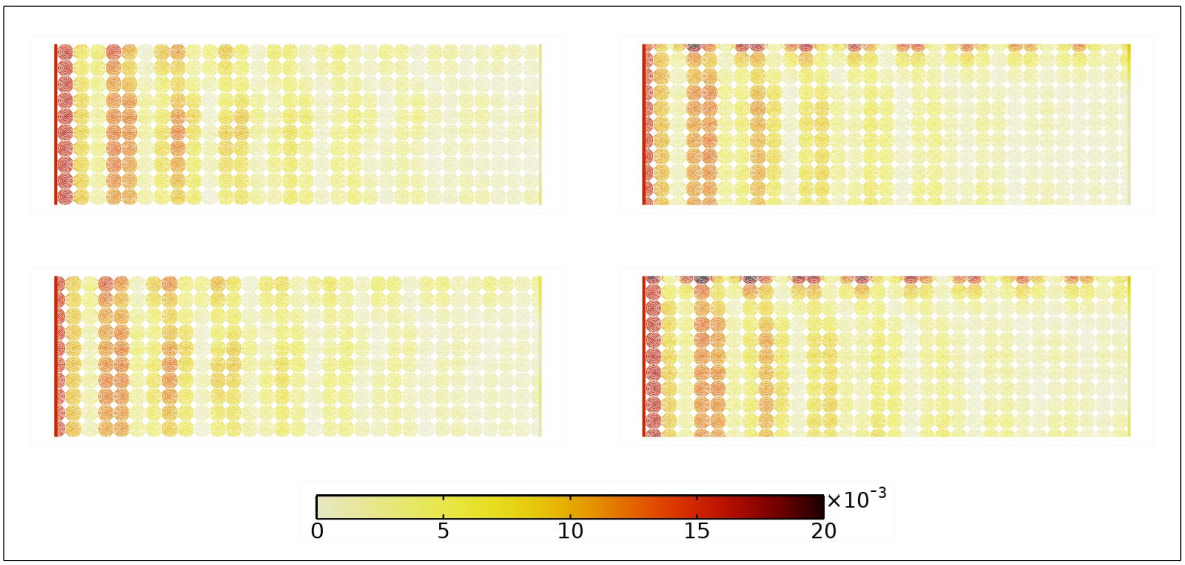

Figure 6.60: Displacement field for the four 30x20 specimens at the frequency of 200 Hz. Specimen made out of cut A(Top Left), cut B(Top Right), cut Γ(Bottom Left) and cut Δ(Bottom Right).

In this case, the wavelength is already 4 times smaller than the size of the specimen consisting of overall 600 unit cells. We notice that the solutions become very similar except at parts close to the boundaries including the free boundary at the top of the sample.

45x30 cells, L_{specimen}=225 cm, wavelength λ=35 cm

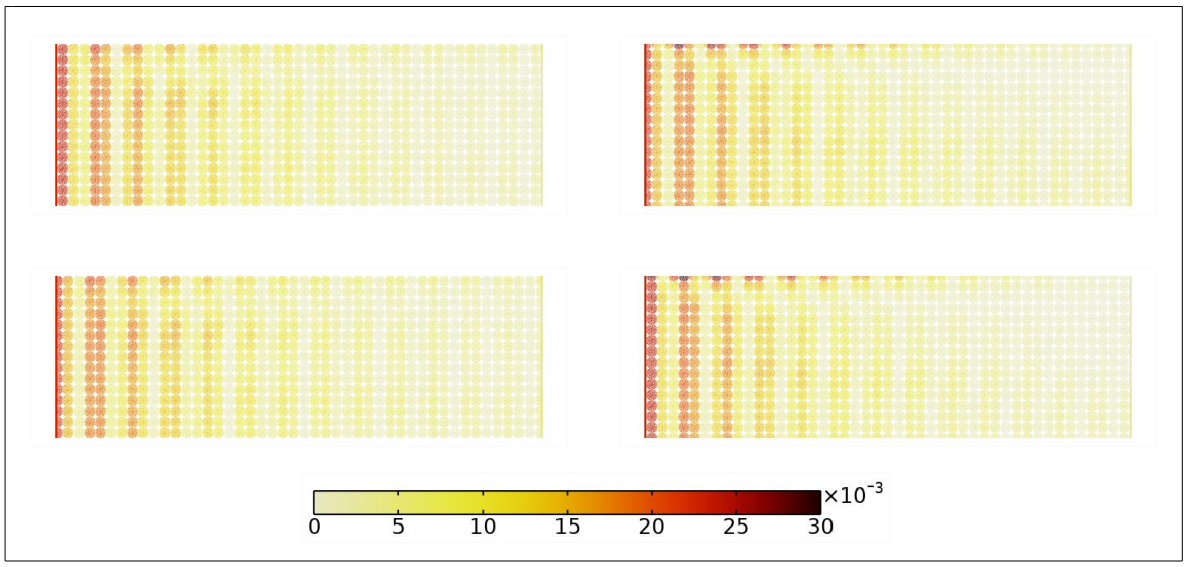

Figure 6.61: Displacement field for the four 45x30 specimens at the frequency of 200 Hz. Specimen made out of cut A(Top Left), cut B(Top Right), cut Γ(Bottom Left) and cut Δ(Bottom Right).

For our biggest samples consisting of 1350 unit cells, all four solutions converge regarding bulk response. However, some boundary effects are still visible.

Summary

The main assumption of Bloch-Floquet analysis is that the material is extended to infinity, i.e. the actual size of the specimen is infinitely big, thus the metamaterial has no boundaries. However, the dispersion curves coming from Bloch-Floquet analysis are inevitably used as a design tool in finite size metamaterial applications, often disregarding boundary effects that we showed can become predominant as soon as reducing the specimen's size to finite-sized problems. Thus the question arises, what is the minimum size of a finite sized metamaterial so that we are allowed to neglect boundary effects?

Usually, the answer given is that a very big number of unit cells must be used to approximate well a metamaterial extended to infinity. By using more unit cells, the length of the boundary of the metamaterial scales linearly while the area of the bulk scales quadratically, and thus the ratio of boundary to bulk tends to zero.

Another more interesting answer coming from the results in this thesis is the following:
Boundary effects can be neglected if the size of the specimen is "big enough", i.e. bigger than a certain threshold, so that finite-sized specimens constructed from different cell's cuts show no qualitative difference in their behavior. This implies that, the RRM modeling of specimens that are bigger of this threshold would not need any interface forces to provide the correct solution, since the infinite metamaterial assumption is approximately true. From the above results, we can see that even for a 45x30 specimen, there are still some different boundary behaviors for the different cuts. Therefore, we have not yet found the appropriate size for which boundary effects can be fully neglected. At this size, our enriched continuum would not need interface forces to reproduce the different response associated to the four different cell's cuts. On the other hand, it can be noticed that the "bulk" response already becomes very similar in the 4 specimen's types as soon as the number of unit cells is increased.

6.4 Conclusions

In this Chapter, we have demonstrated that introducing the concept of interface forces is essential for modeling the response of finite-size metamaterials within a homogenised framework. By using the RRMM which performs well in describing the bulk behavior of metamaterials, we needed to enrich the model by

incorporating the concept of interface forces in order to capture boundary effects, and consequently the correct finite-size response. We showed that for the considered cases, the form that these interface forces should take is, in most cases,

$$f^{\text{interface}} = (\alpha - 1) t_{(RRMM)} + \beta. \tag{6.3}$$

where $t_{\text{RRMM}} = (\widetilde{\sigma} + \widehat{\sigma})\, n$, is the RRM traction on the considered interface, α is a dimensionless parameter and β is a surface force. Our findings explicitly indicate that boundary effects and, consequently, interface forces can significantly impact finite-sized specimens. We also used unit cell "cuts" and homogenised modeling coupled with interface forces in order to define the limits of Bloch-Floquet analysis. This limit was defined in terms of size of the specimen and specifically that size for which any finite-size material constructed from any "cut" shows the same qualitative behavior. This means that in the case of modeling these metamaterials constructed from different "cuts" using an enriched continuum, no interface forces have to be used, as boundary effects would be negligible.

Chapter 7

Implications of the choice of unit cell "cut" on the response of finite-sized microstructured metamaterials

This chapter serves as a brief collection of the so-far discovered implications of the choice of unit cell "cut" on the response of microstructured metamaterials. We remark once more, that in the real world, every metamaterial is inevitably a finite-size metamaterial. As it has been extensively discussed in this thesis, if enough number of unit cells are used for the construction of a finite size metamaterial, so that the infinitely big metamaterial hypothesis is a good approximation, the finite-size metamaterial's response can be described by the Bloch-Floquet dispersion curves and mode shapes. However, if the number of unit cells used in not big enough for the hypothesis to hold, the response then also depends on boundary effects which may or may not appear based on the choice of unit cell "cut". These effects, stemming from the choice of unit cell "cut", can have interesting implications on the metamaterial's response and transmissibility and have interesting potential applications.

In this chapter, we use very often the so-called transmissibility plot in order to discuss the transmission properties of finite-size metamaterial specimens. Transmissibility is defined as the ratio of output to input acceleration (or equivalently displacement, velocity or force) for a given vibration test. In this thesis, all tests shown are tests where a metamaterial is embedded between two homogeneous plates, and the excitation is applied on the left hand plate while the right hand plate is always free. Transmissibility is defined as the ratio of output to input acceleration (or equivalently displacement, velocity or force) for a given vibration test. In our case, we choose the absolute value of the acceleration at each point on the right Cauchy plate as the measure of output, and similarly the input is the absolute value of the acceleration at each point on the left Cauchy plate where the excitation force is applied. To have a single value of transmissibility for each frequency (instead of a point-wise comparison), we take their averages on each plate and call Transmissibility the ratio

$$\text{Transmissibility} = \frac{\text{avg}\,|\ddot{u}_{\text{output}}|}{\text{avg}\,|\ddot{u}_{\text{input}}|}. \tag{7.1}$$

where avg is an average operator that calculates an average on the right plate for the output and on the left plate for the input.

7.1 Increased transmissibility in a band-gap frequency range: shielding, energy focusing and harvesting

For the microstructured simulations presented in Chapter 4, we show here the transmissibility plot (see Fig. 7.1) regarding locally resonant finite-sized metamaterials A and B and compare the transmissibility values in the band-gap region, where real waves should be attenuated. We observe that "cut" A shows much higher values of transmissibility than "cut" B around the eigenfrequency of the resonators (start of the band-gap) which is where locally resonant metamaterials show the highest attenuation. By choosing the former as the unit cell of the finite-sized metamaterial, an edge effect is triggered on the top boundary

which allows the wave to propagate on the boundary of the material (see Fig. 7.2). By choosing to construct our metamaterial using the specific "cut" A, we end up with a specific boundary, which in turn causes the edge effect, showing that for this "cut", the number of unit cells (16), is not a number which suffices in order for the assumption of the infinite medium to be approximately true. When choosing "cut" B as the unit cell, no edge effect appears on the finite-size metamaterial, whose response approximates much better the one of the infinite metamaterial.

Consequently, metamaterial B is a better candidate for a shielding application than metamaterial A, whereas the edge effect appearing in metamaterial A makes it a better candidate for potential energy focusing and harvesting applications around the area where the boundary effect takes place. Energy harvesting applications are usually possible through piezoelectricity.

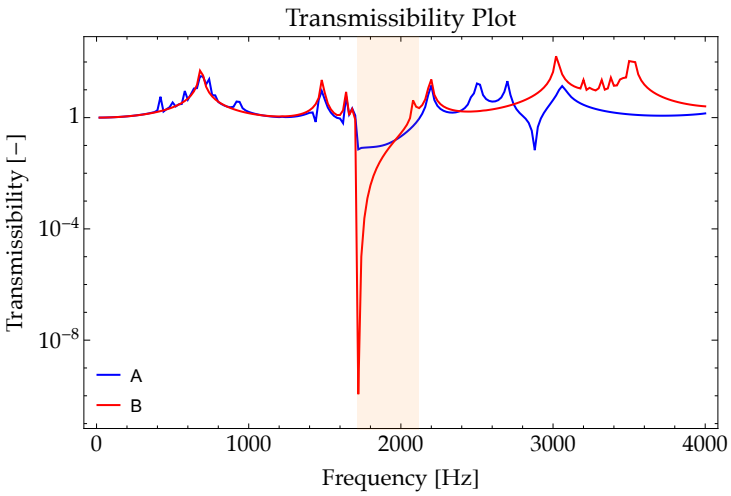

Figure 7.1: Transmissibility plot for the metamaterials A and B (16×16 unit cells). The $y-$axis is presented in a logarithmic scale and the band-gap range is indicated with light orange color.

Regarding the description of the edge effect, which as we saw in Chapter 5, remains invariant with respect to a change in the number of unit cells used in the y-direction, we can say that it is a function of the applied excitation coupled with the geometry of the "cut" and the mass distribution inside the unit cell. The latter causes the unit cell to have low shear stiffness, therefore causing the last row of unit cells on the top boundary of the metamaterial to deform in this specific way.

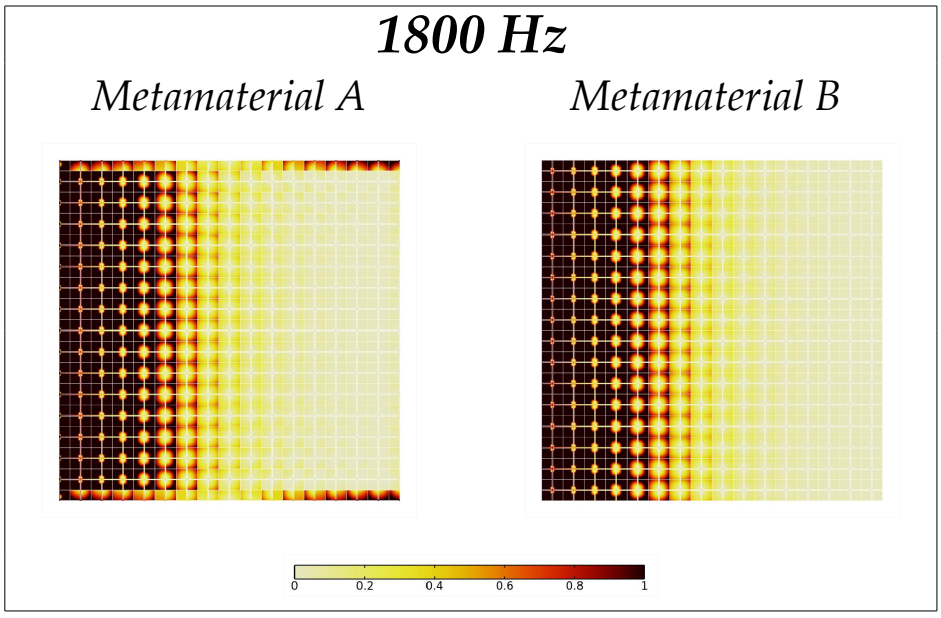

Figure 7.2: Norm of the dimensionless displacement for metamaterials A and B at the frequency of 1800 Hz. An edge effect is evident in a band-gap region.

7.2 Reduced transmissibility in a non-band-gap frequency range

The Transmissibility plot of all the four microstructured metamaterials presented in Chapter 6 can be seen in Fig. 7.3 where we can observe vast differences in the transmissibility values in the band-gap region between the four specimens. This is to show that even if the four "cuts" can produce the same infinitely big metamaterial, given the finite size of real applications, the choice of unit cell "cut" becomes of paramount importance. By choosing one of the four different "cuts" for constructing our finite size specimen, we end up with 4 different metamaterial's specimens of finite size. One could argue that the only common thing between the four periodic structures, is the fact that they should have the same vibrational characteristics because they correspond to the same dispersion curves in an infinitely big domain, However, due to the finite size of these structures, we end up with a different geometry on the boundaries of each specimen, which gives us different boundary effects. Furthermore, different structures can possess different eigenfrequencies of vibration, leading to different results for same frequencies. All these factors lead to the difference in the transmissibility of the four specimens in Fig. 7.3.

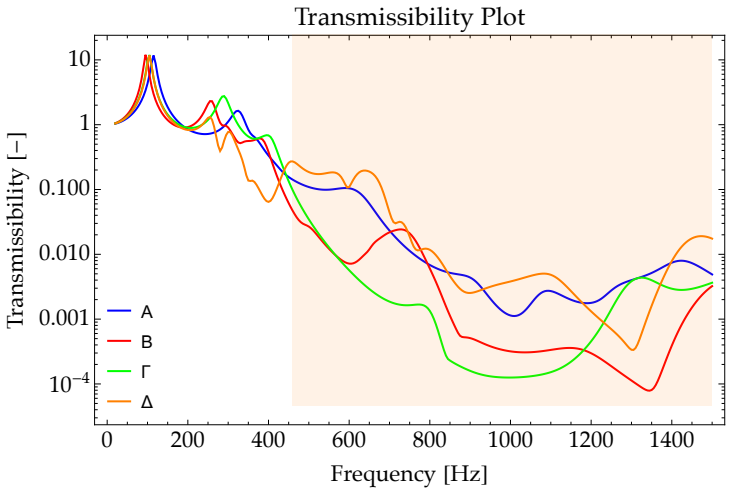

Figure 7.3: Transmissibility plot for the four microstructured specimens (3×2 unit cells). The $y-$axis is presented in a logarithmic scale and the band-gap range is indicated with light orange color.

The transmissibility plot (Fig. 7.3) reveals a small region (340-425 Hz), for which only cut Δ has a reduced transmissibility, and this region does not fall in the frequency region of the band gap. Specifically, the transmissibility values for cut Δ in this region are around 10%. These transmissibility values are not comparable to the band-gap (where we often have values smaller than 0.1%), but still the attenuation is big enough to be used for potential shielding applications.

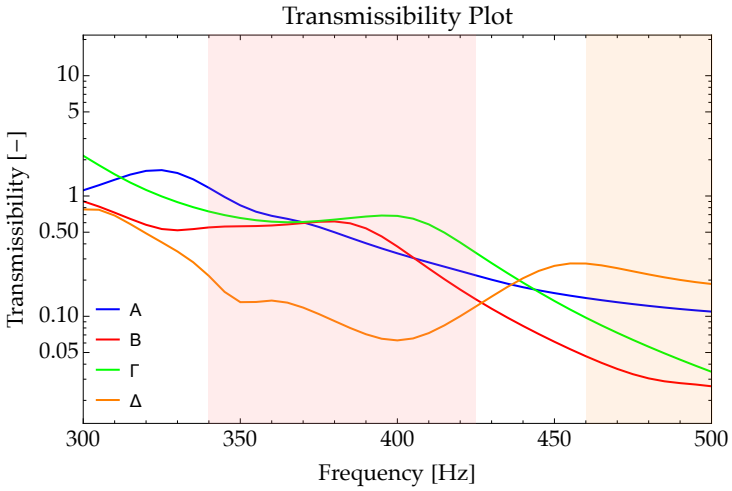

Figure 7.4: Zoom in the Transmissibility plot 7.3: the frequency region of interest before the band-gap is indicated with light red color.

A zoom in the trasmissibility plot shows better the discussed absorption property (see Fig. 7.4), and the

displacement field for an indicative frequency (350 Hz) in this region can be seen in Fig. 7.5.

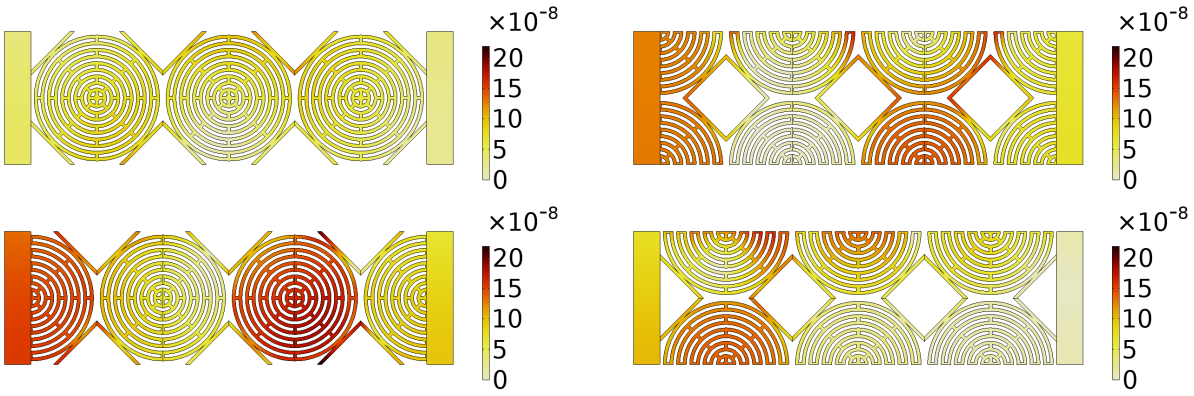

Figure 7.5: Displacement field at 350 Hz for the four specimens. Specimen A (top left), B (top right), Γ (bottom left) and Δ (bottom right).

7.3 Rotational mode suppression

The infinitely big metamaterial with a new geometry shown in Fig. 7.6 (left), produces the dispersion curves for 0° propagation shown in Figure 7.7 (left). These dispersion curves have a unique feature: the acoustic shear and first optic shear, have a region in which they can both be excited, i.e. there are two modes at the same frequency.

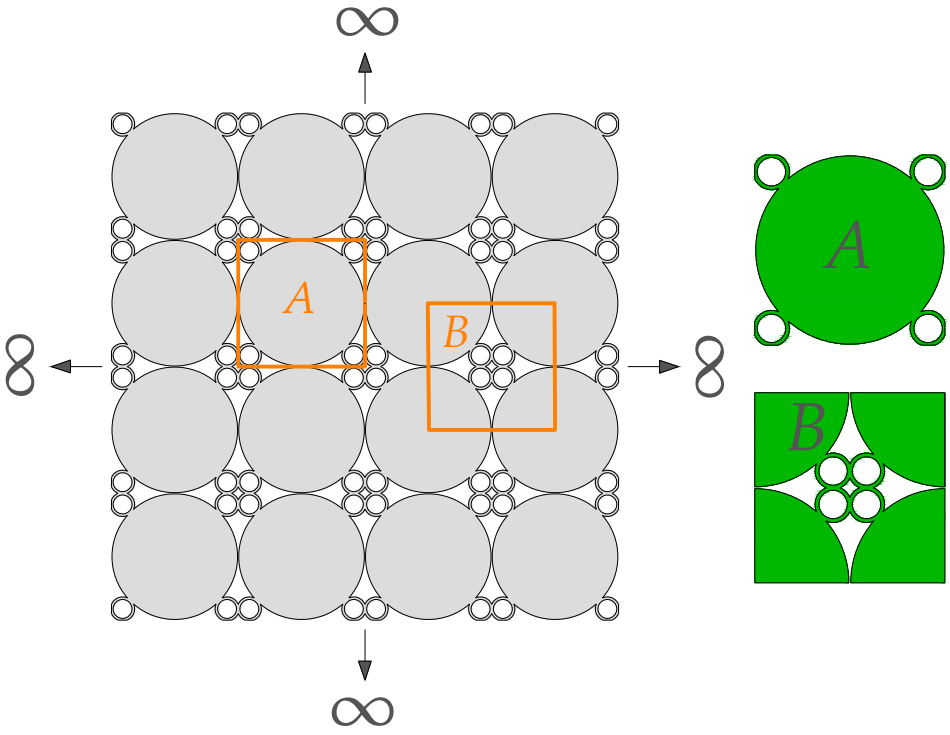

Figure 7.6: Infinitely big metamaterial (top) and "cuts" A and B (bottom).

As seen in the corresponding Bloch-Floquet mode shapes in Fig. 7.7 (right), the acoustic mode corresponds to a transverse wave while the optic mode corresponds to a rotational wave. This feature of the dispersion curves is interesting from an enriched continuum modeling perspective, because it would require the dispersion polynomial for shear waves to be at least fourth order in k in order for the two shear curves to be able to "co-exist" in the same frequency range.

From the point of view of modeling the metamaterial using the full microstructure, the rotational mode is particularly interesting because, as we show here, in the corresponding simulations of shear tests,

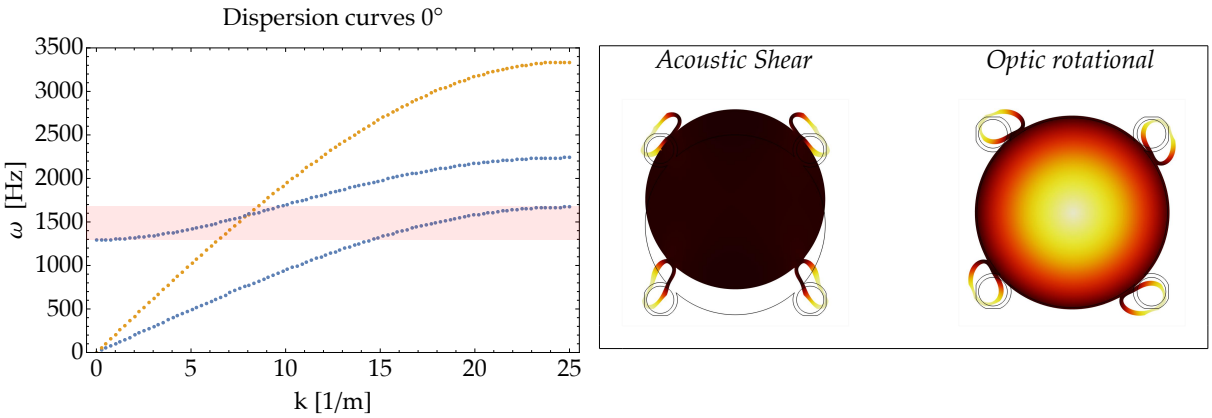

Figure 7.7: (Left) Dispersion curves for 0° propagation with shear curves (blue) and pressure curves (yellow). A frequency region where two shear curves co-exist is colored in light red. (Right) The corresponding mode shapes for the two shear curves: Acoustic shear and Optic rotational. The edges of the undeformed shape are shown in black.

depending on the unit cell "cut" and the particular frequency, the rotational mode may or may not be excited for the same test. In Fig. 7.6 (right), one can see two possible unit cell "cuts" which we (again) name A and B. We construct two 10×10 metamaterials: one from "cut" A and one from "cut" B and we perform a similar test to the one that has been performed throughout this thesis. We have a metamaterial embedded between two Cauchy plates, with the difference being, that now the excitation is a fixed displacement in the $y-$direction (which corresponds to a shear test). We also constrain the $x-$component of the displacement on several boundaries to be zero, to bring the test closer to a pure shear test. The following boundary and interface conditions have been enforced on the relevant boundaries (see Fig. 7.8 for a clearer explanation).

$$
\begin{array}{llll}
u_y = \overline{u} & \text{and} & u_x = 0 & \text{prescribed displacement - red} \\
u^- = u^+ & \text{and} & (\sigma n)^- = (\sigma n)^+ & \text{perfect contact (continuity of displacement and traction) - magenta} \\
\sigma n = 0 & & & \text{stress free - black} \\
u_x = 0 & & & \text{pure shear test condition - green} \\
u_x = 0 & & & \text{antisymmetry - blue}
\end{array}
\tag{7.2}
$$

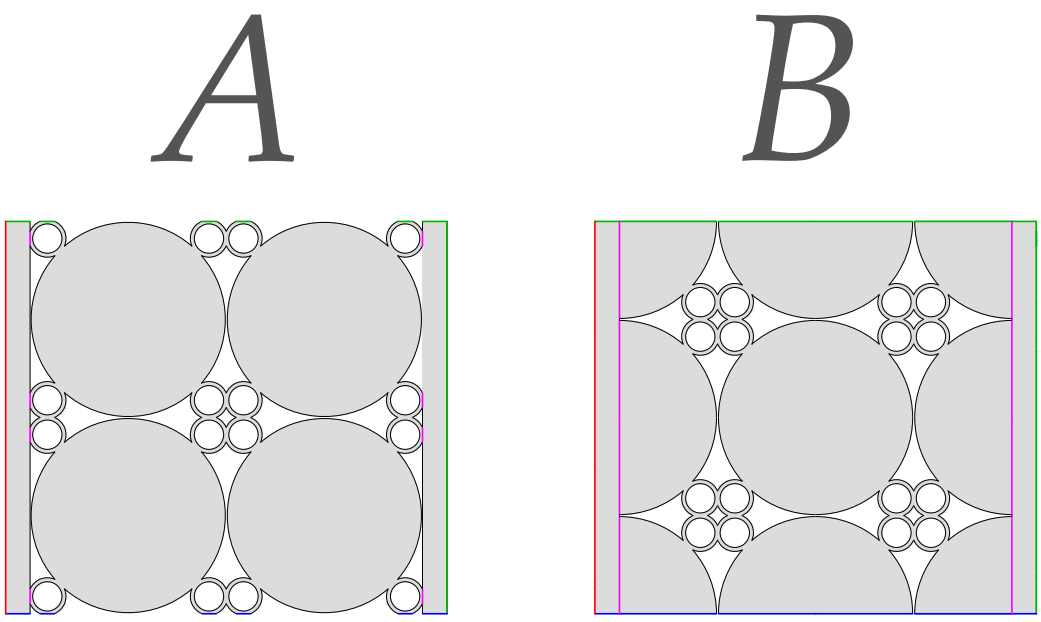

Figure 7.8: Schematic view of the shear tests on microstructured metamaterials A and B with boundary and interface conditions applied.

Interestingly, in the frequency range where only the optic mode can be excited (after the "co-existing" frequency region), there exist frequencies where the rotational mode can only be excited for "cut" A. One example is the frequency of 1800 Hz (see Fig. 7.9). This is a direct consequence of the choice of unit cell "cut", which in turn dictates the boundary of the finite-size metamaterial. In the case of "cut" B, connecting the metamaterial to the left plate, means "clamping" the resonators to the plate, which then for specific frequencies makes the excitation of the rotational mode very difficult, since the resonators are those that must rotate in order for the mode to propagate. We can see this in the mode shape of this specific mode in Fig. 7.7.

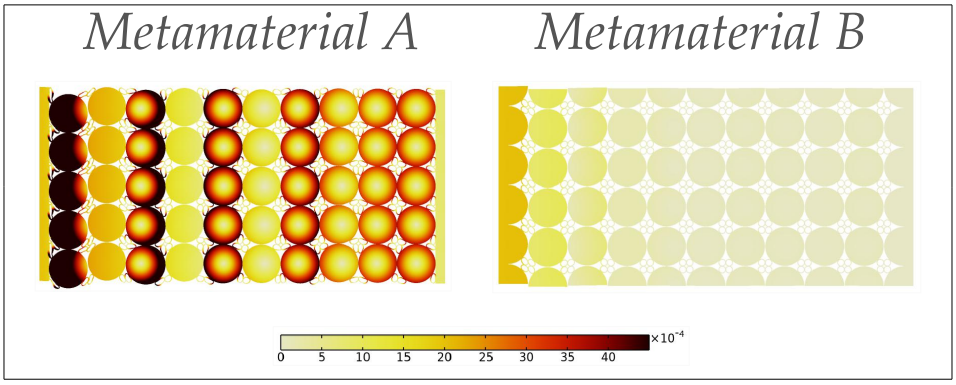

Figure 7.9: Deformed shape for metamaterial A (left) and metamaterial B (right), at the frequency of 1800 Hz (10×10 unit cells). Clearly the rotational mode can only be excited in the case of metamaterial A.

7.4 Conclusions and future perspective

The choice of unit cell "cut" inevitably dictates the response of finite-sized metamaterial specimens if not enough unit cells have been used for their construction, in order for the Bloch-Floquet infinite metamaterial assumption to be a good enough approximation. This choice can have an impact on the finite-size metamaterial's transmissibility, both in the band-gap frequency region, and in different frequency regions. It is also possible that some modes appearing in the Bloch-Floquet dispersion curves for the infinite metamaterial may or may not be excited for a particular test, if specific "cuts" are used for the construction of the finite-size metamaterial. The choice of unit cell "cut" dictates the boundary effects that might appear, the eigenfrequencies of the structure (different unit cell"cut" means a different finite structure), and consequently is responsible for any deviation of the response from that of the infinitely big metamaterial (Bloch-Floquet dispersion curves and mode shapes). As mentioned in this chapter, potential applications exist based on the choice of "cut", ranging from passive vibration control, to focusing and energy harvesting. The implications of the choice of unit cell "cut" call for necessary simulations and experiments before any application, concerning finite-sized specimens from different "cuts", for transmissibility optimization.

In regards to the metamaterial shown in Section 7.3, we already emphasized that such behavior of the two first shear modes calls for a homogenised description with a model that has a dispersion polynomial of a fourth order with respect to k or higher and possesses horizontal asymptotes. Models with dispersion polynomials of this order of k, or higher, already exist in the literature (e.g. the micromorphic model with ∇P and $\nabla \dot{P}$ in its energy density).

As a proof of concept for the fact that the dispersion polynomial must be of the fourth order or higher in order to describe the dispersion, we briefly show a case of how this dispersion could be described by enriching the kinematics of the RRMM. The dispersion polynomial of the RRMM is only of the second order of k, cf. eq. (3.23). We decide to add a new kinematical field (second order tensor) $Q(x,t)$ and its gradient in our model, and modify the Strain energy density of the model (3.2) by adding two new terms W_Q related to this new kinematical field

$$W_Q = \frac{1}{2a} \left\langle \mathbb{C}_c \operatorname{skew} (\nabla u - P + aQ) , \operatorname{skew} (\nabla u - P + aQ) \right\rangle + \frac{b}{2} \left\langle \mathbb{C}_c : \nabla \operatorname{skew} Q, \nabla \operatorname{skew} Q \right\rangle . \tag{7.3}$$

Here, $\mathbb{C}_c$ is the same elastic 4th order elasticity tensor that already appears in the RRMM, $a, b > 0$ are two new scalar material parameters and : is a double contraction. Note that we only add skew Q as

the aim of this concept is to enrich the shear modes of our model. This allows us to have a dispersion polynomial of the fourth order with respect to k (only for shear waves) of the form

$$(q_1 k^4 + q_2 k^4) - (q_3 + q_4 k^2 + q_5 k^4)\omega^2 + (q_6 + q_7 k^2 + q_8 k^4)\omega^4 - (q_9 + q_{10} k^2 + q_{11} k^4)\omega^6 = 0 \qquad (7.4)$$

where $q_1, q_2, ..., q_{11}$ are expressions of the elastic constants of our model (including a and b). The dispersion curves with and without the new additional terms in the Strain energy density, can be seen in Fig. 7.10.

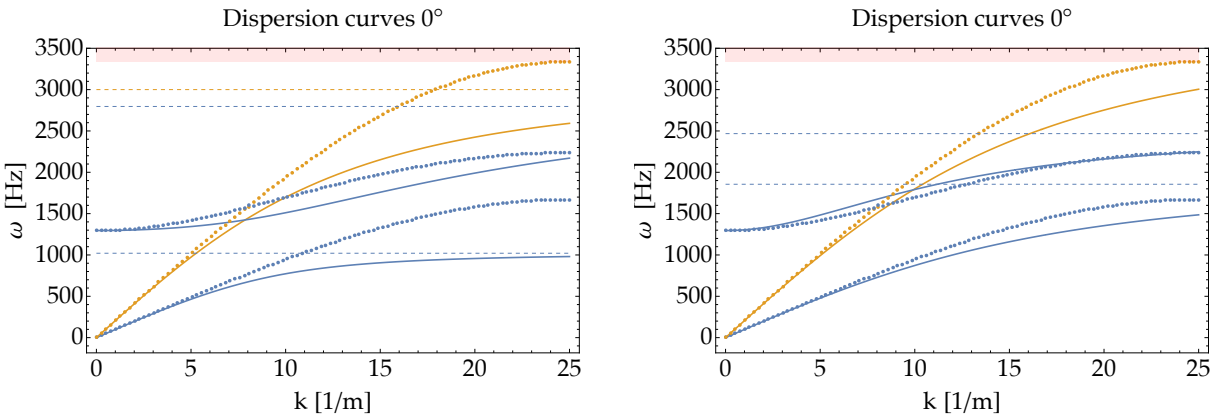

Figure 7.10: Dispersion curves for 0° propagation for the RRMM (left) and the RRMM with enhanced Strain energy density W_Q (right). Shear curves are colored in blue, while pressure curves are colored in yellow. The asymptotes are shown with dashed lines while the band-gap region is colored in light red. The figure shows a close-up of the first three modes and not all six that both models can describe.

We observe that the RRMM, having only a second order polynomial with respect to k, is not able to capture the dispersion of the first two shear modes in the frequency region of interest (at the range where both curves co-exist for the same frequency). On the contrary, the enhanced version with W_Q, having a fourth order polynomial with respect to k, is able to capture the dispersion.

We must, however, re-iterate, that the new model showed is primarily a proof of concept. Enhanced versions of the RRMM are still under investigation (including the present one), and in general one should be careful while arbitrarily adding new terms in the energy density to always check that the well-posedness of the model is conserved, especially if the additions involve new kinematical fields.

Conclusion

When modeling metamaterials of finite-size, boundary effects arise related to the choice of unit cell "cut". Regarding the choice of unit cell "cut" and its implications on microstructured metamaterials, we showed examples of how this choice can lead to lower or higher transmissibility values in the band-gap region, as well as in other frequency regions and discussed some potential applications including shielding, focusing and energy harvesting. We also showed that it is possible this choice could lead to the suppression of a specific mode of Bloch-Floquet analysis.

It is, however, well known that mechanical metamaterials, especially those studied in this thesis (made out of a single phase), possess very intricate geometries that lead to huge computational costs. This calls for a homogenised modeling of the microstructured metamaterials using enriched continua. The homogenised modeling of finite-size mechanical metamaterials can be effectively separated into two important parts that must both be accounted for if one wants an accurate homogenised metamaterial description:

- Modeling of the infinite size metamaterial and
- Modeling of boundary effects related to the finite-size.

For the first part, an enriched continuum must be used that can fulfill one criterion. The model must be able to accurately capture the dispersion of the infinitely big metamaterial (Bloch-Floquet dispersion curves). We showed that this criterion can be separated into two, the one being, that the dispersion polynomial of the enriched model must be of the correct order with respect to frequency ω and wavenumber k, and the other being that the curves must have enough "freedom" to capture the needed dispersion for every angle and polarisation. We saw that the RRMM fulfills this criterion for the dispersion modes excited in our tests, and can therefore be used safely for modeling the infinite metamaterials studied in this thesis.

However, regarding finite-size metamaterials, the RRMM (as every other enriched continuum using the same methodology) needs further enrichment of its boundary conditions to capture various boundary effects that might appear in finite-size microstructured specimens depending on the unit cell "cut" used. This calls for the use of the method of interface forces. The method states that in the case of modeling a finite-size metamaterial using an enriched continuum, any boundary effect taking place in the microstructured metamaterial must lead to the activation of a suitable surface force on an interface/free boundary, of the enriched continuum. A choice of a different unit cell "cut" leads to a different boundary effect in the microstructured metamaterial, and thus to a different surface force on the interfaces/ free boundaries, of the enriched continuum.

We applied this method to two locally resonant metamaterials and demonstrated its versatility in capturing boundary effects, that is, edge effects, boundary effects that propagate in the bulk, and boundary effects that are related to the finite-size of the structure itself. Specifically regarding edge effects, we introduced edge tests and discussed their potential for edge effect prediction. It is possible that edge tests could be generalised as a method to predict edge effects. However to construct an edge test we need to know a-priori how the edge behaves in a similar metamaterial under a similar test, which calls for data collection and/or further understanding of edge effects in general. Furthermore, we showed that for the tests presented, edge effects may be associated to a shear stiffness transfer from the unit cell to the edge of the metamaterial and that edge effects are usually not affected by a change in the number of unit cells used in the y-direction, as long as this number is bigger than one. We explained that for the method of interface forces, this means that the interface force on the "free" boundary remains invariant with respect to a change in the number of unit cells in the y-direction. We discussed the two possible methodologies one can follow to find the appropriate interface forces that accurately describes the boundary effect and explained why, in the cases shown here, the one that includes direct inspection of the displacement field

and deformed shape was preferred. Nevertheless both methods, if applied correctly, should lead to the same result.

Moreover, we applied the method of interface forces on four 3×2 finite-sized labyrinthine metamaterials constructed from different "cuts", showing that even if the size of a metamaterial is very small, the method can still make the response more accurate. We proposed a particular ansatz that the activated interface force on the Cauchy/RRM interface must have in the cases we investigated, and we have seen that this ansatz holds in almost all cases unless the wavelength becomes twice the size of the specimen or smaller while the frequency is not close to a band-gap frequency region.

Given our results, coupling an enriched continuum with the method of interface forces is absolutely necessary if one wants to describe boundary effects in finite-size specimens using a homogenised description. For the future, two open problems that still remain necessary for applications of the method in the design and optimization of structures are:

- Associating interface forces to some physical quantities (i.e. understanding the physical origin of boundary effects). As discussed previously, in the case of some particular edge effects, we could argue that the edge effect can be attributed to some extent to the low shear stiffness of the unit cell, which then gets transferred to the edge, since the edge is a row built by the periodic repetition of the same unit cell. However, this offers an understanding that is more qualitative. If we want to prove claims like this to be true, then shear stiffness and a law for its transfer from the unit cell to the edge must be represented by physical quantities and hence much more research is needed for the complete understanding of this and much more different boundary effects.
- Understanding how interface forces scale when the size of the metamaterial changes, i.e. when we change arbitrarily the number of unit cells in directions x and y for the same test.

It is the author's opinion at this particular point, that the former problem must be addressed before the latter, even though it is not impossible, that a large number of data of calibrated interface forces corresponding to the latter problem could lead to some understanding of the former.

Bibliography

[1] S. Abrate, J.-F. Ferrero, and P. Navarro. "Cohesive zone models and impact damage predictions for composite structures". *Meccanica* 50 (2015), 2587–2620.

[2] A. Aivaliotis, D. Tallarico, M.-V. d'Agostino, A. Daouadji, P. Neff, and A. Madeo. "Frequency-and angle-dependent scattering of a finite-sized meta-structure via the relaxed micromorphic model". *Archive of Applied Mechanics* 90 (2020), 1073–1096.

[3] G. Alfano and E. Sacco. "Combining interface damage and friction in a cohesive-zone model". *International Journal for Numerical Methods in Engineering* 68.5 (2006), 542–582.

[4] F. Bloch. "Über die quantenmechanik der elektronen in kristallgittern". *Zeitschrift für Physik* 52.7 (1929), 555–600.

[5] G. Bordiga, L. Cabras, A. Piccolroaz, and D. Bigoni. "Prestress tuning of negative refraction and wave channeling from flexural sources". *Applied Physics Letters* 114.4 (2019).

[6] L. Brillouin. "Wave propagation in periodic structures" (1946).

[7] R. D. Campilho, M. D. Banea, J. Neto, and L. F. da Silva. "Modelling adhesive joints with cohesive zone models: effect of the cohesive law shape of the adhesive layer". *International Journal of Adhesion and Adhesives* 44 (2013), 48–56.

[8] A. H. Castro Neto, F. Guinea, N. M. Peres, K. S. Novoselov, and A. K. Geim. "The electronic properties of graphene". *Reviews of modern physics* 81.1 (2009), 109–162.

[9] A.-L. Cauchy. "Sur les équations qui expriment les conditions d'équilibre ou les lois du mouvement intérieur d'un corps solide, élastique ou non élastique". *Ex. de Math* 3 (1828), 160–187.

[10] A. Chen and X. Zhang. "Two-sided Acoustic Metascreen for Broadband and Individual Reflection and Transmission Control". *arXiv preprint arXiv:2403.10548* (2024).

[11] V. Cool, E. Deckers, L. Van Belle, and C. Claeys. "A guide to numerical dispersion curve calculations: Explanation, interpretation and basic Matlab code". *Mechanical Systems and Signal Processing* 215 (2024), 111393.

[12] E. M. P. Cosserat and F. Cosserat. *Théorie des Corps Déformables*. A. Hermann et fils, 1909.

[13] S. C. Cowin and J. W. Nunziato. "Linear elastic materials with voids". *Journal of Elasticity* 13 (1983), 125–147.

[14] J. De Ponti, L. Iorio, M. Rosso, F. Maspero, A. Esposito, T. A. Afifi, M. Riani, G. Gattere, A. Di Matteo, A. Corigliano, et al. "Graded Micro-Resonators For Enhanced Sensing and Energy Harvesting In MEMS With Lead-Free Piezoelectric Materials". *2024 IEEE 23rd International Conference on Micro and Miniature Power Systems, Self-Powered Sensors and Energy Autonomous Devices (PowerMEMS)*. IEEE. 2024, 155–158.

[15] P. Demetriou, G. Rizzi, and A. Madeo. "Reduced relaxed micromorphic modeling of harmonically loaded metamaterial plates: investigating boundary effects in finite-size structures". *Archive of Applied Mechanics* 94.1 (2024), 81–98.

[16] P. Demetriou, J. Voss, and A. Madeo. "Effective interface forces to model boundary effects in a finite-size metamaterial through the reduced relaxed micromorphic model". *to appear in: Mathematics and Mechanics of Solids* (2025).

[17] F. Demore, G. Rizzi, M. Collet, P. Neff, and A. Madeo. "Unfolding engineering metamaterials design: Relaxed micromorphic modeling of large-scale acoustic meta-structures". *Journal of the Mechanics and Physics of Solids* 168 (2022), 104995.

[18] F. Erel-Demore, J. Voss, P. Neff, and A. Madeo. "Null-lagrangians in the micro-inertia contribution of the reduced relaxed micromorphic model. Theoretical and computational insights with applications". *Archive of Applied Mechanics* 95.2 (2025), 50.

[19] A. C. Eringen. *Microcontinuum Field Theories: I. Foundations and Solids*. Springer Science & Business Media, 2012.

[20] A. C. Eringen and E. Suhubi. "Nonlinear theory of simple micro-elastic solids—I". *International Journal of Engineering Science* 2.2 (1964), 189–203.

[21] A. C. Eringen. "Mechanics of micromorphic materials". *Applied Mechanics: Proceedings of the Eleventh International Congress of Applied Mechanics Munich (Germany) 1964*. Springer. 1966, 131–138.

[22] G. Floquet. "Sur les équations différentielles linéaires à coefficients périodiques". *Annales Scientifiques de l'École Normale Supérieure*. Vol. 12. 1883, 47–88.

[23] T. Frenzel, M. Kadic, and M. Wegener. "Three-dimensional mechanical metamaterials with a twist". *Science* 358.6366 (2017), 1072–1074.

[24] M. Garau, G. Carta, M. Nieves, I. Jones, N. Movchan, and A. Movchan. "Interfacial waveforms in chiral lattices with gyroscopic spinners". *Proceedings of the Royal Society A: Mathematical, Physical and Engineering Sciences* 474.2215 (2018), 20180132.

[25] P. Germain. "The method of virtual power in continuum mechanics. Part 2: Microstructure". *SIAM Journal on Applied Mathematics* 25.3 (1973), 556–575.

[26] I.-D. Ghiba, P. Neff, A. Madeo, L. Placidi, and G. Rosi. "The relaxed linear micromorphic continuum: existence, uniqueness and continuous dependence in dynamics". *Mathematics and Mechanics of Solids* 20.10 (2015), 1171–1197.

[27] I.-D. Ghiba, G. Rizzi, A. Madeo, and P. Neff. "Cosserat micropolar elasticity: classical Eringen vs. dislocation form". *Journal of Mechanics of Materials and Structures* 18.1 (2023), 93–123.

[28] R. Giusti and G. Lucchetta. "Cohesive Zone Modeling of the Interface Fracture in Full-Thermoplastic Hybrid Composites for Lightweight Application". *Polymers* 15.22 (2023), 4459.

[29] E. Glaessgen, E. Saether, D. Phillips, and V. Yamakov. "Multiscale modeling of grain-boundary fracture: cohesive zone models parameterized from atomistic simulations". *47th AIAA/ASME/ASCE/AHS/ASC Structures, Structural Dynamics, and Materials Conference*. 2006, 1674.

[30] A. E. Green and R. S. Rivlin. "Multipolar continuum mechanics". *Archive for Rational Mechanics and Analysis* 17 (1964), 113–147.

[31] S. Guenneau, A. Movchan, G. Pétursson, and S. A. Ramakrishna. "Acoustic metamaterials for sound focusing and confinement". *New Journal of Physics* 9.11 (2007), 399.

[32] M. E. Gurtin and A. Ian Murdoch. "A continuum theory of elastic material surfaces". *Archive for Rational Mechanics and Analysis* 57 (1975), 291–323.

[33] Z. Hashin. "Thin interphase/imperfect interface in elasticity with application to coated fiber composites". *Journal of the Mechanics and Physics of Solids* 50.12 (2002), 2509–2537.

[34] S. Hermann, K. Billon, A.-M. Parlak, J. Orlowsky, M. Collet, and A. Madeo. "Design and experimental validation of a finite-size labyrinthine metamaterial for vibro-acoustics: enabling upscaling towards large-scale structures". *Philosophical Transactions A* 382.2278 (2024), 20230367.

[35] R. Hooke. *Lectures de Potentia Restitutiva, or of Spring Explaining the Power of Springing Bodies*. 6. John Martyn, 2016.

[36] H. Huang, C. Sun, and G. Huang. "On the negative effective mass density in acoustic metamaterials". *International Journal of Engineering Science* 47.4 (2009), 610–617.

[37] A. Huber. "Numerical modeling of guided waves in anisotropic composites with application to air-cOxford University Pressled ultrasonic inspection" (2021).

[38] Y. Itin and F. W. Hehl. "The constitutive tensor of linear elasticity: its decompositions, Cauchy relations, null Lagrangians, and wave propagation". *Journal of Mathematical Physics* 54.4 (2013).

[39] A. Javili, P. Steinmann, and J. Mosler. "Micro-to-macro transition accounting for general imperfect interfaces". *Computer Methods in Applied Mechanics and Engineering* 317 (2017), 274–317.

[40] M. Kafesaki, M. Sigalas, and E. Economou. "Elastic wave band gaps in 3-D periodic polymer matrix composites". *Solid State Communications* 96.5 (1995), 285–289.

[41] I. Katsivalis, O. T. Thomsen, S. Feih, and M. Achintha. "Development of cohesive zone models for the prediction of damage and failure of glass/steel adhesive joints". *International Journal of Adhesion and Adhesives* 97 (2020), 102479.

[42] H. Khoramishad, A. Crocombe, K. Katnam, and I. Ashcroft. "Predicting fatigue damage in adhesively bonded joints using a cohesive zone model". *International Journal of Fatigue* 32.7 (2010), 1146–1158.

[43] A. O. Krushynska, F. Bosia, and N. M. Pugno. "Labyrinthine acoustic metamaterials with space-coiling channels for low-frequency sound control". *Acta Acustica United with Acustica* 104.2 (2018), 200–210.

[44] M. S. Kushwaha. "Classical band structure of periodic elastic composites". *International Journal of Modern Physics B* 10.09 (1996), 977–1094.

[45] R. Lakes. "Experimental Micro Mechanics Methods for Conventional and Negative Poisson's Ratio Cellular Solids as Cosserat Continua". *Journal of Engineering Materials and Technology* 113.1 (1991), 148–155.

[46] R. Lakes. "Foam structures with a negative Poisson's ratio". *Science* 235.4792 (1987), 1038–1040.

[47] R. S. Lakes. "Size effects and micromechanics of a porous solid". *Journal of Materials Science* 18 (1983), 2572–2580.

[48] R. Lakes. "Dynamical study of couple stress effects in human compact bone." *Journal of Biomechanical Engineering* 104.1 (1982), 6–11.

[49] T. Lenders, L. Liu, and V. G. Kouznetsova. "Efficient and accurate analysis of locally resonant acoustic metamaterial plates using computational homogenization". *Computational Mechanics* (2024), 1–23.

[50] W. Li and T. Siegmund. "An analysis of crack growth in thin-sheet metal via a cohesive zone model". *Engineering Fracture Mechanics* 69.18 (2002), 2073–2093.

[51] Z. Liu, C. T. Chan, and P. Sheng. "Three-component elastic wave band-gap material". *Physical Review B* 65.16 (2002), 165116.

[52] Z. Liu, X. Zhang, Y. Mao, Y. Y. Zhu, Z. Yang, C. T. Chan, and P. Sheng. "Locally resonant sonic materials". *Science* 289.5485 (2000), 1734–1736.

[53] E. Lorentz, S. Cuvilliez, and K. Kazymyrenko. "Modelling large crack propagation: from gradient damage to cohesive zone models". *International Journal of fracture* 178.1 (2012), 85–95.

[54] A. Madeo, P. Neff, I.-D. Ghiba, L. Placidi, and G. Rosi. "Wave propagation in relaxed micromorphic continua: modeling metamaterials with frequency band-gaps". *Continuum Mechanics and Thermodynamics* 27.4 (2015), 551–570.

[55] R. Martínez-Sala, J. Sancho, J. V. Sánchez, V. Gómez, J. Llinares, F. Meseguer, et al. "Sound attenuation by sculpture". *Nature* 378.6554 (1995), 241–241.

[56] R. D. Mindlin. "Micro-structure in linear elasticity". *Archive for Rational Mechanics and Analysis* 16 (1964), 51–78.

[57] R. D. Mindlin and N. Eshel. "On first strain-gradient theories in linear elasticity". *International Journal of Solids and Structures* 4.1 (1968), 109–124.

[58] M. Miniaci, R. K. Pal, R. Manna, and M. Ruzzene. "Valley-based splitting of topologically protected helical waves in elastic plates". *Physical Review B* 100.2 (2019), 024304.

[59] G. Moeckel. "Thermodynamics of an interface". *Archive for Rational Mechanics and Analysis* 57.3 (1975), 255–280.

[60] J. E. Moore. "The birth of topological insulators". *Nature* 464.7286 (2010), 194–198.

[61] A. Movchan, G. Mishuris, and F. Sabina. *Wave generation and transmission in multi-scale complex media and structured metamaterials*. 2022.

[62] A. I. Murdoch. "A thermodynamical theory of elastic material interfaces". *The Quarterly Journal of Mechanics and Applied Mathematics* 29.3 (1976), 245–275.

[63] A. H. Nayfeh. *Wave Propagation in Layered Anisotropic Media: With Application to Composites*. Elsevier, 1995.

[64] P. Neff, B. Eidel, M. V. d'Agostino, and A. Madeo. "Identification of scale-independent material parameters in the relaxed micromorphic model through model-adapted first order homogenization". *Journal of Elasticity* 139.2 (2020), 269–298.

[65] P. Neff, I.-D. Ghiba, M. Lazar, and A. Madeo. "The relaxed linear micromorphic continuum: well-posedness of the static problem and relations to the gauge theory of dislocations". *Quarterly Journal of Mechanics and Applied Mathematics* 68.1 (2015), 53–84.

[66] P. Neff, I.-D. Ghiba, A. Madeo, L. Placidi, and G. Rosi. "A unifying perspective: the relaxed linear micromorphic continuum". *Continuum Mechanics and Thermodynamics* 26 (2014), 639–681.

[67] X. Ni, S. Yves, A. Krasnok, and A. Alu. "Topological metamaterials". *Chemical Reviews* 123.12 (2023), 7585–7654.

[68] J. W. Nunziato and S. C. Cowin. "A nonlinear theory of elastic materials with voids". *Archive for Rational Mechanics and Analysis* 72 (1979), 175–201.

[69] J. B. Pendry, D. Schurig, and D. R. Smith. "Controlling electromagnetic fields". *Science* 312.5781 (2006), 1780–1782.

[70] R. W. Perkins JR and D. Thompson. "Experimental evidence of a couple-stress effect." *AIAA Journal* 11.7 (1973), 1053–1055.

[71] M. Pezzotta, Z. Zhang, M. Jensen, T. Grande, and M.-A. Einarsrud. "Cohesive zone modeling of grain boundary microcracking induced by thermal anisotropy in titanium diboride ceramics". *Computational Materials Science* 43.3 (2008), 440–449.

[72] A. S. Phani and M. I. Hussein. *Dynamics of Lattice materials*. Wiley Online Library, 2017.

[73] G. Piola. *Intorno alle Equazioni Fondamentali del Movimento di Corpi Qualsivogliono, Considerati Secondo la Naturale Loro Forma e Costituzione: Memoria*. Springer, 1846.

[74] L. A. P. Ramirez, F. Erel-Demore, G. Rizzi, J. Voss, and A. Madeo. "Effective surface forces and non-coherent interfaces within the reduced relaxed micromorphic modeling of finite-size mechanical metamaterials". *Journal of the Mechanics and Physics of Solids* 186 (2024), 105558.

[75] L. A. P. Ramirez, G. Rizzi, and A. Madeo. "Multi-element metamaterial's design through the relaxed micromorphic model". *Sixty Shades of Generalized Continua: Dedicated to the 60th Birthday of Prof. Victor A. Eremeyev*. Springer, 2023, 579–600.

[76] S. Y. Ren. *Electronic States in Crystals of Finite Size: Quantum Confinement of Bloch Waves*. Springer, 2006.

[77] G. Rizzi, F. Dal Corso, D. Veber, and D. Bigoni. "Identification of second-gradient elastic materials from planar hexagonal lattices. Part I: Analytical derivation of equivalent constitutive tensors". *International Journal of Solids and Structures* 176 (2019), 1–18.

[78] G. Rizzi, F. Dal Corso, D. Veber, and D. Bigoni. "Identification of second-gradient elastic materials from planar hexagonal lattices. Part II: Mechanical characteristics and model validation". *International Journal of Solids and Structures* 176 (2019), 19–35.

[79] G. Rizzi, M. Collet, F. Demore, B. Eidel, P. Neff, and A. Madeo. "Exploring metamaterials' structures through the relaxed micromorphic model: switching an acoustic screen into an acoustic absorber". *Frontiers in Materials* 7 (2021), 589701.

[80] G. Rizzi, M. V. d'Agostino, P. Neff, and A. Madeo. "Boundary and interface conditions in the relaxed micromorphic model: Exploring finite-size metastructures for elastic wave control". *Mathematics and Mechanics of Solids* 27.6 (2022), 1053–1068.

[81] G. Rizzi, M. V. d'Agostino, J. Voss, D. Bernardini, P. Neff, and A. Madeo. "From frequency-dependent models to frequency-independent enriched continua for mechanical metamaterials". *European Journal of Mechanics A./Solids* 106 (2024), 105269.

[82] G. Rizzi, H. Khan, I.-D. Ghiba, A. Madeo, and P. Neff. "Analytical solution of the uniaxial extension problem for the relaxed micromorphic continuum and other generalized continua (including full derivations)". *Archive of Applied Mechanics* (2021), 1–17.

[83] G. Rizzi, P. Neff, and A. Madeo. "Metamaterial shields for inner protection and outer tuning through a relaxed micromorphic approach". *Philosophical Transactions of the Royal Society A* 380.2231 (2022), 20210400.

[84] G. Rizzi, D. Tallarico, P. Neff, and A. Madeo. “Towards the conception of complex engineering meta-structures: Relaxed-micromorphic modelling of low-frequency mechanical diodes/high-frequency screens”. *Wave Motion* 113 (2022), 102920.

[85] S. Roth, G. Hütter, and M. Kuna. “Simulation of fatigue crack growth with a cyclic cohesive zone model”. *International Journal of Fracture* 188.1 (2014), 23–45.

[86] P. Sharma, S. Ganti, and N. Bhate. “Effect of surfaces on the size-dependent elastic state of nano-inhomogeneities”. *Applied Physics Letters* 82.4 (2003), 535–537.

[87] R. A. Shelby, D. R. Smith, and S. Schultz. “Experimental verification of a negative index of refraction”. *Science* 292.5514 (2001), 77–79.

[88] W. Shockley. “On the surface states associated with a periodic potential”. *Physical Review* 56.4 (1939), 317.

[89] M. Sigalas and E. N. Economou. “Band structure of elastic waves in two dimensional systems”. *Solid State Communications* 86.3 (1993), 141–143.

[90] I. Simonovski and L. Cizelj. “Cohesive zone modeling of intergranular cracking in polycrystalline aggregates”. *Nuclear Engineering and Design* 283 (2015), 139–147.

[91] D. R. Smith, W. J. Padilla, D. Vier, S. C. Nemat-Nasser, and S. Schultz. “Composite medium with simultaneously negative permeability and permittivity”. *Physical Review Letters* 84.18 (2000), 4184.

[92] D. R. Smith and J. B. Pendry. “Homogenization of metamaterials by field averaging”. *Journal of the Optical Society of America B* 23.3 (2006), 391–403.

[93] L. Spannraft, G. Possart, P. Steinmann, and J. Mergheim. “Generalized interfaces enabling macroscopic modeling of structural adhesives and their failure”. *Forces in Mechanics* 9 (2022), 100137.

[94] I. Tamm. “On the possible bound states of electrons on a crystal surface”. *Physikalische Zeitschrift der Sowjetunion* 1 (1932), 733–735.

[95] “Theories of elasticity with couple-stress”. *Archive for Rational Mechanics and Analysis* 17.2 (1964), 85–112.

[96] M. Touboul, B. Vial, R. Assier, S. Guenneau, and R. V. Craster. “High-frequency homogenization for periodic dispersive media”. *Multiscale Modeling & Simulation* 22.3 (2024), 1136–1168.

[97] V. Veselago. “The electrodynamics of substances with simultaneously negative values of ε and μ”. *Soviet Physics Uspekhi* 92.3 (1967), 517–526.

[98] K. Y. Volokh. “Comparison between cohesive zone models”. *Communications in Numerical Methods in Engineering* 20.11 (2004), 845–856.

[99] J. Voss, G. Rizzi, P. Neff, and A. Madeo. “Modeling a labyrinthine acoustic metamaterial through an inertia-augmented relaxed micromorphic approach”. *Mathematics and Mechanics of Solids* 28.10 (2023), 2177–2201.

[100] X. Wang. “A simple proof of Descartes’s rule of signs”. *The American Mathematical Monthly* 111.6 (2004), 525–526.

[101] Y. Wu, Y. Lai, and Z.-Q. Zhang. “Elastic metamaterials with simultaneously negative effective shear modulus and mass density”. *Physical Review Letters* 107.10 (2011), 105506.

[102] J. Yang and R. Lakes. “Transient study of couple stress effects in compact bone: torsion.” *Journal of Biomechanical Engineering* 103.4 (1981), 275–279.

[103] J. Yang and R. S. Lakes. “Experimental study of micropolar and couple stress elasticity in compact bone in bending”. *Journal of Biomechanics* 15.2 (1982), 91–98.

[104] Z. Yang, Z. Zhu, Y. Xia, F. Yang, Y. Sun, and H. Jiang. “Modified cohesive zone model for soft adhesive layer considering rate dependence of intrinsic fracture energy”. *Engineering Fracture Mechanics* 258 (2021), 108089.

[105] C. Yilmaz and G. M. Hulbert. “Dynamics of locally resonant and inertially amplified lattice materials”. *Dynamics of lattice materials* (2017), 233–258.

[106] C. Yilmaz, G. M. Hulbert, and N. Kikuchi. “Phononic band gaps induced by inertial amplification in periodic media”. *Physical Review B* 76.5 (2007), 054309.

Appendix A

Appendix

A.1 Parameter values for the dispersion polynomial of the RRMM

For the reduced relaxed micromorphic model (RRMM), we arrive (3.23) at the dispersion polynomial

$$c_0 k^2 - \left(c_1 + c_2 k^2\right) \omega^2 + \left(c_3 + c_4 k^2\right) \omega^4 - \left(c_5 + c_6 k^2\right) \omega^6 = 0 \tag{A.1}$$

where the coefficients $c_1 , \cdots , c_6$ have the following expressions:

Pressure 0°

Coefficient	Expression
c_0	$4(\kappa_e\kappa_m\mu_e + \kappa_m\mu_e\mu_m + \kappa_e(\kappa_m + \mu_e)\mu_m)$
c_1	$4\rho(\kappa_e + \kappa_m)(\mu_e + \mu_m)$
c_2	$4L_c^2\rho(\gamma_1\kappa_e\kappa_m + \gamma_1(\kappa_e + \kappa_m)\mu_e + (\kappa_e + \kappa_m)\overline{\kappa}_\gamma\mu_e + \kappa_e\kappa_\gamma\mu_e + (\kappa_m\overline{\kappa}_\gamma + \kappa_e(\overline{\kappa}_\gamma + \kappa_\gamma) + \kappa_\gamma\mu_e)\mu_m + \overline{\gamma}_1(\kappa_e + \kappa_m)(\mu_e + \mu_m))$
c_3	$4L_c^2\rho^2(\gamma_1(\kappa_e + \kappa_m) + \kappa_\gamma(\mu_e + \mu_m))$
c_4	$4L_c^4\rho^2(\overline{\gamma}_1\gamma_1(\kappa_e + \kappa_m) + \gamma_1\kappa_m\overline{\kappa}_\gamma + \gamma_1\kappa_e(\overline{\kappa}_\gamma + \kappa_\gamma) + \gamma_1\kappa_\gamma\mu_e + \overline{\gamma}_1\kappa_\gamma(\mu_e + \mu_m) + \overline{\kappa}_\gamma\kappa_\gamma(\mu_e + \mu_m))$
c_5	$4L_c^4\rho^3\gamma_1\kappa_\gamma$
c_6	$4L_c^6\rho^3\gamma_1(\overline{\gamma}_1 + \overline{\kappa}_\gamma)\kappa_\gamma$

Shear 0°

Coefficient	Expression
c_0	$4\mu_c\mu_e^*\mu_m^*$
c_1	$4\rho\mu_c(\mu_e^* + \mu_m^*)$
c_2	$4L_c^2\rho((\overline{\gamma}_2 + \overline{\gamma}_1^* + \gamma_2 + \gamma_1^*)\mu_c\mu_e^* + (\overline{\gamma}_2 + \overline{\gamma}_1^* + \gamma_2)\mu_c\mu_m^* + \gamma_2\mu_e^*\mu_m^*)$
c_3	$4L_c^2\rho^2(\gamma_1^*\mu_c + \gamma_2(\mu_e^* + \mu_m^*))$
c_4	$4L_c^4\rho^2(\overline{\gamma}_2\gamma_1^*\mu_c + \overline{\gamma}_1^*\gamma_2(\mu_c + \mu_e^*) + \overline{\gamma}_2\gamma_1^*(\mu_e^* + \mu_m^*))$
c_5	$4L_c^4\rho^3\gamma_2\gamma_1^*$
c_6	$4L_c^6\rho^3(\overline{\gamma}_2 + \overline{\gamma}_1^*)\gamma_2\gamma_1^*$

Pressure $45°$

Coefficient	Expression
c_0	$4(\kappa_e\kappa_m\mu_e^* + \kappa_m\mu_e^*\mu_m^* + \kappa_e(\kappa_m + \mu_e^*)\mu_m^*)$
c_1	$4\rho(\kappa_e + \kappa_m)(\mu_e^* + \mu_m^*)$
c_2	$4L_c^2\rho(\gamma_1^*\kappa_e\kappa_m+\gamma_1^*(\kappa_e+\kappa_m)\mu_e^*+(\kappa_e+\kappa_m)\overline{\kappa}_\gamma\mu_e^*+\kappa_e\kappa_\gamma\mu_e^*+(\kappa_m\overline{\kappa}_\gamma+\kappa_e(\overline{\kappa}_\gamma+\kappa_\gamma)+\kappa_\gamma\mu_e^*)\mu_m^*+\overline{\gamma}_1^*(\kappa_e+\kappa_m)(\mu_e^*+\mu_m^*))$
c_3	$4L_c^2\rho^2(\gamma_1^*(\kappa_e + \kappa_m) + \kappa_\gamma(\mu_e^* + \mu_m^*))$
c_4	$4L_c^4\rho^2(\overline{\gamma}_1^*\gamma_1^*(\kappa_e + \kappa_m) + \gamma_1^*\kappa_m\overline{\kappa}_\gamma + \gamma_1^*\kappa_e(\overline{\kappa}_\gamma + \kappa_\gamma) + \gamma_1^*\kappa_\gamma\mu_e^* + \overline{\gamma}_1^*\kappa_\gamma(\mu_e^* + \mu_m^*) + \overline{\kappa}_\gamma\kappa_\gamma(\mu_e^* + \mu_m^*))$
c_5	$4L_c^4\rho^3\gamma_1^*\kappa_\gamma$
c_6	$4L_c^6\rho^3\gamma_1^*(\overline{\gamma}_1^* + \overline{\kappa}_\gamma)\kappa_\gamma$

Shear $45°$

Coefficient	Expression
c_0	$4\mu_c\mu_e\mu_m$
c_1	$4\rho\mu_c(\mu_e + \mu_m)$
c_2	$4L_c^2\rho((\overline{\gamma}_1 + \overline{\gamma}_2 + \gamma_1 + \gamma_2)\mu_c\mu_e + (\overline{\gamma}_1 + \overline{\gamma}_2 + \gamma_2)\mu_c\mu_m + \gamma_2\mu_e\mu_m)$
c_3	$4L_c^2\rho^2(\gamma_1\mu_c + \gamma_2(\mu_e + \mu_m))$
c_4	$4L_c^4\rho^2(\overline{\gamma}_1\gamma_1\mu_c+\overline{\gamma}_2\gamma_1\mu_c+\gamma_1\gamma_2(\mu_c+\mu_e)+\overline{\gamma}_1\gamma_2(\mu_e+\mu_m)+\overline{\gamma}_2\gamma_2(\mu_e+\mu_m))$
c_5	$4L_c^4\rho^3\gamma_1\gamma_2$
c_6	$4L_c^6\rho^3(\overline{\gamma}_1 + \overline{\gamma}_2)\gamma_1\gamma_2$

Overall, shear and pressure curves for $0°$ and $45°$ wave incidence depend on the following parameters:

	Shear	Pressure
$0°$	$\overline{\gamma}_2, \overline{\gamma_1}^*, \gamma_2, \gamma_1^*, \mu_c, \mu_e^*, \mu_m^*$	$\gamma_1, \kappa_e, \kappa_m, \overline{\gamma}_1, \overline{\kappa}_\gamma, \kappa_\gamma, \mu_e, \mu_m$
$45°$	$\overline{\gamma}_2, \overline{\gamma}_1, \gamma_2, \gamma_1, \mu_c, \mu_e, \mu_m$	$\gamma_1^*, \kappa_e, \kappa_m, \overline{\gamma_1}^*, \overline{\kappa}_\gamma, \kappa_\gamma, \mu_e^*, \mu_m^*$

A.2 Boundary conditions on a symmetry plane for a relaxed micromorphic medium using Curie's Symmetry Principle

Similarly to the work in [17] and [74], we shall use Curie's Symmetry Principle to define the symmetry conditions of the reduced relaxed micromorphic model. We suppose that our problem has a symmetry with respect to the plane $\mathcal{N}$ of normal $n \in \mathbb{R}^3$, we shall apply Curie's Symmetry Principle on our kinematical fields u and P

$$\begin{cases} u(x^\star) = u^\star(x)\,, \\ P(x^\star) = P^\star(x) \end{cases} \tag{A.2}$$

with $x^\star$ being the symmetric coordinate of x with respect to $\mathcal{N}$. Let's define the corresponding orthonormal bases $\{t_\alpha, t_\beta, n\}$ and $\{t_\alpha^*, t_\beta^*, n^*\}$ where for every base we define two tangent vectors and one normal vector with respect to the symmetry plane $\mathcal{N}$. Since $\mathcal{N}$ is a symmetry plane, it holds

$$t_\alpha^\star = t_\alpha\,, \quad t_\beta^\star = t_\beta \quad \text{and} \quad n^\star = -n\,. \tag{A.3}$$

Let's express u and P in their corresponding base

$$u = u_\alpha t_\alpha + u_\beta t_\beta + u_n n\,, \tag{A.4}$$

$$u^\star = u_\alpha t_\alpha^\star + u_\beta t_\beta^\star + u_n n^\star \tag{A.5}$$

and

$$P = P_{\alpha\alpha}t_\alpha \otimes t_\alpha + P_{\alpha\beta}t_\alpha \otimes t_\beta + P_{\alpha n}t_\alpha \otimes n + P_{\beta\alpha}t_\beta \otimes t_\alpha + P_{\beta\beta}t_\beta \otimes t_\beta + P_{\beta n}t_\beta \otimes n + P_{n\alpha}n \otimes t_\alpha + P_{n\beta}n \otimes t_\beta + P_{nn}n \otimes n\,, \tag{A.6}$$

$$P^\star = P_{\alpha\alpha}t^\star_\alpha \otimes t^\star_\alpha + P_{\alpha\beta}t^\star_\alpha \otimes t^\star_\beta + P_{\alpha n}t^\star_\alpha \otimes n^\star + P_{\beta\alpha}t^\star_\beta \otimes t^\star_\alpha + P_{\beta\beta}t^\star_\beta \otimes t^\star_\beta + P_{\beta n}t^\star_\beta \otimes n^\star + P_{n\alpha}n^\star \otimes t^\star_\alpha + P_{n\beta}n^\star \otimes t^\star_\beta + P_{nn}n^\star \otimes n^\star \tag{A.7}$$

where the components of the displacement u_i and the microdistortion tensor P_{ij} are the same in both bases. From Eq. (A.3) it is apparent that we can rewrite equations (A.5) and (A.7) in the form

$$u^\star = u_\alpha t_\alpha + u_\beta t_\beta - u_n n\,, \tag{A.8}$$

$$P^\star = P_{\alpha\alpha}t_\alpha \otimes t_\alpha + P_{\alpha\beta}t_\alpha \otimes t_\beta - P_{\alpha n}t_\alpha \otimes n + P_{\beta\alpha}t_\beta \otimes t_\alpha + P_{\beta\beta}t_\beta \otimes t_\beta - P_{\beta n}t_\beta \otimes n - P_{n\alpha}n \otimes t_\alpha - P_{n\beta}n \otimes t_\beta + P_{nn}n \otimes n\,. \tag{A.9}$$

We then define the points x and x^* as $x = x_0 + \epsilon n$ and $x^* = x_0 + \epsilon n^*$ where $x_0 \in \mathcal{N}$ and $\epsilon \in \mathbb{R}$. Points x and x^* represent symmetric points with respect to plane $\mathcal{N}$ and therefore it holds

$$x^\star = x_0 - \epsilon n\,. \tag{A.10}$$

For the kinematical field u, substituting in (A.2), one can get

$$u(x^\star) = u_\alpha(x_0 - \epsilon n)t_\alpha + u_\beta(x_0 - \epsilon n)t_\beta + u_n(x_0 - \epsilon n)n = u_\alpha(x_0 + \epsilon n)t_\alpha + u_\beta(x_0 + \epsilon n)t_\beta - u_n(x_0 + \epsilon n)n = u^\star(x)\,. \tag{A.11}$$

By identification for each expression in $\{t_\alpha, t_\beta, n\}$ we have

$$\begin{cases} u_\alpha(x_0 - \epsilon n)t_\alpha = u_\alpha(x_0 + \epsilon n)t_\alpha\,, \\ u_\beta(x_0 - \epsilon n)t_\beta = u_\beta(x_0 + \epsilon n)t_\beta\,, \\ u_n(x_0 - \epsilon n)n = -u_n(x_0 + \epsilon n)n\,. \end{cases} \tag{A.12}$$

In the same way, for the kinematical field P we arrive at

$$\begin{cases} P_{\alpha\alpha}(x_0 - \epsilon n)t_\alpha \otimes t_\alpha = P_{\alpha\alpha}(x_0 + \epsilon n)t_\alpha \otimes t_\alpha\,, \\ P_{\alpha\beta}(x_0 - \epsilon n)t_\alpha \otimes t_\beta = P_{\alpha\beta}(x_0 + \epsilon n)t_\alpha \otimes t_\beta\,, \\ P_{\alpha n}(x_0 - \epsilon n)t_\alpha \otimes n = -P_{\alpha n}(x_0 + \epsilon n)t_\alpha \otimes n\,, \\ P_{\beta\alpha}(x_0 - \epsilon n)t_\beta \otimes t_\alpha = P_{\beta\alpha}(x_0 + \epsilon n)t_\beta \otimes t_\alpha\,, \\ P_{\beta\beta}(x_0 - \epsilon n)t_\beta \otimes t_\beta = P_{\beta\beta}(x_0 + \epsilon n)t_\beta \otimes t_\beta\,, \\ P_{\beta n}(x_0 - \epsilon n)t_\beta \otimes n = -P_{\beta n}(x_0 + \epsilon n)t_\beta \otimes n\,, \\ P_{n\alpha}(x_0 - \epsilon n)n \otimes t_\alpha = -P_{n\alpha}(x_0 + \epsilon n)n \otimes t_\alpha\,, \\ P_{n\beta}(x_0 - \epsilon n)n \otimes t_\beta = -P_{n\beta}(x_0 + \epsilon n)n \otimes t_\beta\,, \\ P_{nn}(x_0 - \epsilon n)n \otimes n = P_{nn}(x_0 + \epsilon n)n \otimes n\,. \end{cases} \tag{A.13}$$

These conditions allow to reconstruct the displacement and microdistorsion fields at any point in space with respect to the symmetry plane, when their value is known on the opposite side of the symmetry plane. In the limit of $\epsilon \to 0$, equations (A.12) and (A.13) simplify to

$$\begin{cases} u_\alpha(x_0)t_\alpha = u_\alpha(x_0)t_\alpha\,, \\ u_\beta(x_0)t_\beta = u_\beta(x_0)t_\beta\,, \\ u_n(x_0)n = -u_n(x_0)n \end{cases} \qquad \text{and} \qquad \begin{cases} P_{\alpha\alpha}(x_0)t_\alpha \otimes t_\alpha = P_{\alpha\alpha}(x_0)t_\alpha \otimes t_\alpha\,, \\ P_{\alpha\beta}(x_0)t_\alpha \otimes t_\beta = P_{\alpha\beta}(x_0)t_\alpha \otimes t_\beta\,, \\ P_{\alpha n}(x_0)t_\alpha \otimes n = -P_{\alpha n}(x_0)t_\alpha \otimes n\,, \\ P_{\beta\alpha}(x_0)t_\beta \otimes t_\alpha = P_{\beta\alpha}(x_0)t_\beta \otimes t_\alpha\,, \\ P_{\beta\beta}(x_0)t_\beta \otimes t_\beta = P_{\beta\beta}(x_0)t_\beta \otimes t_\beta\,, \\ P_{\beta n}(x_0)t_\beta \otimes n = -P_{\beta n}(x_0)t_\beta \otimes n\,, \\ P_{n\alpha}(x_0)n \otimes t_\alpha = -P_{n\alpha}(x_0)n \otimes t_\alpha\,, \\ P_{n\beta}(x_0)n \otimes t_\beta = -P_{n\beta}(x_0)n \otimes t_\beta\,, \\ P_{nn}(x_0)n \otimes n = P_{nn}(x_0)n \otimes n\,. \end{cases} \tag{A.14}$$

Therefore it holds: $u_n = P_{\alpha n} = P_{\beta n} = P_{n\alpha} = P_{n\beta} = 0$. Thus, the following conditions must be satisfied at $\mathcal{N}$

$$\begin{cases} \langle u, n\rangle = 0\,, \\ \langle P, t_\alpha \otimes n\rangle = 0\,, \\ \langle P, t_\beta \otimes n\rangle = 0\,, \\ \langle P, n \otimes t_\alpha\rangle = 0\,, \\ \langle P, n \otimes t_\beta\rangle = 0 \end{cases} \qquad \forall x \in \mathcal{N}\,. \tag{A.15}$$

A.2.1 Pressure test in Chapter 6

In the case of the pressure test in Chapter 6 we have: $u_3 = P_{13} = P_{23} = P_{31} = P_{32} = P_{33} = 0$, $n = \{0, -1, 0\}$, $t_\alpha = \{1, 0, 0\}$ and $t_\beta = \{0, 0, 1\}$ the conditions of equation (A.15) state

$$\begin{cases} \langle u, n\rangle = -u_2 = 0\,, \\ \langle P, t_\alpha \otimes n\rangle = -P_{12} = 0\,, \\ \langle P, t_\beta \otimes n\rangle = 0\,, \\ \langle P, n \otimes t_\alpha\rangle = -P_{21} = 0\,, \\ \langle P, n \otimes t_\beta\rangle = 0 \end{cases} \qquad \forall x \in \mathcal{N}\,. \tag{A.16}$$

where now sub-indices $1, 2$ and 3 refer to coordinates x, y and z respectively, since tangent vector t_α points in the $x-$direction, tangent vector t_β points in the $z-$direction and our normal vector n points in the negative $y-$direction.

A.2.2 Shear test in Section 7.3

Regarding the shear test in Section 7.3, we have the particular case of Antisymmetry. This implies we have to set to zero the components that were free in eq. (A.16), while letting free the components that were set to zero before. Consequently, we have

$$\begin{cases} u_1 = 0\,, \\ P_{11} = 0\,, \\ P_{22} = 0 \end{cases} \qquad \forall x \in \mathcal{N}\,. \tag{A.17}$$

A.3 First variation for Cauchy elasticity

The Langrangian of the model is given by eq. (2.3) as

$$\begin{aligned} W(\operatorname{sym}\nabla u) &= \frac{1}{2}\langle \mathbb{C}_{\mathrm{e}}\ \operatorname{sym}\nabla u, \operatorname{sym}\nabla u\rangle\,, \\ K(\dot{u}) &= \frac{1}{2}\rho\,\langle \dot{u}, \dot{u}\rangle\,, \\ \mathcal{L}(\dot{u}, \operatorname{sym}\nabla u) &= K(\dot{u}) - W(\operatorname{sym}\nabla u)\,. \end{aligned} \tag{A.18}$$

The Cauchy continuum will be in equilibrium when associated the Action functional $\mathcal{A}$ (2.4) is at a minimum. We assume no external forces acting on the body. The internal action functional of the dynamic Cauchy continuum integrates over the body Ω_0 in the time interval $[0, \tau]$

$$\mathcal{A}\,(\dot{u}, \operatorname{sym}\nabla u) \coloneqq \int_{\Omega_0\times[0,\tau]} K(\dot{u})\,\mathrm{d}x\,\mathrm{d}t - \int_{\Omega_0\times[0,\tau]} W(\operatorname{sym}\nabla u)\,\mathrm{d}x\,\mathrm{d}t\,. \tag{A.19}$$

We pose that $\mathcal{A}$ has a minimum at u_0, which implies that for a small variation δu it holds

$$\mathcal{A}\,(\dot{u}_0 + \delta\dot{u}, \operatorname{sym}\nabla[u_0 + \delta u]) \geq \mathcal{A}\,(\dot{u}_0, \operatorname{sym}\nabla u_0)\,. \tag{A.20}$$

By introducing the scalar s, we can parameterize the previous inequality and define the scalar function $h(s)$

$$h(s) \coloneqq \mathcal{A}\,(\dot{u}_0 + s\delta\dot{u}, \operatorname{sym}\nabla[u_0 + s\delta u]) \tag{A.21}$$

$$= \int_{\Omega_0\times[0,\tau]} K\,(\dot{u}_0 + s\delta\dot{u})\,\mathrm{d}x\,\mathrm{d}t - \int_{\Omega_0\times[0,\tau]} W\,(\operatorname{sym}\nabla\,(u_0 + s\delta u))\,\mathrm{d}x\,\mathrm{d}t\,. \tag{A.22}$$

It follows that $h'(s) = 0$ at $s = 0$, and $h(s) \geq h(0)$. Let us consider that K and W are differentiable and well defined, and taking $u(s) = u_0(x,t) + s\delta u(x,t)$, we can write

$$\begin{aligned} 0 &= h'(s)\Big|_{s=0} \\ &= \frac{\mathrm{d}}{\mathrm{d}s}\mathcal{A}\,(\dot{u}, \operatorname{sym}\nabla u)\Big|_{s=0} \\ &= \frac{\mathrm{d}}{\mathrm{d}s}\int_{\Omega_0\times[0,\tau]} [-W(\operatorname{sym}\nabla u) + K\,(\dot{u})]\,\mathrm{d}x\,\mathrm{d}t\Big|_{s=0} \\ &= \int_{\Omega_0\times[0,\tau]} \frac{\mathrm{d}}{\mathrm{d}s}\,[-W(\operatorname{sym}\nabla u) + K\,(\dot{u})]\Big|_{s=0}\,\mathrm{d}x\,\mathrm{d}t \end{aligned} \tag{A.23}$$

$$
\begin{aligned}
&= \int_{\Omega_0\times[0,\tau]} \left[- \left\langle \frac{\partial W}{\partial \operatorname{sym}\nabla u}, \frac{\partial \operatorname{sym}\nabla u}{\partial s} \right\rangle \Big|_{s=0} + \left\langle \frac{\partial K}{\partial \dot{u}}, \frac{\partial \dot{u}}{\partial s} \right\rangle \Big|_{s=0} \right] \mathrm{d}x\,\mathrm{d}t \\
&= \underbrace{\int_{\Omega_0\times[0,\tau]} - \left\langle \frac{\partial W}{\partial \operatorname{sym}\nabla u}, \operatorname{sym}\nabla\delta u \right\rangle \mathrm{d}x\,\mathrm{d}t}_{W_1} + \underbrace{\int_{\Omega_0\times[0,\tau]} \left\langle \frac{\partial K}{\partial \dot{u}}, \delta\dot{u} \right\rangle \mathrm{d}x\,\mathrm{d}t}_{K_1}
\end{aligned}
$$

and thus

$$
\implies \qquad K_1 - W_1 = 0\,. \tag{A.24}
$$

We calculate the contributions of Kinetic and Strain energy densities separately starting with term W_1

$$
\begin{aligned}
W_1 = \int_{\Omega_0\times[0,\tau]} \left\langle \frac{\partial W}{\partial \operatorname{sym}\nabla u}, \operatorname{sym}\nabla\delta u \right\rangle \mathrm{d}x\,\mathrm{d}t &= \int_{\Omega_0\times[0,\tau]} \sigma_{ij}\delta u_{i,j}\,\mathrm{d}x\,\mathrm{d}t \\
&= \int_{\Omega_0\times[0,\tau]} [\sigma_{ij,j}\delta u_i + \sigma_{ij}\delta u_{i,j} - \sigma_{ij,j}\delta u_i]\,\mathrm{d}x\,\mathrm{d}t \\
&= \int_{\Omega_0\times[0,\tau]} \left[(\sigma_{ij}\delta u_i)_{,j} - \sigma_{ij,j}\delta u_i \right] \mathrm{d}x\,\mathrm{d}t \\
&= \int_{\Omega_0\times[0,\tau]} (\sigma_{ij}\delta u_i)_{,j}\,\mathrm{d}x\,\mathrm{d}t - \int_{\Omega_0\times[0,\tau]} \sigma_{ij,j}\delta u_i\,\mathrm{d}x\,\mathrm{d}t \\
&= \int_{\partial\Omega_0\times[0,\tau]} \sigma_{ij}\delta u_i n_j\,\mathrm{d}s\,\mathrm{d}t - \int_{\Omega_0\times[0,\tau]} \sigma_{ij,j}\delta u_i\,\mathrm{d}x\,\mathrm{d}t \\
&= \int_{\partial\Omega_0\times[0,\tau]} \langle \sigma n, \delta u\rangle\,\mathrm{d}s\,\mathrm{d}t - \int_{\Omega_0\times[0,\tau]} \langle \operatorname{Div}\sigma, \delta u\rangle\,\mathrm{d}x\,\mathrm{d}t\,.
\end{aligned} \tag{A.25}
$$

We calculate the contribution K_1 of the Kinetic energy density for the case of a system that exhibits the isochronous condition $\delta u(0) = \delta u(\tau) = 0$ by

$$
\begin{aligned}
K_1 = \int_{\Omega_0\times[0,\tau]} \left\langle \frac{\partial K}{\partial \dot{u}}, \delta\dot{u} \right\rangle \mathrm{d}x\,\mathrm{d}t &= \int_{\Omega_0\times[0,\tau]} \langle \rho\dot{u}, \delta\dot{u}\rangle\,\mathrm{d}x\,\mathrm{d}t \\
&= \cancel{\left[\int_{\Omega_0\times[0,\tau]} \langle \rho\dot{u}, \delta u\rangle\,\mathrm{d}x \right]_0^\tau} - \int_{\Omega_0\times[0,\tau]} \langle \rho\ddot{u}, \delta u\rangle\,\mathrm{d}x\mathrm{d}t \\
&= - \int_{\Omega_0\times[0,\tau]} \langle \rho\ddot{u}, \delta u\rangle\,\mathrm{d}x\mathrm{d}t\,.
\end{aligned} \tag{A.26}
$$

Substituting K_1 and W_1 in eq. (A.24) we end up with the weak form of the equilibrium equations

$$
- \int_{\partial\Omega_0\times[0,\tau]} \langle \sigma n, \delta u\rangle \mathrm{d}s\,\mathrm{d}t \; + \int_{\Omega_0\times[0,\tau]} \langle \operatorname{Div}\sigma, \delta u\rangle \mathrm{d}x\,\mathrm{d}t \; - \int_{\Omega_0\times[0,\tau]} \langle \rho\ddot{u}, \delta u\rangle\,\mathrm{d}x\,\mathrm{d}t = 0\,, \qquad \forall \delta u \tag{A.27}
$$

where $\operatorname{Div}\sigma$ and $\rho\ddot{u}$ are forces per unit volume, and σn is a force per unit area. The condition imposed by eq. (A.27) implies the strong form of the equilibrium equations and the associated Neumann boundary condition

$$
\begin{aligned}
\operatorname{Div}\sigma &= \rho\ddot{u} && \text{in} \quad \Omega_0\,, \\
\sigma n &= 0 && \text{on} \quad \partial\Omega_0\,.
\end{aligned} \tag{A.28}
$$

A.4 First variation for the RRMM

The Langrangian of the RRMM is given by eq. (3.3) as

$$
\begin{aligned}
K(\dot{u}, \nabla\dot{u}, \dot{P}) &= \frac{1}{2}\rho\,\langle \dot{u}, \dot{u}\rangle + \frac{1}{2}\langle \mathbb{J}_{\mathrm{m}}\,\operatorname{sym}\dot{P}, \operatorname{sym}\dot{P}\rangle + \frac{1}{2}\langle \mathbb{J}_{\mathrm{c}}\,\operatorname{skew}\dot{P}, \operatorname{skew}\dot{P}\rangle \\
&\quad + \frac{1}{2}\langle \mathbb{T}_{\mathrm{e}}\,\operatorname{sym}\nabla\dot{u}, \operatorname{sym}\nabla\dot{u}\rangle + \frac{1}{2}\langle \mathbb{T}_{\mathrm{c}}\,\operatorname{skew}\nabla\dot{u}, \operatorname{skew}\nabla\dot{u}\rangle\,, \\
W(\nabla u, P) &= \frac{1}{2}\langle \mathbb{C}_{\mathrm{e}}\,\operatorname{sym}(\nabla u - P), \operatorname{sym}(\nabla u - P)\rangle + \frac{1}{2}\langle \mathbb{C}_{\mathrm{c}}\,\operatorname{skew}(\nabla u - P), \operatorname{skew}(\nabla u - P)\rangle \\
&\quad + \frac{1}{2}\langle \mathbb{C}_{\mathrm{micro}}\,\operatorname{sym} P, \operatorname{sym} P\rangle\,, \\
\mathcal{L}(\dot{u}, \nabla\dot{u}, \dot{P}, \nabla u, P) &= K(\dot{u}, \nabla\dot{u}, \dot{P}) - W(\nabla u, P)\,.
\end{aligned} \tag{A.29}
$$

The RRM continuum will be in equilibrium when the associated Action functional $\mathcal{A}$ (3.4) is at a minimum. We assume no external forces acting on the body. The internal action functional of the dynamic RRM continuum, integrates over the body Ω_0 in the time interval $[0, \tau]$

$$
\mathcal{A}\left(\dot{u}, \nabla\dot{u}, \dot{P}, \nabla u, P\right) := \int_{\Omega_0\times[0,\tau]} K\left(\dot{u}, \nabla\dot{u}, \dot{P}\right) \mathrm{d}x\,\mathrm{d}t \; - \int_{\Omega_0\times[0,\tau]} W(\nabla u, P)\,\mathrm{d}x\,\mathrm{d}t\,. \tag{A.30}
$$

We pose that $\mathcal{A}$ has a minimum at u_0, which implies that for a small variation δu and δP it holds

$$\mathcal{A}\left(\dot{u_0}+\delta\dot{u},\nabla[\dot{u_0}+\delta\dot{u}],\dot{P}_0+\delta\dot{P},\nabla u_0+\delta u,P_0+\delta P\right)\geq\mathcal{A}\left(\dot{u_0},\nabla\dot{u_0},\dot{P}_0,\nabla u_0,P_0\right). \tag{A.31}$$

By introducing the scalar s, we can parameterize the previous inequality and define the scalar function $h(s)$

$$h(s)=\mathcal{A}\left(\dot{u_0}+s\delta\dot{u},\nabla[\dot{u_0}+s\delta\dot{u}],\dot{P}_0+s\delta\dot{P},\nabla u_0+s\delta u,P_0+s\delta P\right). \tag{A.32}$$

It follows that $h'(s)=0$ at $s=0$, and $h(s)\geq h(0)$. Let us consider that K and W are differentiable and well defined. We split the derivative $h'(s)\Big|_{s=0}$ into its Kinetic and Strain energy parts $h'_W(s)\Big|_{s=0}$ and $h'_K(s)\Big|_{s=0}$ so that

$$h'(s)\Big|_{s=0}=-h'_W(s)\Big|_{s=0}+h'_K(s)\Big|_{s=0}=0\,. \tag{A.33}$$

We also consider that $u(s)=u_0(x,t)+s\delta u(x,t)$ and $P(s)=P_0(x,t)+s\delta P(x,t)$. We calculate the two terms separately starting with the contribution of the Kinetic Energy density

$$\begin{aligned}
h'_K(s)\Big|_{s=0} &= \int_{\Omega_0\times[0,\tau]}\frac{\mathrm{d}}{\mathrm{d}s}\left[K\left(\dot{u},\nabla\dot{u},\dot{P}\right)\right]\Big|_{s=0}\mathrm{d}x\,\mathrm{d}t\\
&=\int_{\Omega_0\times[0,\tau]}\left[\left\langle\frac{\partial K}{\partial\dot{u}},\frac{\partial\dot{u}}{\partial s}\right\rangle\Big|_{s=0}+\left\langle\frac{\partial K}{\partial\nabla\dot{u}},\frac{\partial\nabla\dot{u}}{\partial s}\right\rangle\Big|_{s=0}+\left\langle\frac{\partial K}{\partial\dot{P}},\frac{\partial\dot{P}}{\partial s}\right\rangle\Big|_{s=0}\right]\mathrm{d}x\,\mathrm{d}t\\
&=\underbrace{\int_{\Omega_0\times[0,\tau]}-\langle\rho\ddot{u},\delta\dot{u}\rangle\,\mathrm{d}x\,\mathrm{d}t}_{K_1}+\underbrace{\int_{\Omega_0\times[0,\tau]}\langle\mathbb{T}_{\mathfrak{e}}\,\mathrm{sym}\,\nabla\dot{u},\nabla\delta\dot{u}\rangle\,\mathrm{d}x\,\mathrm{d}t}_{K_2}\\
&\quad+\underbrace{\int_{\Omega_0\times[0,\tau]}\langle\mathbb{T}_{\mathfrak{c}}\,\mathrm{skew}\,\nabla\dot{u},\nabla\delta\dot{u}\rangle\,\mathrm{d}x\,\mathrm{d}t}_{K_3}+\underbrace{\int_{\Omega_0\times[0,\tau]}\left\langle\mathbb{J}_{\mathfrak{m}}\,\mathrm{sym}\,\dot{P},\mathrm{sym}\,\delta\dot{P}\right\rangle\mathrm{d}x\,\mathrm{d}t}_{K_4}\\
&\quad+\underbrace{\int_{\Omega_0\times[0,\tau]}\left\langle\mathbb{J}_{\mathfrak{c}}\,\mathrm{skew}\,\dot{P},\mathrm{skew}\,\delta\dot{P}\right\rangle\mathrm{d}x\,\mathrm{d}t}_{K_5}
\end{aligned} \tag{A.34}$$

We calculate the Kinetic energy density's contributions separately in the case of a system that exhibits the isochronous condition $\delta u(0)=\delta u(\tau)=0$ and $\delta P(0)=\delta P(\tau)=0$. Term K_1 is identical to the one in Cauchy elasticity while the rest are calculated by using integration by parts and Gauss's theorem

$$\begin{aligned}
K_1 &= -\int_{\Omega_0\times[0,\tau]}\langle\rho\ddot{u},\delta u\rangle\,\mathrm{d}x\,\mathrm{d}t\,,\\
K_2 &= -\int_{\partial\Omega_0\times[0,\tau]}\langle\mathbb{T}_{\mathfrak{e}}\,\mathrm{sym}\,\nabla\ddot{u}\,n,\delta u\rangle\,\mathrm{d}s\,\mathrm{d}t+\int_{\Omega_0\times[0,\tau]}\langle\mathrm{Div}\left[\mathbb{T}_{\mathfrak{e}}\,\mathrm{sym}\,\nabla\ddot{u}\right],\delta u\rangle\,\mathrm{d}x\,\mathrm{d}t\,,\\
K_3 &= -\int_{\partial\Omega_0\times[0,\tau]}\langle\mathbb{T}_{\mathfrak{c}}\,\mathrm{skew}\,\nabla\ddot{u}\,n,\delta u\rangle\,\mathrm{d}s\,\mathrm{d}t+\int_{\Omega_0\times[0,\tau]}\langle\mathrm{Div}\left[\mathbb{T}_{\mathfrak{c}}\,\mathrm{skew}\,\nabla\ddot{u}\right],\delta u\rangle\,\mathrm{d}x\,\mathrm{d}t\,,\\
K_4 &= -\int_{\Omega_0\times[0,\tau]}\left\langle\mathbb{J}_{\mathfrak{m}}\,\mathrm{sym}\,\nabla\ddot{P},\delta P\right\rangle\mathrm{d}x\,\mathrm{d}t\,,\\
K_5 &= -\int_{\Omega_0\times[0,\tau]}\left\langle\mathbb{J}_{\mathfrak{c}}\,\mathrm{skew}\,\nabla\ddot{P},\delta P\right\rangle\mathrm{d}x\,\mathrm{d}t\,.
\end{aligned} \tag{A.35}$$

For the contribution of the Strain Energy density W we have

$$\begin{aligned}
h'_W(s)\Big|_{s=0} &= \int_{\Omega_0\times[0,\tau]}\frac{\mathrm{d}}{\mathrm{d}s}\left[W\left(\nabla u,P\right)\right]\Big|_{s=0}\mathrm{d}x\,\mathrm{d}t\\
&=\int_{\Omega_0\times[0,\tau]}\left[\left\langle\frac{\partial W}{\partial\nabla u},\frac{\partial\nabla u}{\partial s}\right\rangle\Big|_{s=0}+\left\langle\frac{\partial W}{\partial P},\frac{\partial P}{\partial s}\right\rangle\Big|_{s=0}\right]\mathrm{d}x\,\mathrm{d}t\\
&=\underbrace{\int_{\Omega_0\times[0,\tau]}\langle\mathbb{C}_{\mathfrak{e}}\,\mathrm{sym}\left(\nabla u-P\right),\mathrm{sym}\left(\nabla\delta u-\delta P\right)\rangle\,\mathrm{d}x\,\mathrm{d}t}_{W_1}\\
&\quad+\underbrace{\int_{\Omega_0\times[0,\tau]}\langle\mathbb{C}_{\mathfrak{c}}\,\mathrm{skew}\left(\nabla u-P\right),\mathrm{skew}\left(\nabla\delta u-\delta P\right)\rangle\,\mathrm{d}x\,\mathrm{d}t}_{W_2}\\
&\quad+\underbrace{\int_{\Omega_0\times[0,\tau]}\langle\mathbb{C}_{\mathfrak{m}}\,\mathrm{sym}\,P,\mathrm{sym}\,\delta P\rangle\,\mathrm{d}x\,\mathrm{d}t}_{W_3}\,.
\end{aligned} \tag{A.36}$$

We calculate the Strain energy density's contributions separately by using Gauss's theorem. We end up with

$$
\begin{aligned}
W_1 &= \int_{\partial\Omega_0\times[0,\tau]} \langle \mathbb{C}_{\mathrm{e}} \operatorname{sym}(\nabla u - P)\, n, \delta u\rangle \,\mathrm{d}s\,\mathrm{d}t - \int_{\Omega_0\times[0,\tau]} \langle \operatorname{Div}\left[\mathbb{C}_{\mathrm{e}} \operatorname{sym}(\nabla u - P)\right], \delta u\rangle \,\mathrm{d}x\,\mathrm{d}t \\
&\quad - \int_{\Omega_0\times[0,\tau]} \langle \mathbb{C}_{\mathrm{e}} \operatorname{sym}(\nabla u - P), \delta P\rangle \,\mathrm{d}x\,\mathrm{d}t\,, \\
W_2 &= \int_{\partial\Omega_0\times[0,\tau]} \langle \mathbb{C}_{\mathrm{c}} \operatorname{skew}(\nabla u - P)\, n, \delta u\rangle \,\mathrm{d}s\,\mathrm{d}t - \int_{\Omega_0\times[0,\tau]} \langle \operatorname{Div}\left[\mathbb{C}_{\mathrm{c}} \operatorname{skew}(\nabla u - P)\right], \delta u\rangle \,\mathrm{d}x\,\mathrm{d}t \\
&\quad - \int_{\Omega_0\times[0,\tau]} \langle \mathbb{C}_{\mathrm{c}} \operatorname{skew}(\nabla u - P), \delta P\rangle \,\mathrm{d}x\,\mathrm{d}t\,, \\
W_3 &= \int_{\Omega_0\times[0,\tau]} \langle \mathbb{C}_{\mathfrak{m}} \operatorname{sym} P, \delta P\rangle \,\mathrm{d}x\,\mathrm{d}t\,.
\end{aligned}
\tag{A.37}
$$

According to (A.33) we must have

$$
K_1 + K_2 + K_3 + K_4 + K_5 - W_1 - W_2 - W_3 = 0\,. \tag{A.38}
$$

The condition imposed above implies the strong form of the equilibrium equations of the RRMM as

$$
\rho\ddot{u} - \operatorname{Div}\widehat{\sigma} = \operatorname{Div}\widetilde{\sigma} \qquad \text{and} \qquad \overline{\sigma} = \widetilde{\sigma} - s \qquad \text{in} \quad \Omega_0 \tag{A.39}
$$

where

$$
\begin{aligned}
&\widetilde{\sigma} \coloneqq \mathbb{C}_{\mathrm{e}} \operatorname{sym}(\nabla u - P) + \mathbb{C}_{\mathrm{c}} \operatorname{skew}(\nabla u - P)\,, && \widehat{\sigma} \coloneqq \mathbb{T}_{\mathrm{e}} \operatorname{sym}\nabla\ddot{u} + \mathbb{T}_{\mathrm{c}} \operatorname{skew}\nabla\ddot{u}\,, \\
&s \coloneqq \mathbb{C}_{\mathrm{micro}} \operatorname{sym} P\,, && \overline{\sigma} \coloneqq \mathbb{J}_{\mathrm{m}} \operatorname{sym}\ddot{P} + \mathbb{J}_{\mathrm{c}} \operatorname{skew}\ddot{P}
\end{aligned}
\tag{A.40}
$$

with the associated Neumann boundary condition

$$
\widetilde{t} \coloneqq (\widetilde{\sigma} + \widehat{\sigma})\, n = 0\,, \qquad \text{in} \quad \partial\Omega_0 \tag{A.41}
$$

where $\widetilde{t}$ is the generalized traction and n is the normal to the boundary.